Stable tungsten isotopes as a tracer for the redox state of the past oceans: testing the potential and limits of the proxy

Dissertation
der Mathematisch-Naturwissenschaftlichen Fakultät
der Eberhard Karls Universität Tübingen
zur Erlangung des Grades eines
Doktors der Naturwissenschaften
(Dr. rer. nat.)

vorgelegt von
MSc Lucile Roué
aus Brest/Frankreich

Tübingen
2021

Gedruckt mit Genehmigung der Mathematisch-Naturwissenschaftlichen Fakultät der Eberhard Karls Universität Tübingen.

Tag der mündlichen Qualifikation:	13.04.2022
Dekan:	Prof. Dr. Thilo Stehle
1. Berichterstatter:	Prof. Dr. Ronny Schoenberg
2. Berichterstatter:	Prof. Dr. Harald Strauss

Contents

Acknowledgements

I would like to express my deep gratitude to Professor Ronny Schoenberg, who gave me the opportunity to work on this thesis for the past four years. I would like to thank him for the trust he put in my work all of this time, and for all the freedom I had for exploring the stable W isotopes world. I am most grateful to the experience gained in the Isotope Geochemistry facilities of the University of Tübingen and for the amazing fieldtrip in South Africa 2018.

The help, expertise and support provided by Assistant Prof. Michael Babechuk, Dr. Florian Kurzweil, and Dr. Martin Wille during this project are deeply appreciated. Thank you for all the constructive discussions that greatly improved the quality of our manuscript. I learned a lot from you !

Many thanks to all the group of Isotope geochemistry, Heinrich Taubald, Elmar Reitter, Bernd Steinhilber, Luise Wagner, Benny Eickmann, Gulüm Albut, Marie-Laure Pons, Julius Havsteen, Markus Gogouvitis, Maria Isabel Varas Reus, Stephan König, Yunfeng Wang, Ilka Kleinhanns, Carolina Rosca. It was fun being around you !

I will always remember the first time I saw Tübingen during my PhD interview, and how I already felt like home even thought I did not understand a single spoken word. This thesis has been a roller-coaster journey with ups and many downs, and I would like to thank Luise Wagner, Benny Eickmann, Gulüm Albut, Marie-Laure Pons, the French mafia and many others for funny coffee breaks, after-work beers, memorable Barbara parties, but especially for lending me a shoulder at times when I needed it the most. A very special thank for the new friends from the department next door who made the Morgenstelle campus a very fun place to be.

I would like to finally thank my family who supported me ever since I decided to walk on the research road, and I feel the most proud to become the second doctor in our family. Finally, all of my gratitude to Manu, his family, his friends, and our furry friend that made home much warmer and cosy.

Contributions of others

Chapter 2: Published paper

Title: Stable W and Mo isotopic evidence for increasing redox-potentials from the Paleoarchean towards the Paleoproterozoic deep Ocean

Authors: Lucile Roué, Florian Kurzweil, Martin Wille, Antje Wegwerth, Olaf Dellwig, Carsten Münker, Ronny Schoenberg

Status: published in 2021 (Geochimica et Cosmochimica Acta, Volume 309, Pages 366-387)

Declaration contributions by author :

Position in list of authors	1
Scientific ideas	80%
Data generation	95%
Analysis and interpretation	90%
Writing	80%

Chapter 3

Title: Stable W and Mo isotope variations of organic-rich shales from the Zaonega Formation: Interaction between continental rifting, redox changes and post-depositional hydrothermal alteration

Authors: Lucile Roué, Benjamin Eickmann and Ronny Schoenberg

Status: unpublished

Declaration contributions by author:

Scientific ideas	90%
Data generation	100%
Analysis and interpretation	95%
Writing	90%

Chapter 4

Title: Stable W isotopes behaviour during anoxic continental weathering: evidence from two paleosols profiles of the 2.77 Ga Mt Roe Basalt

Authors: Lucile Roué, Michael Babechuk and Ronny Schoenberg

Status: unpublished

Declaration contributions by author :

Scientific ideas	90%
Data generation	80%
Analysis and interpretation	95%
Writing	90%

Chapter 5

Title: W stable isotopes in carbonates: leaching, chemical separation and preliminary results

Authors: Lucile Roué, Michael Babechuk and Ronny Schoenberg

Status: unpublished

Declaration contributions by author :

Scientific ideas	90%
Data generation	90%
Analysis and interpretation	95%
Writing	95%

For this study 98 % of the new laboratory work and data collection, and about 90 % of the data evaluation and interpretation, and 85 % of writing were performed by myself. In the following the scientific contributions of others are listed:

Project idea

The project idea for the use of W isotopes as a proxy for ancient redox state of the ocean was developed by Prof. Ronny Schoenberg (University of Tübingen, Germany). Collaboration with Assistant Prof. Michael Babechuk (Memorial University of Newfoundland and Labrador, Canada) resulted with the study of W isotopes in paleosol samples.

Sample collection

The shale samples of the ABDP 2-3-5-6-9 shales were previously obtained for the research of Dr. Martin Wille (University of Bern, Switzerland) and Dr. Florian Kurzweil (University of Cologne, Germany) and were stored in the facilities of the University of Tübingen.

Shale samples of the core 12 AB and carbonates samples of the cores 5A and 8B from the FAR-DEEP project were sampled by Dr. Mark van Zuilen (IPGP, France), Prof. Ronny Schoenberg (University of Tübingen, Germany), Assistant Prof. Benjamin Eickmann (Universidad de los Andes, Colombia) from the Geological Survey of Norway, National Drill Core and Sample Centre between 2009 and 2018.

The paleosol samples of the ABDP-6 core were obtained from Dr. Eva Stuecken (University of St. Andrews, Scotland) and Assistant Prof. Michael Babechuk (Memorial University of Newfoundland and Labrador, Canada).

The samples of modern sapropels from the Black Sea were obtained from Dr. Antje Wegwerth and Dr. Olaf Dellwig (Leibniz Institute for Baltic Sea Research Warnemünde, Germany).

The samples of modern carbonate sands were collected and obtained from Associate Prof. Achim Herrmann (Louisiana State University, USA).

Samples from the AGP1-2 and MP-72 cores were sampled by myself with the assistance of Assistant Prof. Benjamin Eickmann (Universidad de los Andes, Colombia), Prof. Nicolas Beukes and Dr. Albertus Smith (University of Johannesburg, South Africa) during a field campaign in 2018.

Various igneous rocks were provided by Prof. Ronny Schoenberg , Dr. Ilka Kleinhanns, Ms. Luise Wagner (University of Tübingen, Germany).

Analyses

100 % of the digestion, chemical separation and measurement for stable W isotopes determination were performed by myself.

100 % of the new digestion, chemical separation and measurement for stable Mo isotopes determination were performed by myself.

The digestion, chemical separation and measurement for new stable Cr isotopes determination were performed by Dr. Florian Kurzweil (University of Cologne, Germany) in the facilities of the University of Tübingen.

100 % of the preparation for new major (sample powder dilution with spectromelt powder) and trace (digestion, dilution and addition of internal standard) elements reported in this thesis were performed by myself. Bernd Steinhilber and Dr. Heinrich Taubald (University of Tübingen, Germany) conducted the measurements, data reduction and quality evaluation.

Text, figures and tables

Prof. Ronny Schoenberg (University of Tübingen, Germany), Dr. Martin Wille (University of Bern, Switzerland), Dr. Florian Kurzweil (University of Cologne, Germany), Assistant Prof. Michael Babechuk (Memorial University of Newfoundland and Labrador, Canada), Assistant Prof. Benjamin Eickmann (Universidad de los Andes, Colombia) and Dr. Olaf Dellwig (Leibniz Institute for Baltic Sea Research Warnemünde, Germany) partly edited this thesis.

Chapter 2 (”Stable W and Mo isotopic evidence for increasing redox-potentials from the Paleoarchean towards the Paleoproterozoic deep Ocean”) has been published in the international journal Geochimica et Cosmochimica Acta (DOI: 10.1016/j.gca.2021.05.013).

The chapters 3 (”Stable W and Mo isotope variations of organic-rich shales from the ZaonegaFm. : Interaction between continental rifting, redox changes and post-depositional hydrothermal alteration”) and 4 (”Stable W isotopes behaviour during anoxic continental weathering:evidence from two paleosols profiles ofthe 2.77 Ga Mt Roe Basalt”) are under preparation for submission to peer-review international journals.

All figures and tables were prepared by myself.

Scientific ideas

Many discussions and suggestions from Prof. Ronny Schoenberg (University of Tübingen, Germany), Dr. Martin Wille (University of Bern, Switzerland), Dr. Florian Kurzweil (University of Cologne, Germany), Assistant Prof. Michael Babechuk (Memorial University of Newfoundland and Labrador, Canada), Assistant Prof. Benjamin Eickmann (Universidad de los Andes, Colombia) helped me with the data interpretation.

Abstract

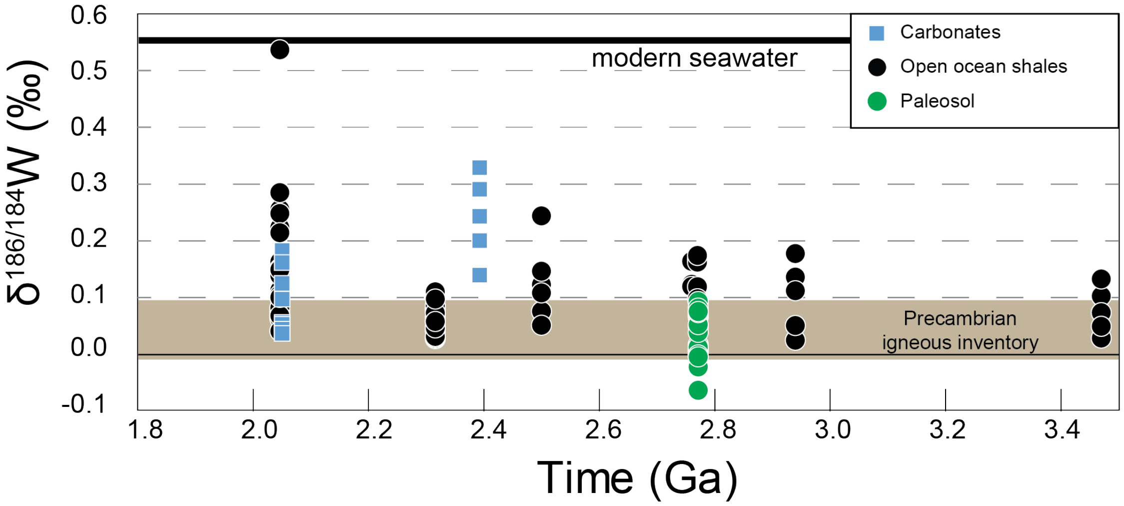

Figure 1: Compilation of all $\delta^{186/184}$W values measured on Paleoproterozoic to Paleoarchean marine shales, carbonates and paleosol profiles samples during the course of this study. Seawater $\delta^{186/184}$W value originates from Fujiwara et al. (2020) and Kurzweil et al. (2021).

Tungsten belongs to the group 6 of the Periodic Table of the elements and shares numerous properties with Mo, such as a long residence time in the modern ocean and a seawater stable W isotopic composition ($\delta^{186/184}$W value) of ∼+0.55 ‰ controlled by adsorption of tungstate (WO_4^{2-}) onto Mn-Fe oxides with a well characterized associated isotopic fractionation of +0.59 to +0.51 ‰, respectively. Tungsten exists as soluble WO_4^{2-} over a very large range of Eh-pH values and as such is considered as a promising proxy for the redox state of ancient and reducing oceans. In this thesis, the $\delta^{186/184}$W values of ancient and modern sediments as well as weathered profiles are investigated in order to test the potential of W for tracking the earliest changes in the redox state of the ocean.

Following a general introduction in chapter 1, chapter 2 of this thesis focuses on establishing the foundations of the use of W isotopes in Precambrian marine samples. First, the stable W isotopic composition of igneous rocks representative of the Precambrian continental crust (Precambrian Igneous Inventory, PII) was investigated and revealed a narrow range in

$\delta^{186/184}$W values from -0.007 to +0.097 ‰, similar to that of modern igneous rocks (-0.010 to +0.110 ‰). Subsequently, well characterized euxinic sapropel samples deposited during the Holocene in the Black Sea revealed crustal-like W concentrations and $\delta^{186/184}$W values, in accordance with models predicting little to no W authigenic enrichments in euxinic depositional settings. Similarly, marine shales deposited around 2.32 Ga revealed a very narrow $\delta^{186/184}$W range, and suggest porewater or bottom water euxinic conditions during deposition. The study of open ocean ferruginous marine shales deposited between 3.47 to 2.5 Ga showed a large spread in $\delta^{186/184}$W values from the PII range towards heavier $\delta^{186/184}$W values, reaching up to +0.246 ‰ at 2.5 Ga. The isotopically heavy W component in these shales was interpreted as originating from an authigenic marine W source with a heavy $\delta^{186/184}$W value. These findings contrast to the crustal-like stable Mo isotopic compositions ($\delta^{98/95}$Mo values) of these samples, which were interpreted as indicating low redox potential disabling Mo as a soluble oxyanion until 2.6 Ga. This study concludes that W was present in the ocean as early as 3.47 Ga and can authigenically accumulate in ferruginous ancient marine sediments.

Chapter 3 of this thesis investigated combined Mo and W isotopes in organic rich-marine shales of the Zaonega Fm (Karelian Craton, Fennoscandian Shield), deposited during the Shunga Event (2.0 Ga), representing the termination of the Great Oxidation Event (GOE). Many studies previously interpreted the chemical signals of the Zaonega Fm. as evidence for a global collapse in molecular dioxygen, or changes in the depositional settings. Using new Mo and W isotopes data, we reveal opposed $\delta^{98/95}$Mo and $\delta^{186/184}$W trends associated with increasing concentrations in V, Mo and W upwards in the sedimentary sequence. The evolution in these chemical signals in the Zaonega Fm. are related to the opening of the Onega paleobasin to the open ocean, inducing changes in depositional environments from restricted-euxinic to an oxygen minimum zone-like environment. The $\delta^{98/95}$Mo and $\delta^{186/184}$W values of these sediments are characteristic of the isotopic fractionation measured for Mo and W adsorption onto Fe-oxides, indicating that the cycling of these elements was controlled by Fe-oxides, rather than Mn-oxides. This observation implies that the termination of the GOE did not enable Mn-oxides persistence in the global ocean.

Chapter 4 focuses on W concentrations and $\delta^{186/184}$W values in two weathered profiles of the 2.77 Ga Mt Roe Basalt (Pilbara Craton, Australia). These two profiles were weathered under an anoxic atmosphere resulting in W loss. The association between $\delta^{186/184}$W values and plagioclase alteration proxies revealed that isotopically light W was likely retained in weathering products such as clays and aluminum oxides, while the residual dissolved W was removed from the profile with meteoritic waters. The $\delta^{186/184}$W and associated loss of W values follow an equilibrium isotopic fractionation in a closed system with an isotopic fractionation factor $\varepsilon^{186/184}\mathrm{W}_{dissolved-adsorbed}$ of +0.126 ‰. This study reveals that W, unlike U and Mo, was very efficiently removed from exposed surfaces before the atmosphere became oxidized, unlike U and Mo. The riverine inputs of W to the oceans likely drove the ocean W isotopic composition towards heavier values, and likely can explain the earliest fractionated $\delta^{186/184}$W values from the 3.47 Ga to 2.77 Ga marine shales reported in the chapter 2.

Chapter 5 reports method development for W isotopes determination in carbonates. First, the trace element concentrations of four carbonate reference materials leached with 3 M HCl, 5 %v HNO_3, 5 M acetic acid were compared with the aim of selecting the most efficient leaching method for high authigenic W concentrations in the leachates. Then, the efficiency of the equilibration of sample and double spike-sourced W was investigated in both HNO_3 and HCl leachates. Based on W concentrations and $\delta^{186/184}$W values of the leachates, the method of choice for chemical separation of W from carbonate matrix involve a HCl leaching step, followed by double spiking in the same media before column chemistry, in order to reduce the use of different acids before column chemistry. This chapter reports $\delta^{186/184}$W values of carbonates from various depositional environments, from modern to 2.39 Ga, and reveal the potential of W isotopes in open marine carbonates as a proxy for the evolution of the ocean's redox state through time.

In conclusion, this study confirms that W stable isotopes in ancient ferruginous marine sediments has very high potential to fill the knowledge gap of the evolution of the redox states of the Paleoarchean to Paleoproterozoic oceans. The W isotopes proxy is based on a well constrained detrital background (PII $\delta^{186/184}$W values), on early W mobility, either from anoxic weathering ($\delta^{186/184}$W values up to +0.174 ‰) or from hydrothermal fluids (source-like $\delta^{186/184}$W values), and on large isotopic fractionation during WO_4^{2-} adsorption onto Fe-oxides (+0.51 ‰) resulting in isotopically heavy residual WO_4^{2-}. As a result, this thesis proposes a three step increase in redox potential during the Archean: (1) at 3.47 Ga, the low W isotopic composition (<0.132 ‰) of marine shales reveal that the W inputs to the ocean were mostly controlled by hydrothermal fluids leaching igneous W. (2) Then, from 2.94 to 2.77 Ga, marine shales reveal $\delta^{186/184}$W values reaching up to +0.177 ‰, interpreted as resulting from the rise of continental masses and associated increasing inputs of W from anoxic subaerial weathering, rather than W cycling onto oxides in proximal-shallow environments. (3) Finally, carbonates and ferruginous shales deposited from 2.5 to 2.0 Ga recorded increasing $\delta^{186/184}$W values reaching up to modern-like seawater, indicating a global increase of redox potential with intensive Fe-(Mn)-oxides cycling.

Zussammenfassung

Wolfram gehört zur Gruppe 6 des Periodensystems und hat zahlreiche Eigenschaften mit Mo gemeinsam, z. B. eine lange Verweildauer im modernen Ozean und eine stabile W-Isotopenzusammensetzung ($\delta^{186/184}$W-Wert) im modernen Ozean, die durch die Adsorption von Wolframat (WO_4^{2-}) an Mn-Fe-Oxide mit einer damit verbundenen Isotopenfraktionierung gesteuert wird. Wolfram liegt als lösliches WO_4^{2-} über einen sehr großen Bereich von Eh-pH-Werten vor und gilt daher als vielversprechender Indikator für den Redoxzustand alter und reduzierender Ozeane. In dieser Arbeit werden die $\delta^{186/184}$W-Werte von alten und modernen Sedimenten sowie von verwitterten Profilen untersucht, um das Potenzial von W für die Verfolgung der frühesten Veränderungen im Redoxzustand des Ozeans zu testen.

Nach einer allgemeinen Einführung in Kapitel 1 konzentriert sich Kapitel 2 dieser Arbeit darauf, die Grundlagen für die Verwendung von W-Isotopen in präkambrischen Meereproben zu schaffen. Zunächst wurde die stabile W-Isotopenzusammensetzung von Eruptivgesteinen untersucht, die für die präkambrische kontinentale Kruste (PII) repräsentativ sind, und es zeigte sich, dass die $\delta^{186/184}$W-Werte in einem engen Bereich von -0.007 bis +0.097 ‰ liegen, ähnlich wie bei den modernen Eruptivgesteinen (-0.010 bis +0.110 ‰). Gut charakterisierte euxinische Sapropel-Proben, die während des Holozäns im Schwarzen Meer abgelagert wurden, wiesen krustenähnliche W-Konzentrationen und $\delta^{186/184}$W-Werte auf, was mit Modellen übereinstimmt, die eine geringe bis gar keine Anreicherung von W in euxinischen Ablagerungsgebieten vorhersagen. Meeresschiefer, die um 2.32 Ga abgelagert wurden, wiesen eine sehr enge $\delta^{186/184}$W-Spanne auf, die der von modernen euxinischen Sedimenten gleicht und auf euxinische Porenwasser- oder Bodenwasserbedingungen während der Ablagerung schließen lässt. Die Untersuchung von eisenhaltigen Schiefergesteinen aus dem offenen Ozean, die zwischen 3.47 und 2.5 Ga abgelagert wurden, zeigte eine große Streuung der $\delta^{186/184}$W-Werte vom PII-Bereich hin zu schwereren $\delta^{186/184}$W-Werten, die bei 2.5 Ga bis zu +0.246 ‰ erreichten. Die isotopisch schwere W-Komponente in diesen Schiefergesteinen wurde als von einer authigenen

marinen W-Quelle mit einem schweren $\delta^{186/184}$W-Wert stammend interpretiert. Diese Ergebnisse stehen im Gegensatz zu den krustenähnlichen stabilen Mo-Isotopenzusammensetzungen ($\delta^{98/95}$Mo-Werte) dieser Proben, die wir als Hinweis auf ein niedriges Redoxpotential interpretierten, das Mo bis 2.6 Ga als lösliches Oxyanion ausschließt. Aufgrund des fehlenden Wissens über den W-Zyklus und die damit verbundenen $\delta^{186/184}$W-Werte können wir nicht zu dem Schluss kommen, dass die in den Schieferproben gemessenen hohen $\delta^{186/184}$W-Werte die Werte des umgebenden Ozeans widerspiegeln. Dennoch kommt diese Studie zu dem Schluss, dass W bereits vor 3.47 Ga im Ozean vorhanden war und sich in eisenhaltigen alten Meeressedimenten authigen anreichern kann.

In Kapitel 3 dieser Arbeit wurden kombinierte Mo- und W-Isotope in organisch reichen marinen Schiefergesteinen der Zaonega Fm (Karelischer Kraton, Fennoskandischer Schild) untersucht, die während des Shunga-Ereignisses (∼2.0 Ga) abgelagert wurden, das das Ende des Großen Oxidationsereignisses (GOE) darstellt. In vielen Studien wurden die chemischen Signale der Zaonega Fm. bisher als Beweis für einen globalen Zusammenbruch des molekularen Sauerstoffs oder für Veränderungen in den Ablagerungsbedingungen interpretiert. Unter Verwendung neuer Mo- und W-Isotopendaten zeigen wir gegenläufige $\delta^{98/95}$Mo- und $\delta^{186/184}$W-Trends, die mit steigenden Konzentrationen von V, Mo und W in der Sedimentabfolge nach oben verbunden sind. Die Entwicklung dieser chemischen Signale in der Zaonega-Fm. steht im Zusammenhang mit der Öffnung des Onega-Paleobasins zum offenen Ozean, was zu einer Veränderung des Ablagerungsmilieus von einer euxinischen zu einer Sauerstoffminimumzonen-ähnlichen Umgebung führte. Die Werte $\delta^{98/95}$Mo und $\delta^{186/184}$W sind charakteristisch für die Isotopenfraktionierung, die für die Adsorption von Mo und W an Fe-Oxide gemessen wurde, was darauf hindeutet, dass der Kreislauf dieser Elemente von Fe-Oxiden und nicht von Mn-Oxiden gesteuert wurde. Diese Beobachtung deutet darauf hin, dass die Beendigung des GOE das Fortbestehen von Mn-Oxiden im globalen Ozean nicht ermöglicht hat.

Kapitel 4 befasst sich mit den W-Konzentrationen und $\delta^{186/184}$W-Werten in zwei verwitterten Profilen des 2.7-Ga-Basalts von Mt Roe (Pilbara-Kraton, Australien). Diese beiden Profile wurden in einer anoxischen Atmosphäre verwittert, was zu W-Verlusten und damit verbundenem isotopisch schwerem W führte. Die Assoziation zwischen $\delta^{186/184}$W-Werten und Plagioklas-Alterationsproxies zeigte, dass isotopisch leichtes W wahrscheinlich in Verwitterungsprodukten wie Tonen und Aluminiumoxiden zurückgehalten wurde, während das restliche gelöste W mit meteoritischem Wasser aus dem Profil entfernt wurde. Die $\delta^{186/184}$W-

Werte und der damit verbundene W-Verlust folgen einer Gleichgewichtsisotopenfraktionierung in einem geschlossenen System mit einem Isotopenfraktionsfaktor gelöst-adsorbiert von 0.126 ‰. Diese Studie zeigt, dass W im Gegensatz zu U und Mo sehr effizient von exponierten Oberflächen entfernt wurde, bevor die Atmosphäre oxidiert wurde. Die W-Einträge aus den Flüssen in die Ozeane führten wahrscheinlich dazu, dass die W-Isotopenzusammensetzung der Ozeane in Richtung schwererer Werte verschoben wurde, und können wahrscheinlich die frühesten fraktionierten $\delta^{186/184}$W-Werte aus den marinen Schiefern von 3.47 Ga bis 2.77 Ga erklären, über die in Kapitel 2 berichtet wird.

Kapitel 5 berichtet über Methodenentwicklungen zur Bestimmung von W-Isotopen in Karbonaten. Zunächst wurden die Spurenelementkonzentrationen von vier Karbonat- Referenzmaterialien, die mit 3 M HCl, 5 %v HNO_3 und 5 M Essigsäure ausgelaugt wurden, mit dem Ziel verglichen, die effizienteste Auslaugungsmethode für hohe authigene W-Konzentrationen in den Auslaugungen auszuwählen. Anschließend wurde die Effizienz der Äquilibrierung von W aus Proben und Doppelspikes sowohl in HNO_3- als auch in HCl-Sickerwässern untersucht. Auf der Grundlage der W-Konzentrationen und der $\delta^{186/184}$W-Werte der Sickerwässer ist die Methode der Wahl für die chemische Abtrennung von W aus der Karbonatmatrix ein HCl-Auslaugungsschritt, gefolgt von einer doppelten Aufstockung in demselben Medium vor der Säulenchemie, um die Verwendung verschiedener Säuren vor der Säulenchemie zu reduzieren. In diesem Kapitel werden $\delta^{186/184}$W-Werte von Karbonaten aus verschiedenen Ablagerungsumgebungen, von der Neuzeit bis 2.39 Ga, berichtet und das Potenzial von W-Isotopen in offenen marinen Karbonaten als Stellvertreter für die Entwicklung des Redoxzustands des Ozeans im Laufe der Zeit aufgezeigt.

Zusammenfassend bestätigt diese Studie, dass die stabilen W-Isotope in alten eisenhaltigen Meeressedimenten ein sehr hohes Potenzial haben, die Wissenslücke über die Entwicklung des Redoxzustands der Ozeane vom Paläoarchäikum bis zum Paläoproterozoikum zu schließen. Der W-Isotopenproxy basiert auf einem gut abgesicherten detritischen Hintergrund (PII $\delta^{186/184}$W-Werte), auf einer frühen W-Mobilität, entweder durch anoxische Verwitterung ($\delta^{186/184}$W-Werte bis zu +0.174 ‰) oder durch hydrothermale Flüssigkeiten (PII-ähnliche $\delta^{186/184}$W-Werte), und auf einer starken Isotopenfraktionierung während der WO_4^{2-}-Adsorption an Fe-Oxide (+0.51 ‰), die zu isotopenreichem Rest-WO_4^{2-} führt. Infolgedessen wird in dieser Arbeit ein dreistufiger Anstieg des Redoxpotentials während des Archaikums vorgeschlagen: (1) Bei 3.47 zeigt die niedrige W-Isotopenzusammensetzung (<0.132 ‰) der marinen

Schiefer, dass die W-Einträge in den Ozean größtenteils durch hydrothermales W gesteuert wurden. (2) Von 2.94 bis 2.77 weisen die marinen Schiefer dann $\delta^{186/184}$W-Werte auf, die bis zu +0.177 ‰ erreichen, was als Folge des Aufstiegs kontinentaler Massen und der damit verbundenen zunehmenden W-Einträge durch anoxische subaerische Verwitterung interpretiert wird und nicht als Folge des W-Zyklus auf Oxiden in proximalen, seichten Umgebungen. (3) Karbonate und eisenhaltige Schiefer, die zwischen 2.5 und 2.0 Ga abgelagert wurden, wiesen steigende $\delta^{186/184}$W-Werte auf, die bis zu modernem Meerwasser reichten, was auf einen globalen Anstieg des Redoxpotenzials mit intensivem Fe-(Mn)-Oxidkreislauf hindeutet.

Chapter 1

Introduction

1.1 Motivation of the study

The evolution of the redox state of the atmosphere and ocean system during the Precambrian has been thoroughly investigated using non-conventional isotopic systematics such as molybdenum (Mo), chromium (Cr), and uranium (U) in the sedimentary and paleosol archives. However, the availability and mobility of these elements require specific chemical conditions such as oxidative weathering or high redox potential in aqueous environments, which were hardly met at Precambrian times. As a result, the present knowledge about environmental changes in the pre-2.7 Ga ocean and atmosphere system is limited by the lack of chemical proxies for low redox potential environments.

The goal of this study was to test the tungsten (W) isotopic composition ($\delta^{186/184}$W values) of marine sediments as a potential proxy for the redox state of ancient oceans. Tungsten exists as tungstate ($W^{VI}O_4^{2-}$) within a very large range of Eh-pH values (Takeno, 2005), and potentially was mobilized under anoxic weathering. Moreover, a previous study revealed that WO_4^{2-} efficiently adsorbs onto Mn-Fe oxides with an associated equilibrium isotopic fractionation from +0.59 and +0.51 ‰, respectively (Kashiwabara et al., 2017), which is similar to the offset ($\Delta^{186/184}$W) between modern igneous rocks (-0.010 to +0.110 ‰) and the well-oxygenated modern seawater (+0.54 to +0.55 ‰) (Fujiwara et al., 2020; Kurzweil et al., 2021). This observation demonstrates that the removal of W from seawater mainly occurs via adsorption of tungstate onto oxides, and push the stable W isotopic composition of the seawater towards heavy values. The seawater $\delta^{186/184}$W value then depends on the proportions of W removed from the seawater with oxides, themselves depending on the redox state of the ocean enabling their persistence.

As such, if the seawater $\delta^{186/184}$W value is efficiently mirrored in marine sediments, then the $\delta^{186/184}$W value of ancient sedimentary rocks can be a very important source of information about past redox changes in the atmosphere-ocean system.

The stable W isotopes proxy is relatively new and considerable work is still needed to fully understand W cycling in the modern and ancient oceans. Three main research topics are approached in this study:

- Track the changes in $\delta^{186/184}$W values of marine sediments deposited from 3.47 to 2.0 Ga and compare them with published $\delta^{98/95}$Mo values of contemporaneously deposited sediments.
- Aim at constraining the W continental inputs to the marine realm under under an anoxic weathering regime.
- Measure carbonates $\delta^{186/184}$W values and test for their ability to mirror the ocean $\delta^{186/184}$W signature.

1.2 Scope of the study

This study is divided into five chapters. Chapter 1 provides a state of the art of the evolution of the oxidation states of the atmosphere and oceans during the Archean to Paleoproterozoic, with an emphasize on the contribution of the Cr, U, and Mo geochemical tools to that knowledge. Then, the principles of stable isotope geochemistry are briefly presented, with an introduction to the stable isotope systematics of Mo and W.

Chapter 2 (published as a research paper) focuses on W concentrations and $\delta^{186/184}$W values in shales deposited in open marine environments between 3.47, 2.94, 2.77, 2.76, 2.5 and 2.32 Ga, from drill cores of the Pilbara Craton (Australia; ABDP2-3-5-6-9 cores) and from the Kaapvaal Craton (South Africa; AGP1-2 cores). Fractionated $\delta^{186/184}$W values from the detrital background were reported as early as 3.47 Ga in these marine sediments, and interpreted as early mobility of W in ancient oceans due to its low redox potential in aqueous environments.

Chapter 3 focuses on W and Mo concentrations and isotopic compositions in highly organic-rich marine sediments deposited during the 2.0 Ga Shunga Event. The Shunga Event is interpreted as being the termination of the GOE, with a collapse of atmospheric O_2 content prior to the so-called Boring Billion. The 2.0 Zaonega Fm. marine sediments (Onega paleobasin, Fennoscandinavian Belt) recorded changes in U, Fe, Se and Mo isotopic compositions and resulted in a controversy between global scale signals versus redox effects. Using combined W and Mo isotopes in organic rich sediments, this chapter reports gradual changes in depositional environments associated with changes in the delivery modes of redox sensitive elements (RSE) to the sediments, and highlights the importance of combined RSE isotope systematics to reconstruct paleoenvironment changes.

Chapter 4 focuses on W concentrations and $\delta^{186/184}$W values in two paleosols profiles of the 2.77 Ga Mt Rae Basalt (Pilbara Craton, Australia) altered under anoxic subaerial weathering regime. This chapter reports evidence for isotopically heavy W loss during anoxic continental weathering, supporting the conclusions of the chapter 2.

Chapter 5 focuses on analytical development and improvement of W chemistry aiming at chemical separation of W in carbonate matrixes, and tests the potential of W in carbonates as a redox proxy for shallow environments.

1.3 Environmental changes in the Precambrian ocean and atmosphere system

In this thesis, depositional environments are described as either oxic (over 5 µM of O_2), suboxic (below 5 µM of O_2), anoxic (no O_2, no H_2S), ferruginous (no O_2, dissolved Fe^{II}) or euxinic ($H_2S >$ detection limit).

The Phanerozoic eon (541 Ma – present) is marked by continuous changes in environmental conditions, with the diversification of metazoans, colonization of landmasses by complex organisms, mass extinctions, and multiple cycles of continental breakdown, abundantly documented within the terrestrial and marine rock record. In comparison, the Precambrian (pre 541 Ma) environmental changes are less well understood, even though great changes in the solid Earth, ocean and atmosphere system occurred, such as the onset of plate tectonics, the first documented evidence for multicellular organisms, global and long lasting low-latitude global glaciations, and the and the change from an anoxic to an oxic atmosphere-hydrosphere system (Albani et al., 2010; Holland, 2002; Kaufman et al., 1997; Kirschvink, 1992; Knoll et al., 2016).

The vision of the Precambrian ocean and atmosphere evolution is continuously refined with the advent of new tools, such as the isotope geochemistry of redox-sensitive transition

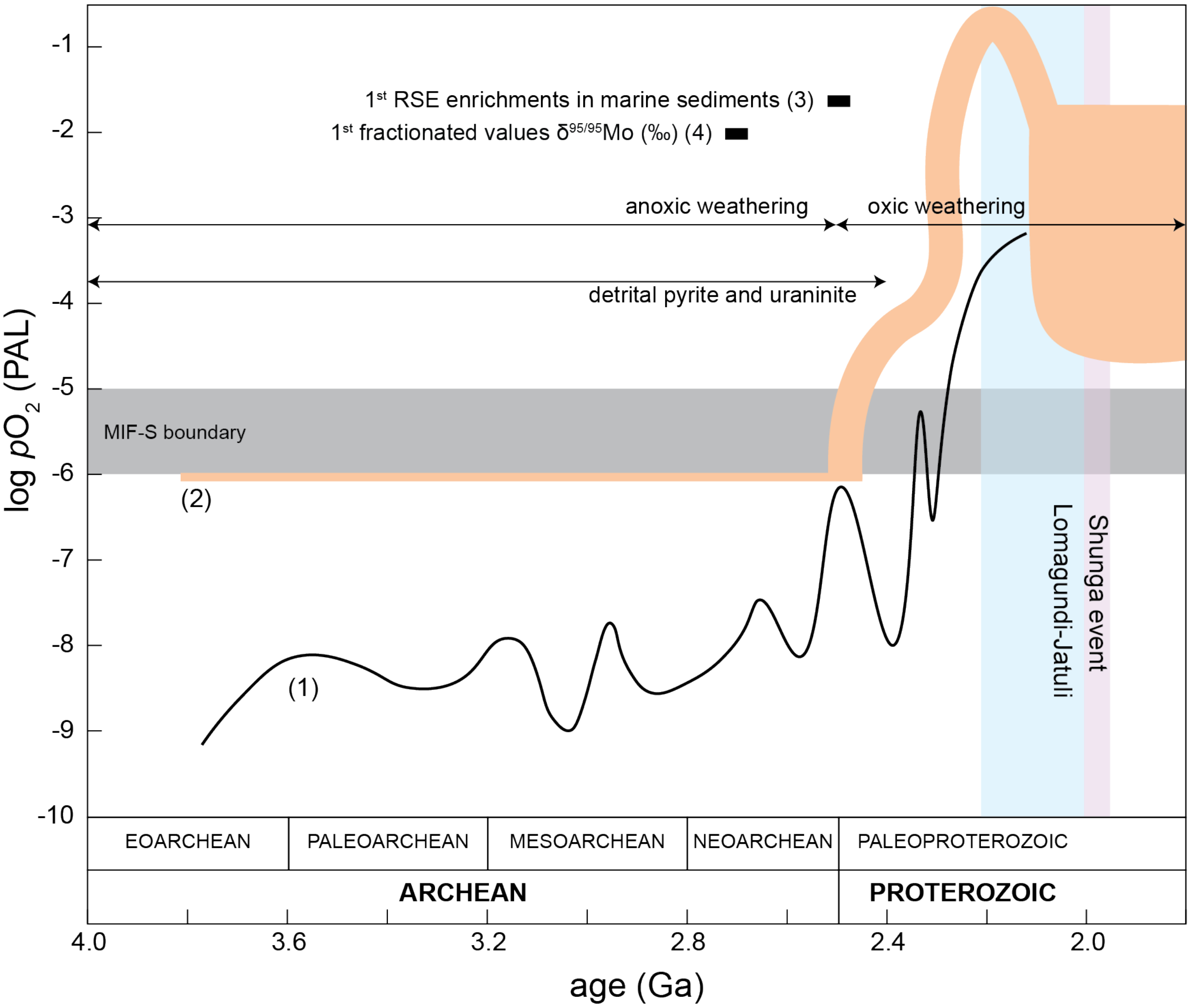

Figure 1.1: Evolution of the pO_2 of the atmosphere from 4.0 to 1.8 Ga. Model (1) (black contineous line) originates from Ostrander et al. (2021). Model (2) (orange) originates from Lyons et al. (2014). Data for RSE enrichments in marine sediments (3) originate from Anbar et al. (2007) and Wille et al. (2007). Evidence for the first fractionated $\delta^{98/95}$Mo values in marine shales (4) originates from Wille et al. (2007) and Ostrander et al. (2020). MIF-S boundary range is encompassed by Pavlov and Kasting (2002) and Catling and Zahnle (2020).

metals, associated with high resolution trace elements determinations. It is widely accepted that the pre-2.45 to 2.32 Ga atmosphere was strongly anoxic as shown by the presence of mass-independent sulfur isotopic fractionation (MIF-S) in sediments deposited prior to 2.45 to 2.32 Ma (Bekker et al., 2004; Farquhar et al., 2000; Hannah et al., 2004; Pavlov and Kasting, 2002; Philippot et al., 2018). This theory is supported by detrital pyrite and uraninite found in deltaic sediments in the 2.415 Koegas Subgroup (Johnson et al., 2019; Johnson et al., 2014), and evidence of an anoxic weathering regime in 2.77 Ma paleosols and pre-2.5 Ga glacial diamictites (Gaschnig et al., 2014; Greaney et al., 2020; Macfarlane et al., 1994). Such geochemical and sedimentological markers point towards molecular oxygen levels lower than 10^{-5} to 10^{-6} present atmospheric levels (PAL) until 2.45 to 2.32 Ga (Catling and Zahnle, 2020; Farquhar et al., 2000; Johnson et al., 2019; Johnson et al., 2014; Pavlov and Kasting, 2002).

However, signals interpreted as signs of oxidation of Cr^{III} with Mn-oxides during continental weathering – requiring molecular oxygen levels exceeding 10^{-4} PAL – were reported for 2.75 Ga banded-iron formations (BIF) (Frei et al., 2009), 2.95 Ga Ijzermijn iron formation (IF) and 3.0 Ga paleosols (Crowe et al., 2013). By contrast, the study of Planavsky et al. (2014b) reported unfractionated $\delta^{53/52}$Cr values in marine sediments deposited prior to 0.8 Ga. Such contradictory chemical signals raised a controversy regarding the evolution of the Archean atmosphere. Yet, other studies described non-redox dependent Cr isotopic fractionation that could produce similar signals in the geological record (Babechuk et al., 2018; Farkaš et al., 2013; Konhauser et al., 2011). Additionally, the studies of Albut et al. (2018) and Albut et al. (2019) highlight the influence of modern weathering onto the fractionated $\delta^{53/52}$Cr values reported for the 2.95 Ga Ijzermijn iron formation of Crowe et al. (2013) by comparing the $\delta^{53/52}$Cr values and $^{234}U/^{238}U$ activity ratios of core and outcrop samples. As such, the pre-2.45 to 2.32 Ga atmosphere is considered largely anoxic and reducing, below the 10^{-5} to 10^{-6} PAL threshold. A new model based on Mo concentrations and stable isotopic compositions of pre-GOE marine sediments proposes that the levels of atmospheric molecular oxygen were not evenly distributed and might have accumulated with local production of 0.02 Tmoles of O_2 per year, enabling local oxidative weathering (Johnson et al., 2021).

The global ocean remained ferruginous until the Neoarchean (Canfield, 1998; Canfield and Raiswell, 1999; Louis and Stein, 1990; Poulton et al., 2004), with very limited expression of redox sensitive elements such as Mo, Cr, Re, U in marine sediments until 2.69 to 2.5 Ga (Anbar et al., 2007; Brüske et al., 2020a; Duan et al., 2010; Kendall et al., 2013; Kurzweil et al., 2015; Ostrander et al., 2020; Wille et al., 2007; Wille et al., 2013). However, shallow or restricted depositional marine environments revealed higher redox potentials enabling Fe and/or Mn oxide cycling. Oxygen oasis, per example were reported for multiple continental margins and epicontinental seas, such as the 3.2 Ga Manzimnyama BIF (Satkoski et al., 2015) and the 2.97-2.95 Ga Pongola Supergroup (Albut et al., 2019; Eickmann et al., 2018; Ossa Ossa et al., 2016; Planavsky et al., 2014a).

The first significant increase in redox potential for the open ocean is recorded in the 2.69 Ga euxinic marine shales from the Jeerinah Fm. (Australia) with the first occurrence of fractionated $\delta^{98/95}$Mo values in deeper marine facies reaching up to 1.02 ‰ in $\delta^{98/95}$Mo

(NIST+0.25) (Ostrander et al., 2020). The following increase in $\delta^{98/95}$Mo values up to 1.72 ‰ reported for 2.6 Ga to 2.5 Ga marine sedimentary successions of the Hamersley Group (Australia) and from the Ghaap Group (South Africa) indicate a homogenous isotopically heavy seawater $\delta^{98/95}$Mo value controlled by draw-down of light Mo by oxides and/or organic matter (Kurzweil et al., 2015; Wille et al., 2007).

One explanation of the increase in oceanic redox potential starting at 2.7 Ga lays in the rise of major subaerial landmasses between 3.0 to 2.7 Ga (Hawkesworth and Kemp, 2006; Liu and He, 2021; McCulloch and Bennett, 1994; Rino et al., 2004), leading to an increase in surfaces available for anoxic weathering. The acidic weathering fluids sourcing from the CO_2-rich Archean atmosphere enhanced the leaching of phosphorous from exposed surfaces to levels comparable or exceeding the modern rates (Hao et al., 2020). Such P-fluxes fueled primary production and might have played an important role in the rise of redox potentials in the ocean and atmosphere over time. Similarly, local weathering of continental surfaces in freshwater, estuarine and soil environments triggered by oxygenic or anoxygenic phototrophs could have been a source of trace metals and nutrients to the ocean as early as 3.2 Ga (Homann et al., 2018; Lalonde and Konhauser, 2015). As such, despite low O_2 contents in the atmosphere, the accumulation of redox sensitive elements in the Neoarchean ocean led to the first local enrichments of Re and Mo in the euxinic intervals of the Mt McRae Shale and of the Klein Naute Fm. (Anbar et al., 2007; Wille et al., 2007).

The disappearance of mass-independent sulfur isotopic fractionation (MIF-S) between the deposition of the Rooihoogte/Duitschland Fm. and the Timeball Hill Fm. (South Africa) sediments at 2.32 Ma marks a significant increase in atmospheric dioxygen levels from 10^{-6} to 10^{-5} PAL (Bekker et al., 2004; Farquhar et al., 2000; Hannah et al., 2004; Luo et al., 2016; Pavlov and Kasting, 2002). Recent data reveal shifts from MIF-S to mass-dependent S isotopes (MDF-S) in marine sediments from Western Australia dated at 2.45 Ga, ∼100 Ma earlier than in South Africa sedimentary successions, and call for asynchronous rise in atmosphere molecular oxygen (Philippot et al., 2018). Regardless of the timing, this significant increase in molecular oxygen is defined as the so-called Great Oxidation Event (GOE; Holland, 2002) and marks the onset of oxidative weathering, as observed in Mo- and V-depleted glacial diamictites associated with isotopically light $\delta^{98/95}$Mo values deposited between 2.5 and 2.3 Ga (Gaschnig et al., 2014; Greaney et al., 2020). Such weathering mode led to large run-off of sulfur and trace metals from exposed surfaces to the Paleoproterozoic ocean, enabling the shift from ferruginous to alternating euxinic-ferruginous conditions in the open ocean for most of the Proterozoic (Canfield et al., 2008; Planavsky et al., 2011; Reinhard et al., 2009).

The Lomagundi-Jatuli Event (LJE) marks the end of the GOE and is characterized by the largest positive $\delta^{13}C_{carb}$ excursion ever recorded, with atmospheric O_2 levels estimated from 10 to 22 times that of the modern atmosphere (Karhu and Holland, 1996). The LJE marine sediments from Gabon bear the first evidence for multicellular life in the fossil record (Albani et al., 2010), although this issue is controversially debated in the literature. The $\sim$2.0 Ga Shunga Event postdates the LJE and is characterized by unprecedented accumulation of massive organic carbon worldwide and oil generation and is regarded as the termination of the oxygen-overshoot preceding the Boring Billion (Asael et al., 2013).

1.4 Redox proxies as tools to reconstruct paleoenvironment changes

The redox changes in the ocean and atmosphere system during the Archean and Paleoproterozoic are widely investigated, however, very few geochemical proxies enable to track such changes in the geological record.

The Mo and W stable isotope systematics as proxies for the redox state of the ocean are based on the adsorption of these elements onto Mn-Fe oxides in aqueous environments and their associated isotopic fractionation (Barling and Anbar, 2004; Goldberg et al., 2009; Kashiwabara et al., 2017). However, the formation pathways of these oxides do not rely directly on the interaction with dissolved O_2, but rather on biologically induced oxidation. Studies revealed that the production of Mn-oxides with photo-oxidation requires wavelengths incompatible with the Archean atmosphere, which attenuates UV intensity even with O_2 levels as low as 10^{-5} PAL (Anbar and Holland, 1992). Furthermore, the discovery of photoautotroph communities that biomineralize Mn-oxides in the absence of O_2 provided strong evidence for non-oxygen dependency on the formation of Mn-oxides in the marine realm (Daye et al., 2019). Similarly, the formation of Fe-oxides depends on photochemical and biological pathways, even in the absence of O_2 (Kappler et al., 2005; Konhauser et al., 2007; Swanner et al., 2015). Moreover, the abundant Fe^{II} in the ferruginous Precambrian oceans likely limited the oxidation of Mn^{II} (Liu et al., 2020).

However, the stability of Mn-Fe oxides – regardless on the formation pathway – is dependent on the redox state of the aqueous environments, enabling the persistence of such chemical components. Mn-oxides can be considered stable in aqueous environments characterized by Eh values exceeding +0.6 V for a pH of 8, similar to the modern ocean (Becking et al., 1960), while Fe-oxides only require Eh values of -1 V for a pH of 8 (Takeno, 2005). In this thesis, the evidence of Mo and W cycling onto Mn-Fe oxides are not used as a proxy for the O_2 content of the ocean, but rather as indicators of the redox state of various environments enabling the persistence of Fe and Mn-oxides in the ocean.

1.4.1 Molybdenum isotope systematics

Molybdenum is a transition metal with atomic number 42 in the Periodic Table of the elements. Molybdenum has seven stable isotopes with masses 92 (14.65 %), 94 (9.19 %), 95 (15.87 %), 96 (16.67 %), 97 (9.58 %), 98 (24.29 %) and 100 (9.74 %) (Mayer and Wieser, 2014). Molybdenum isotopic composition is noted in $\delta^{98/95}$Mo notation, in permill – or parts per thousand – deviation from the NIST 3134 reference solution commonly set to +0.25 ‰ (Greber et al., 2012) following the formulas :

$$\delta^{98/95}Mo_{NIST\ 3134} = [\frac{^{98}Mo/^{95}Mo_{sample}}{^{98}Mo/^{95}Mo_{NIST\ 3134}} - 1] \tag{1.1}$$

$$\delta^{98/95}Mo_{NIST\ 3134+0.25} = 1.00025 \times \delta^{98/95}_{NIST\ 3134} + 0.25 \tag{1.2}$$

Molybdenum is a trace metal in the continental crust with an average concentration of 1.1 µg.g^{-1} (Rudnick and Gao, 2014) and an isotopic composition between +0.35 to +0.60 ‰ (to NIST 3134 +0.25 ‰; Willbold and Elliott (2017)). The modern input of dissolved Mo ($Mo^{(VI)}O_4^{2-}$, molybdate) to the ocean is dominated by riverine fluxes with an average $\delta^{98/95}$Mo value of +0.7 ‰ and a concentration of 6.2 nM (Archer and Vance, 2008), with minor contribution from low temperature-hydrothermal inputs with variable $\delta^{98/95}$Mo values (Miller et al., 2011; Wheat et al., 2002). Molybdenum exists as Mo(VI) in the modern ocean with a long residence time of ∼440-800 ka exceeding the ocean mixing time, and as such is considered as conservative element with a concentration of 110 nM and a $\delta^{98/95}$Mo value of +2.3 ‰ (Firdaus et al., 2008; Miller et al., 2011; Morford and Emerson, 1999; Siebert et al., 2003).

Such isotopically heavy seawater results from efficient drawdown of isotopically light dissolved Mo during inner-sphere complexation of MoO_4^{2-} onto Mn-oxides, with an equilibrium isotopic fractionation of 2.7 ‰ (Barling and Anbar, 2004; Kashiwabara et al., 2011). Manganese oxides (or $Mn^{(VI)}O2$) are stable in well oxygenated water masses with an Eh exceeding +0.6 V

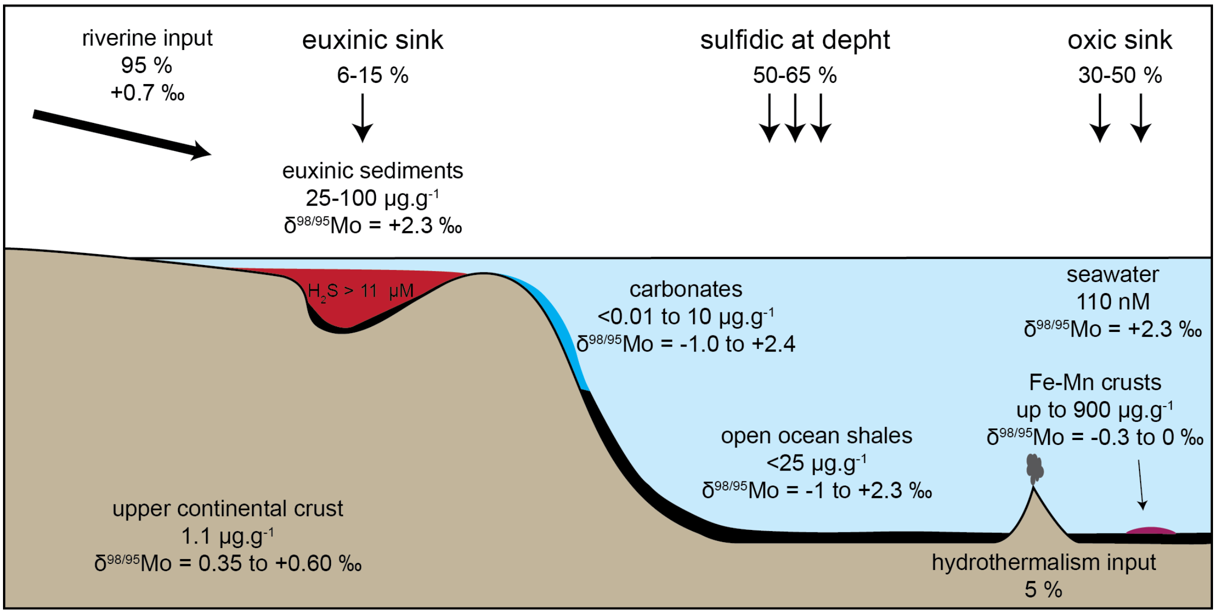

Figure 1.2: Mo concentrations and $\delta^{98/95}$Mo values of modern (< 1 Ma) surface environments. The values given in this figure are global estimates. Mo concentrations and $\delta^{98/95}$Mo values of riverine fluxes originate from Archer and Vance (2008), the 5 % of missing Mo sources are identified as originating from low-temperature hydrothermalism (not represented). The proportions of output sinks originate from Kendall et al. (2017). The Mo concentrations and $\delta^{98/95}$Mo values of modern carbonates and open ocean shales originate from Thoby et al. (2019), while the ones of restricted euxinic sediments originate from Scott and Lyons (2012). Mo concentration and $\delta^{98/95}$Mo values of seawater and Fe-Mn crusts originate from Siebert et al. (2003). Crustal Mo concentration value originate from Rudnick and Gao (2014) and $\delta^{98/95}$Mo values from Willbold et al. (2016).

for a pH of 8 (Takeno, 2005). As such, the seawater $\delta^{98/95}$Mo value indirectly mirrors the redox state of the ocean and the proportions of oxic sinks.

Under euxinic conditions aqueous MoO_4^{2-} undergoes a chain of reaction with H_2S to forms mono – di – tri and tetrathiomolybdate (MoS_4^{2-}) species (Erickson and Helz, 2000), with isotopic fractionations associated to each of these steps (Tossell, 2005). In solution with H_2S concentration exceeding 11 µM, the so-called switch point of activation, the transformation of MoO_4^{2-} to MoS_4^{2-} is quantitative (Erickson and Helz, 2000), and the $\delta^{98/95}$Mo value of the initial dissolved Mo pool is preserved. As a result, marine sediments deposited under euxinic conditions in restricted environment with ambient H_2S levels exceeding 11 µM mirror the one of the open ocean, and are key target for tracking the redox state of the past oceans (Barling et al., 2001). On the other hand, marine sediments deposited under open and euxinic settings or restricted sediments with H_2S concentrations lower than 11 µM reveal $\delta^{98/95}$Mo values lighter than the one of the open ocean (Arnold et al., 2004; Dahl et al., 2010; Nägler et al., 2011; Nägler et al., 2005; Noordmann et al., 2015; Poulson et al., 2006; Wegwerth et al., 2018).

1.4.2 Tungsten isotopes systematics

Tungsten belongs to the group 6 of elements with the atomic number 74 and exists as five stable isotopes with masses of 180 (0.12 %), 182 (26.5 %, produced by beta decay of ^{182}Hf in the early stages of the solar stage of solar system formation, considered as stable in low temperature W systematics), 183 (14.31 %), 184 (30.64 %) and 186 (28.43 %) (Sharp, 2017). Tungsten isotope systematics first focused on W radiogenic isotopes (μ^{182}W) as a proxy for the timing of the Earth core formation (Dauphas and Pourmand, 2011; Kleine et al., 2002; Kruijer et al., 2014; Schoenberg et al., 2002; Yin et al., 2002). Recent analytical advances enable the precise measurement of stable W isotopes with an improved separation chemistry, and measurement on a MC-ICPMS with the use of a W double spike (Kurzweil et al., 2018; Tusch et al., 2019).

Tungsten is a moderately siderophile element and is enriched in Earth's core relative to the mantle. It behaves incompatible during partial melting and is found to be enriched in silicate melts and in the upper continental crust with a concentration of ~1.9 µg.g^{-1} (Rudnick and Gao, 2014), ten times more enriched than the residual mantle with a concentration of 12 ng.g^{-1} (König et al., 2011). The recent investigation of modern igneous rocks from MORBs, OIBs, lavas from subduction zones revealed a large spread of $\delta^{186/184}$W values from -0.072 to +0.249 ‰, but non-metamorphic or fluid-related igneous rocks yield a narrower $\delta^{186/184}$W range from -0.010 to +0.110 ‰ (Kurzweil et al., 2020; Kurzweil et al., 2018; Mazza et al., 2020). The partition coefficients of W between silicate-melts and minerals such as plagioclase, olivine, clinopyroxene, orthopyroxene are in the range of 10^{-1} and 10^{-4} at various oxygen fugacities, and reveal that W is likely not incorporated into the mineral structure of major rock forming minerals (Fonseca et al., 2014). In situ trace element determination of modern Kilauea Iki lava lake samples revealed that W behaves as a lithophile element during magmatic differentiation and is found enriched in the glass fraction (up to 2.51 µg.g^{-1}) compared to sulfides (partition coefficients sulfide/glass < 0.10), while olivine and augite do not host detectable W (Greaney et al., 2017). Overall, the distribution of W in igneous rocks is not yet well constrained, with the lack of basic understanding of where is W hosted in the mineral matrix.

No W concentration and $\delta^{186/184}$W values of modern soils were reported yet, but dissolved W, or WO_4^{2-}, efficiently adsorbs onto clay minerals and organic matter-rich soils and is likely efficiently retained in modern soils (Petruzzelli and Pedron, 2017, 2020; Sen Tuna and Braida, 2014; Tuna et al., 2012).

The modern input of dissolved W to the oceans is dominated by riverine water

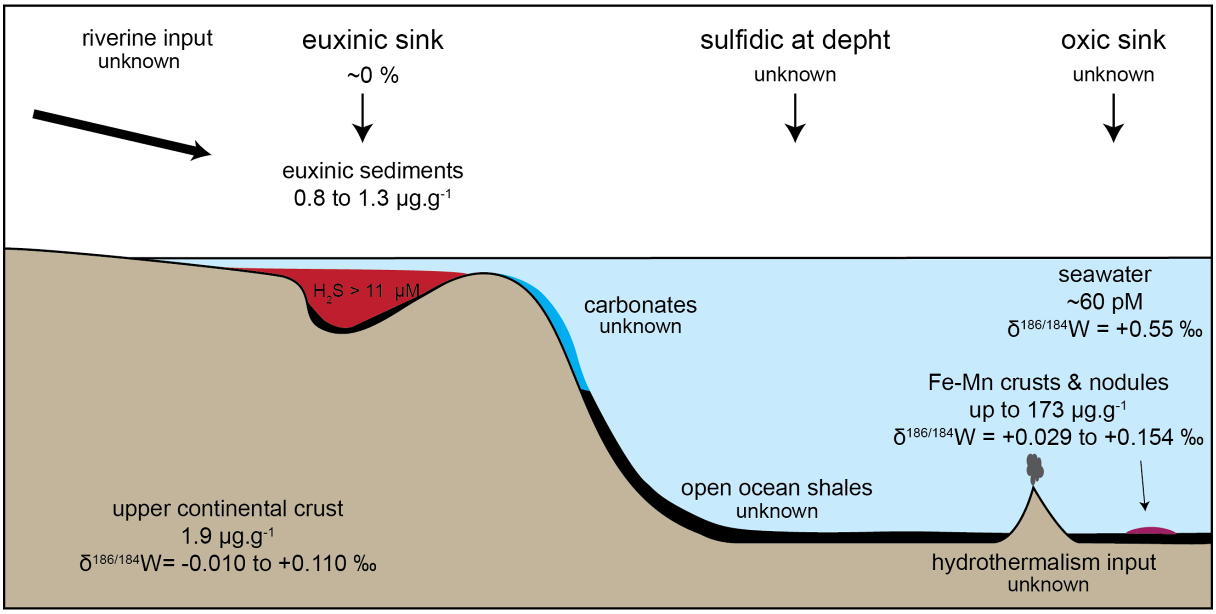

Figure 1.3: W concentrations and $\delta^{186/184}$W values of published modern aqueous reservoir and depositional environments. W conc. and $\delta^{186/184}$W values of the modern seawater originate from Kurzweil et al. (2021) and Fujiwara et al. (2020). Modern W concentrations and/or $\delta^{186/184}$W values of Fe-Mn nodules and crust originate from Mn-Fe nodules reference material data published in Kurzweil et al. (2018) and Kunzendorf and Glasby (1992). W concentrations of euxinic sediments originate from Dellwig et al. (2019). Upper continental crust $\delta^{186/184}$W range originate from $\delta^{186/184}$W values published by Kurzweil et al. (2019), Kurzweil et al. (2018) and Mazza et al. (2020) for non-subduction of fluid related igneous rocks, such as MORBs, OIBs, andesite and diabase.

(550 pM; (Viers et al., 2009)), groundwater (14-180 pM; (Johannesson et al., 2013), and hydrothermal vent fluids (200 to 120,000 pM; (Kishida et al., 2004). Tungsten is particle scavenging and is ten times more enriched in the suspended fraction of riverine discharge than in the dissolved phase (Viers et al., 2009).

Tungsten is a conservative element in the modern oceans with a residence time of 14-60 kyrs, a concentration of 49 to 60 pM (Firdaus et al., 2008; Sohrin et al., 1987) and a homogeneous $\delta^{186/184}$W value of +0.543 ±0.046 ‰ for the Western Pacific and Southern Atlantic oceans (Kurzweil et al., 2021) to +0.55 ±0.12 ‰ for the western North Pacific ocean (Fujiwara et al., 2020). The major sinks for dissolved W in the ocean are not yet constrained, but unlike Mo, W is not efficiently scavenged in sediments deposited in sulfidic environments (Dellwig et al., 2019; Mohajerin et al., 2016). Mohajerin et al. (2016) reported increasing WO_4^{2-} concentrations in estuarine sulfidic porewaters, interpreted as release of particle-bound W, while MoO_4^{2-} was efficiently removed to the sediment. Tungstate, like Mo, interacts with H_2S and forms thiotungstate species, but only at high H_2S levels of 1000 µM (Mohajerin et al., 2014). The experiments of Cui and Johannesson (2017) revealed that both tetrathiotungstate and tungstate adsorb onto pyrite, which does not fit to observations of modern euxinic sediments that do not yield any W authigenic enrichments (Dellwig et al., 2019). The study of sediments deposited under an oxic water column (without particle shuttle) in the modern Japan Sea similarly did not reveal high W authigenic enrichments (Tsujisaka et al., 2020). However, ferromanganese deposits from the Pacific ocean and Mn-rich sediments from the Baltic sea are found highly enriched in W with concentrations reaching up to 173 and 23.07 $\mu g.g^{-1}$, respectively (Dellwig et al., 2019; Kunzendorf and Glasby, 1992).

The adsorption experiments of Kashiwabara et al. (2013) confirmed that WO_4^{2-} is very efficiently adsorbed onto Mn and Fe oxides with strong inner-sphere complexations. Later, the study of Kashiwabara et al. (2017) revealed that the adsorption of WO_4^{2-} onto Mn (birnessite) and Fe (ferrihydrite) oxides is associated with a change of coordination from tetrahedral to octahedral, leading to an equilibrium isotopic fractionation between dissolved and adsorbed W ($\varepsilon^{186/184}W_{\ dissolved-adsorbed}$) of +0.59 and +0.51 ‰, respectively. These values are in very good agreement with the offset between seawater and igneous inventory, and demonstrate that like Mo, the stable W isotopic composition of the seawater is controlled by Mn-oxide drawdown.

Very few studies so far reported stable W isotopic compositions of modern marine sediments, and none revealed modern seawater-like W signatures (Fujiwara et al., 2020; Kurzweil et al., 2019). The study of marine sediments from the semi-closed Japan Sea without oxide cycling in the water column revealed crustal-like $\delta^{186/184}W$ values, highlighting the dependency of the W delivery to the water column-sediment interface (Fujiwara et al., 2020).

Chapter 2

Stable W and Mo isotopic evidence for increasing redox-potentials from the Paleoarchean towards the Paleoproterozoic deep Ocean

A version of this chapter has been published as a research paper in the Journal Geochimica et Cosmochimica Acta, Volume 309, 2021, Pages 366-387, DOI 10.1016/j.gca.2021.05.013

Abstract

The scavenging of dissolved trace metals such as chromium (Cr), molybdenum (Mo) and tungsten (W) and their authigenic enrichment in sedimentary archives mainly occur by particle shuttling that cause resolvable isotope fractionation. Because their scavenging is also dependent on the local marine redox potential and the overall marine chemical environment, the stable isotope composition of these elements in Archean sediments is widely used as paleoredox proxy. Tungsten, a new element in this tool box, is dissolved as the oxyanion tungstate (WO_4^{2-}) at extremely low marine redox potentials and can thus help to reconstruct the earliest changes in the marine redox state.

We tested the applicability of stable W isotopes as a new paleoredox proxy of the atmosphere-ocean system. We analyzed the $\delta^{186/184}$W of Precambrian igneous rocks to investigate the detrital background $\delta^{186/184}$W signature. This Precambrian igneous inventory (PII) shows $\delta^{186/184}$W values between -0.007 and +0.097 ‰, identical to the range of modern igneous crustal rocks, which indicates that the average Earth's crust $\delta^{186/184}$W remained constant over billions of years. Furthermore, we present $\delta^{186/184}$W values of euxinic sediments from the Black Sea as a modern sedimentary analog, which we then compare with data of Archean and Proterozoic black shales (3.47 to 2.3 Ga). Modern Black Sea sapropels reveal crustal-like $\delta^{186/184}$W values between +0.050 and +0.071 ‰ suggesting limited authigenic enrichment of W in euxinic environments. Similarly, post-Great Oxidation Event shales (2.3 Ga) show crustal- or PII-like $\delta^{186/184}$W values indicating the deposition in euxinic or oxic environment. However, the Archean shale sample suites show elevated W concentrations and fractionated $\delta^{186/184}$W values up to +0.246 ‰, which we attribute to authigenic enrichment of heavy seawater W in a ferruginous setting. Thus, black shales $\delta^{186/184}$W values can help to distinguish between anoxic-ferruginous and euxinic depositional environments.

Furthermore, we combine previously published Cr and Mo isotope data with new Cr and W isotope data to quantify the evolution of the marine redox state during the Archean. By combining the Eh-pH stability fields of W and Mo with the $\delta^{186/184}$W and $\delta^{98/95}$Mo values of Precambrian sediments, we suggest a 3-step evolution of the Precambrian ocean. (1) From 3.47 to 3.0 Ga, the Eh of a dominantly ferruginous ocean was between -0.4 V and -0.25 V, enabling the persistence of soluble WO_4^{2-} but not MoO_4^{2-} and thus only the authigenic enrichment of isotopically fractionated W. (2) Starting from 3.0 Ga, the Eh of some shallow-marine environments increased above -0.25 V, as indicated by $\delta^{98/95}$Mo values above the detrital background in

shallow-marine sediments, while the Eh of the deep ocean still remained below -0.25 V indicated by the lack of authigenic Mo enrichment and fractionated $\delta^{98/95}$Mo values in deep-sea shales. (3) After 2.7 Ga elevated $\delta^{186/184}$W and $\delta^{98/95}$Mo values in deep-marine sediments suggest that the Eh of the ferruginous open-ocean now also increased above -0.25 V. We therefore suggest that the combination of $\delta^{186/184}$W and $\delta^{98/95}$Mo values of shales is a very promising tool to investigate earliest changes in marine redox conditions during the Archean.

2.1 Introduction

The redox states of the Precambrian ocean and atmosphere have been studied for almost one century, with countless discoveries providing detailed understanding of their compositional evolution (Canfield et al., 2000; Farquhar et al., 2000; Lyons et al., 2014; Pavlov and Kasting, 2002). The Archean oceans are generally considered to be anoxic and ferruginous as indicated for example by sulfur (S) isotopic variation, iron (Fe) speciation data and rare earth element (REE) distribution in marine sediments (Canfield, 1998; Canfield and Raiswell, 1999; Holland, 1984; Louis and Stein, 1990; Poulton et al., 2004). Evidence for free oxygen in shallow, near shore environments or epicontinental seas as old as 3.2 Ga points to the existence of oxygen oases before the atmosphere and ocean system became permanently oxidized (Eickmann et al., 2018; Ossa Ossa et al., 2016; Planavsky et al., 2014a; Satkoski et al., 2015). Other geochemical studies suggest towards increasing oceanic redox potentials in the Neoarchean leading to globally stratified oceans with oxic/suboxic surface water and anoxic deep-water masses after ca. 2.7 Ga (Anbar et al., 2007; Czaja et al., 2012; Eroglu et al., 2015; Kendall et al., 2010; Kurzweil et al., 2016; Kurzweil et al., 2015; Ostrander et al., 2020; Siebert et al., 2005; Voegelin et al., 2010; Wille et al., 2007). The disappearance of mass-independent fractionation of sulfur isotopes (MIF-S) in the Proterozoic marine sedimentary archive marks the transition from a reduced to a slightly oxidized atmosphere with a molecular oxygen concentration above 10^{-6} to 10^{-5} of the present atmospheric level (PAL) (Catling and Zahnle, 2020; Farquhar et al., 2000; Pavlov and Kasting, 2002). This significant change in the redox state of the atmosphere referred to as the Great Oxidation Event (GOE) took place between approximatively 2.32 and 2.45 Ga (Bekker et al., 2004; Gumsley et al., 2017; Hannah et al., 2004; Hoffman, 2013; Philippot et al., 2018) and led to increasing oxidative weathering of sulfides and continental run-off of trace metals to the ocean (Anbar et al., 2007; Konhauser et al., 2011; Reinhard et al., 2009). The resulting sulfur flux to the oceans has been proposed to cause a chemical transition of the deep ocean from ferruginous (Fe^{II} dominated) to euxinic (H_2S dominated) conditions for most of the Proterozoic (Canfield, 1998; Holland, 1984; Poulton et al., 2004; Reinhard et al., 2009), although S and Mo isotope and Fe speciation data of marine shales indicate continuous widespread anoxic ferruginous co-existing with locally euxinic conditions throughout the mid-Proterozoic (Arnold et al., 2004; Gilleaudeau et al., 2019; Gilleaudeau et al., 2020; Kendall et al., 2011; Planavsky et al., 2011).

One of the most frequently used geochemical tools to study environmental redox changes throughout Earth's history are Mo isotopic variations in marine sediments, expressed as $\delta^{98/95}$Mo normalized to $\mathrm{NIST}_{3134+0.25}$, especially in Archean to Neoproterozoic times (e.g. Archer and Vance (2008); Asael et al. (2018); Czaja et al. (2012); Duan et al. (2010); Kurzweil et al. (2015); Nägler et al. (2005); Ossa Ossa et al. (2018a); Ostrander et al. (2020); Ostrander et al. (2019); Planavsky et al. (2014a); Thoby et al. (2019); Voegelin et al. (2010); Wille et al. (2013)). Molybdenum is dissolved as highly soluble molybdate ($\mathrm{Mo}^{(VI)}$) in the modern oxygenated ocean, with a residence time of 440 to 800 kyrs, a concentration from 97 to 105 nM, a conservative behavior in the water column, and a stable isotopic composition of +2.3 ‰ in $\delta^{98/95}$Mo, although concentration and isotopic anomalies were reported for the coastal ocean (Dellwig et al., 2007; Firdaus et al., 2008; Kowalski et al., 2013; Miller et al., 2011; Morford and Emerson, 1999; Siebert et al., 2003).

Dissolved molybdate ($\mathrm{Mo(VI)}_4^{2-}$) is tetrahedrally coordinated but changes to octahedral coordination during adsorption onto Mn oxides, forming strong inner sphere complexes (Kashiwabara et al., 2011). The adsorption of molybdate onto Mn oxides is accompanied by an equilibrium isotope fractionation $\varepsilon^{98/95}$Mo solution adsorbed of +2.7 ‰, between isotopically heavy dissolved and isotopically light adsorbed Mo (see equation 2.3; Barling and Anbar (2004)). Additional isotopic fractionations have been determined for the adsorption of Mo onto Fe-oxy(hydroxi)des with $\varepsilon^{98/95}\mathrm{Mo}_{solution-adsorbed}$ of +0.8 ±0.6 ‰ on magnetite, +1.1 ±0.2 ‰ on ferrihydrite, +1.4 ±0.5 ‰ on goethite and +2.2 ±0.5 ‰ on hematite (Goldberg et al., 2009). The preferential adsorption of isotopically light Mo onto Mn and Fe oxides is the main driver for isotopically heavy modern seawater (Barling and Anbar, 2004).

The Mo isotopic composition of shales deposited in restricted basins under euxinic conditions with $\mathrm{H_2S}_{aq}$ concentrations above the threshold value of 11 µM (eg. Black Sea, Kyllaren Fjord) has been shown to mirror that of open ocean seawater (Barling et al., 2001; Erickson and Helz, 2000; Helz et al., 2004; Noordmann et al., 2015; Siebert et al., 2003). Under these conditions, the formation of highly particle reactive thiomolybdate species $\mathrm{MoO}_x\mathrm{S}_{4-x}$ and MoS_4^{2-} is responsible for (near) quantitative scavenging of dissolved Mo into the sediment thus preserving the seawater $\delta^{98/95}$Mo value (Adelson et al., 2001; Calvert and Pedersen, 1993; Crusius et al., 1996; Helz et al., 1996; Zheng et al., 2000). However, in less restricted basins, at continental margins, and under euxinic conditions with $\mathrm{H_2S}$ concentrations below 11 µM, the conversion of molybdate to particle-reactive thiomolybdate and the scavenging of Mo into the sediment are not quantitative (Noordmann et al., 2015; Poulson et al., 2006). This results in a significantly lower sedimentary $\delta^{98/95}$Mo value compared to the open ocean $\delta^{98/95}$Mo value of +2.3 ‰ due to Mo isotopic fractionation during thiolation (Brüske et al., 2020b; Nägler et al., 2011; Poulson Brucker et al., 2009; Scheiderich et al., 2010; Tossell, 2005; Wegwerth et al., 2018).

Although the distinction between the two sinks comprising isotopically light Mo (namely sediments from oxic and weakly sulfidic settings, respectively) is difficult, the Mo isotope composition of ancient euxinic sediments has been used to reconstruct redox-changes in the atmosphere-ocean system throughout Earth's history (Arnold et al., 2004; Asael et al., 2018; Duan et al., 2010; Kendall et al., 2011; Ostrander et al., 2020; Siebert et al., 2003; Wegwerth et al., 2018). Shales deposited under ferruginous conditions show little or no Mo enrichment and crustal $\delta^{98/95}$Mo values until the mid-Neoarchean, 2.7 Ga ago (Kurzweil et al., 2015; Ostrander et al., 2020; Wille et al., 2007; Wille et al., 2013). However, carbonates and shallow-water iron formations deposited as early as 2.98 Ga (Albut et al., 2019; Ossa Ossa et al., 2018b; Planavsky et al., 2014a; Thoby et al., 2019) depict fractionated $\delta^{98/95}$Mo seawater signals indicating the existence of Mo redox cycling in neritic environments already at that time. These observations clearly indicate that the Mo isotope composition of shales from ferruginous settings gives little information about the redox state of the global Archean ocean prior to 2.7 Ga (Thoby et al., 2019).

The particular geochemical behavior of the redox-sensitive element tungsten (W) in modern marine environments bears the potential that its stable isotopic variations in shales deposited under anoxic ferruginous conditions may reflect the redox state of the seawater and thus overcome the shortcomings of Mo isotopes in such depositional environments. Tungsten and Mo have similar concentrations in the upper continental crust of approximately 1 to 2 µg.g^{-1}, with a molar W/Mo ratio of $\sim$0.9 (Rudnick and Gao, 2014; Taylor and McLennan, 1995). Tungsten has a strong affinity for soils and is efficiently retained by organic matter and clay minerals (Tuna et al., 2012). Thus, W is much less mobile than Mo during weathering, erosion and riverine/groundwater transport (Bauer et al., 2018b; Gaillardet et al., 2014). This results in a eight times lower dissolved molar W concentration in modern river water compared to Mo with values of 0.55 and 4.4 nM, respectively (Viers et al., 2009). Other W input sources to the modern ocean are groundwater with 14 to 184 pmol.L^{-1} (Johannesson et al., 2013) and hydrothermal vent fluids with 0.2 to 120 nmol.L^{-1} (Kishida et al., 2004). Tungsten has a modern oceanic residence time of 14 to 60 kyrs (Firdaus et al., 2008; Sohrin et al., 1998; Sohrin et al., 1987) resulting in a globally uniform W concentration of 53 to 60 pmol.L^{-1} (or 9.54 to 10.8 ng.L^{-1}), which translates to approximately 1,100 – 2,000 times lower dissolved W than Mo (molar ratio) in the modern ocean (Firdaus et al., 2008; Sohrin et al., 1987). The large discrepancy between the molar W/Mo ratios of seawater and rivers has been explained by the stronger adsorption of dissolved WO_4^{2-} to ferric and manganese oxides, organic matter and clay minerals compared to MoO_4^{2-}, resulting in very efficient W removal from oxic seawater to the sediment (Cui et al., 2021; Dermatas et al., 2004; Gaillardet et al., 2014; Iwai and Hashimoto, 2017; Kashiwabara et al., 2013; Kashiwabara et al., 2011; Muir et al., 2017; Sen Tuna and Braida, 2014; Sohrin et al., 1987). Unlike for MoO_4^{2-}, euxinic conditions do not provide a direct and effective burial pathway from ocean water WO_4^{2-} to shaly sediments (Dellwig et al., 2019). Dissolved tungstate requires very high H_2S_{aq} concentrations in excess of 1000 µM to be effectively transformed to thiotungstate species and WS_4^{2-} (Cui et al., 2020; Mohajerin et al., 2014). Additionally, WS_4^{2-} is more soluble and less particle reactive than MoS_4^{2-} and is thus not easily scavenged to the sediment under euxinic conditions (Cui and Johannesson, 2017; Mohajerin et al., 2016).

The resolution of stable W isotopic differences is analytically challenging because W concentrations in geological materials are relatively low, W purification from rock matrices is demanding and natural isotopic variations are expected to be very narrow due to small relative mass differences (Abraham et al., 2015; Breton and Quitte, 2014; Krabbe et al., 2017). However, in recent years resolvable stable W isotopic variations have been reported for marine sediments as well as for igneous rocks (Abraham et al., 2015; Breton and Quitte, 2014; Krabbe et al., 2017; Kurzweil et al., 2019; Kurzweil et al., 2020; Kurzweil et al., 2018; Mazza et al., 2020; Tsujisaka et al., 2020; Tsujisaka et al., 2019). Kurzweil et al. (2019) reported a homogeneous $\delta^{186/184}$W value for modern mid-ocean ridge basalts (MORBs; n = 8) and oceanic island basalts (OIBs; n = 17) of +0.085 ±0.019 ‰, in accordance with previously published data for basaltic rocks (Krabbe et al., 2017; Kurzweil et al., 2018), and proposed this to represent a homogenous mantle $\delta^{186/184}$W signature. Subduction related mafic rocks such as boninites, arc tholeiites and calc-alkaline basalt are more variable in $\delta^{186/184}$W values (from -0.009 to +0.195 ‰), potentially due to the addition of recycled sedimentary material to the melt source and the involvement of magmatic fluids (Kurzweil et al., 2019; Mazza et al., 2020). Eoarchean meta-igneous rocks from the Itsaq Gneiss Complex, SW Greenland, yield a wide span of $\delta^{186/184}$W values – from -0.072 to +0.249 ‰ – and illustrate the influence of mobilization and re-enrichment of W by metasomatic fluids (Kurzweil et al., 2020). Overall, $\delta^{186/184}$W values of igneous rocks – non-fluid and subduction related – range from -0.010 to +0.120 ‰ (Krabbe et al., 2017; Kurzweil et al., 2019; Mazza et al., 2020). Recent studies reveal a homogenous seawater W isotope composition, which is distinctly heavier than igneous crustal rocks showing +0.55 ±0.12 ‰ in $\delta^{186/184}$W for the western North Pacific (Fujiwara et al., 2020) and +0.543 ±0.046 ‰ for the Southern Atlantic and Western Pacific (Kurzweil et al., 2021).

The cycling of W and its associated $\delta^{186/184}$W values in reservoirs of the modern Earth's system is still poorly understood, particularly in terms of the marine environments. Still, in an experimental study, Kashiwabara et al. (2017) determined large equilibrium isotopic fractionation during adsorption of WO_4^{2-} with inner-sphere complexation onto Mn- and Fe-oxides with $\varepsilon^{186/184}W_{solution-adsorbed}$ of +0.59 ±0.14 ‰ and +0.51 ±0.06 ‰, respectively. Preferential adsorption of isotopically light W onto marine Mn- and Fe-oxides might thus explain the isotopically heavy seawater $\delta^{186/184}$W value, similar to the marine Mo isotope systematics (Fujiwara et al., 2020; Kurzweil et al., 2021).

Interestingly, marine sediments from the semi-closed Japan Sea deposited under oxic bottom water conditions showed little to no authigenic enrichments of W, with a strong positive correlation of W and Ti concentrations, and crustal-like $\delta^{186/184}$W values (Fujiwara et al., 2020). Ferromanganese crusts and nodules, on the other hand, are highly enriched in W (Hein and Koschinsky, 2014; Kunzendorf and Glasby, 1992), and isotopically lighter than seawater (Fujiwara et al., 2020; Kurzweil et al., 2018). These observations may indicate limited W scavenging in oxic settings with no Fe and Mn oxide formation, but the preferential removal of isotopically light W by FeMn-oxide shuttling. Importantly, WO_4^{2-} forms strong inner sphere complexes with Fe-oxides, while Mo_4^{2-} only forms much weaker outer sphere bonds with these minerals (Kashiwabara et al., 2013). This might cause the more efficient scavenging of seawater W by Fe oxides compared to Mo. Therefore, stable W isotopes are also a promising and additional new tool to trace redox changes in the lower Eh range, when Fe^{2+} is oxidized while Mn^{2+} remains reduced.

The motivation for this study was to test whether modern sediments deposited under euxinic conditions indeed show no authigenic seawater W isotopic signatures but are purely dominated by detrital $\delta^{186/184}$W values. We further investigated whether the low redox potential of W and the effective adsorption of WO_4^{2-} onto Fe-oxides make W isotopic compositions of Archean marine shales a suitable proxy for the redox evolution of the global Archean ocean.

To do so, we analyzed (i) the stable W isotopic compositions of Archean ultramafic, mafic and felsic igneous rock samples to reconstruct the W isotopic composition of the Archean detrital background; (ii) we determined the stable W isotopic compositions of the modern Black Sea sapropel that was deposited under euxinic conditions with variable H_2S_{aq} concentrations; (iii) we analyzed the W concentration and stable W isotopic compositions of 3.46 to 2.3 Ga black shales from the Pilbara Terrane, Australia, and the Transvaal Basin, South Africa, to investigate the redox history of the Archean-Paleoproterozoic ocean.

2.2 Samples and methods

2.2.1 Samples

Igneous Archean-Proterozoic rocks: Komatiites and komatiitic basalts originate from the 2.7 Ga old Reliance and Zeederbergs Formations, Ngezi Group, of the Belingwe greenstone belt, Zimbabwe craton. Details about the regional geology, formation ages, and the geochemistry of these samples were previously reported (Bolhar et al., 2003; Chauvel et al., 1993). The 3.5 to 3.1 Ga tonalite-tronjdemite-granodiorite (TTG) and granidioritic-granitic-monzongranitic (GGM) suite samples originate from the Theespruit Formation, Onverwacht Group, of the Barberton greenstone belt, South Africa (De Ronde and Kamo, 2000; Kamo and Davis, 1994; Kleinhanns et al., 2003). Their trace element patterns suggest a common melt source (Kleinhanns et al., 2003). Felsic magma intruded the 3.1 Ga old Theespruit Formation. During later metamorphic events GGMs and TTGs were highly deformed and metamorphosed to greenschist facies (Lowe and Byerly, 1999). Paleoproterozoic granitoids (1.95 to 1.8 Ga) of this study originate from the Västervik area, belonging to the Svecofennian Domain, Southeast Sweden. The granitoid's petrogenesis occurred in a large subduction related magmatic arc system along the Laurentia-Baltica margin (Karlstrom et al., 2001). More details can be found in Nolte et al. (2011).

Black sea sapropel: samples were collected from gravity core 22GC-3, which was recovered during a Black Sea cruise with RV Meteor (M72/5) in 2007. These sediments were deposited under various bottom water conditions ranging from weakly euxinic (∼5 µM H_2S_{aq}) to euxinic (∼18 µM H_2S_{aq}) during the Holocene (0 to 8.7 ka BP). A detailed description of the depositional environments and their chemical compositions (major and trace elements; Mo and Fe isotopic composition) are provided in Wegwerth et al. (2018) and Dellwig et al. (2019).

The modern Black Sea is a strongly stratified basin with an oxic upper layer (Eh of +0.390 V) and a reducing bottom water (Eh down to -0.170 V, Sorokin (1972)).

Archean and Paleoproterozoic marine sediments: Black shale samples were selected from five drill cores of the Archean Biosphere Drilling Project (ABDP) covering various formations of the Pilbara Craton, W-Australia that have an age between 3.46 and 2.5 Ga. These sediments were deposited below the wave base under anoxic conditions and underwent only low-grade metamorphism. In more detail, ABDP-2 (3.47 Ga) samples originate from the 200 m thick black shale unit in the lower part of the Duffer Fm. of the Warrawoona Group (Coongan Subgroup). The ca. 2.94 Ga old ABDP-5 shales were sampled from the deep-water depositional environment of the Nullagine Group (De Grey Supergroup). The 2.76-2.77 Ga ABDP-3-6 cores cover the Hardey Fm. of the Fortescue Group (Mount Bruce Supergroup) and the 2.54 to 2.5 Ga old ABDP-9 core samples cover the Wittenoom Fm. to the Mount McRae Shale Fm. of the Hamersley Group (Hickman, 2012; Van Kranendonk et al., 2007; Wille et al., 2013). Samples from the AGP 1 and AGP 2 cores of the CIMERA-Agouron GOE and Biomarker Drilling Project cover sediments of the Rooihoogte/Duitschland and Timeball Hill Fm. of the Transvaal basin, Kaapvaal Craton, South Africa, which were deposited in the lead-up, during and the wake of the GOE. The core is characterized by shales, with minor layers of silt, fine sand and carbonate. A few meter-scale igneous intrusions altered the sediments, at contact. The shale units were deposited under wave base, in deep-water environments, with planar laminations and a few Bouma sequences. During sampling diagenetic pyrites and cross cutting beds were avoided, even if small disseminated pyrite grains can be abundant in the shale matrix. The selected shale samples are homogeneous, with few silt layers, characterized by planar laminations.

2.2.2 Methods

The sources of the already published data (trace elements, major elements, Mo and Cr isotopic composition) from this study samples are listed in table 2.5. Details about the chemical procedures can be found in the listed references. The use of tungsten carbide tools has been avoided throughout the whole procedure.

Major element analyses

Major element concentrations for samples of the AGP 1 and AGP 2 drill cores were determined in the Isotope Geochemistry laboratories at the University of Tübingen, Germany. 1.5 g of agate-milled and dried sample powders were mixed with 7.5 g of lithium tetraborate flux and fused at 1200 °C. Glass beads were analyzed using a Bruker AXS S4 Pioneer XRF instrument. Loss of volatiles (i.e. loss on ignition LOI) was determined by heating 1 g of sample powder in an oven at 1050 °C for 3 hours. A detailed description of the full method can be found in Albut et al. (2018).

Trace element determinations

Briefly, 30 mg of ashed silicate sample powders were weighted into PFA beakers and digested using 2 mL of a 1:3 mix of concentrated HNO_3 –HF at 120 °C for 4 days. Upon drying down, the samples were re-dissolved in 4 mL of concentrated HCl and placed on the hot plate at 120 °C for 48 hours to break down fluorides. All fully digested or leached samples were converted to nitric form, taken up in 2 % HNO_3 to a total sample dilution of 10,000 for silicates. They were analyzed with a ThermoFisher Scientific iCAP-Qc® quadrupole ICP-MS at the University of Tübingen. More details about sample preparation, mass spectrometry and data evaluation can be found in Albut et al. (2018). Trace element concentrations of the Black Sea sapropel samples were previously reported in Wegwerth et al. (2018) and Dellwig et al. (2019).

W isotope analyses

Up to 100 mg of ashed shale sample powder, and up to 3.4 g of igneous rock material was weighed in PFA beakers, and doped with an adequate amount of ^{180}W-^{183}W double-spike (DS) to yield a 3:2 sample-to-spike ratio (Kurzweil et al., 2018). Shale and carbonate samples were digested in adequate volumes – depending on sample weights – of a 1:3 mix of concentrated HNO_3–HF for 48 hours at 85 °C. High-pressure bomb digestions at 200 °C for 4 days were necessary for igneous rocks to ensure full digestion of resistant minerals (e.g. spinel and zircon). After drying down, all digested samples were dissolved in concentrated HCl and placed on a hotplate for 48 hours at 130 °C to break down fluorides. Finally, the samples were taken up in 10 mL of 1 M HCl.

The method for W purification used in this study is based on the protocol of Tusch et al. (2019) and Kurzweil et al. (2018), but has been adapted for lower (shales) and higher

(Precambrian igneous rocks) sample loads. 100 µL of 30 % H_2O_2 were added to the 10 ml of sample solutions to yield 1 M HCl + 1 %v H_2O_2 and were then centrifuged for 10 minutes at 5000 rpm prior to loading onto the first column (5 mL of Biorad AG50W-8 200-400 mesh for shales and carbonate sample, or 15 mL for igneous rock sample). Tungsten was collected with an additional 15 mL of 1 M HCl + 1 %v H_2O_2 and loaded directly, without further treatment, on the second column (2 mL Biorad AG1-x8 100-200 mesh). Upon elution of residual matrix elements using 1 M HCl + 1%v H_2O_2 and 2 M HF, W was collected in 15 mL of HNO_3-HF. Tungsten fractions were dried down, treated twice with concentrated $HNO_3 - H_2O_2$, re-dissolved overnight in 2 mL of 6 M HCl and loaded on the third column containing 2 mL of TEVA resin B. Residual matrix elements were eluted from this column by further adding 1 mL of 6 M HCl before final collection of W in 4 mL 6 M HCl followed by 6 mL of 4 M HCl. After drying down the W fractions, resin residues were destroyed twice, using a mixture of concentrated HNO_3 – H_2O_2. The dried samples were finally taken up in the analyte solution (HNO_3 [0.56 M] + HF [0.24 M]). Tungsten separation yields are typically between 60-95 %. As a general rule in the Isotope Geochemistry laboratory in Tübingen, the measured W isotope data of samples with separation yields lower than 50 % are not considered for publication, even though low yields do not seem to influence the $\delta^{186/184}$W values of samples (see appendices, Table 2.8, Fig. 2.9).

Stable W isotopic compositions of the samples were determined on a ThermoFisher Scientific NeptunePlus MC-ICP-MS hosted at the Isotope Geochemistry facilities of the University of Tübingen. Measurements were carried out as reported in detail in Kurzweil et al. (2018). Stable W isotope data are presented in the δ-notation according to the formula:

$$\delta^{186/184}W = [(^{186}W/^{184}W)_{sample})/(^{186}W/^{184}W)_{NIST\ 3163}) - 1] \times 1,000 \tag{2.1}$$

The isotopic fractionation factor α observed for a process between two reservoirs is defined as:

$$\alpha_{A-B} = (^{186}W/^{184}W_{reservoirA})/(^{186}W/^{184}W_{reservoirB}) \tag{2.2}$$

And the isotopic fractionation ε is expressed accordingly as:

$$\varepsilon = (\alpha_{A-B} - 1) \times 1000 \tag{2.3}$$

Cr isotope analyses

For this study, stable Cr isotopes were measured on the ABDP-9 core samples covering the Wittenoom Formation and the Mt McRae Shale of the Hamersley Group, Australia. All other stable Cr isotope data have been published previously (Wille et al., 2013). For Cr isotope analyses, 15-100 mg of ashed shale sample powders were doped with a ^{50}Cr-^{54}Cr double spike (sample-spike ratio of 1:1) prior to full digestion in HF-HNO_3 in PFA beakers at 150 °C. The Cr purification method applied for samples of this study was described in detail in Schoenberg et al. (2008) and Wille et al. (2013), and is the former protocol that the Isotope Geochemistry work group in Tübingen applies nowadays. Briefly, Cr was purified from Fe by a liquid-liquid extraction method using trialkylphosphine oxide Cyanex® 923. The Fe-free samples were then dried down, dissolved in 0.5 mL of 0.25 M HCl in a PFA beaker and diluted with 4 mL of H_2O. The solutions were transferred to 25 mL Erlenmeyer flasks to which 0.5 mL of 0.2 M ammonium peroxydisulfate (APS; $(NH_4)_2\ S_2O_8$) was added. The flasks were covered with a watch glass and placed on a hot plate at 120 °C for 2 hours to ensure complete oxidation of Cr^{III} to Cr^{VI}. Upon cooling to room temperature samples were transferred to 15 mL centrifuge tubes and centrifuged at 5000 rpm for 5 minutes. The samples were loaded in 5 mL of 0.025 M HCl onto columns containing 2 mL of Dowex AG 1x8, 100-200 mesh. Matrix elements were eluted with HCl and H_2O, prior to reduction of Cr^{VI} to Cr^{III} with 1 mL of 2 M HNO_3 for 30 minutes. Chromium was then collected in 9 mL of 2 M HNO_3 + H_2O_2. The determination of stable Cr isotopic ratios was carried out on the ThermoFisher Scientific NeptunePlus MC-ICP-MS at the University of Tübingen following the procedure described in Schoenberg et al. (2008). The isotopic ratios are reported as $\delta^{53/52}$Cr relative to the standard solution SRM 979, with an external reproducibility (2SD) of 0.027 ‰.

2.3 Results

The concentrations of major and trace elements and the W, Mo and Cr isotopic compositions of all samples used in this study are presented in the tables 2.1, 2.2, 2.3 and table 2.9 (appendices).

Precambrian igneous rocks: The W concentration of Archean GGMs (3.2 to 3.1 Ga) and TTGs (3.5 to 3.2 Ga) from the Barberton Greenstone Belt in South Africa range from 0.016 to 0.190 µg.g^{-1} (Kleinhanns et al., 2003). The W isotopic compositions of these samples range from -0.007 to +0.097 ‰, with averages of +0.021 ±0.085 ‰ (n = 5) and +0.048 ±0.070 ‰ (n = 4), respectively (Table 2.1). The Ni/Th ratio is a good proxy to distinguish between ultramafic (∼20,000), mafic (∼1,000), and felsic ($\leq$ 50) rock reservoirs. The Ni/Th ratios of the Barberton Greenstone Belt GGMs and TTGs range from 0.34 to 32.90, with averages of 0.56 ±0.66 and 16.26 ±25.04, respectively (Kleinhanns et al., 2003).

Archean komatiites/komatiitic basalts (2.8 Ga, n=2) from the Belingwe Greenstone Belt in Zimbabwe have W concentrations between 0.016 and 0.019 µg.g^{-1} and $\delta^{186/184}$W values of +0.070 ‰ and +0.096 ‰, respectively. Their Ni/Th ratios are the highest within or our sample set with values of 21,164 and 1,025, respectively (Bolhar et al., 2003).

The Paleoproterozoic granitoids from Västervik in Sweden show W concentrations between 0.530 and 1.050 µg.g^{-1} (Nolte et al., 2011) and $\delta^{186/184}$W between +0.070 and +0.093 ‰ (n = 5). Their Ni/Th ratios are comprised from 0.20 to 1.66 with an average of 0.79 ±1.05 (Nolte et al., 2011).

The W/Th (weight ratio) of our Precambrian igneous rocks vary from 0.009 to 0.271, similar to the W/Th ratio of the upper mantle (König et al., 2011).

Modern sediments: The W concentrations in the Holocene sapropels samples (0 to 8.7 ka) from the Black Sea span from 0.81 to 1.30 µg.g^{-1} (Dellwig et al., 2019), and strongly correlate with Al concentrations (R^2 = 0.92). They show a narrow range of $\delta^{186/184}$W values, from +0.050 to +0.071 ‰, with an average of +0.061 ±0.013 ‰ (n = 7) (Table 2.2).

Precambrian samples: The W concentration of Precambrian black shale samples vary from 0.35 to 5.04 µg.g^{-1}, with younger samples tending to have higher W concentration. The Precambrian shale samples can be divided into 3 groups related to age, based on Al_2O_3/TiO_2 and Cr/Sc ratios. Oldest samples (3.47 to 2.94 Ga) are characterized by Al_2O_3/TiO_2 ratios from 21.1 to 31.2, with the highest Cr/Sc ratios of the sample set, ranging from 13.8 to 23.9. Early Neoarchean shale samples (2.77 to 2.76 Ga) have lower Al_2O_3/TiO_2 and Cr/Sc ratios of 15.7 to 22.5 and 10.0 to 18.7, respectively. Finally, 2.5 to 2.32 Ga shale samples have the

Table 2.1: W concentration and isotopic composition of the Precambrian igneous rock samples reported in this study.

sample ID	lithology	age [Ma]	W [µg.g^{-1}]	$\delta^{186/184}$W [‰ NIST 3163]	2SE	Ni/Th
Barberton Mountain Land granitoids						
99/118	GGM	3106	0.040	0.003	0.009	0.34
99/117	GGM	3107	0.190	0.006	0.008	0.64
99/127	GGM	3107	0.140	0.009	0.009	0.22
99/115	GGM	3109	0.050	0.097	0.009	1.07
99/108	GGM	3216	0.100	-0.007	0.009	0.51
99/128	TTG	3227	0.060	0.097	0.008	32.92
99/107	TTG	3443	0.080	0.046	0.010	13.40
99/109	TTG	3509	0.020	0.018	0.008	16.02
99/106	TTG	3236	0.030	0.029	0.016	2.69
Zeederbergs Fm., B-Z-3	high-Mg tholeiite	2700	0.019	0.096	0.008	1,025
Reliance Fm., B-R-1	komatiite	2700	0.016	0.070	0.008	21,164
Västervik, southeast Sweden granitoids						
08-05	quartzdiorite-tonalite	1850	0.530	0.082	0.010	1.66
03-05	quartzmonzonite-monzogranite	1850	0.828	0.083	0.008	0.53
19-05	quartzmonzonite-monzogranite	1850	0.651	0.084	0.010	0.81
21-05	monzogranite-syenogranite	1850	0.916	0.093	0.010	0.20
15-05	monzogranite-syenogranite	1850	0.922	0.070	0.008	0.44

Ages of the Granodiorite-granitic-monzogranite (GGM) and Tonalite-tronjdemite-granodiorite (TTG) originate from De Ronde and Kamo (2000) and Kamo and Davis (1994); W, Ni and Th concentrations of Precambrian TTG, GGM and Västervik granitoids samples originate from Kleinhanns et al. (2003) and Nolte et al. (2011). W concentration of komatiite and tholeiite were measured with MC-ICPMS in this study; Th and Ni concentrations of the mafic to ultramafic samples from the Belingwe Greenstone Belt originate from Bolhar et al. (2003).

highest Al_2O_3/TiO_2 ratios measured, from 18.1 to 37.0, and the lowest Cr/Sc ratios from 4.3 to 13.5. Their Ni/Th ratios scatter from 58 to 1.4.

Archean shale samples from ABDP drill cores show a large variation in $\delta^{186/184}$W values ranging from +0.028 to +0.246 ‰ (n=26). In contrast, Proterozoic post-GOE samples from the AGP-1 and AGP-2 cores (2.32 Ga, South Africa) show lower values, from +0.027 to +0.110 ‰ (average $\delta^{186/184}$W = +0.061 ±0.046 ‰; n=19) (Table 2.3).

The chromium concentration of black shales from the ABDP-9 core (~2.5 Ga) determined in this study range from 98.7 to 841.7 µg.g^{-1}. These samples show a very narrow range in $\delta^{53/52}$Cr values from -0.075 to +0.045 ‰ (Table 2.3). The Paleoproterozoic shale samples of the drill core AGP1-2 have vanadium (V) concentrations ranging from 31.61 to 195.87 µg.g^{-1}, with an average of 94.01 ±69.17 µg.g^{-1}. Their Mo/Al and V/Al weight ratios range from 0.06 to 0.47 and 20.38 to 27.79, respectively (Table 2.9, Figure 2.7).

Table 2.2: W content and isotopic composition of the modern sapropels reported in this study.

sample depth [m]	lithology	age [ka BP]	W [µg.g^{-1}]	$\delta^{186/184}$W [‰ NIST 3163]	2SE
Black Sea sapropels, core M72/-5 22GC-3					
0.20	sapropel deposited under intermediate reducing conditions	2.70	1.30	0.062	0.011
0.24	sapropel deposited under intermediate reducing conditions	3.50	1.26	0.063	0.008
0.30	sapropel deposited under weakly euxinic conditions	4.80	1.30	0.064	0.008
0.38	sapropel deposited under weakly euxinic conditions	6.40	1.11	0.060	0.012
0.41	sapropel deposited under intermediate reducing conditions	7.10	0.98	0.050	0.007
0.44	sapropel deposited under intermediate reducing conditions	7.70	0.83	0.059	0.011
0.48	sapropel deposited under oxic conditions	8.70	0.81	0.071	0.011

Black Sea sapropel ages were reported by Wegwerth et al. (2018), W contents originate from Dellwig et al. (2019).

Table 2.3: W, Mo and Cr concentrations and isotopic compositions of the Precambrian shales reported in this study. $\delta^{186/184}$W values normalized to NIST 3163, $\delta^{98/95}$Mo normalized to NIST 3134 +0.25 ‰, $\delta^{53/52}$Cr values normalized to NIST 979.

Sample	Age [Ma]	W [µg.g^{-1}]	$\delta^{186/184}$W ‰	2SE 2SD§	Mo [µg.g^{-1}]	$\delta^{98/95}$Mo	2SE ‰	Cr [µg.g^{-1}]	$\delta^{53/52}$Cr ‰	2SE
Pilbara Craton										
ABDP-2										
58.2	3470	2.09	0.028	0.013	3.6	0.46	0.05	408.5	-0.069	0.062
102.4	3470	2.90	0.103	0.018	3.1	0.51	0.02	384.3	-0.139	0.107
158.7	3470	2.32	0.073	0.020	3.9	0.29	0.02	429.9	-0.102	0.02
190.9	3470	3.57	0.132	0.015	2.4	0.41	0.02	252	-0.126	0.065
219.2	3470	0.34	0.049	0.014	2.6	0.24	0.02	221.9	-0.063	0.073
ABDP-5										
74.5	2940	2.36	0.024	0.026	1.5	0.51	0.02	546.2	0.031	0.098
86	2940	1.03	0.051	0.015	1.5	0.59	0.02	603.3	-0.158	0.061
122	2940	1.33	0.177	0.013	1.6	0.46	0.02	553.9	-0.028	0.118
164.6	2940	1.39	0.136	0.011	1.5	0.44	0.02	599.2	-0.161	0.160
183.9	2940	1.31	0.112	0.017	1.5	0.50	0.02	540.0	-0.092	0.057
ABDP-6										
85.3	2770	2.36	0.167	0.011	2.5	0.59	0.02	276.0		
95.9	2770	2.79	0.162	0.013	2.7	0.41	0.02	238.2	-0.046	0.094
113.9	2770	3.33	0.119	0.015	3.4	0.24	0.02	291.4	-0.051	0.069
173.5	2770	1.78	0.18	0.015	4.5	0.52	0.02	2310.	-0.144	0.041
	Replicate		0.168	0.013						
	Average		*0.174*	*0.018*						
267.7	2770	3.68	0.098	0.012	3.6	0.27	0.02	348.0	-0.155	0.038
ABDP-3										
98.3	2760	4.94	0.123	0.016	3.4	0.50	0.01	332.8	-0.112	0.054
111.1	2760	4.65	0.119	0.011	2.9	0.50	0.02	318.9	-0.12	0.071
124.3	2760	3.82	0.164	0.030	2.8	0.43	0.02	274.5	-0.147	0.047
141.2	2760	5.04	0.119	0.010	3.6	0.55	0.02	356.0	-0.112	0.084
ABDP-9										
132.7	2500	2.2	0.233	0.012	13.1	1.37	0.01	50.14	-0.045	0.035
	Replicate		0.259	0.010						
	Average		*0.246*	*0.027*						
176.7	2500	2.76	0.110	0.010	2.9	0.97	0.02	66.36	-0.075	0.047
218.65	2500	3.64	0.076	0.009	3.8	1.10	0.02	121.38	-0.065	0.015
239.5	2500	2.33	0.122	0.016	2.1	0.58	0.03			

Table 2.3 continued from previous page

Sample	Age	W	$\delta^{186/184}$W	2SE	Mo	$\delta^{98/95}$Mo	2SE	Cr	$\delta^{53/52}$Cr	2SE
	[Ma]	[µg.g^{-1}]	‰	2SD§	[µg.g^{-1}]		‰	[µg.g^{-1}]	‰	
259.38	2500	4.05	0.051	0.013	2.5	0.89	0.03			
316	2500	2.47	0.146	0.043	4.4	0.61	0.02	167.36	-0.067	0.015
340	2500	3.67	0.108	0.012	3.8	0.62	0.02			
Post Archean Kaapvaal craton										
AGP-1										
57.77	2320	3.08	0.078	0.015						
	Replicate		0.082	0.014						
	Average		*0.08*	*0.005*						
61.18	2320	3.38	0.056	0.016						
63.4	2320	5.05	0.076	0.016						
	Replicate		0.075	0.018						
	Average		*0.076*	*0.002*						
71.6	2320	3.47	0.084	0.013						
	Replicate		0.075	0.013						
	Average		*0.08*	*0.013*						
86.71	2320	3.33	0.027	0.011						
87.48	2320	1.87	0.086	0.010						
92.53	2320	2.03	0.110	0.011						
102.1	2320	3.71	0.033	0.017						
	Replicate		0.052	0.017						
	Average		*0.043*	*0.027*						
105.21	2320	4.07	0.060	0.011						
AGP-2										
62.34	2320	4.29	0.033	0.013						
	Replicate		0.055	0.013						
	Replicate		0.085	0.013						
	Average		*0.057*	*0.052*						
66.22	2320	4.15	0.050	0.014						
67.48	2320	3.53	0.065	0.017						
76.13	2320	2.82	0.073	0.011						
83.14	2320	2.93	0.019	0.013						
	Replicate		0.040	0.012						
	Average		*0.029*	*0.030*						
86.3	2320	3.12	0.031	0.010						
	Replicate		0.034	0.011						
	Replicate		0.029	0.011						

Table 2.3 continued from previous page

Sample	Age	W	$\delta^{186/184}$W	2SE	Mo	$\delta^{98/95}$Mo	2SE	Cr	$\delta^{53/52}$Cr	2SE
	[Ma]	[µg.g^{-1}]	‰	2SD§	[µg.g^{-1}]		‰	[µg.g^{-1}]	‰	
	Average		*0.031*	*0.006*						
89.22	2320	2.67	0.042	0.013						
	Replicate		0.050	0.012						
	Average		*0.046*	*0.013*						
92.53	2320	2.80	0.096	0.010						
	Replicate		0.040	0.012						
	Replicate		0.036	0.012						
	Average		*0.057*	*0.067*						
108.23	2320	4.10	0.113	0.014						
	Replicate		0.082	0.012						
	Average		*0.097*	*0.044*						

§ 2.SD of the average of measured duplicates and replicates Mo and Cr data of the core ABDP-2-5-6-3 originate from Wille et al. (2013) ; Mo data of the core ABDP-9 originates from Kurzweil et al. (2015).

2.4 Discussion

2.4.1 The stable W isotopic composition of the Archean and Paleoproterozoic continental crust

The W isotopic compositions of bulk sedimentary samples are a mixture of the $\delta^{186/184}$W signals of their detrital and authigenic components. The use of black shales' W isotopic compositions as redox tracer for their paleodepositional environments is thus based on the conditions that detrital components only show very limited $\delta^{186/184}$W variations, and that the authigenic components' $\delta^{186/184}$W values exceed the detrital range as a result of isotopic fractionation by W redox-cycling in Earth's surface reservoirs.

The chemical composition of the continental crust continuously changed from a predominately mafic-ultramafic during the Archean to a largely felsic one during the Paleoproterozoic, even though the precise proportions are still debated (Chen et al., 2019; Condie, 1993; Gaschnig et al., 2016; Greber and Dauphas, 2019; Greber et al., 2017; Greber et al., 2015b; Rudnick and Gao, 2014; Tang et al., 2016). Furthermore, Earth's mantle was hotter in the Archean compared to the Proterozoic and Phanerozoic, due to still higher abundances in radioactive elements and potential residual heat from late accretion and core crystallization (Nisbet et al., 1993; Vacquier, 1991). This resulted, for example, in higher melt fractions of up to 40 % during Archean komatiite genesis compared to melt fractions between approximately 7-15 % for Phanerozoic MORBs and OIBs (Langmuir and Forsyth, 2007; Walter, 1998). This large variation in melt fractions during basalt genesis bears the potential for a change in the W isotopic composition of mafic crust components through Earth's history. The use of the stable W isotope composition of the ancient shales of this study as potential paleoredox indicator thus require first (i) to determine the relative proportions of the detrital components of these 3.47 to 2.32 Ga old black shales and (ii) to measure the W isotopic composition of Paleoarchean to Paleoproterozoic igneous rocks to determine the range in detrital $\delta^{186/184}$W signatures during these Eras.

The chemical composition of shales has previously been used to quantify the contributions of ultramafic-mafic-felsic components to the emerging Archean crust (Condie, 1993; Greber and Dauphas, 2019; Hessler and Lowe, 2006; Wille et al., 2013; Wronkiewicz and Condie, 1987). Greber and Dauphas (2019), for example, used weight ratios of shales in Al_2O_3/TiO_2 vs. Cr/Sc space to establish that ca. 3.25 Ga Archean crust consisted of 60 % felsic, 30 % mafic, and 10 % komatiitic components, with regional variability across cratons mainly related

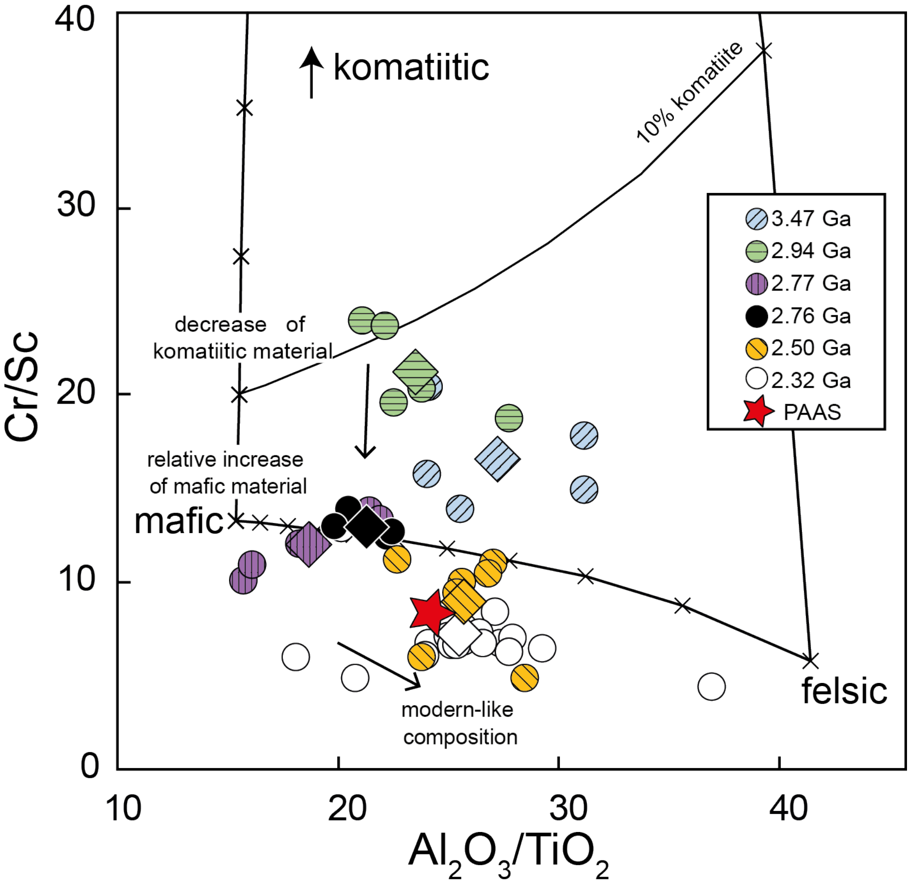

Figure 2.1: Al_2O_3/TiO_2 versus Cr/Sc ternary space (weight ratios). The endmembers values originate from Greber and Dauphas (2019). Color pattern refers to each core examined. Single data point is represented by circles, average of each core is represented by diamonds. Each tick mark on the ternary space limits corresponds to a 10 % interval. The post-Archean average shale (PAAS) values originate from Condie (1993). (For interpretation of the references to colour in this figure legend, the reader is referred to the web version of this article.)

to different incorporation of komatiitic material. Here, the endmember space defined by komatiite, mafic, and felsic compositions in the same diagram was used to investigate the relative proportions of detrital components of the Archean black shales from the Hamersley Basin, Pilbara Craton and the Paleoproterozoic black shales from the Transvaal Basin, Kaapvaal Craton (Fig. 2.1; Table 2.9). The 3.47 Ga old black shales have an average komatiitic:mafic:felsic proportion of 4:30:66 %, while the 2.94 Ga old ones have higher komatiitic contents with an average komatiitic:mafic:felsic proportion of 8:42:50 % respectively.

The 2.77 and 2.76 Ga shales are devoid in any komatiitic component, as are all younger shales as well. However, they display a significant increase in their mafic components compared to the older shales, and have mafic:felsic ratios of 74:26 % (2.77 Ga) and 57:43 % (2.76 Ga), respectively. Neoarchean (2.5 Ga Mt Mc Rae black shales; Hamersley Basin) and Paleoproterozoic shales (2.32 Ga old Duitschland/Timeball Hill; Transvaal Basin) are composed of higher

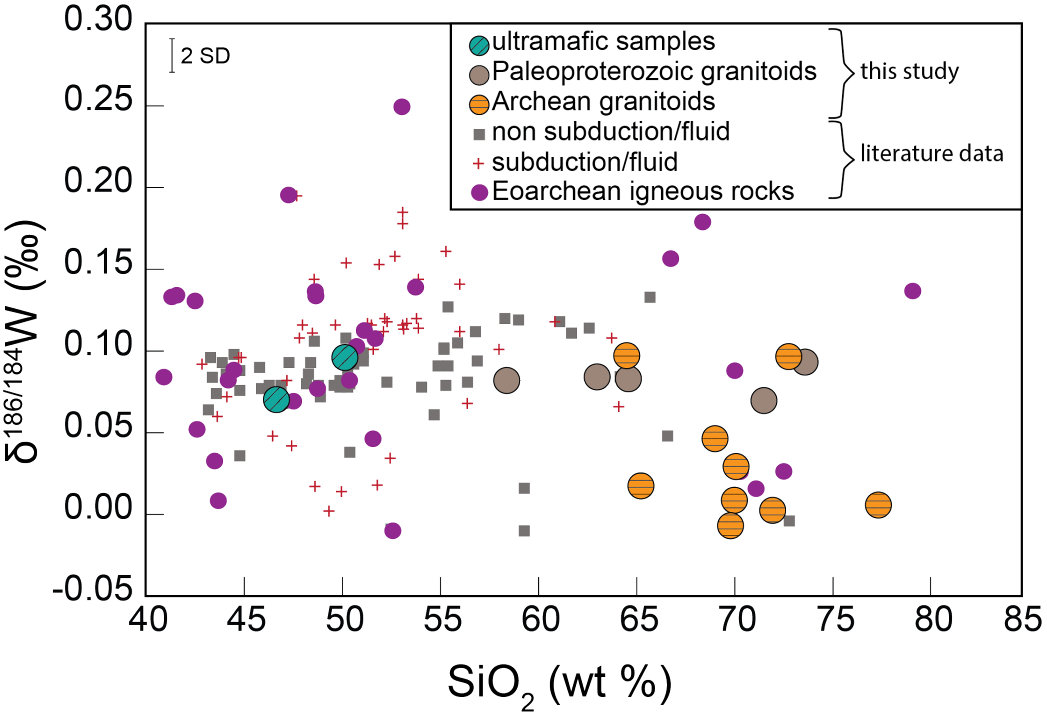

Figure 2.2: SiO_2 (wt. %) relative to $\delta^{186/184}$W values (relative to NIST 3163) of igneous rock samples originating from this study and literature data. Literature values originate from Kurzweil et al. (2020), Kurzweil et al. (2019), Kurzweil et al. (2018), Krabbe et al. (2017), Mazza et al. (2020). Rock standards values (BHVO-2, AGV-2, W-2a, RGM-2, GSP-2) SiO_2 (wt. %) originate from the GeoRem online database. Literature $\delta^{186/184}$W values (n = 102) were measured on various lithologies (basalt, picrite, basaltic glass, basaltic andesite, boninite, tholeiite, absarokite, granitoids, rhyolite, dolerite).

proportions of felsic components, with similar mafic:felsic ratios of 36:64 %, very close to the Post Archean Average Shale (PAAS) described by Condie (1993). While some of the variations in the relative abundance of detrital components of the Hamersley Terrane shales may be due to regional differences in the geology of the eroded hinterland (Greber and Dauphas, 2019), a clear trend in the evolution of the detrital composition through time, from komatiitic bearing sediments in the Paleo- and Mesoarchean, to mafic-dominated sediments in the early Neoarchean to more felsic ones in late Neoarchean and the Paleoproterozoic seems evident.

The large span of $\delta^{186/184}$W values previously reported for meta-igneous rocks of the 3.85 to 3.62 Ga Itsaq Gneiss Complex (-0.072 to +0.249 ‰) is considered to represent alteration effects (Kurzweil et al., 2020). The W/Th ratios of these rocks with values from 0.008 to 143 strongly differ from the range of modern mantle W/Th ratios of 0.09 to 0.24 (König et al., 2011; Kurzweil et al., 2020). As such the W isotopic compositions of the Itsaq samples do not represent that of typical Archean crust. The W/Th ratios of Archean and Paleoproterozoic igneous rocks presented in this study, on the other hand, vary from 0.009 to 0.271 – similar to the modern mantle W/Th ratio (König et al., 2011) – indicating that these samples were not affected by secondary processes during metasomatism.

The W isotopic composition of all Archean and Paleoproterozoic igneous rocks, including Paleo- and Mesoarchean mafic and felsic granitoids (3.5 to 3.1 Ga, Barberton Greenstone Belt, South Africa), komatiites (2.8 Ga, Zeederberg formation, Belingwe Greenstone Belt, Zimbabwe), and Paleoproterozoic felsic granitoids (1.85 Ga, Västervik area, Sweden), lie between -0.007 ‰ and +0.097 ‰ in $\delta^{186/184}$W, which we henceforth define as the W isotopic range of the Precambrian Igneous Inventory (PII; $\delta^{186/184}\mathrm{W}_{PII}$ values). We further assume that the detrital components of all Archean and Paleoproterozoic black shales lie within this range of $\delta^{186/184}\mathrm{W}_{PII}$.

The range of $\delta^{186/184}\mathrm{W}_{PII}$ values agrees very well with that of Phanerozoic igneous crustal rocks of -0.010 to +0.120 ‰ (Table 2.1, Figure 2.2) previously reported by Krabbe et al. (2017), Kurzweil et al. (2019), Kurzweil et al. (2018) and Mazza et al. (2020). This indicates that different proportions of mantle melting and melt differentiation are accompanied by little to no W isotopic fractionation (Mazza et al., 2020) and that the $\delta^{186/184}$W value of Earth's igneous crust did not (significantly) change over billions of years.

2.4.2 The W isotopic composition of modern and ancient anoxic sediments

The stable W isotopic signature of modern euxinic Black Sea sapropels

The strong positive correlation of W with Al contents in the Black Sea sapropels strongly indicates the lack of a substantial authigenic W enrichment and thus a predominantly detrital origin of W in these samples as was previously suggested (Dellwig et al., 2019). This agrees with the observation that WO_4^{2-} is not readily scavenged by sediments deposited under euxinic conditions from the Mediterranean Sea (Dellwig et al., 2019) due to the high solubility of tungstate in such hydrochemical environments (Cui et al., 2021; Mohajerin et al., 2016). A purely detrital W source for the Black Sea sapropels is further supported by their homogenous $\delta^{186/184}$W of +0.061 ±0.013 ‰ (n = 7), which lies well within the range of the modern igneous crust discussed in the previous section of this study ($\delta^{186/184}$W values between -0.010 and +0.120 ‰). Therefore, our results indicate that sediments deposited in modern and potentially ancient euxinic environments do not authigenically accumulate W. Their W isotopic compositions reflect their detrital components and can certainly not be used to trace the ocean's redox state through time.

The stable W isotopic composition of Archean and Paleoproterozoic shales

In contrast to modern samples from the Black Sea, Archean and Proterozoic sediments show no co-variations between W and elements that are insoluble and immobile during chemical weathering such as Al, Ti, Zr and Th. The heterogeneity of the shales' detrital components sourced from continental crust through time has already been shown in section 2.4.1, and is further discussed in the appendices section 2.6.5. This complicates the determination of the extent of authigenic W enrichment using Al, Ti, Zr or Th concentrations of our shale samples relative to the reference values of PAAS or UCC (Figure 2.7 of the appendices). For example, most of the Precambrian black shales investigated in this study show significant enrichments in Th_{UCC}-normalized W contents, including the two Paleoproterozoic shale suites (Fig 2.4 of the appendices). However, these 2.32 Ga shales are characterized by PII-like $\delta^{186/184}$W values (+0.027 to +0.113 ‰), inconsistent with any authigenic W enrichments. This observation might indicate that the W/Th ratio of the detrital component was temporally above that of UCC, while the $\delta^{186/184}$W value of the detritus remained within the PII range.

Black shales from each of the 3.47 to 2.5 Ga old formations of the Pilbara Craton not only show elevated W/Th but also partially exceed the span of the above established Archean igneous inventory with overall $\delta^{186/184}$W values between +0.027 and +0.246 ‰ (Figure 2.4). In accordance with other redox-sensitive stable isotope systems, such as stable Mo and Cr isotopes, this observation may indicate mixing of various proportions of isotopically light detrital W with authigenic and isotopically heavier W in the Archean black shales from the Pilbara Craton. It is, however, difficult to assess the exact extent of authigenic W enrichment for the different suites of Archean and Paleoproterozoic black shales of this study (section 4.1, appendices section 2.6.5).

In order to better constrain the relevance of authigenic W, Figure 2.4a combines the $\delta^{186/184}$W values of Precambrian shales with their Ni/Th values to investigate the relation of potentially authigenic W with compositionally very variable detrital components. Nickel is highly enriched in komatiitic and mafic components, while Th is more abundant in evolved igneous rocks (Arndt, 1991; Condie, 1993). Therefore, high Ni/Th ratios are typical for ultramafic and mafic igneous rocks, while lower Ni/Th ratios are found in felsic ones. The Ni/Th ratios of the Archean mafic/ultramafic igneous rocks of this study have indeed very high values ranging from 1,000 to 22,000, while those of Precambrian felsic igneous rocks of 0.20 to 58 are several

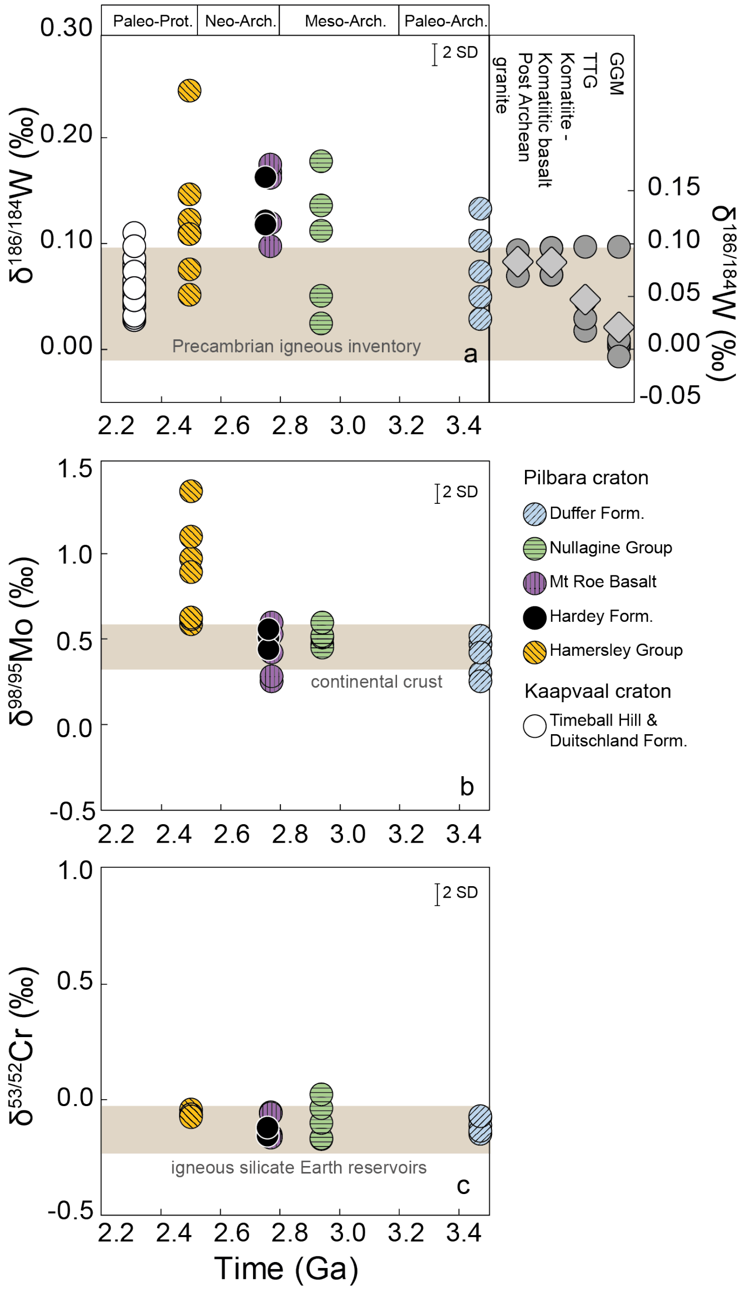

Figure 2.3: a: Tungsten stable isotopic composition of Precambrian shales depending on their age and igneous rocks from the Archean and Proterozoic. Gray circles represent single measurements; gray diamonds represent the averages of each igneous rock type. See results for more detailed information. GGM (Granodiorite-granitic-monzogranite) and TTG (Tonalite-trondjemite-granodiorite) are dated from 3.5 Ga to 2.7 Ga. Post Archean granite are dated at 1.95–1.8 Ga. Komatiite and komatiitic basalt are dated at 2.7 Ga. 3b: Molybdenum stable isotopic composition ($\delta^{98/95}$Mo NIST 3134= 0.25 ‰) of the Archean shale samples measured in this study, data originates from Wille et al. (2013) (ABDP 2–3-5–6) and Kurzweil et al. (2015) (ABDP-9). The external long reproducibility was determined at 0.12 ‰ (Wille et al., 2013) and 0.09 ‰ (Kurzweil et al., 2015). Molybdenum ratios are reported relative NIST 3134 standard, set to +0.25 ‰. The shaded area represents the value reported for the bulk continental crust (Willbold and Elliott, 2017), consistent with the $\delta^{98/95}$Mo of Archean igneous rocks (Greber et al., 2015a). 3c: Chromium isotopic composition ($\delta^{53/52}$Cr (‰)) of the Archean shale samples measured in this study, originating from Wille et al. (2013) (ABDP 2–3-5–6) and this study (ABDP 9). Reproducibility was determined at 0.1 ‰ on $\delta^{53/52}$Cr. The shaded area represents the Igneous silicate Earth reservoir, set at -0.124 ±0.101 ‰ (2 SD) (Schoenberg et al., 2008) to the NIST SRM 979.

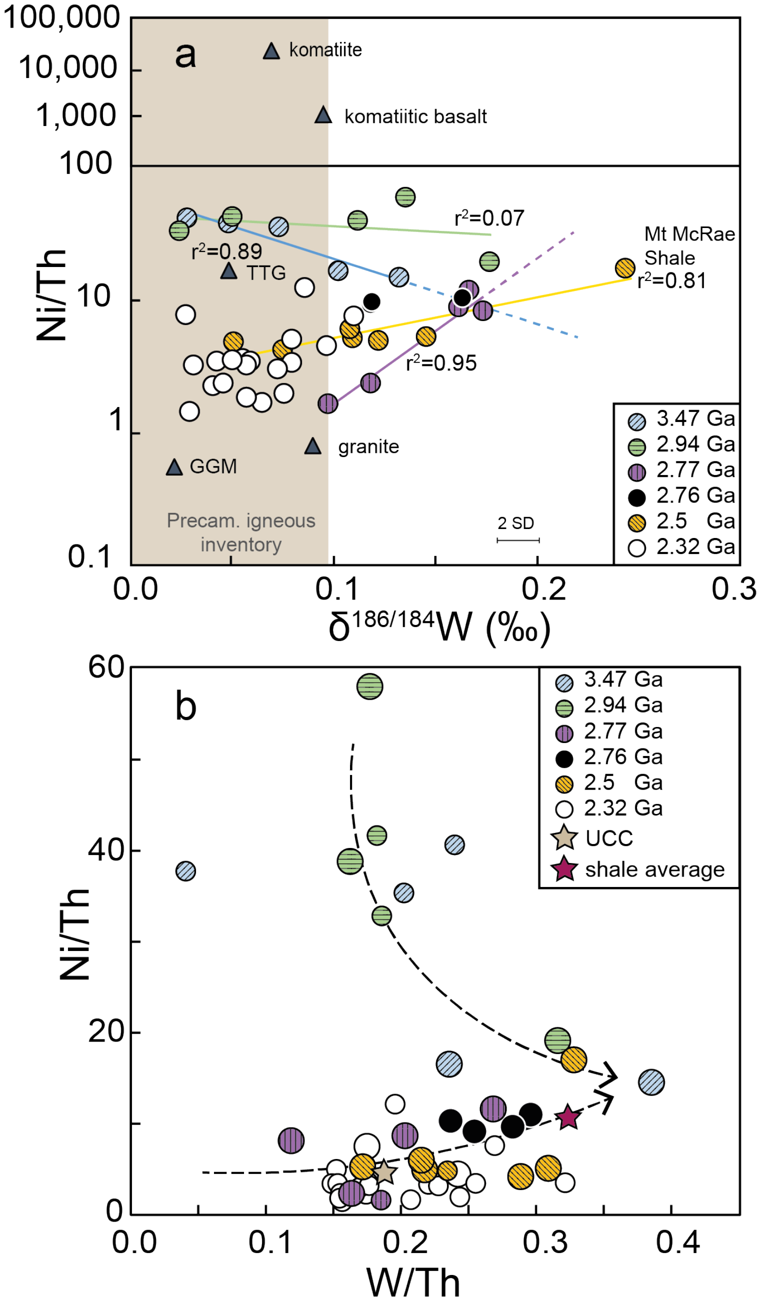

Figure 2.4: a) $\delta^{186/184}$W/Ni/Th (weight ratios) of Precambrian shales and igneous rocks plotted against the average $\delta^{186/184}$W of each rock type measured in this study. Shaded gray area indicates the estimated Precambrian igneous inventory. Triangles represent the average of each major component of the Archean-Paleoproterozoic crust composition. Ni/Th ratios of igneous rocks originate from Kleinhanns et al. (2003), Nolte et al. (2011) and Bolhar et al. (2003), the shales samples ratios originate from the trace element data of this study. The exponential trend R^2 of the 2.32 Ga combined samples of the AGP1-2 cores is equal to 0.16. 4b) W/Th space Ni/Th (weight ratios). The values of the UCC ratios originate from (Rudnick and Gao, 2014), the terrigenous, volcanic-sedimentary shales values originate from Ketris and Yudovich (2009). Arrows represent mixing trends between authigenic and detrital W. Small circles correspond to samples with $\delta^{186/184}$W values typical of the Archean igneous inventory, bigger circles correspond to shale samples with $\delta^{186/184}$W values heavier than the Archean igneous inventory. (For interpretation of the references to colour in this figure legend, the reader is referred to the web version of this article.)

orders of magnitude lower (Figure 2.4a). As a result, it can be expected that the Ni/Th ratios of clastic sedimentary components in the Archean to Paleoproterozoic shales of this study will also greatly vary depending on their relative komatiitic:mafic:felsic proportions. Figure 2.4a reveals exponential two-component mixing trends in Ni/Th vs. $\delta^{186/184}$W space (R^2 ranging from 0.81 to 0.95) for most of the Archean black shale suites, but not for the Paleoproterozoic shale sample suites of this study (R^2=0.16, combined 2.32 Ga samples). The first endmember is identified as detrital component with $\delta^{186/184}$W values typical for the Precambrian igneous inventory (-0.007 to +0.097 ‰) with highly variable Ni/Th ratios. The oldest sample suites (3.47 and 2.94 Ga) have the highest Ni/Th ratios (41), linked to their large proportions of ultramafic and mafic components (see section 2.4.1 and Fig. 2.1). The detrital endmembers of the younger black shale suites (2.77 to 2.32 Ga) are characterized by lower Ni/Th (< 10) due to higher proportions of felsic detrital material in the emerging Neoarchean and Paleoproterozoic crust (Fig. 2.1). The second endmember of the mixing trends is relatively constant in Ni/Th vs. $\delta^{186/184}$W space with a Ni/Th ratio between 8 and 19 and a converging $\delta^{186/184}$W value of +0.170 ‰. Remarkably, a non-euxinic shale from the Mount McRae Fm has an even heavier W isotopic composition of +0.246 ‰ in $\delta^{186/184}$W (Anbar et al., 2007; Reinhard et al., 2009). When plotting W/Th vs. Ni/Th (Figure 2.4b), the endmember data-points with Ni/Th between 8 and 19, for each individual sample set of the Archean black shales have the highest W/Th ratios and as such the strongest authigenic W enrichment. It is thus proposed here that the W enriched source, with a W isotopic composition heavier than the range of the Precambrian igneous inventory, is indeed authigenic in origin. The heavy W isotopic composition of this authigenic component is most likely the result of W scavenging from the oceans (following section 2.4.3). As a first important result, the stable W isotopic composition of ancient shales bears the potential to record the redox state of the Archean ocean due to efficient W authigenic enrichments in ferruginous sediments.

2.4.3 Combined stable W-Mo isotopic evolution in the Archean and Paleoproterozoic ocean

As outlined above, we ascribe the heavy stable W isotopic compositions found in Archean shales to an authigenic component in these sediments. We speculate that partial oxidation of mineral-bound tetravalent W to soluble hexavalent WO_4^{2-}, during continental weathering led to an Archean ocean input source that was isotopically heavy. Alternatively, if W in Archean igneous rocks and minerals already was hexavalent as suggested by Fonseca et al. (2014)

and Che et al. (2013), a change in the bonding environment during weathering may have preferentially released isotopically heavy W from the continents to the oceans.

Another important W input source to the Archean oceans would have been hydrothermal vents (Kishida et al., 2004) of yet unknown W isotopic composition. Further adsorption of tungstate onto Mn-oxides and Fe-hydroxides in proximal less reducing shallow water environments compared to deep water environments may have further pushed the seawater W isotopic composition towards higher $\delta^{186/184}$W values. A prerequisite for such a W cycling in the Archean is that the ambient redox-potential Eh of continental meteoric water and of proximal shallow-oceans was above -0.4 V, which corresponds to the minimal value for the water stability at pH 7. Figure 2.5 present the individual W-O-H, Mo-O-H and Cr-O-H Pourbaix diagrams according to Takeno (2005), calculated for a temperature of 25 °C, elemental concentration of 10^{-10} mol and a pressure of 1 atm. Pourbaix diagrams reveal the differences in redox potentials for various elements, however, translation to natural systems and the use of absolute Eh values have to be taken with caution. Limitations are for example the poorly constrained concentrations of soluble W, Mo and Cr in deep versus shallow Precambrian ocean water masses and their heterogeneous temperatures and pressures. Nevertheless, Eh-pH models may still help to constrain the solubility of certain redox species for different elements and thus provide a first order estimate of Precambrian ocean redox evolution.

The model used here predicts that even at the lowest Eh value in the water stability field of -0.4 V at a pH of 7, mineral-bound W would be released from the bed rock to meteoritic water in form of WO_4^{2-}. This dissolved WO_4^{2-} would then be delivered to the oceans by rivers and ground water fluxes with a yet unknown but potentially heavy stable W isotopic composition. Marine WO_4^{2-} might further adsorb onto Mn and Fe oxides, preferentially scavenging light W isotopes. Manganese oxides already formed in up to 3.0 Ga old proximal depositional environments (Albut et al., 2019; Ossa Ossa et al., 2018b; Planavsky et al., 2014a). While there are no reports for the existence of this oxide phase at 3.47 Ga, the time of deposition of our oldest suite of samples from the Pilbara Craton, Fe(III)-hydroxides already formed by microbial Fe(II) oxidation at that time as is also indicated by the existence of contemporaneous banded iron formations (Bolhar et al., 2005; Ghosh, 2020; Li et al., 2013; Trendall, 2002).

In contrast to the fractionated W isotopic compositions of the 3.47 to 2.5 Ga old black shales reported here, no previous studies found authigenic Mo enrichment and fractionated $\delta^{98/95}$Mo signatures in open ocean deep water marine sediments older than 2.7 billion years

(Czaja et al., 2012; Kurzweil et al., 2015; Ostrander et al., 2020; Wille et al., 2007; Wille et al., 2013). However, fractionated Mo isotopic values have been reported for shallow water carbonates and iron formations as old as 2.93 Ga (Thoby et al., 2019) and 2.95 Ga (Albut et al., 2019; Planavsky et al., 2014a), while the Mo isotopic compositions of shallow water iron formations older than 3.0 Ga are characterized by unfractionated $\delta^{98/95}$Mo values (Siebert et al., 2005; Wille et al., 2007). It has been proposed that the discrepancy in the $\delta^{98/95}$Mo records of shallow and deep marine sediments between ca. 3.0 and 2.7 Ga is the result of (i) non-euxinic bottom water conditions and thus limited removal of MoO_4^{2-} from the seawater into deep water shales, and (ii) very low concentrations of dissolved and isotopically heavy MoO_4^{2-}, which isotopic signature could only be preserved in shallow water chemical sediments such as carbonates and iron formations, but not in deep water shales with higher detrital proportions (Thoby et al., 2019; Wille et al., 2007; Wille et al., 2013).

Here we would like to add another possibility to this discussion and postulate that the redox state of the Archean open ocean, in contrast to shallow ocean areas, prior to 2.7 Ga was too reducing to allow the formation of a persistent open ocean MoO_4^{2-} pool. The seawater pH has been estimated between 6.5 and 7.6 for the early Archean to be 7.0 at the Archean-Proterozoic boundary (Halevy and Bachan, 2017; Krissansen-Totton et al., 2018). For a hypothetical and constant pH value of the Archean to Paleoproterozoic ocean of 7, WO_4^{2-}, MoO_4^{2-}, and CrO_4^{2-} stability requires minimal Eh values to keep these elements in their oxidized soluble form of -0.40 V, -0.25 V, and +0.45 V, respectively (Figure 2.5; Takeno (2005)).

Fractionated Cr isotope values were reported by Frei et al. (2009) in deep-sea Algoma-type banded iron formations as old as 2.75 Ga. These authors interpreted their data as the onset of oxidative Cr weathering on the continents, requiring significant amounts of free molecular oxygen in the atmosphere at that time above 1 x 10^{-5} to 1 x 10^{-6} PAL, contradicting with the MIF signatures found in the sedimentary record (Catling and Zahnle, 2020; Farquhar et al., 2000). Konhauser et al. (2011) refuted this interpretation and suggested that these fractionated $\delta^{53/52}$Cr values are due to small kinetic adsorption effects of Cr(III) released from increased acidic leaching of ultramafic rocks and soils mediated by bacterial pyrite oxidation. In addition, no fractionated $\delta^{53/52}$Cr values were found in carbonates before the mid-Proterozoic and in tidal granular iron formations before the Neoproterozoic (Gilleaudeau et al., 2016; Planavsky et al., 2014b). Modern black shales show little to no stable Cr isotopic fractionation and are thus not suitable to reflect the ocean redox state (Bauer et al., 2018a; Frank et al., 2019). Accordingly, none of the 3.47 to 2.5 Ga old black shales of this study and of the literature shows any fractionated $\delta^{53/52}$Cr values (Fig 3c, Table 2.4; Cole et al. (2016); Wille et al. (2013)). Thus, stable Cr isotopes do not seem to be a good redox tracer for the Archean oceans anyway, since the redox potential needed to keep CrO_4^{2-} oxidized and soluble at circumneutral pH conditions is Eh $> +0.45$ V, which is more or less the value of the modern oxidized ocean (Becking et al., 1960).

The 3.47 to 3.0 Ga ocean: If our hypothesis holds true, then the shallow and deep oceans from 3.47 to 3.0 Ga were characterized by a redox potential of -0.40 V $<$ Eh $<$ -0.25 V, defined by the fact that authigenic W but no Mo is detected in deep ocean anoxic ferruginous black shales, and shallow water carbonates do not yet show any fractionated $\delta^{98/95}$Mo values (Figure 2.6a). Such highly reducing conditions seem realistic as they have even been reported for modern bathyal basins where porewaters at the interface of seawater with highly reducing black and green clays show an Eh of -0.40 V (Becking et al., 1960).

The 3.0 to 2.7 Ga ocean: After 3.0 Ga it appears that the global ocean started to develop a redoxcline between proximal shallow water and distal deep-water masses. We postulate that between 3.0 and 2.7 Ga the proximal shallow oceans were characterized by a redox potential Eh > -0.25 V to allow local redox cycling of Mo as demonstrated by fractionated $\delta^{98/95}$Mo values of carbonates and iron formations, while the deep ocean remained at a redox potential of -0.40 V $<$ Eh $<$ -0.25 V, since black shales still show fractioned $\delta^{186/184}$W but unfractionated $\delta^{98/95}$Mo values (Figure 2.6 b).

The 2.7 to 2.4 Ga ocean: A significant increase in the atmospheric and ocean oxidation states occurred around 2.7 to 2.4 Ga (Bosco-Santos et al., 2020; Brüske et al., 2020a; Czaja et al., 2012; Kurzweil et al., 2015; Ostrander et al., 2020; Ostrander et al., 2019; Scott et al., 2008; Wille et al., 2007), demonstrated by an increase of Mo concentrations and fractionated Mo isotopic compositions in deep sea euxinic shales. This remarkable surge in Mo concentrations and $\delta^{98/95}$Mo values of euxinic sediments has been interpreted to result from the onset of oxidative weathering and increasing redox potentials of open ocean water masses (Eroglu et al., 2015; Kurzweil et al., 2015; Scott et al., 2008; Voegelin et al., 2010) surpassing the minimum Eh value of -0.25 V that is required to keep MoO_4^{2-} oxidized and soluble (Fig. 2.6c). Consistent with this deep water Eh value, authigenic W enrichments and $\delta^{186/184}$W values of the 2.5 Ga old shales from the Pilbara Craton are similar as for older shales, with the exception of the non-euxinic Mt McRae shale sample (132.70 m) that shows the highest $\delta^{186/184}$W value of our

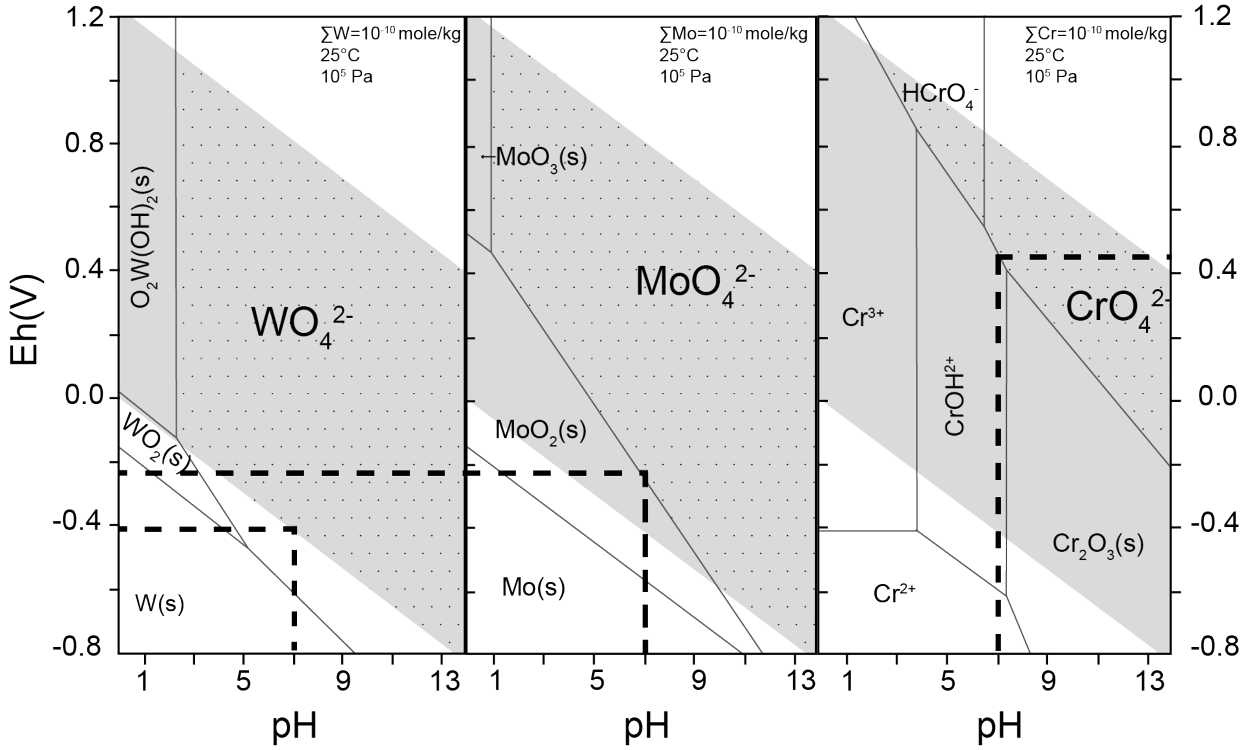

Figure 2.5: pH versus Eh space. The species data originates from Takeno (2005) following the FACT/FACTSTAGE model. The grey shading represents the water stability field; dashed lines represent the minimal Eh values to produce dissolved WO_4^{2-}, MoO_4^{2-} and CrO_4^{2-} with a pH range of 7 to represent the Archean ocean chemical parameters. The doted areas represent the stability fields of the dissolved species.

dataset (+0.246 ‰). Interestingly, this shale deposited after the euxinic interval characterized by strong enrichments in redox-sensitive Mo and Re, which were interpreted to result from a "whiff of oxygen" ca. 100 Ma years before the GOE (Anbar et al., 2007; Reinhard et al., 2009).

Shallow water masses probably further increased in their redox potential compared to before 2.7 Ga, as pointed out by fractionated $\delta^{98/95}$Mo values of carbonates, banded iron formations and shales (Duan et al., 2010; Eroglu et al., 2015; Kurzweil et al., 2016; Kurzweil et al., 2015; Planavsky et al., 2014a; Siebert et al., 2005; Thoby et al., 2019; Voegelin et al., 2010; Wille et al., 2007). However, the seawater Eh value remained below +0.45 V, as indicated by still crustal-like Cr concentrations and $\delta^{53/52}$Cr values in 2.5 Ga old shales (this study, Cole et al. (2016)). Unfortunately, it remains difficult to further improve the constraints of the upper Eh limit of both shallow and deep ocean water at that time, because isotope data from less redox sensitive elements are scarce or controversial.

The post 2.4 Ga ocean: The absence of strong authigenic W and Mo enrichments and fractionated $\delta^{186/184}$W values in the Paleoproterozoic shale samples from the Transvaal Basin deposited in a sub-tidal environment indicates unfavorable depositional conditions for

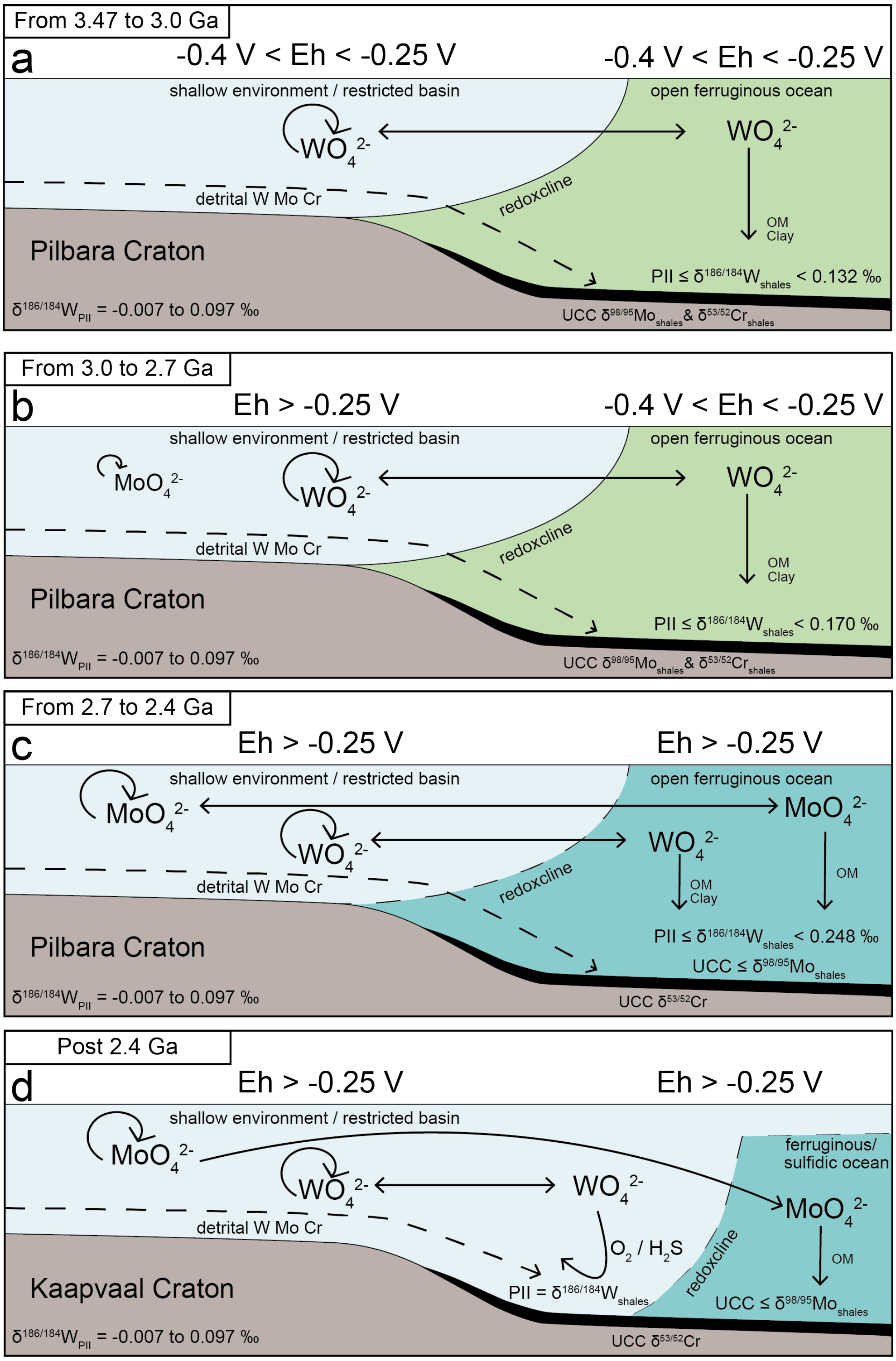

Figure 2.6: Simplified model of the redox state evolution of the Paleoarchean to the Paleoproterozoic ocean, with combined W, Mo, and Cr isotopic composition. PII stands for Precambrian Igneous Inventory. A chemocline separates the strongly reducing open ocean from more oxidizing water masses from shallow / restricted environments. a) The evidence of isotopically heavy authigenic W in open ocean sediments as early as 3.47 Ga indicates a minimal Eh value of -0.4 V in the depositional environment. b) The redox conditions were less reducing in shallow / restricted environments, where iron rich sediments and carbonates record an ongoing Mo redox cycling starting from 3.0 Ga. c) The Eh of the open ocean increases with the first record of fractionated $\delta^{98/95}$Mo in 2.7 Ga shales, indicating an Eh value of minimum -0.25 V. d) The GOE marks a change in the $\delta^{186/184}$W shales of open ocean sediments related local pore water euxinia or to an overlying oxidized water column.

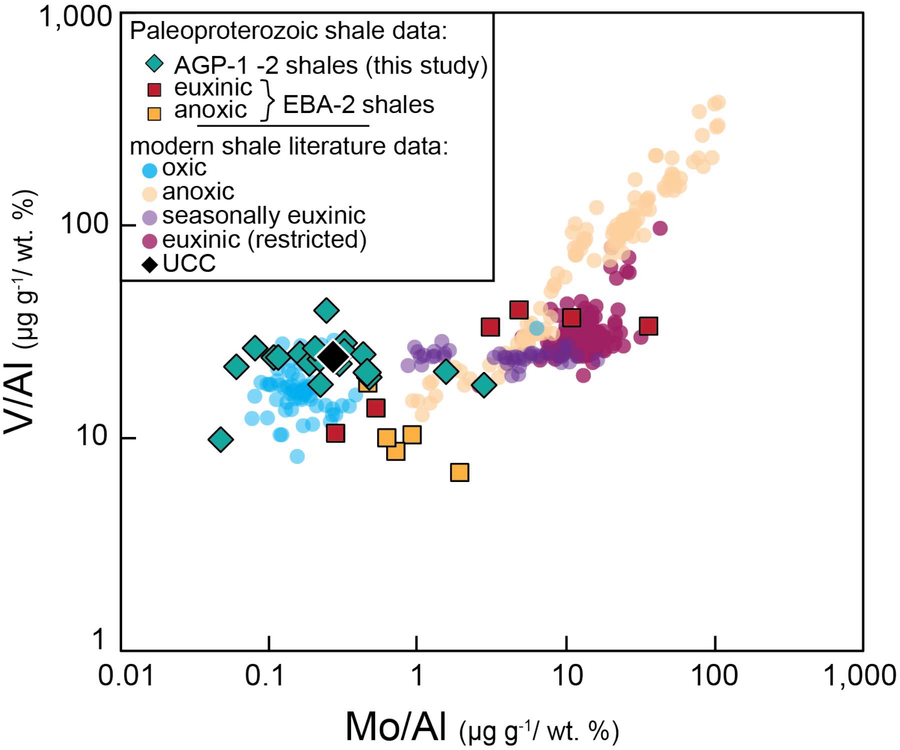

Figure 2.7: Comparison of Paleoproterozoic and modern shales in Mo/Al vs V/Al space. Modern shale Mo/Al and V/Al ratios are a compilation of literature data reported by Bennett and Canfield (2020).

scavenging W and Mo from the seawater. Interestingly, time-equivalent shales of the Timeball Hill Fm deposited in a very dynamic deltaic environment show enrichments in Mo (4.3 up to 67.7 µg.g^{-1}) and V (63 to 227 µg.g^{-1}), combined with fractionated $\delta^{98/95}$Mo values (-0.38 to +1.25 ‰) (Asael et al., 2018). This discrepancy in redox sensitive element concentrations within the scale of the Transvaal Basin may be explained by differences in local redox conditions of various depositional environments.

Low concentrations of H_2S_{aq} (below 5 µM) in the sediment pore water could have inhibited any authigenic W enrichment and only permitted limited Mo scavenging (Erickson and Helz, 2000; Mohajerin et al., 2016; Poulson Brucker et al., 2009; Wegwerth et al., 2018). Such environmental conditions would have resulted in near crustal concentrations of W and Mo, and $\delta^{186/184}W_{PII}$ values observed for the Paleoproterozoic shales of this study.

Alternatively, modern oxic environments (without Mn-oxides shuttle), such as the modern Japan Sea, are also characterized by low W and Mo concentrations and unfractionated $\delta^{186/184}$W values (Tsujisaka et al., 2020). The recent study of Bennett and Canfield (2020) showed that Al-normalized Mo and V concentrations in shale samples are a good proxy to distinguish sediments deposited in oxic (Mo/Al < 0.4 µg.g^{-1} /wt. % and V/Al < 23 µg.g^{-1}

/wt. %) from those deposited in restricted euxinic environments (Mo/Al > 5 µg.g^{-1} /wt. % and V/Al > 23 µg.g^{-1} /wt. %). The Archean ocean contained dissolved V in various redox states (IV, V) with concentrations mainly being controlled by the extent of chemical weathering and continental runoff (Moore et al., 2020). The existence of a dissolved V pool is traceable back to the Paleoarchean ocean, as indicated by elevated V concentrations in up to 3.5 Ga old shale samples (from 875 up to 2252 µg.g^{-1}, Large et al. (2014)), compared to the UCC value of 97 µg.g^{-1} (Rudnick and Gao, 2014). Figure 2.7 compares Mo/Al and V/Al ratios of Paleoproterozoic shales from the Transvaal basin reported by Asael et al. (2018) (drill core EBA-2) and this study (drill cores AGP-1 and -2) to modern shales deposited under various redox conditions (Bennett and Canfield, 2020). The EBA-2 samples have highly variable Mo/Al and V/Al ratios consistent with mainly anoxic and euxinic depositional conditions, in agreement with iron speciation data of these shales (Asael et al., 2018). The Paleoproterozoic shale samples investigated in this study have Mo/Al and V/Al ratios typical of modern oxic depositional environments. However, the composition of the UCC plots in the midst of modern oxic depositional environments in Mo/Al vs V/Al space. It is thus not clear whether the position of our Transvaal basin shales in Fig. 2.7 is the result of depositional conditions, or simply a detrital signal. As a result, it is impossible to determine whether the 2.32 Ga shales of this study were deposited under low H_2S pore water conditions or in an oxidized depositional environment.

Table 2.4: Mo and W concentrations and isotopic compositions found in shale sediments deposited under various redox conditions.

	oxic no Mn-Fe shuttle	hypoxic with Mn-Fe shuttle	ferruginous	euxinic
examples	Japan Sea	Landsort Deep (Mn>1 wt%)	Post 2.7 Ga shales	Black Sea (restricted) Mediterranean Sea (open)
Mo conc.	low Mo_{authi} (2)	high Mo_{authi} (3)	low Mo_{authi}	very high Mo_{authi} (3)
W conc.	low W_{authi} (2)	high W_{authi} (3)	$>_{UCC}$	low W_{authi} (3)
Mo/W	1-3	~5-100	<1	~10-100 (restricted) >>100 (open)
$\delta^{98/95}$Mo	variable	$<\delta^{98/95}Mo_{seawater}$	variable	up to $\delta^{98/95}Mo_{\ seawater}$
$\delta^{186/184}$W	$\sim \delta^{186/184}W_{\ UCC}$ (2)	unknown	above $\delta^{186/184}W_{\ UCC}$ (1)	$\sim \delta^{186/184}W_{\ UCC}$ (1)

Mo/W in weight ratios. $\delta^{98/95}$Mo and$\delta^{186/184}$W data from this study (1), Tsujisaka et al. (2020) (2), Dellwig et al. (2019) (3).

2.5 Summary and conclusions

This investigation aims to assess the potential of W isotopic compositions as a redox proxy in anoxic non-sulfidic shales deposited before the GOE. In this study, we measured the W isotopic compositions (1) of modern euxinic shales, (2) of the Archean igneous inventory and (3) of Precambrian shales deposited under anoxic conditions (3.46 to 2.3 Ga).

- The detrital composition of the shale suites from this study displays a shift from mafic-ultramafic dominated (3.47 to 2.9 Ga) towards a modern-like felsic composition at 2.5 Ga. Their $\delta^{186/184}$W values range from -0.007 to +0.097 ‰ and are indistinguishable from Phanerozoic igneous rocks analyzed during previous studies. These results suggest that the W isotopic composition of the continental crust remained relatively constant since the Archean.

- In contrast to Mo, euxinic shales, even at low H_2S_{aq} concentrations (5µM L^{-1}), show no authigenic enrichment of W. Their W isotopic composition is characteristic of the detrital component. The Mo/W ratio is hence a good indicator of euxinic conditions in the depositional environment, but the minimum amount of H_2S_{aq} required to keep W in solution needs to be further investigated.

- The W isotopic composition of Precambrian shale sample suites of this study are characterized by two W components, a detrital one with $\delta^{186/184}$W values within the PII range of -0.007 to +0.097 ‰ and an authigenic one with heavier values of up to +0.248 ‰. The seawater $\delta^{186/184}$W value cannot be directly extrapolated from the isotopically heavy W component due to lack of knowledge about W inputs into the ocean - such as hydrothermal vents - and adsorption processes of WO_4^{2-} onto clay minerals, organic matter and the magnitude of associated W isotopic fractionation. Still, the observation of a heavy sourced W authigenic component implies the presence of dissolved W in the ocean as early as 3.46 Ga.

- The discrepancy of $\delta^{186/184}$W and $\delta^{98/95}$Mo values in the shale record reveals that the ocean was too reducing for MoO_4^{2-} persistence in Meso- Neoarchean time. We argue that the open Archean ocean Eh value remained between -0.40 to -0.25 V until 2.7 Ga (Ostrander et al., 2020). In contrast, shallow environments were less reducing (Eh > -0.25 V) and permitted the buildup of a heavy seawater $\delta^{98/95}$Mo. This elevated $\delta^{98/95}$Mo is responsible for the fractionated $\delta^{98/95}$Mo values recorded in chemical sediments as early as 2.93 and 2.97 Ga (Albut et al., 2019; Planavsky et al., 2014a; Thoby et al., 2019). Then, the first record of fractionated $\delta^{98/95}$Mo values in open ocean shales at 2.7 Ga marks a chemical transition of the deep ocean over the threshold of -0.25 V in Eh value. The chromium isotopic composition of shales does not provide constrains onto the Archean ocean redox state as its sensitivity is too low for contemporaneous molecular dioxygen levels.

The similar behavior of Mo and W in oxic environments but opposite behavior in euxinic environments make the Mo/W ratio and the stable isotopic compositions of these elements a powerful tool to distinguish between oxic, ferruginous and euxinic conditions (see table 2.4). However, this study is limited by the lack of information on modern W isotopic cycling. Investigating the modern W cycling in modern ferruginous and anoxic continental margin sediments is key to further support the conclusions drawn from the W isotopic composition of ancient sediments proposed in this study.

Acknowledgements

Elmar Reitter and Bernd Steinhilber are thanked for their help and technical support during laboratory work. We are grateful to Gareth Izon, Ilka Kleinhanns and Luise Wagner for providing rock samples and acknowledge the support from the Department of Geology, University of Johannesburg, for sample acquisition. Financial support by the German Research Foundation (DFG) grant KU3788/1-1 to FK and grant SCHO1071/12-1 to RS, both as part of the DFG priority program 1833 “Building a Habitable Earth”, is thankfully acknowledged.

2.6 Supplements

2.6.1 Sources for major and trace element determinations of Precambrian shales used in this study

Table 2.5: list of the source for major and trace element concentrations, and isotopic determination of tungsten, molybdenum and chromium. Preparation and measurement methods are detailed in the following references.

samples	major elements	trace elements	isotope ratios
ABDP 2-3-5-6 cores (Pilbara craton)	Wille et al. (2013)	this study	$\delta^{98/95}$Mo: Wille et al. (2013) $\delta^{53/52}$Cr: Wille et al. (2013) $\delta^{186/184}$W: this study
ABDP 9 core (Pilbara craton)	Kurzweil et al. (2015)	this study	$\delta^{98/95}$Mo: Kurzweil et al. (2015) $\delta^{186/184}$W: this study $\delta^{53/52}$Cr: this study
AGP-1-2 cores (Kaapvaal Craton)	this study	this study	$\delta^{186/184}$W: this study
Black Sea samples	Wegwerth et al. (2018)	Wegwerth et al. (2018) Dellwig et al. (2019)	$\delta^{98/95}$Mo: Wegwerth et al. (2018) $\delta^{186/184}$W: this study
Paleoproterozoic granitoids (Vastervik area)	Nolte et al. (2011)	Nolte et al. (2011)	$\delta^{186/184}$W: this study
TTG, GGM (South Africa)	Kleinhanns et al. (2003)	Kleinhanns et al. (2003)	$\delta^{186/184}$W: this study
komatiites and komatiitic basalt	Bolhar et al. (2003)	Bolhar et al. (2003)	$\delta^{186/184}$W: this study

2.6.2 Control standards and comparison of published $\delta^{186/184}$W values of various rock reference materials

There are so far only few publications are focused on W isotopic determination with a ^{180}W-^{183}W double spike technique (Abraham et al., 2015; Krabbe et al., 2017; Kurzweil et al., 2019; Kurzweil et al., 2018; Mazza et al., 2020) and standard sample bracketing (Breton and Quitte, 2014; Tsujisaka et al., 2020; Tsujisaka et al., 2019). Previous studies reported following long-term reproducibility for the standard reference material SRM 3163:

- $\delta^{186/184}$W = 0.00 ±0.17 ‰ (2 s.d., n=30; Breton and Quitte (2014)); standard-sample bracketing; external correction with Hafnium
- $\delta^{186/184}$W = -0.01 ±0.05 ‰ (2 s.d., n=171; Abraham et al. (2015)); double spike technique
- $\delta^{186/184}$W = 0.00 ±0.04 ‰ (2 s.d., n=94; Tsujisaka et al. (2019)); standard-sample bracketing; external correction with Rhenium
- $\delta^{186/184}$W = 0.000 ±0.013 ‰ (2 s.d., n=42; Kurzweil et al. (2018)); double spike technique

- $\delta^{186/184}$W = 0.000 ±0.013 ‰ (2 s.d., n=118; Kurzweil et al. (2019)); double spike technique
- $\delta^{186/184}$W = 0.00 ±0.02 to 0.09 ‰ (2 s.d., n=82; Tsujisaka et al. (2020); Tsujisaka et al. (2019)); standard-sample bracketing; external correction with Rhenium
- $\delta^{186/184}$W = 0.000 ±0.036 ‰ (2 s.d., n=400; Mazza et al. (2020)); double spike technique

The long-term reproducibility for SRM 3163 of 0.000 ±0.021 ‰ (2 s.d., n=258) in $\delta^{186/184}$W of this study using a double spike technique is in good accordance to previously reported accuracies.

Additionally, the long-term reproducibility for an in-house Alfa Aesar W standard solution of $\delta^{186/184}$W = +0.056 ±0.026 ‰ (2 s.d., n=149) determined during the course of this study agrees very well with previously reported values of $\delta^{186/184}$W = +0.053 ±0.013 ‰ (2 s.d., n=42; Kurzweil et al. (2018)) and $\delta^{186/184}$W = +0.055 ±0.016 ‰ (2 s.d., n=113; Kurzweil et al. (2019)) for the same standard solution.

Rock reference materials were measured to check for consistency with previously reported $\delta^{186/184}$W rock standard values. The results are listed in the table 2.6. Our values agree very well with previously reported values for all these materials with the exception of BCR-2, for which our W isotopic composition is slightly lighter than previously reported ones. We can give no explanation for this observation, particularly since the values reported by Kurzweil et al. (2018, 2019) were partly determined on the same batch of BCR-2 (thus excluding batch heterogeneity), using the same ^{180}W-^{183}W double spike solution and the same W purification protocol.

2.6.3 Ashing effect on shale samples

Organic matter is a major component of black shales, which may not fully decompose during beaker-digestion with inorganic acids and thus may cause potential polyatomic interferences during mass spectrometric measurements. Ashing is an important step to enable full black shale digestion, proper chemical separation and accurate isotope ratio measurements. To test the potential effect (volatilization/isotopic fractionation) of ashing on shale matrices, the W isotopic compositions of the shaly rock reference materials SCo-1 (3 % C_{org}) and OU-6 (3.6 % m/m LOI) were determined on ashed and non-ashed sample aliquots.

Briefly, 500 mg of each rock reference material was weighed into ceramic crucibles

Table 2.6: Comparison of $\delta^{186/184}$W values of international rock reference materials

standard	[W] ±2S.D. (ng.g^{-1})	$\delta^{186/184}$W ±2S.D.	N	reference
OU-6	**1323 ±23**	**0.080 ±0.024 ‰**	**12**	**this study**
SCo-1	**1484 ±70**	**0.062 ±0.020 ‰**	**9**	**this study**
AGV-2	**474 ±8**	**0.015 ±0.021 ‰**	**5**	**this study**
	501 ±58	0.016 ±0.032 ‰	5	Kurzweil et al. (2018)
		0.007 ±0.013 ‰	6	Kurzweil et al. (2019)
		-0.010 ±0.078 ‰	3	Krabbe et al. (2017)
		0.18 ±0.05 ‰	6	Abraham et al. (2015)
		0.72 ± 0.02 ‰	5	Breton and Quitte (2014)
		-0.02 ±0.04 ‰	3	Tsujisaka et al. (2019)
BCR-2	**457 ±10**	**0.045 ±0.011 ‰**	**4**	**this study**
		0.064 ±0.006 ‰	6	Kurzweil et al. (2019)
		0.078 ±0.046 ‰	3	Krabbe et al. (2017)
W-2a	**257 ±1.1**	**0.088 ±0.017 ‰**	**2**	**this study**
	260 ±6	0.081 ±0.014 ‰	5	Kurzweil et al. (2018)

and heated to 600 °C for 12 h. Independent digestions were performed on ashed and non-ashed aliquots of the two rock reference materials, all of which then went through the ion-exchange W purification procedure. The results are given in Table 2.7 and figure 2.8. There is no difference in the $\delta^{186/184}$W values of ashed and non-ashed samples, which shows that sample ashing at 600 °C for 12 h does not cause any W loss and W isotopic fractionation.

Table 2.7: Rock reference standards $\delta^{186/184}$W values of ashed and non-ashed sample aliquots.

	$\delta^{186/184}$W	2SE
OU-6 ashed	0.063	0.011
	0.070	0.011
	0.092	0.012
average	0.081	0.017
+0.079 ±0.022 ‰ (n=6)	0.081	0.015
	0.086	0.015
OU-6 non-ashed	0.080	0.012
	0.083	0.010
	0.065	0.017
average	0.067	0.016
+0.081 ±0.027 ‰ (n=6)	0.091	0.017
	0.101	0.010
SCo-1 ashed	0.048	0.008
average	0.059	0.007
+0.056 ±0.011 ‰ (n=4)	0.057	0.018
	0.061	0.013
SCo-1 non-ashed	0.069	0.008
	0.083	0.011
average	0.056	0.014
+0.067 ±0.021 ‰ (n=5)	0.063	0.016
	0.063	0.010

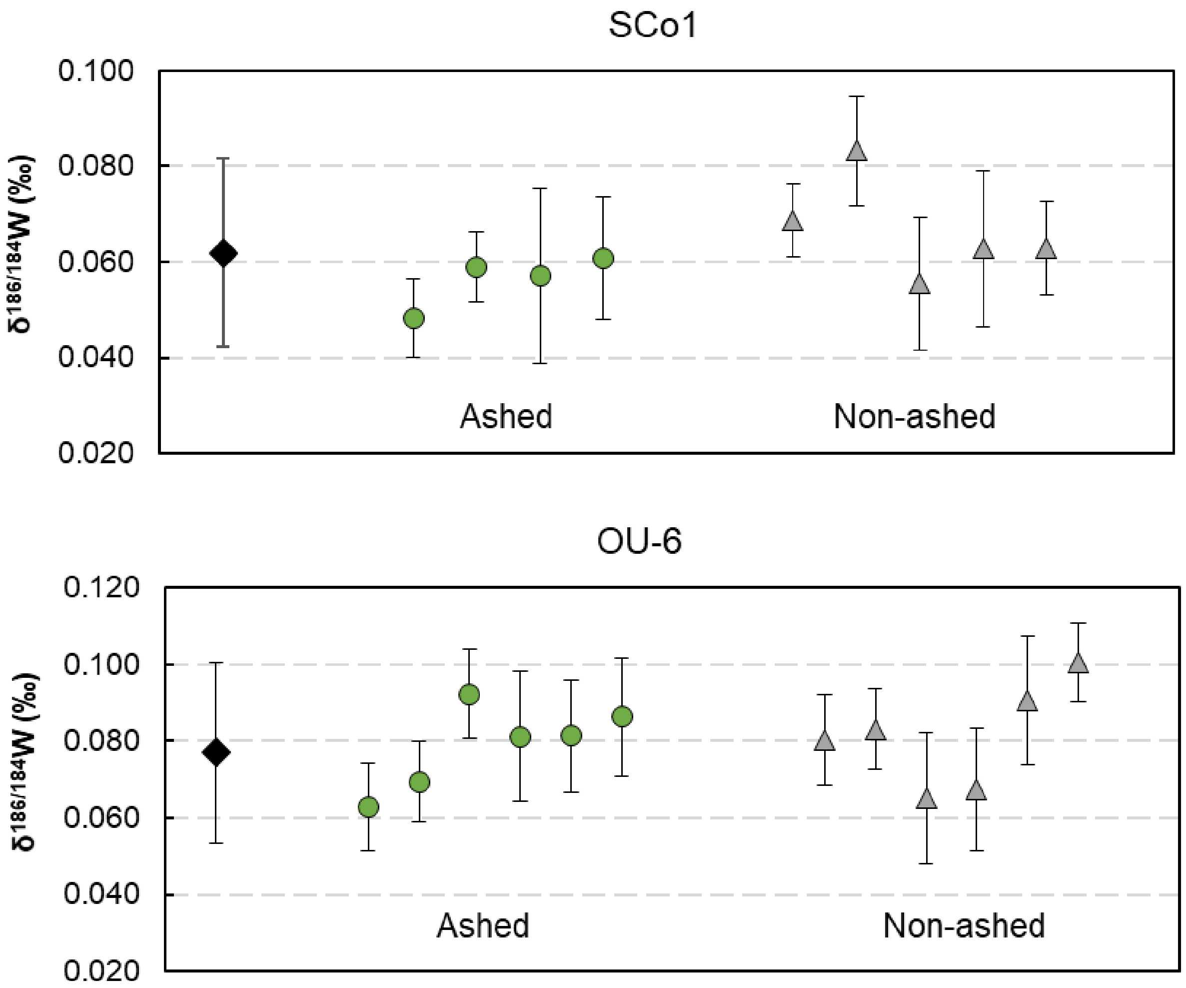

Figure 2.8: SCo-1 and OU-6 $\delta^{186/184}$W values measured on ashed and non-ashed sample powder aliquots. The black diamonds represent the respective averages of all data values measured for each rock standard powder, the error bars represent the 2 s.d. of the averages. Green circles (ashed rock standards) and gray triangles (non-ashed) represent single measurements of each rock standard, vertical error bars represent their 2 s.e.

2.6.4 Effects of the yield on the $\delta^{186/184}$W values

Table 2.8: $\delta^{186/184}$W values and yields of the rock standards OU-6 and AGV-2

OU-6 (split 8/31)

#	$\delta^{186/184}$W (‰)	2SE	yield
1	0.102	0.021	13%
2	0.093	0.016	30%
3	0.080	0.017	31%
4	0.098	0.014	33%
5	0.081	0.017	33%
6	0.086	0.015	35%
7	0.065	0.017	35%
8	0.067	0.016	39%
9	0.091	0.017	40%
10	0.101	0.016	41%
11	0.081	0.015	42%
12	0.080	0.012	45%
13	0.063	0.011	47%
14	0.092	0.012	50%
15	0.085	0.015	50%
16	0.070	0.011	50%
17	0.101	0.010	51%
18	0.101	0.010	51%
19	0.083	0.010	51%
20	0.087	0.012	51%
21	0.094	0.014	53%
22	0.119	0.014	56%
23	0.087	0.009	64%
24	0.065	0.009	65%
25	0.084	0.012	65%

AGV-2 (split 863)

#	$\delta^{186/184}$W (‰)	2SE	yield
1	0.002	0.015	22%
2	0.018	0.009	31%
3	-0.008	0.014	32%
4	0.001	0.007	32%
5	0.005	0.009	43%
6	0.000	0.010	45%
7	0.009	0.005	55%
8	0.032	0.010	61%
9	0.018	0.008	69%
10	0.003	0.007	70%
11	0.013	0.008	71%
12	-0.007	0.008	73%
13	-0.003	0.007	77%
14	0.013	0.010	77%
15	0.012	0.008	77%
16	0.014	0.006	79%
17	-0.008	0.007	82%
18	0.004	0.008	85%
19	0.004	0.007	88%
20	0.016	0.007	88%

yield OU-6	<50%	>50%
average $\delta^{186/184}$W (‰)	0.084	0.089
count	13	12
2sd	0.026	0.029

yield AGV-2	<50%	>50%
average $\delta^{186/184}$W (‰)	0.003	0.008
count	6	14
2sd	0.017	0.022

At the beginning of the establishment of the W purification we faced recurrent low yields, especially in the OU-6 standard. We then adapted the chemistry to ensure yields between 60 and 100 %. The extremely low yields in the tables above represent the $\delta^{186/184}$W acquired during the phase of improvement of the chemistry. In some cases, low yields were caused by aging resin, in both AGV-2 and OU-6 standards. Nevertheless, our comparison of earliest OU-6 and AGV-2 show no influence of W loss during chemistry on $\delta^{186/184}$W values.

Individual values for $\delta^{186/184}$W and chemical yields for the reference materials OU-6

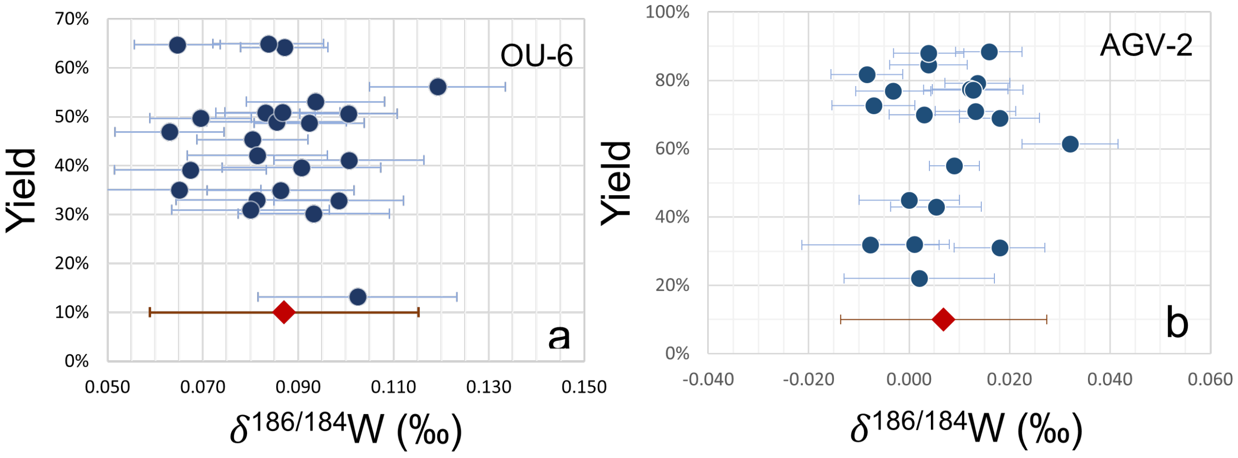

Figure 2.9: (a) $\delta^{186/184}$W (‰) versus chemistry yield (%) of the slate rock reference material OU-6 (A) and the andesite rock reference material AGV-2. (b) The horizontal error bars of individual measurement (circles) represent their 2SE measurement uncertainties. The red diamonds give the average values of all individual measurements of the two reference materials with the respective 2SD uncertainties.

(slate powder, split 8/31) and AGV-2 (andesite, split 863) shown in Fig. 2.9 are reported in table 2.8. Each data point represents an individual W purification from an individual sample powder digest.

The table 2.8 and the figure 2.9 demonstrate that the $\delta^{186/184}$W value of each standard is independent of the chemistry yield. Still, low yield samples typically have a higher 2SE during the measurement, which can be expected due to the lower intensity of the measured signal. Typically, we measure a purified W solution of 30 ppb (sample + spike), which results in between 2 to 2.5 V signal intensity on 184W (10^{11} ohm resistor). Samples with a yield lower than 50 % are characterized by a signal intensity below 1 V, and consequently a higher 2SE. Then, the 50 % threshold is an empirical value, based on our observations on the data quality.

Table 2.9: major and trace elements of the Precambrian shale samples of this study (1/6).

Drill Core ID	ABDP #2	ABDP #2	ABDP #2	ABDP #2	ABDP #2	ABDP #5	ABDP #5	ABDP #5
Sample ID	58.2	102.4	158.7	190.9	219.2	74.5	86.0	122.0
	Duffer Fm	Duffer Fm	Duffer Fm	Duffer Fm	Duffer Fm	Nullagine Group	Nullagine Group	Nullagine Group
Major elements [wt %]								
SiO_2	59.39	54.55	55.21	57.44	62.51	64.43	62.98	61.26
Al_2O_3	20.98	25.21	25.29	22.45	18.68	17.75	15.85	19.49
TiO_2	0.87	1.05	0.99	0.72	0.6	0.64	0.75	0.88
Fe_2O_3	7.03	6.94	4.14	3.89	3.01	9.4	10.01	10.22
MnO	0.05	0.08	0.06	0.05	0.03	0.1	0.1	0.09
MgO	2.52	2.78	2.16	2.19	3.69	3.96	4.39	4.32
CaO	0.35	1.44	1.61	3.27	0.62	0.1	0.09	0.1
Na_2O	5.48	2.72	5.33	7.82	9.03	1.11	0.91	1.07
K_2O	3.4	5.16	4.51	1.93	0.77	2.21	2.31	2.54
P_2O_5	0.12	0.08	0.06	0.06	0.06	0.1	0.07	0.07
TOC	13.38	1.38	8.98	1.85	1.69	2.41	1.66	1.26
Trace elements [µg g^{-1}]								
Li	11.87	18.8	9.99	15.82	5.82	24.27	86.21	123.84
Be	1.79	2.06	2.58	2.29	0.86	1.73	1.05	1.36
Sc	21.07	23.87	29.91	15.94	12.19	37.4	28.94	32.26
Ti	4519	6081	5319	3859	3015	6025	4544	5659
V	135.37	175.98	205.09	123.95	78.03	250.74	196.13	228.38
Cr	427.69	374.04	411.73	235.43	216.3	698.54	690.91	760.49
Co	48.48	40.12	77.76	18.17	69.95	47.95	53.47	50.27
Ni	354.23	203.35	405.44	134.65	320.23	143.12	337.88	318.47
Cu	295.53	118.52	1022.4	297.76	1040.23	113.14	79.78	92.45
Zn	1039.03	1066.83	4671.33	1027.35	7151.97	85.66	165.47	185.77
Ga	23.68	33.33	29.65	27.33	13.72	25.06	20.27	25.17
As	18.24	0.62	199.24	0.34	45.25	71.63	34.29	29.24
Rb	107.4	126.76	123.8	30.3	22.11	111.65	81.13	91.31
Sr	75.33	52.8	105.39	546.77	161.83	147.85	87.35	111.41
Y	19.39	20.92	29.4	26.27	18.92	21.97	17.09	20.44
Zr	105.7	124.77	116.39	64.84	57.07	127.76	108.3	122.66
Nb	11.65	16.23	11.21	12.81	9.85	8.66	7.07	8.77
Mo	2.6	2.36	3.16	2.23	1.94	1.4	1.26	1.47
Cd	0.27	0.48	10.11	1.63	60.94	0.15	0.22	0.16
Sn	4.35	5.41	7.74	0.72	1.15	2.63	1.72	2.37
Sb	0.26	0.11	0.8	0.14	0.24	9.31	10.93	11.37
Cs	2.79	0.73	0.78	0.32	1.13	16.16	7.96	11.48
Ba	846	962	1249	2840	216	553	440	456
La	28.6	33.56	41.93	30.19	24.89	25.86	20.93	29.66
Ce	57.75	65.37	81.91	57.87	47.35	51.68	42.33	60.02
Pr	6.6	7.37	9.23	6.53	5.31	5.95	4.95	6.95
Nd	24.62	27.12	34.23	24.2	19.93	22.49	18.78	26.08
Sm	5.16	5.52	7.08	5.08	4.07	4.58	3.84	5.26
Eu	1.45	1.07	2.3	1.6	0.67	1.16	0.99	1.3
Tb	0.68	0.74	0.97	0.77	0.58	0.68	0.54	0.64
Gd	4.7	4.92	6.53	4.85	3.81	4.35	3.54	4.4
Dy	3.75	4.24	5.57	4.68	3.51	4.13	3.25	3.8
Ho	0.74	0.86	1.15	0.98	0.75	0.87	0.68	0.8
Er	2.07	2.39	3.18	2.75	2.13	2.47	1.93	2.31
Tm	0.31	0.36	0.47	0.41	0.32	0.38	0.29	0.35
Yb	2	2.34	3.02	2.64	2.08	2.45	1.92	2.32
Lu	0.31	0.36	0.45	0.39	0.32	0.37	0.29	0.35
Hf	2.88	3.49	3.21	1.88	1.76	3.43	2.87	3.32
Ta	1.16	1.58	1.19	1.36	1.01	0.66	0.53	0.68
W	2.09	2.9	2.32	3.57	0.34	2.36	1.03	1.33
Tl	1.38	1.06	1.62	0.28	0.55	0.81	0.64	0.69
Pb	10.35	14.64	32.48	92.58	7.62	13.47	17.68	19.56
Th	8.71	12.28	11.46	9.25	8.48	7.47	5.82	8.2
U	2.48	4.05	3.58	2.54	2.5	2.28	1.68	2.42
Ni/Th	40.67	16.56	35.38	14.56	37.76	19.16	58.05	38.84
W/Th	0.24	0.24	0.2	0.39	0.04	0.32	0.18	0.16
Mo/Al	0.47	0.35	0.47	0.38	0.39	0.3	0.3	0.28
V/Al	24.39	26.38	30.66	20.87	15.8	53.35	46.81	44.26

Drill Core ID	ABDP #5	ABDP #5	ABDP #6	ABDP #6	ABDP #6	ABDP #6	ABDP #6	ABDP #3
Sample ID	164.6	183.9	85.3	95.9	113.9	173.5	267.7	98.3
	Nullagine Group	Nullagine Group	Hardey Fm	Hardey Fm	Hardey Fm	Hardey Fm	Hardey Fm	Hardey Fm
Major elements [wt %]								
SiO_2	61.39	63.42	60.11	61.60	55.11	57.45	55.03	57.58
Al_2O_3	19.34	19.25	22.90	21.44	31.54	22.42	32.22	22.49
TiO_2	0.86	0.81	1.07	0.98	2.01	1.23	2.00	1.10
Fe_2O_3	9.52	8.31	6.64	5.14	2.06	5.81	1.06	6.98
MnO	0.09	0.08	0.05	0.04	0.01	0.06	0.01	0.05
MgO	4.24	3.63	3.78	2.71	0.98	2.64	0.48	3.58
CaO	0.30	0.07	0.12	0.10	0.39	4.12	0.30	0.21
Na_2O	0.99	0.89	0.84	0.41	0.79	1.94	0.43	1.59
K_2O	3.69	3.64	4.66	4.40	7.33	4.73	8.46	3.95
P_2O_5	0.10	0.08	0.11	0.08	0.31	0.13	0.25	0.15
TOC	1.98	1.52	0.54	0.60	2.26	0.36	1.44	0.36
Trace elements [µg g^{-1}]								
Li	66.35	58.74	24.27	16.11	4.32	10.62	2.02	67.17
Be	1.84	1.61	1.73	2.26	2.85	2.48	2.67	2.85
Sc	35.48	31.62	37.40	22.46	36.52	22.61	36.56	29.53
Ti	5596	5022	6025	6030	11329	6844	11473	6831
V	239.13	222.48	250.74	159.71	291.77	161.16	281.66	217.23
Cr	690.24	640.33	698.54	297.32	363.62	269.95	395.28	407.62
Co	46.86	54.53	47.95	16.30	19.39	34.28	15.86	47.31
Ni	245.69	300.86	143.12	119.33	48.23	122.18	32.61	183.95
Cu	102.24	82.85	113.14	46.76	49.12	47.37	67.68	67.37
Zn	133.30	133.95	85.66	122.80	198.62	100.93	106.78	140.17
Ga	24.94	24.47	25.06	26.40	34.92	25.93	38.79	30.97
As	44.06	56.49	71.63	2.54	4.08	17.34	4.26	16.21
Rb	128.65	123.98	111.65	137.61	205.91	154.68	241.95	179.76
Sr	119.43	104.24	147.85	188.22	393.30	403.67	86.14	93.46
Y	22.81	19.67	21.97	25.31	49.11	40.80	51.02	29.97
Zr	120.09	111.54	127.76	267.50	444.63	291.05	495.39	162.46
Nb	8.45	8.02	8.66	17.36	23.81	18.76	24.54	15.94
Mo	1.41	1.37	1.40	2.74	2.78	3.54	2.93	3.19
Cd	0.17	0.15	0.15	0.20	0.29	0.18	0.26	0.14
Sn	2.43	2.65	2.63	3.46	3.93	3.14	4.43	4.41
Sb	14.41	10.11	9.31	0.45	0.78	0.37	0.72	1.97
Cs	11.62	10.24	16.16	7.64	8.61	10.19	9.14	11.13
Ba	715	670	553	1247	2138	6085	1874	873
La	26.56	26.07	25.86	63.96	125.66	77.61	55.97	52.68
Ce	52.89	51.60	51.68	134.28	256.90	158.39	102.31	100.43
Pr	6.13	5.95	5.95	14.07	28.87	16.72	10.57	10.97
Nd	23.10	22.40	22.49	49.87	102.91	60.08	36.68	38.65
Sm	4.76	4.49	4.58	8.07	16.56	10.40	7.58	7.04
Eu	1.21	1.10	1.16	1.34	3.03	2.11	1.71	1.56
Tb	0.71	0.62	0.68	0.75	1.67	1.28	1.54	0.93
Gd	4.53	4.02	4.35	5.39	12.31	8.58	9.79	5.97
Dy	4.29	3.75	4.13	4.55	9.50	7.54	9.27	5.59
Ho	0.90	0.79	0.87	0.98	1.92	1.55	1.96	1.16
Er	2.52	2.25	2.47	2.98	5.30	4.34	5.63	3.28
Tm	0.38	0.34	0.38	0.48	0.78	0.65	0.85	0.50
Yb	2.46	2.21	2.45	3.25	4.89	4.11	5.57	3.22
Lu	0.36	0.33	0.37	0.50	0.72	0.61	0.83	0.48
Hf	3.28	2.99	3.43	6.49	10.08	6.70	10.94	4.28
Ta	0.65	0.62	0.66	1.27	1.62	1.37	1.70	1.57
W	1.39	1.31	2.36	2.79	3.33	1.78	3.68	4.94
Tl	0.95	0.92	0.81	1.06	1.64	0.95	1.54	1.51
Pb	21.84	22.09	13.47	17.36	10.18	22.97	7.82	21.36
Th	7.48	7.22	7.47	13.72	20.37	14.97	19.85	16.69
U	1.96	1.93	2.28	3.39	4.67	3.53	4.42	4.20
Ni/Th	32.85	41.67	19.16	8.70	2.37	8.16	1.64	11.02
W/Th	0.19	0.18	0.32	0.20	0.16	0.12	0.19	0.30
Mo/Al	0.28	0.27	0.23	0.48	0.33	0.60	0.34	0.54
V/Al	46.71	43.71	41.38	28.17	34.94	27.18	33.02	36.51

Table 2.9 (*continued*) 2/6

Drill Core ID Sample ID	ABDP #3 111.1	ABDP #3 124.3	ABDP #3 141.2	ABDP #9 132.7	ABDP #9 176.7	ABDP #9 218.65	ABDP #9 239.5	ABDP #9 259.38
	Hardey Fm	Hardey Fm	Hardey Fm	Mt McRae Shale	Mt McRae Shale	Mt Sylvia Fm	Wittenoom Fm	Wittenoom Fm
Major elements [wt %]								
SiO_2	58.92	61.64	59.37	55.10	56.70	52.00	64.80	64.90
Al_2O_3	22.46	22.02	23.35	11.40	11.90	12.80	12.70	10.80
TiO_2	1.01	0.98	1.18	0.40	0.50	0.50	0.50	0.40
Fe_2O_3	6.32	6.20	6.15	10.30	9.90	13.30	6.80	10.20
MnO	0.05	0.05	0.04	0.40	0.10	0.10	0.10	0.10
MgO	3.17	3.15	3.07	3.60	2.20	3.50	3.00	3.40
CaO	0.77	0.81	0.23	2.80	0.50	1.30	1.30	1.40
Na_2O	1.94	2.18	2.28	0.30	0.50	0.10	0.80	0.60
K_2O	3.73	3.25	3.35	3.20	5.90	6.10	3.20	1.40
P_2O_5	0.15	0.13	0.15	0.10	0.10	0.10	0.00	0.10
TOC	0.29	0.31	0.44	4.70	5.50	9.20	1.40	1.10
Trace elements [µg g^{-1}]								
Li	63.34	59.60	62.33	25.09	85.76	63.72	78.87	102.08
Be	2.78	2.59	2.95	0.53	2.56	6.11	2.50	4.39
Sc	27.19	26.06	28.61	10.52	11.38	13.04	13.90	18.67
Ti	6284	6075	7211	1299	2432	3035	2874	4568
V	201.27	194.27	215.94	41.71	79.14	86.09	95.68	133.72
Cr	333.86	327.98	367.59	50.14	66.36	128.41	130.03	203.94
Co	43.84	45.15	48.10	34.03	22.12	17.76	13.58	24.45
Ni	167.58	166.77	172.65	114.36	45.70	53.19	53.10	83.74
Cu	79.82	77.95	81.67	132.19	124.12	35.63	35.80	71.41
Zn	145.36	137.29	135.10	312.58	363.31	133.29	99.90	153.12
Ga	31.23	29.27	31.36	9.20	17.10	16.96	19.42	25.41
As	15.07	12.68	18.14	466.27	14.07	14.68	7.81	16.30
Rb	170.26	147.38	153.18	45.84	249.30	182.51	193.52	225.03
Sr	118.74	126.91	152.90	19.04	25.89	20.00	31.25	37.87
Y	23.11	22.97	23.30	15.20	12.00	18.02	10.01	19.85
Zr	153.32	152.19	192.03	74.74	80.50	102.47	81.39	126.46
Nb	16.06	14.65	16.08	13.83	16.93	24.24	18.31	47.77
Mo	2.52	3.03	2.98	11.81	2.74	3.09	1.52	4.06
Cd	0.16	0.14	0.16	0.49	0.59	0.24	0.12	0.41
Sn	4.61	4.20	4.16	0.42	2.89	3.42	2.80	4.15
Sb	1.85	1.84	2.17	14.66	1.64	3.45	2.03	4.45
Cs	10.53	9.95	10.77	3.72	12.35	2.82	15.06	14.78
Ba	849	756	804	88	275	378	356	503
La	48.48	47.59	63.56	15.27	21.33	36.65	24.34	62.42
Ce	93.91	109.46	123.09	31.30	41.87	68.34	47.36	126.46
Pr	10.29	14.34	13.41	3.68	4.74	7.27	5.24	14.17
Nd	36.81	62.48	47.22	13.83	16.93	24.24	18.31	47.77
Sm	6.85	17.01	7.86	2.82	3.06	4.00	3.19	7.07
Eu	1.47	3.17	1.60	0.64	0.82	1.01	0.76	1.52
Tb	0.71	0.91	0.70	0.42	0.38	0.50	0.34	0.75
Gd	4.97	9.08	5.07	2.67	2.49	3.21	2.41	5.24
Dy	4.20	4.52	4.23	2.52	2.19	3.05	1.89	4.08
Ho	0.89	0.90	0.91	0.55	0.47	0.67	0.39	0.82
Er	2.58	2.56	2.74	1.57	1.33	1.98	1.17	2.25
Tm	0.41	0.40	0.44	0.25	0.21	0.31	0.19	0.34
Yb	2.72	2.62	2.96	1.66	1.37	2.05	1.31	2.21
Lu	0.41	0.40	0.45	0.26	0.21	0.31	0.20	0.33
Hf	4.13	4.05	5.01	2.23	2.28	2.78	2.30	3.54
Ta	1.67	1.53	1.50	0.48	0.65	0.91	0.81	1.29
W	4.65	3.82	5.04	2.20	2.76	3.64	2.33	4.05
Tl	1.50	1.29	1.46	1.67	2.42	2.39	1.10	1.43
Pb	22.89	21.40	23.28	43.86	17.84	20.03	12.88	38.32
Th	18.27	16.13	17.82	6.71	8.93	12.62	10.72	17.27
U	4.63	3.91	4.82	1.66	2.42	3.43	2.64	5.12
Ni/Th	9.17	10.34	9.69	17.04	5.12	4.21	4.95	4.85
W/Th	0.25	0.24	0.28	0.33	0.31	0.29	0.22	0.23
Mo/Al	0.42	0.52	0.48	3.91	0.87	0.91	0.45	1.42
V/Al	33.88	33.32	34.94	13.81	25.12	25.40	28.48	46.76

Table 2.9 (*continued*) 3/6

Drill Core ID	ABDP #9	ABDP #9	AGP-1	AGP-1	AGP-1	AGP-1	AGP-1	AGP-1
Sample ID	316.0	340.0	57.77	61.18	63.4	67.38	70.88	71.6
	Wittenoom Fm	Wittenoom Fm	Upper Duitschland Fm	Upper Duitschland Fm	Upper Duitschland Fm	Upper Duitschland Fm	Upper Duitschland Fm	Upper Duitschland Fm
Major elements [wt %]								
SiO_2	59.30	57.10	59.48	63.77	63.85	70.73	68.40	69.11
Al_2O_3	16.10	15.90	16.16	15.65	15.16	11.83	14.57	13.09
TiO_2	0.60	0.70	0.59	0.65	0.59	0.32	0.70	0.51
Fe_2O_3	5.50	6.90	8.31	6.63	5.88	2.00	3.17	3.45
MnO	0.10	0.20	0.11	0.07	0.06	0.11	0.07	0.04
MgO	4.20	4.50	2.86	2.47	2.51	1.38	1.86	1.66
CaO	1.40	2.10	1.58	0.45	0.47	1.80	0.75	0.28
Na_2O	3.50	1.30	0.02	0.48	0.58	0.78	1.40	1.06
K_2O	3.60	3.10	3.90	3.73	3.67	3.25	3.63	3.20
P_2O_5	0.10	0.10	0.07	0.09	0.08	0.06	0.09	0.06
TOC	1.00	2.00	N.D.	N.D.	N.D.	N.D.	N.D.	N.D.
Trace elements [µg g^{-1}]								
Li	69.09	91.59	54.75	47.46	47.35	26.37	35.18	31.14
Be	2.12	3.03	3.60	3.50	3.82	3.18	3.27	3.06
Sc	16.19	20.81	19.02	19.46	15.75	10.47	13.94	12.62
Ti	3619	5262	3369	3734	3305	1699	4065	2798
V	100.56	146.42	105.95	108.82	95.64	31.61	69.43	67.16
Cr	167.36	229.84	131.38	135.07	122.49	46.78	12.84	90.00
Co	21.69	26.27	36.37	16.59	8.13	4.24	8.57	2.12
Ni	75.85	102.48	101.19	68.92	40.57	47.53	62.18	52.91
Cu	58.77	64.67	29.55	100.42	22.06	442.31	77.91	89.84
Zn	124.10	181.48	114.88	192.38	160.50	88.06	30.23	505.67
Ga	20.42	25.23	21.43	20.58	20.09	16.91	18.01	16.63
As	24.99	21.03	58.73	28.07	9.25	13.56	5.36	4.69
Rb	123.44	154.82	202.19	200.05	195.49	168.35	172.26	144.13
Sr	41.25	40.27	41.48	41.80	39.53	69.94	75.32	46.50
Y	17.17	24.17	23.90	29.65	26.03	19.45	21.46	23.94
Zr	120.03	138.00	135.81	151.65	168.12	171.20	181.59	139.18
Nb	28.50	29.50	12.53	11.35	13.82	11.97	14.42	16.19
Mo	4.28	4.86	0.71	0.34	0.44	0.15	1.75	1.69
Cd	0.19	0.19	83.94	292.13	251.52	128.23	88.49	479.63
Sn	3.12	3.94	5.61	5.31	5.11	6.66	6.13	4.45
Sb	3.56	3.57	2.26	1.72	1.65	0.58	2.06	3.54
Cs	4.79	15.23	10.04	9.54	8.98	5.88	6.38	6.42
Ba	266	435	1765	1867	1912	1669	2007	1560
La	34.55	38.90	33.52	48.28	52.19	51.87	38.45	33.00
Ce	69.21	74.38	64.52	95.71	107.32	105.51	77.82	64.03
Pr	7.93	8.26	7.05	10.94	11.47	11.04	8.85	7.54
Nd	28.50	29.50	24.96	39.33	40.38	38.24	31.97	27.66
Sm	5.16	5.34	4.78	7.31	7.14	6.80	6.13	5.28
Eu	1.05	1.21	1.08	1.36	1.30	0.88	0.95	0.80
Tb	0.61	0.73	0.72	0.95	0.85	0.73	0.72	0.66
Gd	4.10	4.54	4.42	6.36	5.79	5.17	4.94	4.39
Dy	3.36	4.46	4.36	5.52	4.70	4.01	3.94	3.90
Ho	0.69	0.95	0.94	1.17	0.98	0.81	0.82	0.87
Er	1.88	2.68	2.75	3.41	2.86	2.29	2.36	2.67
Tm	0.28	0.41	0.44	0.54	0.45	0.35	0.36	0.44
Yb	1.77	2.64	2.93	3.59	2.97	2.23	2.30	2.98
Lu	0.26	0.39	0.45	0.57	0.47	0.33	0.35	0.50
Hf	3.31	3.92	3.73	3.93	4.20	4.42	4.58	3.73
Ta	1.03	1.30	1.22	1.10	1.25	1.12	1.14	1.08
W	2.47	3.67	3.08	3.38	5.05	3.66	5.67	3.47
Tl	0.89	1.11	2.06	2.16	2.08	1.95	2.21	1.82
Pb	55.79	19.20	6.15	8.50	8.46	4.76	8.26	8.52
Th	14.37	17.03	20.25	19.26	20.73	21.02	17.63	15.76
U	4.67	5.44	4.71	5.79	5.64	7.67	6.04	6.36
Ni/Th	5.28	6.02	5.00	3.58	1.96	2.26	3.36	5.28
W/Th	0.17	0.22	0.15	0.18	0.24	0.17	0.22	0.17
Mo/Al	1.00	1.15	0.17	0.08	0.11	0.05	0.49	1.00
V/Al	23.61	34.78	24.75	26.29	23.85	10.10	19.41	23.61

Table 2.9 (*continued*) 4/6

Drill Core ID	AGP-1	AGP-1	AGP-1	AGP-1	AGP-1	AGP-2	AGP-2	AGP-2
Sample ID	86.71	87.48	92.53	102.1	105.21	62.34	66.22	67.48
	Upper Duitschland Fm	Upper Duitschland Fm	Upper Duitschland Fm	Upper Duitschland Fm	Upper Duitschland Fm	Timeball-Hill Fm	Timeball-Hill Fm	Timeball-Hill Fm
Major elements [wt %]								
SiO_2	76.24	77.34	54.61	61.06	60.44	61.14	65.29	64.60
Al_2O_3	9.22	9.36	18.96	16.29	16.63	17.24	15.82	16.37
TiO_2	0.34	0.32	1.05	0.81	0.80	0.69	0.66	0.62
Fe_2O_3	3.49	1.40	14.37	8.35	8.53	7.16	5.94	5.21
MnO	0.16	0.11	0.27	0.10	0.10	0.03	0.03	0.03
MgO	2.51	1.30	1.46	3.28	3.40	2.10	1.91	1.94
CaO	0.76	0.80	0.09	0.37	0.46	0.11	0.13	0.14
Na_2O	0.00	0.00	0.17	1.15	0.98	0.49	0.33	0.65
K_2O	2.22	2.85	4.66	4.14	4.18	3.88	3.96	4.07
P_2O_5	0.04	0.04	0.06	0.13	0.14	0.07	0.06	0.07
TOC	N.D.	N.D.	N.D.	N.D.	N.D.	N.D.	N.D.	N.D.
Trace elements [µg g^{-1}]								
Li	31.89	18.29	42.98	40.40	41.48	36.32	35.79	36.04
Be	1.97	2.39	4.11	3.41	3.78	2.43	3.21	3.14
Sc	8.76	7.96	34.83	17.25	16.32	21.24	18.81	16.50
Ti	1821	1686	6009	4698	4676	3909	3776	3587
V	50.22	44.27	195.87	96.63	98.28	126.72	96.08	93.92
Cr	74.14	52.61	210.26	226.34	226.75	155.92	117.32	123.67
Co	8.31	79.42	29.09	27.11	25.11	18.71	14.84	8.17
Ni	93.92	116.06	87.39	85.73	91.81	60.09	56.45	28.49
Cu	65.77	13.99	14.85	23.71	30.42	80.08	71.82	24.37
Zn	42.63	19.92	113.95	84.54	79.16	111.22	83.27	58.32
Ga	12.66	12.21	22.39	21.72	22.43	21.87	20.77	20.07
As	2.43	229.96	0.44	1.07	0.96	16.89	4.88	1.67
Rb	77.62	104.67	215.88	207.70	209.11	197.60	205.43	207.08
Sr	25.75	23.93	48.13	94.43	95.07	34.75	30.61	44.52
Y	29.34	18.22	14.40	31.70	32.89	38.05	30.73	25.39
Zr	96.71	111.73	159.85	215.28	206.73	146.61	170.52	162.07
Nb	8.43	8.56	11.57	22.45	21.93	12.69	12.83	11.80
Mo	3.93	7.24	1.25	0.82	1.35	1.51	1.21	0.26
Cd	40.36	48.71	70.86	97.45	92.43	79.56	72.98	68.78
Sn	4.22	5.87	4.21	8.98	8.65	5.34	6.02	5.35
Sb	0.60	1.89	0.43	1.05	1.17	2.73	2.67	0.90
Cs	3.32	3.61	12.94	14.88	14.31	7.94	7.00	7.46
Ba	2592	2518	1847	1057	1052	1370	1635	1686
La	34.11	25.14	28.71	50.81	51.27	52.95	59.14	9.52
Ce	64.29	48.75	58.07	101.19	98.74	107.51	118.22	19.92
Pr	7.42	5.59	5.68	10.85	10.69	11.85	12.64	2.41
Nd	26.50	20.06	18.54	38.31	37.24	43.05	44.22	9.04
Sm	5.02	3.71	3.16	7.25	7.03	8.27	8.11	2.00
Eu	0.87	0.66	0.78	1.42	1.35	1.66	2.03	0.51
Tb	0.72	0.50	0.47	0.99	0.99	1.16	0.97	0.52
Gd	4.54	3.17	2.74	6.37	6.20	7.57	6.67	2.65
Dy	4.47	2.99	3.00	5.74	5.80	6.73	5.37	3.64
Ho	1.00	0.67	0.65	1.19	1.22	1.42	1.14	0.90
Er	2.97	2.03	1.99	3.38	3.51	4.06	3.37	2.73
Tm	0.46	0.33	0.33	0.52	0.54	0.62	0.53	0.43
Yb	3.02	2.24	2.27	3.34	3.43	3.94	3.48	2.79
Lu	0.48	0.37	0.34	0.49	0.50	0.60	0.55	0.45
Hf	2.50	2.46	4.22	5.70	5.51	3.84	4.21	3.80
Ta	0.77	0.60	1.01	2.30	2.28	1.22	1.13	1.08
W	3.33	1.87	2.03	3.71	4.07	4.29	4.15	3.53
Tl	1.13	1.31	1.33	1.09	1.10	1.65	1.51	1.70
Pb	3.68	3.91	2.67	17.50	12.71	18.65	12.53	5.22
Th	12.35	9.54	11.61	24.93	26.55	18.81	16.24	17.06
U	5.92	4.49	2.32	6.67	6.81	5.58	4.45	4.90
Ni/Th	7.60	12.17	7.53	3.44	3.46	3.19	3.48	1.67
W/Th	0.27	0.20	0.17	0.15	0.15	0.23	0.26	0.21
Mo/Al	1.61	2.92	0.25	0.19	0.31	0.33	0.29	0.06
V/Al	20.58	17.85	39.02	22.42	22.34	27.79	22.93	21.69

Table 2.9 (*continued*) 5/6

Drill Core ID	AGP-2	AGP-2	AGP-2	AGP-2	AGP-2	AGP-2
Sample ID	76.13	83.14	86.3	89.22	92.53	108.23
	TimeballHill Fm	TimeballHill Fm	TimeballHill Fm	TimeballHill Fm	Upper Duitschland Fm	Upper Duitschland Fm
Major elements [wt %]						
SiO_2	59.54	63.60	62.43	61.21	62.20	58.97
Al_2O_3	16.25	15.89	17.58	14.59	16.38	13.46
TiO_2	0.64	0.57	0.70	0.55	0.59	0.53
Fe_2O_3	9.16	7.64	6.40	12.35	7.66	2.57
MnO	0.06	0.03	0.03	0.07	0.06	0.03
MgO	2.77	2.18	2.14	2.46	2.51	1.82
CaO	1.26	0.12	0.10	0.36	0.11	0.21
Na_2O	0.64	0.82	0.36	0.47	0.39	0.40
K_2O	3.45	3.59	4.15	2.58	4.02	4.06
P_2O_5	0.07	0.07	0.06	0.15	0.06	0.05
TOC	N.D.	N.D.	N.D.	N.D.	N.D.	N.D.
Trace elements [µg g^{-1}]						
Li	48.62	46.13	52.00	49.73	52.92	38.83
Be	2.85	3.98	4.27	4.07	3.38	3.19
Sc	18.25	16.59	19.84	16.79	19.71	13.79
Ti	3646	3337	3494	3228	3417	2981
V	109.41	98.38	114.51	101.37	103.29	72.56
Cr	128.51	118.31	134.82	114.56	126.18	105.06
Co	18.69	8.14	22.88	17.51	3.97	1.71
Ni	50.39	27.13	56.82	40.51	33.23	76.00
Cu	44.67	35.95	109.74	36.47	17.28	86.73
Zn	123.36	82.99	122.20	289.81	62.54	180.27
Ga	20.70	20.44	20.87	19.08	21.89	17.41
As	26.51	5.23	21.78	17.03	3.10	3.73
Rb	187.71	208.95	180.85	148.12	224.00	196.47
Sr	68.32	43.91	35.46	35.33	32.60	37.01
Y	30.81	32.68	26.24	29.88	25.88	35.96
Zr	133.11	136.02	130.95	179.14	151.70	174.71
Nb	11.14	11.85	12.20	12.23	10.69	11.98
Mo	1.42	0.94	2.06	0.81	0.51	1.68
Cd	146.17	122.19	63.53	93.50	68.47	175.10
Sn	4.63	5.66	5.89	5.81	5.59	4.76
Sb	1.02	1.83	1.77	2.07	0.80	2.70
Cs	8.74	9.49	8.85	7.06	11.75	11.50
Ba	1581	2033	1645	1460	2070	1527
La	41.06	61.86	31.02	36.43	24.51	34.12
Ce	80.49	130.91	63.07	72.68	49.90	66.39
Pr	9.08	14.44	7.28	8.33	5.67	7.84
Nd	32.77	52.54	26.35	30.42	20.45	28.48
Sm	6.20	9.77	5.03	6.00	4.10	5.43
Eu	1.22	1.86	1.08	1.36	0.85	0.93
Tb	0.91	1.18	0.74	0.92	0.70	0.87
Gd	5.65	8.22	4.38	5.56	3.91	5.25
Dy	5.48	6.34	4.69	5.51	4.54	5.46
Ho	1.18	1.29	1.06	1.19	1.04	1.24
Er	3.42	3.61	3.27	3.56	3.17	3.76
Tm	0.52	0.54	0.53	0.57	0.51	0.60
Yb	3.30	3.48	3.53	3.74	3.41	3.91
Lu	0.50	0.55	0.56	0.58	0.54	0.64
Hf	3.45	3.62	3.38	4.31	3.87	3.96
Ta	1.09	1.09	1.20	1.08	0.97	1.07
W	2.82	2.93	3.12	2.67	2.80	4.10
Tl	1.89	2.25	2.44	1.66	2.41	2.24
Pb	7.83	11.58	12.30	11.68	3.84	16.81
Th	16.66	18.73	17.67	17.18	18.14	16.93
U	4.76	7.51	4.51	5.83	4.75	5.95
Ni/Th	3.02	1.45	3.22	2.36	1.83	4.49
W/Th	0.17	0.16	0.18	0.16	0.15	0.24
Mo/Al	0.33	0.22	0.44	0.21	0.12	0.47
V/Al	25.44	23.42	24.63	26.26	23.85	20.38

Table 2.9 (*continued*) 6/6

2.6.5 Effects of the changing detrital composition on W, Mo and Cr concentrations in Precambrian shales

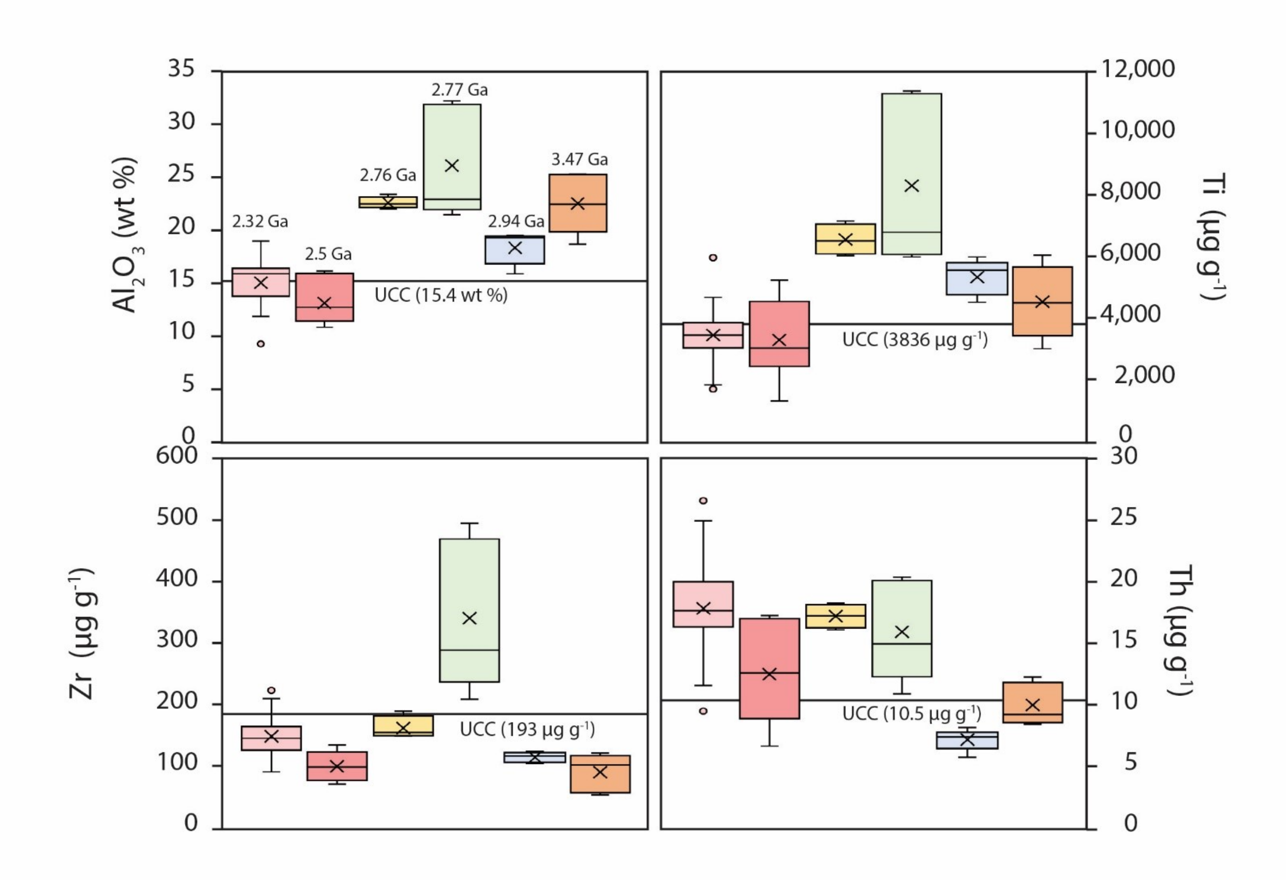

Figure 2.10: Box and whisker statistical representation of the Precambrian shale sample suites Al_2O_3, Zr, Th and Ti concentrations measured in this study. Crosses represent the medians of each sample suite, straight lines the averages. The outliners are represented by circles.

The absolute amount and average of each element commonly used for calculation of enrichment factors (Al_2O_3, Ti, Zr, Th) is fluctuating through time. The section 2.4.1 of the dissertation describes the relation of element ratios with the transition from a mafic-ultramafic to a felsic rich / modern-like emerged continental crust at the Archean-Proterozoic boundary (Condie, 1993). Not only Cr and Sc concentrations varied, the average chemical composition in Th, Ti, Zr and Al2O3 of the juvenile UCC greatly changed throughout the Archean, with large regional heterogeneity.

These variations themselves are making the normalization of redox sensitive elements complicated, especially with shale samples suites whom ages are spanning over one billion year. Moreover, additional complications arise from the specificities of each detrital-related element and the way the samples were treated in this study.

Tribovillard et al. (2006) suggested the use of Al_2O_3 and TiO_2 wt % to normalize elements

Table 2.10: comparison of the Zr concentrations of table-top and bomb digested shale-slate rock standards.

method	Zr (ppm)	Offset	#	method	Zr (ppm)	Offset	#
Ou-6 table top	148,475	12%	7	SCo-1 table top	114,516	35%	2
Ou-6 bomb	168,476		72	SCo-1 bomb	175,852		5

Table 2.11: comparison of the Zr concentrations of table-top and bomb digested shale-slate rock standards.

Type of endmember or shale	Al_2O_3 (wt %)	TiO_2 (wt %)	Sc ($\mu g\ g^{-1}$)	Cr ($\mu g\ g^{-1}$)
Felsic	14.9	0.36	6.4	37.3
Mafic	14.3	0.93	37.8	499.9
Komatiitic	5.9	0.32	23.1	2736.7

to their detrital fraction. However, Kryc et al. (2003); Perdue et al. (1976) demonstrated the combined effect of Al and Ti scavenging from the water column by organic matter and particles, leading to significant authigenic enrichment of both these elements in shaly sediments (Kryc et al., 2003). Our shale sample suites from the ABDP2-3-5-6-9 have various TOC contents, and combined with variable detrital sources, the representation of Al and Ti content in our shale sample suites present a wide dispersion of concentration (by a factor of 2 for both elements) with time, and within the same shale sample suite, as seen in Figure 2.1 of the dissertation.

The distribution of the incompatible elements Zr and Th in shales through time is mainly controlled by the proportion of felsic crust in the detrital component (see general increase of [Zr] and [Th] from older to younger shales in Fig. 2.2 with the 2.77 Ga ones clearly lying off the trend in [Zr]). Moreover, zirconium will be mainly stored in the mineral zircon, if present, which requires high-pressure bomb treatment with concentrated HF-HNO_3 (at 220°C for several days) to fully dissolve. The shales of this study, however, were digested with the table top method (digesting the samples in Teflon beakers using HF-HNO_3, on a hot plate at 85°C, with low internal pressure) to avoid W and Mo contamination from the steel mantle of the high-P bombs, which is significant. As a result, our long-term measurements of the shale rock reference materials OU-6 and SCo-1 show that bomb digestions yield higher Zr concentration (12 and 35 %) compared to a table top digestion (table 2.10).

2.6.6 Proportions of detrital components in Precambrian shales

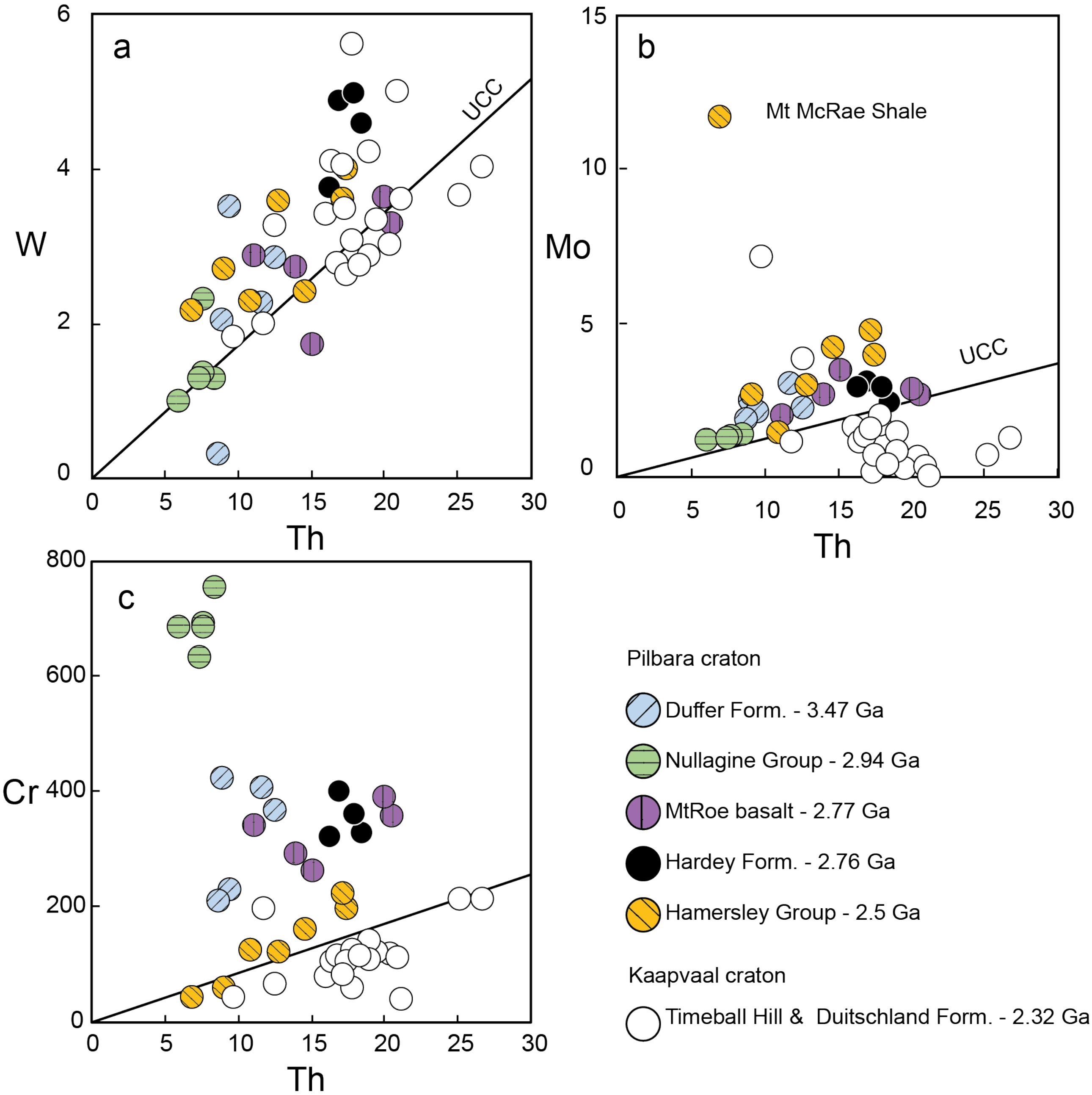

Figure 2.11: W, Mo and Cr (µg g^{-1}) versus Th (µg g^{-1}) spaces. The black linear trends represent the UCC concentrations of the respective elements, reported by Rudnick and Gao (2014). This trend represents the expected W, Mo and Cr concentrations for their respective Th concentration if the shale sample suites are solely composed of detrital components. Any enrichment in W and Mo from the UCC correspond to the authigenic component contribution, while Cr concentration is related to the rock source type, enriched in basalt and komatiites in the Meso and Paleoarchean.

Chapter 3

Stable W and Mo isotope variations of organic-rich shales from the Zaonega Formation : Interaction between continental rifting, redox changes and post-depositional hydrothermal alteration

3.1 Introduction

The Archean-Paleoproterozoic boundary is marked by a multistep evolution in atmospheric oxidation. The increase $\delta^{98/95}$Mo values over the detrital signature in open ocean sedimentary successions revealed a global increase in redox potential starting from 2.7 Ga towards the beginning of the Paleoproterozoic (Kurzweil et al., 2015; Ostrander et al., 2019; Wille et al., 2007). Still, the Archean to early-Paleoproterozoic atmosphere remained anoxic enabling the mass-independent fractionation of sulfur isotopes (MIF-S) by photolysis in an atmosphere with dioxygen levels lower than 10^{-5} to 10^{-6} PAL (present atmospheric levels) (Catling and Zahnle, 2020; Farquhar et al., 2000; Pavlov and Kasting, 2002). As a result, anoxic weathering limited the inputs of Mo and U from the continents' surfaces, until the initiation of oxidative weathering of uranium at 2.5 Ga (Brüske et al., 2020a) and 2.43 Ga for molybdenum (Greaney et al., 2020), with minimum atmospheric levels expected from $\sim 10^{-5}$ (Johnson et al., 2019) down to $\sim 10^{-4}$ PAL (Greber et al., 2015a). The Great Oxidation Event (GOE) is defined by the disappearance of MIF-S signals in sediments deposited from 2.42 to 2.32 Ga, signaling molecular oxygen levels exceeding the 10^{-5} to 10^{-6} PAL threshold (Bekker et al., 2004; Catling and Zahnle, 2020; Hannah et al., 2004; Philippot et al., 2018). However, an on-going debate questions whether this increase in atmospheric dioxygen was a single or a fluctuating event, based on the interpretation of the Duitschland and Rooihoogte Formations as one or two distinct sedimentary units, and with globally asynchronous MIF-S signals in sedimentary rocks (Coetzee, 2001; Gumsley et al., 2017; Luo et al., 2016; Philippot et al., 2018; Poulton et al., 2021; Warke and Schröder, 2018). This increase in molecular dioxygen led to the onset of intense oxidative weathering and nutrients input to the oceans. The GOE termination – during the Lomagundi-Jatuli Event (or LJE; 2.22 to 2.06 Ga) is interpreted as a so-called oxygen overshoot with molecular oxygen levels from 0.01 to 0.5 PAL (Johnson et al., 2014; Rye and Holland, 1998), associated with the longest and most extreme positive $\delta^{13}C_{carb}$ signals (reaching up to +28 ‰ V-PDB) found in the sedimentary record (Bekker et al., 2003; Karhu and Holland, 1996). The positive $\delta^{13}C_{carb}$ excursion is conventionally linked to intense burial rates of ^{13}C-depleted organic matter (Holland, 2002; Karhu and Holland, 1996). However, no time equivalent organic matter-rich sediments were reported for this timeframe to support this hypothesis. More recent theories involve enhancement of bioproductivity due to an increased phosphorous-flux to the ocean (Bekker and Holland, 2012) or paleoenvironmental changes during deposition of these sediments (Bakakas Mayika et al., 2020; Prave et al., 2021). The ~2.0 Ga Shunga Event postdates the LJE and is characterized by unprecedented and worldwide accumulation of organic carbon and oil generation and is regarded as the termination of the oxygen-overshoot. The geochemical signals of sediments deposited during the Shunga Event were previously used to interpreted it as a global decline in atmosphere dioxygen (Asael et al., 2018; Asael et al., 2013; Bellefroid et al., 2018; Canfield et al., 2013; Ossa Ossa et al., 2018a; Partin et al., 2013), while others interpreted them as local effects (Mänd et al., 2021; Mänd et al., 2020; Paiste et al., 2018; Qu et al., 2012).

In this study, we apply the W stable isotope systematic, a new geochemical proxy for paleoenvironmental reconstitution, in combination with Mo stable isotopes to marine sediments deposited during the Shunga Event. We targeted marine sediments from the well-known and studied Zaonega Formation (Fennoscandian Shield, Russia).

The volcano-sedimentary succession of the Zaonega Formation covers the end of the LJE and the following Shunga Event and revealed elevated concentrations in redox sensitive elements (RSE), such as Mo, Re, V, W, U, sourcing by either extremely low sedimentation rates or by access to a large oceanic RSE inventory (Algeo and Lyons, 2006; Mänd et al., 2020). The Zaonega Fm. is characterized by one of the earliest migrated oil field, whose TOC reached up to 98 wt. % in veinlets of migrated oil (Melezhik et al., 2004). The sediments' deposition, magmatic activity and organic matter migration occurred simultaneously during the emplacement of the Zaonega Fm., as indicated by tar or tar-coated balls (carbonaceous clay balls), brecciated sedimentary clasts, and peperites (Qu et al., 2012; Qu et al., 2018; Qu et al., 2020). Still, the syn-depositional magmatic activity of the Zaonega Fm. did not influenced the organic matter $\delta^{13}C_{org}$ values more than an offset of 4 ‰, and as such the $\delta^{13}C_{org}$ values of the ZF recorded the C isotopic characteristics of the primary biomass (Qu et al., 2018).

3.1.1 The W, Mo and V proxies

Tungsten

Tungsten is a trace metal in the upper continental crust with an average concentration of 1.9 µg.g^{-1} (Rudnick and Gao, 2014). Igneous rocks of various compositions, from different geodynamic settings and of ages reveal $\delta^{186/184}W$ values from -0.072 to +0.249 ‰ (Krabbe et al., 2017; Kurzweil et al., 2019; Kurzweil et al., 2020; Mazza et al., 2020; Roué et al., 2021). However, the range in $\delta^{186/184}W$ values is strongly narrowed to -0.010 to +0.110 ‰ for non-metamorphic or fluid related igneous rocks. The investigation of ancient igneous rocks from the Paleoarchean to the Mesoarchean revealed a similar range in $\delta^{186/184}W$ values from -0.010 to +0.097 ‰, and is described as the PII (Precambrian Igneous Inventory) (Roué et al., 2021).

The modern dissolved W inputs are overall poorly constrained in terms of fluxes and isotopic compositions, but are globally assumed to be dominated by riverine water (550 pM; (Viers et al., 2009)), groundwater (14-180 pM; (Johannesson et al., 2013), and hydrothermal vent fluids (200 to 120,000 pM; (Kishida et al., 2004). Dissolved W behaves as a conservative element in the modern ocean with a long residence time of 14-61 kyrs (Firdaus et al., 2008; Sohrin et al., 1998), a concentration of 53 to 60 pM (Sohrin et al., 1987), and a homogeneous $\delta^{186/184}W$ value of +0.543 ±0.046 ‰ (Kurzweil et al., 2021) to +0.55 ±0.12 ‰ (Fujiwara et al., 2020). Experimental studies revealed an equilibrium isotopic fractionation upon dissolved W adsorption onto Mn and Fe oxides with $\varepsilon^{186/184}W_{dissolved-adsorbed}$ of +0.59 and +0.51 ‰, respectively (Kashiwabara et al., 2017). The isotopic offset between W adsorption onto Mn-oxides is responsible for the heavy $\delta^{186/184}W$ value of the open ocean (Fujiwara et al., 2020; Kurzweil et al., 2021), and highlights the use of stable W isotopes as a proxy for the redox state of the ocean in a similar fashion as Mo.

Even though both Mo and W belong to group VI of the periodic table of the elements they behave differently in aqueous environments (Cui et al., 2021; Dellwig et al., 2019; Mohajerin et al., 2016). Unlike for MoO_4^{2-}, euxinic depositional environments are not an effective burial pathway for WO_4^{2-} to the sediment (Cui et al., 2021; Cui et al., 2020; Dellwig et al., 2019). The thiolation of WO_4^{2-} occurs only at very high H_2S levels of 1000 µM and produces very soluble thiotungstate species (Cui et al., 2020; Mohajerin, 2014). As a result, Black Sea sapropels deposited under low H_2S ($\leq$ 5 µM) concentrations during the Eemian (128,000-120,000 ky BP) are characterized by crustal-like $\delta^{186/184}$W values and concentrations (Roué et al., 2021; Wegwerth et al., 2018). Similarly, oxic depositional environments without Mn-Fe oxide shuffle are typified by low to no W authigenic enrichments (Fujiwara et al., 2020). On the other hand, anoxic non-sulfidic environments – such as the Archean ferruginous ocean – show significant authigenic W enrichments with $\delta^{186/184}$W values above that of the Precambrian igneous inventory (PII) (Roué et al., 2021). Still, the environmental conditions enabling the seawater $\delta^{186/184}$W values to be efficiently recorded in the sedimentary archive have yet to be constrained.

Molybdenum

The average Mo content in the continental crust is 1.1 µg.g^{-1} (Rudnick and Gao, 2014) with a $\delta^{98/95}$Mo value between +0.35 to +0.60 ‰ (to NIST 3134 +0.25 ‰; Willbold and Elliott (2017)). The modern Mo inputs are largely dominated by riverine waters with an average $\delta^{98/95}$Mo value of +0.7 ‰ (Archer and Vance, 2008), while the minor hydrothermal input is characterized by $\delta^{98/95}$Mo values between +0.8 ‰ to +2.1 ‰ (McManus et al., 2002; Neely et al., 2018). Dissolved Mo, or $Mo(VI)_4^{2-}$, behaves as a conservative element in the modern ocean with a residence time of 440-800 kyrs (Firdaus et al., 2008; Miller et al., 2011; Morford and Emerson, 1999), a concentration of ~110 nM and a $\delta^{98/95}$Mo value of +2.3 ‰ (Siebert et al., 2003). Such heavy seawater $\delta^{98/95}$Mo value results from isotopically light Mo drawdown during adsorption to Mn-Fe oxides in oxic depositional environments (Barling and Anbar, 2004; Goldberg et al., 2009). As such the sedimentary $\delta^{98/95}$Mo signature is a powerful tool to track the global ocean redox state.(Siebert et al., 2003).

The marine $\delta^{98/95}$Mo value is efficiently mirrored in sediments deposited in restricted and euxinic environments when the dissolved H_2S content exceeds 11 µM, at which thiolation of MoO_4^{2-} becomes quantitative and Mo is effectively drawn down into early diagenetic sulfides (Erickson and Helz, 2000; Helz et al., 1996; Nägler et al., 2005; Noordmann et al., 2015). On the other hand, if the ambient H_2S concentration is lower than 11 µM, incomplete thiolation of MoO_4^{2-} leads to sedimentary $\delta^{98/95}$Mo values lighter than the one of the ambient seawater (Arnold et al., 2004; Dahl et al., 2010; Nägler et al., 2011; Nägler et al., 2005; Noordmann et al., 2015; Wegwerth et al., 2018). Similarly, sediments deposited in open euxinic sediments (e.g. Mediterranean Pleistocene sapropels) are typified by lighter $\delta^{98/95}$Mo values (+0.2 to +1.7 ‰) than that of the open ocean (Scheiderich et al., 2010). As such, a high degree of restriction and permanently strong euxinic conditions are required to mirror the seawater $\delta^{98/95}$Mo value into the sediment.

Vanadium

Vanadium has an average abundance of 97 µg.g^{-1} in the upper continental crust (Rudnick and Gao, 2014). Vanadium is a redox sensitive element with the oxidation states V^{III}, V^{IV} and V^{V} in aqueous environments, with vanadate ($V^{V}O_4^{3-}$) and its hydrolyzed forms ($HV^{V}O_4^{3-}$, $H_2V^{V}O_4^{3-}$) dominating in oxidized environments, while vanadyl ($V^{IV}O^{2+}$) and its hydrolyzed forms ($V^{IV}O(OH)^+$, $V^{IV}O(OH)_2$) in hypoxic environments (Gustafsson, 2019; Sadiq, 1988; Takeno, 2005; Turner et al., 1981). Dissolved V in the modern ocean has a concentration of 34-45 nM and behaves as a conservative element with a residence time estimated from 42 to 130 kyrs (Emerson and Huested, 1991; Schlesinger et al., 2017).

Early studies showed that dissolved H_2S in anoxic sedimentary porewaters efficiently reduces dissolved V^{IV} and V^{V} to insoluble V^{III} (Wanty and Goldhaber, 1992). (Scott et al., 2017) reported hyper-enrichment of V ($>$ 500 to 1000 µg.g^{-1}) in $\sim$ 360 Ma old black shales which deposited under euxinic conditions with H_2S concentrations as high as 10 mM in bottom waters or in sediment porewaters. As such, vanadium hyper enrichments in sediments are commonly associated with hyper-sulfidic ($H_2S > 10$ mM) depositional environments. Still, water renewal rate is an important factor to the degree of V enrichments, as observed by the relatively low V content in sediments from the modern Black Sea compared to open environments such as the Peruvian margin (see references within Bennett and Canfield (2020)). However, V hyper enrichments also occur with dynamic Fe-Mn particulate fluxes in open ocean environments (Scholz et al., 2011).

In summary, the V content of organic-rich marine sediments depends on the rate of water renewal and supply of V (dependent on the depositional environment connection to the ocean), associated with bottom water euxinia that reduce V^{IV} and V^{V} to insoluble V^{III} or with an active Mn-Fe oxide shuttle transport of V to the sediment interface. As a result, sedimentary V concentrations normalized to Al (wt. %) values are used to discriminate between euxinic-like basins (from 23 to 46 µg.g^{-1} / wt. %), anoxic ($>$ 46 µg.g^{-1} / wt. %) and oxic depositional environments ($<$ 23 µg.g^{-1} / wt. %; Bennett and Canfield (2020)).

3.2 Samples

The Onega paleobasin is located on the Archean Karelian Craton (Fennoscandian Shield) and is composed of ∼5,000 m thick sedimentary and volcanic rocks, deposited in a large variety of depositional environments on a continental margin. The Lomagundi-Jatuli Event (LJE) and the Shunga Event (SE) were recorded in the volcano-sedimentary successions of the Tulomozero and Zaonega Fm., respectively, and were key interests of the International Continental Scientific Drilling Program's (ICDP) Fennoscandia Arctic Russia – Drilling Early Earth Project (FAR-DEEP). Details of the geology of the Onega paleobasin can be found in Melezhik et al., (2012a) and references therein.

The Zaonega Fm. deposition is encompassed by dating the underlying upper Tulomozero and of the overlying Suisari Formations between a maximum age of 2090 ±70 Ma (Pb-Pb isochron) to a minimum age of 1976 ±9 Ma (U-Pb zircon age) to 1969 ±18 Ma (Re-Os isochron) (Ovchinnikova et al., 2007; Puchtel et al., 1998; Puchtel et al., 1999). Martin et al. (2015) reported a younger maximum depositional age of 1975.3 ±2.8 Ma ±3.5 based on a lava flow of the underlying Jangozero Fm., but the significance of this age is highly debated. It is generally accepted that deposition the of the Zaonega Fm. occurred between 2060 to 1988 Ma.

An early study suggested brackish-water to lagoonal depositional environment for the lowermost part of the Zaongea Fm. (Melezhik et al., 1999), but detailed sedimentologic evidence from the cores 12A, 12B and 13A argue for an active margin or intraplate rift setting during the opening of the Kola ocean and Svecofennian Sea (Črne et al., 2013; Melezhik et al., 2012a; Melezhik et al., 2015). The lithology of the Zaonega Fm. is dominated by organic-rich mudstones, siltstones and dolostones with a TOC content reaching up to 75 % (Melezhik et al., 1999).

Numerous intervals of massive organic rich layers occur throughout the Zaonega Fm. and represent the earliest oil generation and migration reported yet (Melezhik et al., 2009; Qu et al., 2012). The $\delta^{13}C_{org}$ values of the organic-rich intervals are typical of biologically-sourced C, with values from -45 to -17 ‰ (Melezhik et al., 1999). The Zaonega Fm. sedimentary-volcanic succession deposited on a high geothermal gradient (>25 °C/km) enabling the formation of hydrocarbons in the oil window (60-120 °C), even at relatively shallow burial depth (starting

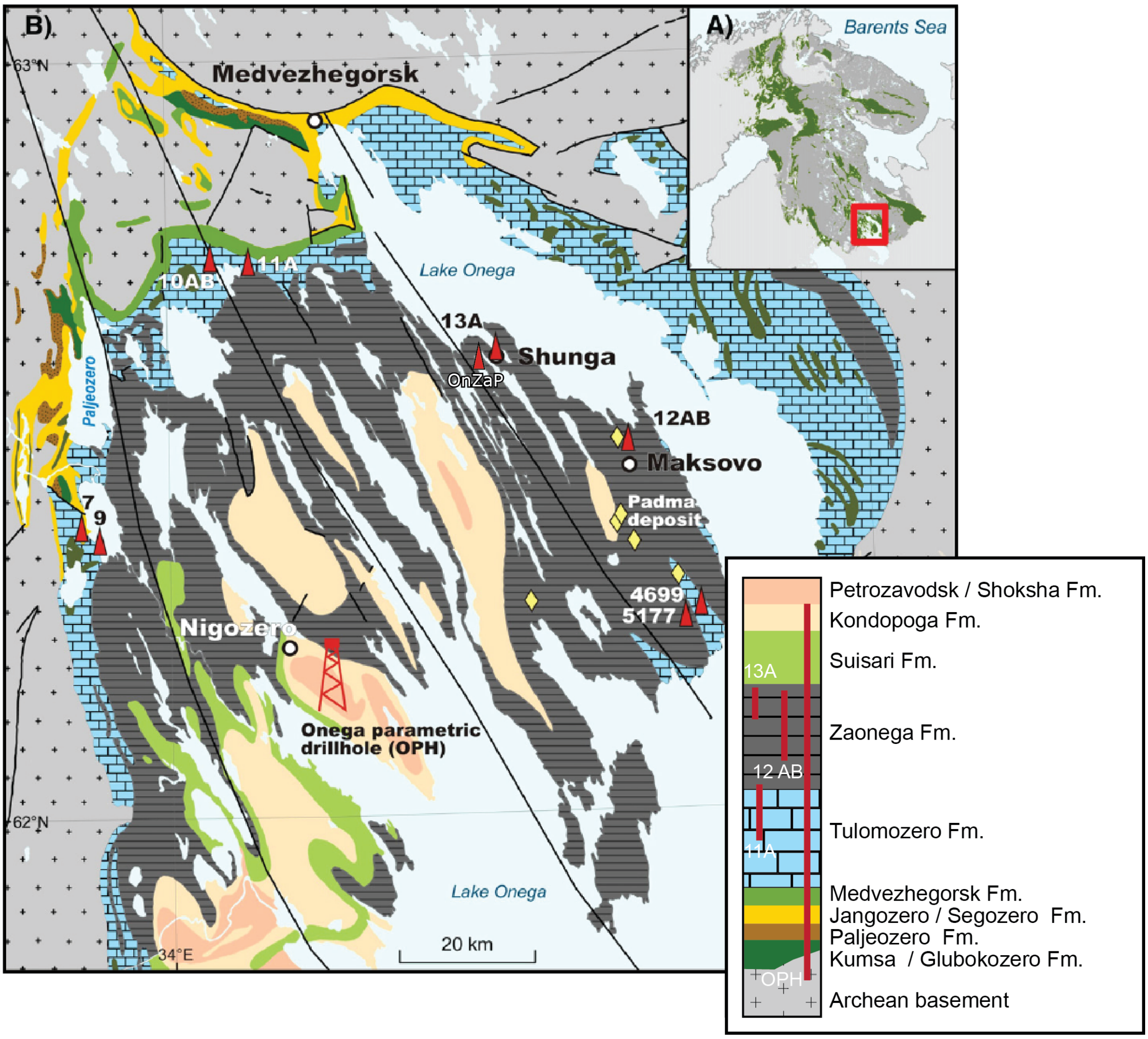

Figure 3.1: Simplified geological map of the Onega Paleobasin, modified after Koistinen et al. (2001). Locations of drillcores are indicated by red triangles.

from 1-2 km; Melezhik et al. (2012a)). The produced oil and gas migrated upwards through veins and veinlets, cutting various lithologies. Most of the oil is found in voluminous brecciated dolostones, sandstones and siltstones and indicates that the timing of the oil migration occurred during the deposition of the Zaonega Fm. sediments (Qu et al., 2012). One massive organic rich layer found in the 12AB (130-150 m) – so-called maksovite unit – results from submarine hydrocarbon expulsion, or oil seepage, with characteristic sharp contact to the underlying sedimentary units and conformable transition to the organic-rich upper shale unit. Large extrusive bodies, mostly lava flows, are found in the core 12AB from 504-498 m, 367-315 m, 119-113 m and 95-45 m. Magmatic intrusions locally altered the Zaonega Fm. organic-rich sedimentary succession, with the largest one at depth of 484–413 m, forming a peperitic contact with the wet and unconsolidated sediments (Qu et al., 2020).

The samples investigated in this study originates from cores 12A and 12B (combined 12AB) and cover 504 m of the member A and B of the Zaonega Fm.'s stratigraphy. Four organic carbon-rich layers were identified at 414-404 m, 250-253 m, 156-132 m and 56-47 m, and referred as layers 1, 2, 3 and 4, in this study. Twenty-two organic rich sediments from these four intervals were sampled.

3.3 Methods

The sample powder aliquots were ashed at 600 °C in ceramic crucibles for 12 h. The resulting loss of mass is referred as "ashing loss" and is used to correct for trace elements determination concentration.

Between 140 to 400 mg of ashed sample powders were weighted in PFA beakers and digested with 4 mL of concentrated HF and HNO_3 (3:1 ratio) for 48 h at 80 °C. Black-gray residues were observed upon digestion. The samples were carefully dried down and refluxed with 0.5 mL of concentrated HNO_3 for 24h at 100 °C and dried down. The samples were fluxed with concentrated HCl in order to destroy potential fluorides and the solutions revealed graphite-like crystals. Concentrated H_2O_2 was added (100, 200, 200 µL) three times to the samples still diluted in 9 M HCl over the course of five days at room temperature in order to digest these particles. Finally, the samples were dried down and re-converted to HNO_3 matrix. The samples were carefully centrifuged and transferred to new PFA beakers. An aliquot of the samples (in nitric form) was taken out and treated for trace element determination with ThermoFisher Scientic iCAP-Qc® quadrupole ICP-MS. The remaining solution was dried down and stored for later W and Mo isolation by wet chemical procedures.

W purification

The W purification of the shungite samples were carried out as described in the chapter 2.2.2 of the thesis and as published in Roué et al. (2021). The measurement session of this study yielded and $\delta^{186/184}$W value of 0.000 ±0.015 ‰ (2SD, n=16) on the isotopically certified international reference material NIST 3163, and a $\delta^{186/184}$W value of +0.060 ±0.012 ‰ (2SD, n=13) on the in-house Alfa Aesar standard solution. Single measurement of OU-6 (slate powder, split 8/31) rock reference material yielded a $\delta^{186/184}$W value of +0.108 ±0.019 ‰ (2SE) and is in good agreement with previously reported average $\delta^{186/184}$W value of +0.080 ±0.024 ‰ (2SD, n=12) (Roué et al., 2021). Total procedure blanks yielded W concentration of 212 pg.

Mo purification

The Mo separation chemistry is based on the one reported by Willbold et al. (2016).

The sample amounts remaining after aliquoting for W wet chemical procedures were not enough to enable $\delta^{98/95}$Mo determination on all samples, and only samples from layers 1,3 and 4 contained enough material for stable Mo isotopic composition determination.

Briefly, a ^{100}Mo-^{97}Mo double spike was added to an aliquot of the original digested samples refluxed with HNO_3 3 M in order to yield a 50 % Mo spike and 50 % sample Mo. Due to the very large variations in Mo concentrations in the shungite samples, the total amounts of Mo processed with chemistry ranged from 50 to 600 ng.

The samples equilibrated for 48 h on a hotplate at 85 °C with an additional 1 mL of concentrated HF-HNO_3. Upon dryness, the pellets were fluxed in 2 mL HCl 6 M and put on a hotplate at 100 °C overnight. A solution of aqueous 1 M ascorbic acid was prepared from ≥99 % p.a. powder (Carl Roth©) in order to reach a molarity of 1 M. Ascorbic acid efficiently reduce Fe^{III} to Fe^{II} in the sample solutions, and as such decrease the exchange competition during elution and enhance the Mo yields and purity during column chemistry. The solution was prepared the day prior to chemistry and left at room temperature. Between 100 to 200 µL of 1 M ascorbic acid solution was added to the samples, and adequate amounts of H_2O were added to reach a final molarity of 3 M HCl, in 1.8 mL. The samples were centrifuged 10,000 rpm for 10 min and were loaded onto a 7 mL column filled with 2 mL of resin 100-200 mesh Eichrom AG1-x8. The samples were rinsed with an additional 10 mL of 3 M HCL, 21 mL of 0.5 M HCl + 0.5 % v/v H_2O_2, 10 mL of 1 M HF, 6 mL of H_2O and were then collected in 10 mL of 3 M HNO_3.

The collected fractions were carefully dried down at 85 ° and taken up in 100 µL of conc. H_2O_2-HNO_3 to digest potential resin residues. The samples were dried down at 85 °C and dissolved in the analyte solution of 1 mL 0.3 M HNO_3 and centrifuged 10 min at 10,000 rpm. Finally, aliquots of 50 µL of the solutions were taken out and diluted with an extra 450 µL of the analyte solution for pre-measurement of the intensity of the signals on a Thermofisher Scientific Neptuneplus MC-ICPMS connected to an CETAC Aridus II. Upon determination of the signal intensity, the original solutions were diluted to yield a 50 ng.g^{-1} solution. The samples and standards were measured for 90 cycles with an integration time of 3.4 s. The blanks intensities were corrected from the on-peak-zero solution.

The Mo isotopic data is nowadays commonly reported in the delta notation relative to the isotopically certified international reference material NIST 3134 with the following formula 3.1. This formula is mostly used for high temperature applications for stable Mo isotopes and is only used in this study to compare the $\delta^{98/95}$Mo values of the rock reference material JB-2 to published literature data.

$$\delta^{98/95}Mo_{NIST\ 3134} = [\frac{^{98}Mo/^{95}Mo_{sample}}{^{98}Mo/^{95}Mo_{NIST\ 3134}} - 1] \tag{3.1}$$

Early studies referred their Mo isotopic data to other reference solutions, and proposed to match new $\delta^{98/95}$Mo values by normalization to the reference solution NIST 3134 with an additional offset of +0.25 with the following formula:

$$\delta^{98/95}Mo_{NIST\ 3134+0.25} = 1.00025 \times \delta^{98/95}_{NIST\ 3134} + 0.25 \tag{3.2}$$

The measurement session yielded an $\delta^{98/95}$Mo$_{NIST3134\ +0.25}$ value of +0.250 ±0.048 ‰ (2SD, n=12) and a $\delta^{98/95}$Mo$_{NIST3134\ +0.25}$ of -0.029 ±0.033 ‰ (2SD, n=9) on our in-house Johnson Matthey ICP solution (602332B). The $\Delta^{98/95}$Mo$_{NIST3134\ -JM}$ between the two solutions revealed an offset of +0.279 ‰, in good agreement with previous values reported by Greber et al. (2012) and Goldberg et al. (2013) with values of -0.25 ±0.08 ‰ (2SD) and -0.27 ±0.06 (2SD), respectively. Two powder aliquots of the rock reference materials JB-2 ((basalt powder, split 2 position 27) yielded $\delta^{98/95}$Mo$_{NIST3134}$ values of -0.012 ±0.018 ‰ (2SE) and +0.029 ±0.15 ‰ (2SE), in accordance to long-term measurements of +0.037 ±0.044 ‰ (2SD, n=22) at the isotope geochemistry of Tübingen, but slightly lighter than published values of +0.05 ±0.03 ‰ (2SD; Willbold et al. (2016)), +0.062 ±0.025 ‰ (2SD, Freymuth et al. (2015)). Two powder aliquots and OU-6 (slate powder, split 8/31) yielded $\delta^{98/95}$Mo$_{NIST3134\ +0.25}$ values of -0.504 ±0.019 ‰ and -0.476 ±0.019 ‰, in good agreement with the long-term measurements of -0.500 ±0.113 ‰ (2SD, n=19) at the isotope geochemistry facilities of Tübingen. Total procedure blanks yielded Mo concentrations of 384 and 863 pg.

3.4 Results

Trace element data is presented in table 3.1 and W and Mo stable isotope compositions in table 3.2.

The W concentrations of the organic-rich sediments range from 4 up to 5,750 ng.g^{-1}. The two lower organic rich layers 1 and 2 have the lowest W concentrations with values from 4 to 364 ng.g^{-1}. The third layer 3 displays higher W content from 0.17 to 1.15 µg.g^{-1}. Finally,

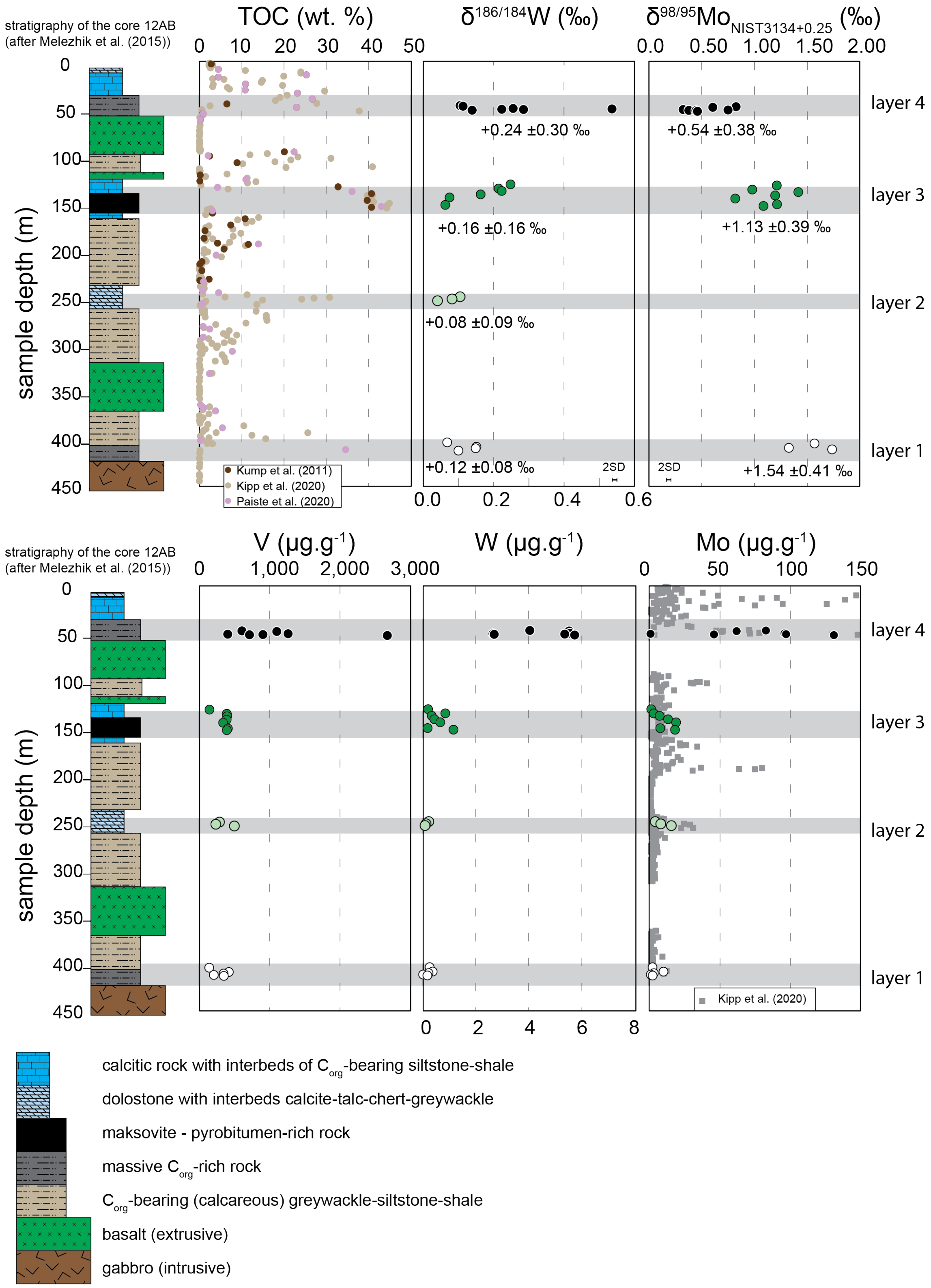

Figure 3.2: Mo, V and W concentrations, Mo and W isotopes of the cores 12AB of the Zaonega Fm., combined with TOC and Mo concentrations literature data from Kipp et al. (2020), Kump et al. (2011) and Paiste et al. (2020). The values presented in the $\delta^{98/95}$Mo and $\delta^{186/184}$W graph represent the averages (2SD) of each layer. The 2SD of the measurement session for W was of 0.015 ‰ (n=16) on NIST 3163 and of 0.048 ‰ (n=12) for Mo on NIST 3134. Some of the Mo concentrations of samples reported by Kipp et al. (2020) exceed the range of Mo concentrations (up to 430 μg.g^{-1}) reported in this Figure.

Table 3.1: Trace elements concentrations of the organic-rich samples of the core 12AB (1/3)

	layer 4	layer 4	layer 4	layer 4	layer 4	layer 4	layer 4	layer 3	layer 3
sample depth	47.69	48.38	50.75	51.23	51.57	51.84	52.55	131.20	135.54
conc. [µg.g^{-1}]									
Li	15.64	17.28	14.31	14.48	13.60	11.76	22.31	24.93	69.82
Be	0.91	1.53	1.27	0.94	1.02	0.85	2.37	1.45	2.65
Sc	8.59	11.18	10.34	36.30	12.89	10.30	18.99	12.52	33.67
Ti	1,462	2,248	2,067	6,654	2,004	1,482	3,234	2,428	6,616
V	605.56	1,100	1,261	403.54	904.40	712.34	2,672	143.77	390.46
Cr	115.76	177.01	358.85	61.58	277.42	187.75	681.03	114.25	170.65
Co	55.61	12.21	5.87	24.27	10.16	2.55	9.68	91.90	64.77
Ni	614.54	265.25	140.13	212.86	283.45	41.41	233.04	96.70	131.13
Cu	594.77	164.90	325.48	661.54	322.94	381.27	238.80	167.32	238.82
Zn	7,602	1,298	2,681	183.11	2,855	1,099	2,138	85.14	139.75
Ga	8.12	13.35	12.31	15.19	11.25	8.44	20.63	16.00	26.88
Rb	24.67	37.07	38.48	49.05	39.86	28.58	66.78	14.92	74.18
Sr	58.08	20.74	25.84	48.68	14.99	67.69	5.43	10.61	11.78
Y	15.07	25.58	29.95	43.03	27.66	18.49	35.43	8.54	26.78
Zr	39.81	64.73	73.36	162.72	60.13	38.40	91.24	109.65	235.25
Nb	2.95	6.12	6.27	5.47	3.60	4.62	9.96	4.16	9.80
Mo	82.72	61.79	95.95	0.42	97.07	45.70	131.12	1.00	2.69
Cd	33.74	5.65	12.31	0.75	13.72	5.16	9.99	0.25	0.34
Sn	0.66	5.98	4.33	1.52	2.96	1.59	4.97	0.64	1.25
Sb	6.66	0.43	0.34	0.37	0.37	0.16	0.58	3.02	4.52
Cs	1.68	1.63	2.47	4.75	3.43	2.23	4.84	0.42	2.09
Ba	232.00	458.59	316.79	88.94	255.25	257.49	602.19	410.95	1,074
La	23.94	25.43	3.48	12.83	5.14	3.68	4.31	9.73	33.65
Ce	37.11	39.18	6.04	27.40	8.93	5.99	6.63	23.31	74.12
Pr	5.46	6.16	1.18	4.28	1.70	1.06	1.16	3.10	9.16
Nd	20.50	24.12	5.91	20.18	8.37	4.81	5.13	13.08	37.66
Sm	3.61	4.51	1.99	5.86	2.44	1.37	1.55	2.95	8.35
Eu	0.65	0.80	0.62	2.18	0.71	0.48	0.53	0.82	1.84
Tb	0.45	0.63	0.61	1.21	0.58	0.37	0.61	0.46	1.01
Gd	3.25	4.14	2.87	7.37	3.23	1.87	2.60	2.78	7.67
Dy	2.55	3.82	4.40	7.55	4.10	2.60	4.83	2.79	5.37
Ho	0.55	0.87	1.05	1.65	0.98	0.63	1.24	0.57	1.08
Er	1.57	2.53	3.06	4.66	2.90	1.90	3.90	1.55	3.05
Tm	0.24	0.39	0.45	0.69	0.43	0.29	0.62	0.23	0.47
Yb	1.72	2.64	2.86	4.43	2.76	1.93	4.22	1.41	3.20
Lu	0.32	0.46	0.45	0.65	0.41	0.34	0.71	0.19	0.51
Hf	1.00	1.59	1.86	4.33	1.54	0.97	2.29	2.93	6.11
Ta	0.21	0.42	0.49	0.34	0.34	0.25	0.56	0.17	0.30
W	4.04	5.54	5.56	2.65	5.37	2.70	5.75	0.19	0.84
Tl	1.13	0.81	1.09	2.04	1.25	0.90	1.58	0.32	0.62
Pb	21.92	3.20	3.56	2.83	2.89	1.85	4.95	33.89	41.87
Th	2.02	5.80	6.81	2.14	5.69	2.80	8.94	2.09	5.05
U	4.02	10.34	18.05	0.72	11.33	6.74	17.31	1.50	3.26
W/Th	2.0034	0.9541	0.8165	1.2376	0.9437	0.9615	0.6430	0.0903	0.1671
V/Ti	0.4142	0.4894	0.6102	0.0606	0.4514	0.4805	0.8262	0.0592	0.0590
Mo/Ti	0.0566	0.0275	0.0464	0.0001	0.0484	0.0308	0.0405	0.0004	0.0004

Table 3.1 (*continued*) 2/3

	layer 3	layer 3	layer 3	layer 3	layer 3	layer 2	layer 2	layer 2
sample depth	138.15	141.79	145.09	151.22	153.03	250.38	252.70	254.58
conc. [µg.g^{-1}]								
Li	46.89	42.75	46.16	60.75	51.36	40.13	26.05	48.84
Be	2.32	1.91	1.59	2.01	1.83	1.48	0.90	1.49
Sc	24.27	14.63	12.86	17.00	16.14	13.10	19.72	22.29
Ti	3,248	2,967	2,885	2,295	3,920	2,749	2,511	3,306
V	393.58	388.88	337.49	406.10	390.65	285.79	234.16	496.80
Cr	189.50	149.60	127.61	164.51	154.66	273.31	253.18	246.67
Co	44.73	34.29	34.00	35.50	33.09	18.88	29.89	44.68
Ni	467.57	663.68	604.62	695.02	679.26	342.35	309.37	451.48
Cu	247.41	230.73	223.25	231.96	243.72	1,188	291.87	503.92
Zn	166.60	404.16	446.30	263.34	313.75	123.98	528.76	441.33
Ga	18.02	16.15	13.45	17.46	15.95	13.59	8.83	13.62
Rb	68.98	52.41	51.11	66.54	59.47	53.63	35.70	36.80
Sr	16.02	11.48	9.42	12.56	11.79	12.88	8.80	9.52
Y	32.82	27.62	23.24	32.40	30.35	20.29	32.37	10.05
Zr	146.25	114.05	96.61	127.95	120.00	109.44	59.29	75.97
Nb	4.15	6.31	7.10	3.76	9.60	7.45	4.68	2.73
Mo	6.90	12.92	18.69	7.46	17.96	3.81	7.79	15.31
Cd	0.48	1.64	1.96	1.10	1.28	0.31	1.17	1.12
Sn	1.31	2.07	1.69	2.04	2.00	2.15	0.44	1.26
Sb	3.71	7.34	10.69	6.05	12.06	6.56	4.57	4.41
Cs	1.84	1.91	1.56	2.08	1.93	2.28	1.56	2.08
Ba	1,052	663.48	636.92	813.81	830.18	1,042	503.61	1,720
La	33.23	27.75	23.79	33.63	31.56	7.76	15.05	2.46
Ce	64.46	55.51	46.70	65.84	62.14	17.97	25.89	6.66
Pr	7.82	6.81	5.72	8.00	7.54	2.91	3.57	1.05
Nd	30.04	25.79	21.57	30.21	28.44	12.22	14.72	4.69
Sm	6.19	5.06	4.19	5.86	5.47	2.66	3.41	1.26
Eu	1.45	1.11	0.93	1.29	1.20	0.80	0.73	0.58
Tb	0.92	0.70	0.58	0.80	0.74	0.51	0.76	0.25
Gd	5.88	4.62	3.79	5.31	4.95	2.89	4.30	1.46
Dy	5.52	4.26	3.53	4.88	4.57	3.41	5.10	1.65
Ho	1.15	0.90	0.76	1.05	0.98	0.79	1.14	0.40
Er	3.23	2.59	2.18	3.01	2.81	2.39	3.19	1.24
Tm	0.48	0.40	0.34	0.46	0.43	0.38	0.46	0.20
Yb	3.07	2.58	2.16	2.96	2.78	2.56	2.79	1.38
Lu	0.45	0.38	0.32	0.44	0.41	0.40	0.39	0.22
Hf	3.88	2.75	2.31	3.02	2.85	3.02	1.55	2.00
Ta	0.12	0.40	0.46	0.13	0.60	0.64	0.39	0.20
W	0.33	0.43	0.65	0.17	1.15	0.22	0.12	0.07
Tl	0.17	0.07	0.04	0.05	0.08	0.45	0.35	1.19
Pb	30.01	24.24	18.85	21.82	21.13	15.47	9.40	21.86
Th	8.68	7.36	6.24	8.41	7.83	9.12	4.09	1.14
U	17.77	19.36	15.84	20.38	18.54	4.83	3.42	8.13
W/Th	0.0379	0.0581	0.1041	0.0202	0.1474	0.0239	0.0281	0.0638
V/Ti	0.1212	0.1311	0.1170	0.1769	0.0996	0.1040	0.0933	0.1503
Mo/Ti	0.0021	0.0044	0.0065	0.0032	0.0046	0.0014	0.0031	0.0046

Table 3.1 (*continued*) 3/3

	layer 1	layer 1	layer 1	layer 1	layer 1
sample depth	404.82	409.46	410.99	412.53	413.59
conc. [µg.g^{-1}]					
Li	7.63	28.13	31.61	18.94	13.75
Be	0.29	1.20	1.34	1.00	0.96
Sc	16.29	19.37	21.37	14.91	20.72
Ti	2,908	4,170	1,777	1,067	5,000
V	139.38	419.38	344.64	205.15	348.77
Cr	109.73	288.54	198.81	164.45	157.77
Co	17.45	33.39	50.69	12.21	76.86
Ni	69.71	427.90	420.61	132.96	356.61
Cu	27.33	56.73	231.81	33.16	390.54
Zn	118.14	224.12	45.89	27.94	50.92
Ga	15.07	17.04	19.71	11.74	14.63
Rb	0.63	28.03	30.73	11.01	2.54
Sr	89.47	39.15	38.92	31.98	24.68
Y	17.92	34.12	39.30	34.73	26.40
Zr	33.37	153.57	161.19	141.39	92.60
Nb	1.80	8.89	6.32	0.66	4.86
Mo	1.85	9.69	2.84	0.61	1.95
Cd	0.53	0.91	0.08	0.06	0.04
Sn	0.57	0.95	2.91	0.26	0.39
Sb	0.51	0.33	1.32	0.06	0.33
Cs	0.03	1.34	1.20	0.30	0.08
Ba	65.84	1,362	1,437	574.90	34.31
La	8.30	24.21	31.61	29.73	14.49
Ce	14.39	51.52	71.28	63.62	31.76
Pr	1.82	6.56	8.50	7.91	3.97
Nd	7.95	24.56	32.04	30.87	15.46
Sm	2.05	5.30	6.80	6.74	3.78
Eu	1.09	1.36	1.67	1.05	1.15
Tb	0.43	0.88	1.00	0.93	0.74
Gd	2.56	5.20	6.29	6.26	4.20
Dy	2.75	5.61	6.15	5.48	4.81
Ho	0.61	1.22	1.33	1.15	1.05
Er	1.66	3.57	3.79	3.16	2.95
Tm	0.24	0.56	0.57	0.48	0.42
Yb	1.49	3.70	3.69	3.08	2.50
Lu	0.22	0.54	0.54	0.45	0.35
Hf	0.67	3.75	4.00	3.35	2.45
Ta	0.09	0.57	0.32	0.02	0.29
W	0.25	0.36	0.21	0.01	0.17
Tl	0.13	1.13	0.36	0.16	0.06
Pb	4.30	9.85	20.26	9.02	3.56
Th	0.12	6.76	11.77	11.76	2.84
U	1.09	15.55	25.29	14.49	3.48
W/Th	2.0533	0.0538	0.0175	0.0003	0.0582
V/Ti	0.0479	0.1006	0.1940	0.1922	0.0698
Mo/Ti	0.0006	0.0023	0.0016	0.0006	0.0004

the upper organic-rich layer 4 is the most concentrated in W with values ranging from 2.65 to 5.75 µg.g^{-1} (Figure 3.2). The W/Th weight ratios of the organic rich layers range from 0.0003 to 2.05.

The stable W isotopic compositions of organic-rich shales from core 12AB range in $\delta^{186/184}$W values from +0.041 ‰ to +0.536 ‰. The two bottom layers 1 and 2 display $\delta^{186/184}$W values from +0.041 to +0.151 ‰, while the two upper layers 3 and 4 have a larger span of $\delta^{186/184}$W values from +0.063 to +0.536 ‰.

The Mo and V concentrations distributed in the core 12AB are similarly distributed. The lower three layers – 1, 2 and 3 – are characterized by relatively low Mo and V concentrations ranging from 0.61 to 18.69 µg.g^{-1} and 139.38 to 496.80 µg.g^{-1}, respectively. The upper layer 4 has Mo and V contents from 0.42 to 131.1 µg.g^{-1} and 403.54 to 2,672. µg.g^{-1}, respectively. The Mo contents (µg.g^{-1}) normalized to Ti (µg.g^{-1}) (Mo/Ti weight ratios) of the organic-rich samples range from 0.00006 to 0.057. The V contents (µg.g^{-1}) normalized to Ti (µg.g^{-1}) or (V/Ti weight ratios) of the organic rich samples range from 0.047 to 0.82.

The $\delta^{98/95}\text{Mo}_{NIST3134\ +0.25}$ values of the organic layers scatter from +0.165 to +1.736 ‰, with higher $\delta^{98/95}\text{Mo}_{NIST3134\ +0.25}$ values from +1.327 to +1.569 ‰ down in the organic rich layer 1, while the layers 3 and 4 yield lower $\delta^{98/95}\text{Mo}_{NIST3134\ +0.25}$ values from +0.979 to +1.416 ‰ and +0.325 to +0.826 ‰, respectively.

3.5 Discussion

The following discussion refers to various hydrocarbons, for the description of which we use the definitions from Tissot and Welte (1984). Briefly, kerogen refers to the sediments' organic matter formed during mild thermal degradation associated with diagenesis and catagenesis. During diagenesis (<350 °C), heteroatomic bonds, functional groups, CO_2, H_2O and isotopically heavy N, S, O are released from the immature kerogen. Then, catagenesis (350 to 500 °C) corresponds to the stage where hydrocarbons chains and cycles are eliminated, forming kerogen composed of medium to low molecular hydrocarbons. Metagenesis corresponds to the stage where only dry gas (methane) is generated. Three main types of kerogen are found in the sedimentary record and originate from different organisms, such as marine algal (type I), mixed terrestrial and marine (type II) and terrestrial (type III). These three types of kerogen can be discriminated following their H/C and O/C atomic ratios.

Bitumen refers to the solvent-extracted fraction of kerogen. Asphaltene is high-molecular weight bitumen. Further maturation leads to the formation of solvent-insoluble pyrobitumen.

3.5.1 Autochthonous or allochthonous signals ?

Many previous studies used C, N, O, S, Fe, Mo, U, Se concentrations and isotopes of organic-rich samples from the Zaonega Fm. as proxies for the Paleoproterozoic atmosphere and ocean redox states following the Lomagundi-Jatuli Event (Karhu and Holland, 1996; Kipp et al., 2020; Kump et al., 2011; Mänd et al., 2021; Mänd et al., 2020; Melezhik et al., 2015; Paiste et al., 2018; Paiste et al., 2020; Qu et al., 2012; Qu et al., 2018; Scott et al., 2014). However, the geochemical composition of the organic-rich samples from the Zaonega Fm. might reflect variations sourcing from the autochthonous authigenic sedimentary enrichments combined with and/or overprinted by different proportions of migrated kerogen from underlying units. There are numerous sedimentary evidences that migrated hydrocarbons infiltrated the host sediments before consolidation, with the exception of the layer of maksovite ($\sim$130-150 m; core 12AB), which is regarded as a seafloor oil spill (Melezhik et al., 2012a). As such, using the chemical signals of these exceptionally organic-rich sediments as proxies for paleoenvironmental reconstructions can be critical as they may originate from a combination of autochthonous and/or allochthonous sources. The following discussion aims at stating the present knowledge about the effects of thermal maturation, migration and injection onto Mo, V and W concentrations,

Table 3.2: Stable W and Mo isotopic compositions of the organic rich samples of the core 12AB

	$\delta^{184/186}$W	2SE	W conc.	$\delta^{98/95}$Mo	2SE	Mo conc.
	‰ [NIST 3163]		[µg.g^{-1}]	‰ [NIST 3134+0.25]		[µg.g^{-1}]
47.69	0.105	0.014	3.59	0.826	0.021	63.41
48.38	0.113	0.012	5.69	0.606	0.020	49.22
50.75	0.255	0.017	5.00	0.325	0.022	81.01
51.23	0.536	0.018	2.31	0.750	0.021	0.38
51.57	0.223	0.014	4.45	0.378	0.017	77.43
51.84	0.285	0.015	2.44	0.446	0.019	38.16
52.55	0.139	0.016	6.48	0.461	0.018	78.15
131.20	0.248	0.019	0.26	1.213	0.019	0.91
135.54	0.214	0.020	1.46	0.979	0.019	2.41
138.15	0.223	0.022	0.65	1.416	0.018	5.83
141.79	0.163	0.013	0.38	1.197	0.021	9.44
145.09	0.075	0.019	0.62	0.818	0.019	13.59
151.22				1.214	0.019	9.55
153.03	0.063	0.016	1.39	1.086	0.019	12.01
250.38	0.105	0.020	0.20			
252.70	0.082	0.017	0.18			
254.58	0.041	0.016	0.07			
404.82	0.068	0.018	0.19	1.569	0.019	2.02
409.46	0.151	0.017	0.31	1.327	0.018	6.55
410.99	0.149	0.018	0.23	1.736	0.034	1.35
413.59	0.100	0.020	0.17			

and the $\delta^{98/95}$Mo values of kerogen.

Artificial thermal maturation previously revealed little change in the Mo isotopic composition of bitumen and asphaltene compared to that of the original bulk rock, but the products were significantly depleted in Mo with less than 10 % of the original concentrations (Dickson et al., 2020). In the case of this study, the kerogen source of the migrated hydrocarbons in the Zaonega Fm. deposited in lacustrine to brackish waters masses, and likely were not enriched in Mo (Melezhik et al., 2012b). Then, the migration and injection of pyrobitumen into the upper sedimentary units of the Zaonega Fm. likely did not fully overprint the autochthonous Mo concentrations and $\delta^{98/95}$Mo values of the sedimentary rocks. For example, the maksovite layer (submarine oil seepage) can be found at the interval 131-153 m of the core 12AB but is not intersected in its stratigraphic equivalent in the core 13A. The Mo concentrations of the maksovite layer are lower than the corresponding interval of the core 13A (0.997 to 17.96 µg.g^{-1} compared to 1.7 to 72.3 µg.g^{-1}, respectively (Asael et al., 2013)), while the $\delta^{98/95}$Mo values of the core 12AB is higher (+1.132 ±0.38 ‰; 2SD, n=7, this study)) than the one of the core 13A (+0.67 ±0.52 ‰; 2SD, n=45, Asael et al. (2013)). Such variations in Mo signals can be interpreted as signals of different depositional environments with occasional overlapping $\delta^{98/95}$Mo values rather than the injection of Mo-depleted oil into the sedimentary units.

Szalay and Szilagyi (1967) reported reduction of dissolved vanadate to insoluble vanadyl by humic acids in aqueous environments, likely accounting for the strong V enrichments in organic-rich marine sediments. Extracted bitumen from various natural organic-rich sedimentary rocks revealed a large spread of V concentrations reaching up to 4,000 µg.g^{-1}, significantly lower than the bulk V concentrations reaching up to 25,000 µg.g^{-1} (Lewan and Maynard, 1982). Ripley et al. (1990) proposed that V was desorbed from organics during diagenesis to form V-bearing clays, resulting in residual hydrocarbons with less than 3-8 % of the whole rock V content (Ripley et al., 1990). Vanadium in type I and II kerogens (marine-lacustrine) is associated with tetrapyrrole complexes (e.g. chlorophyll component) (Lewan, 1984). Tetrapyrrole complexes are preferentially preserved under anoxic conditions with negative Eh values (for a pH of 7), where VO^{2+} and Ni^{2+} substitute for Mg^{2+} bound to tetrapyrrole. As a result, V and Ni remain in crude oil during high maturation temperatures, migration and reservoir alteration and can be used to identify their organic matter source type (Hodgson and Baker, 1957; Lewan and Maynard, 1982), even if the partition coefficient between bulk rock and hydrocarbon is relatively low.

Very little W data has been published for kerogen or petroleum systems. Fuchs et al. (2016) reported W concentrations in the Mesoarchean (∼3 Ga) pyrobitumen for marine-sourced oil of the Carbon Leader Reef (Witwatersrand Supergroup, South Africa) with relatively high averages ranging from 1.68 to 12 µg.g^{-1}, that correlates with the ones of Th whose concentrations range from 1,016 to 4,940 µg.g^{-1}. These samples are depleted in V compared to the UCC, with concentrations from 0.48 to 4 µg.g^{-1}. However, these samples are not representative of typical pyrobitumen as they experienced multiple post-depositional regional metamorphism. Marine to continental-sourced natural crude oil samples revealed very low levels of W from below detection limits to up to 90 ng.g^{-1} (Yang et al., 2018).

The literature data available show a very large spectrum of enrichments/depletions of various elements, but globally Mo, V and possibly W concentrations are relatively low in bitumen/pyrobitumen compared to the ones of the organic-rich source rocks. The correlation between Mo and V of the four organic rich layers (R^2=0.76; not shown in any figure) of this study indicates that these metal contents originate mainly from authigenic enrichment rather than allochthonous oil migration and injection in the sediments. As such, we speculate that the Mo, W and V signals in the Zaonega Fm. samples investigated in this study result from authigenic marine enrichments, prior to the injection of oil, or contemporaneous to the oil seepage of the layer 3.

3.5.2 Gradual changes in the degree of restriction and in depositional environment

Bennett and Canfield (2020) introduced the use of Mo/Al vs. V/Al space of marine sediments as a tool to discriminate between depositional environments such as oxic, hypoxic, anoxic, and euxinic (permanent, seasonal, open, restricted). Unfortunately, no major element data is available for the sample powder aliquots measured in this study, but Ti ($\mu g.g^{-1}$) was measured during trace element concentration determinations. Titanium (Ti; $\mu g.g^{-1}$) and Al (wt. %) concentrations from the data compilation of Bennett and Canfield (2020) strongly correlate (R^2=0.88, linear fit) with an average Ti/Al ($\mu g.g^{-1}$/wt. %) of 524.44, which is lower than that of the UCC (941.24; Rudnick and Gao (2014)). We used this factor to convert the Mo/Al and V/Al ratios reported by Bennet and Canfield (2020) to Mo/Ti and V/Ti ratios when no Ti ($\mu g.g^{-1}$) or TiO_2 (wt. %) values were available, allowing for comparison to our own data. As a consequence, the different depositional environments from various depositional environments distinguished by their degree of restriction (closed basin, semi-open sea, continental margin) and redox state (oxic, euxinic, anoxic), as well as their position relative to the modern Oxygen Minimum Zones (OMZ) defined by Bennett and Canfield (2020) in Mo/Al vs. V/Al space were also translated to Ti-normalized Mo and Ti axes (i.e. Mo/Ti vs. V/Ti ($\mu g.g^{-1}$ / $\mu g.g^{-1}$ space; Figure 3.3). We compared data of restricted modern sediments (various Baltic Sea localities, the Red Sea, Cariaco Basin, Saanich inlet) and open continental margins OMZ (Böning et al., 2004; Borchers et al., 2005; Brumsack, 1989; Morford and Emerson, 1999; Scholz et al., 2011; Yano et al., 2020) with our data from the organic-rich sediments of the Zaonega Fm. to investigate the environmental conditions that might have led to the deposition of the latter.

The Mo/Ti and V/Ti weight ratios of the samples from the layers 1, 2 and 3 scatter mainly in the restricted environment field of modern samples, while the data from the upper layer 4 plots in the field for open ocean environments, with the exception of one sample (51.23 m) with Mo/Ti and V/Ti values characteristic of modern oxic environments (Figure 3.3). Such change in the degree of restriction agrees well with the general idea that the Fennoscandian Shield experienced continental rifting during the opening of the Kola Ocean and Svecofennian Sea and the deposition of the Zaonega Fm. (Lahtinen et al., 2008). The deposition of

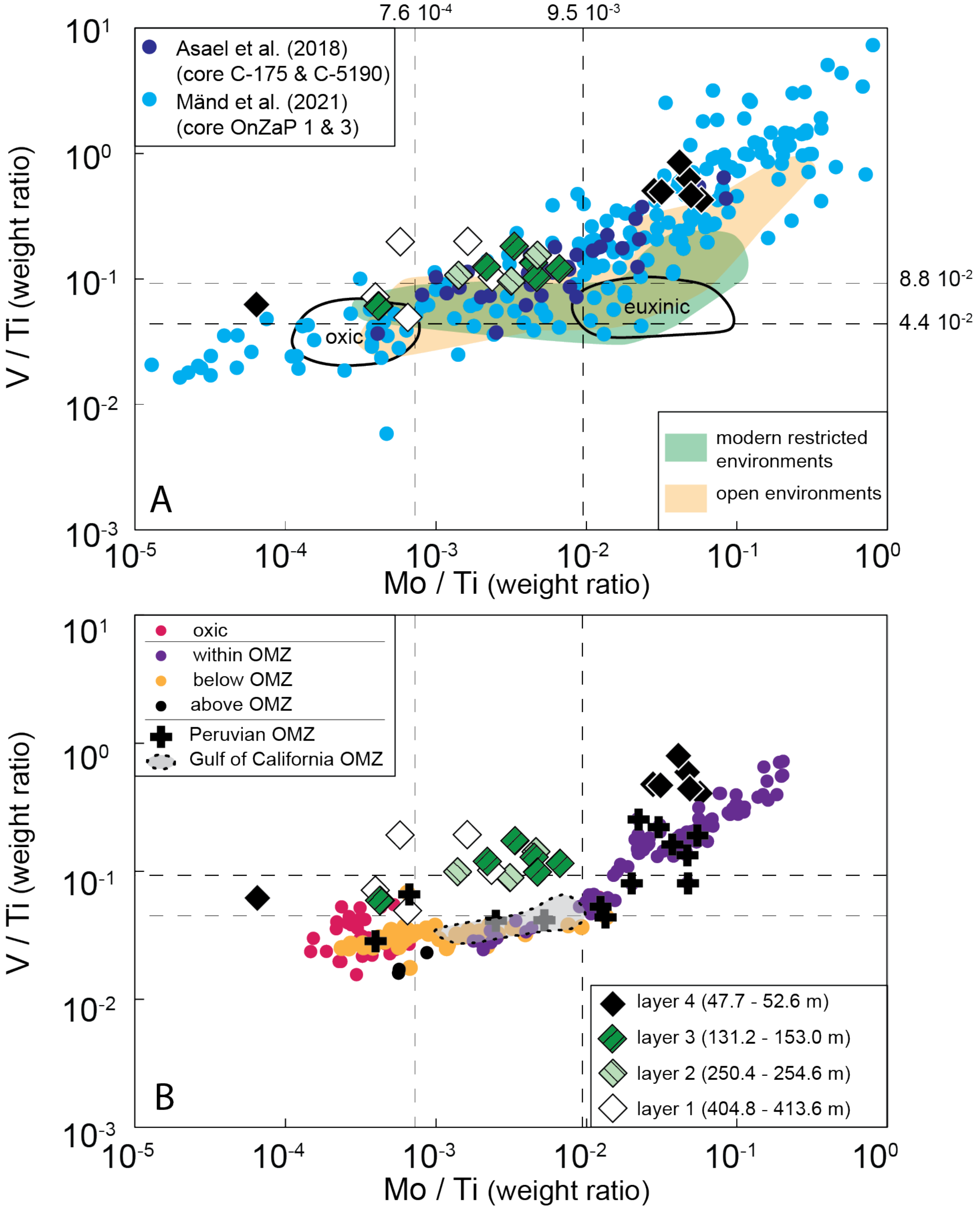

Figure 3.3: Mo/Ti vs. V/Ti weigh ratios of samples from this study (diamonds) compared to literature data. A. the data used to represent the various fields (modern restricted and open environments, oxic and euxinic settings) source from Yano et al. (2020) and from the data compilation of Bennett and Canfield (2020). B: the data source from the data compilation of Bennett and Canfield (2020) with an highlight on the Peruvian (black crosses; Böning et al. (2004)) and Gulf of California OMZs (gray field; Brumsack (1989)).

the sedimentary units below the Zaonega Fm. took place in long-lasting shallow marine to continental depositional environments above the Archean basement of the Onega Paleobasin. These deposits include massive red beds, conglomerates, sandstones, evaporites, carbonates and sabkha sedimentary successions forming the Kumsa, Paljeozero, Jangozero, Medvezhegorsk and Tulomozero Formations (Blättler et al., 2018; Melezhik et al., 2012a; Melezhik et al., 2015; Ojakangas et al., 2001). Early studies interpreted the depositional environment of the lower Zaonega Fm. as brackish and sulfate-poor non-euxinic lagoon based on outcrop observations (Melezhik et al., 1999; Melezhik et al., 2004). However, the drill cores 12AB and 13A revealed lateral variations in depositional environments with distal water facies (turbidites, slumped beds) for the base of the Zaonega Fm. (Melezhik et al., 2012a). As such, the change in Mo/Ti and V/Ti ratios seen in the core 12AB likely originate from a deeper depositional environment in the Onega paleobasin.

Trace element data from the Zaonega Fm. were previously published in the studies of Mänd et al. (2021) and Asael et al. (2018) using samples from the core 13A and OnZap13. These studies reported Mo, V, Ti or Al contents of diverse marine sediments (organic rich mudstones, limestones, mudstones, dolostones, cherts) and reveal a larger spread of Mo/Ti and V/Ti ratios than the ones measured for organic-rich sediments in this study (Figure 3.3), but these two cores intersect the upper part of the Zaonega Fm., and agree well with the data distribution of the upper layer 4 of the core 12AB.

The crustal-like W concentrations and associated PII-like $\delta^{186/184}$W values (with the exception of sample 409.46 m with $\delta^{186/184}$W value of +0.151 ±0.017, 2SE) in the two bottom layers 1 and 2 are similar to the ones reported for the modern Black Sea sapropels and point towards euxinic bottom water during deposition (Roué et al., 2021). Furthermore, these samples are characterized by relatively low V/Ti and Mo/Ti weight ratios, characteristic of restricted modern marine environments (Figure 3.3) compared to other Zaonega Fm. sediments (Asael et al., 2013; Mänd et al., 2020). Consequently, the two lowermost organic rich layers 1 and 2 likely deposited in a Black Sea-like environment (restricted basin with bottom water euxinia and limited exchange with the open ocean RSE reservoir). Authigenic $\delta^{98/95}$Mo values of euxinic environments with H_2S levels exceeding 11 µM are expected to reflect the open ocean $\delta^{98/95}$Mo value due to quantitative Mo drawdown (Erickson and Helz, 2000; Helz et al., 1996; Nägler et al., 2005; Noordmann et al., 2015). As such, the layer 1 likely recorded the $\delta^{98/95}$Mo value of the prevalent open Paleoproterozoic ocean, encompassed between +1.327 and +1.736 ‰ (Figure

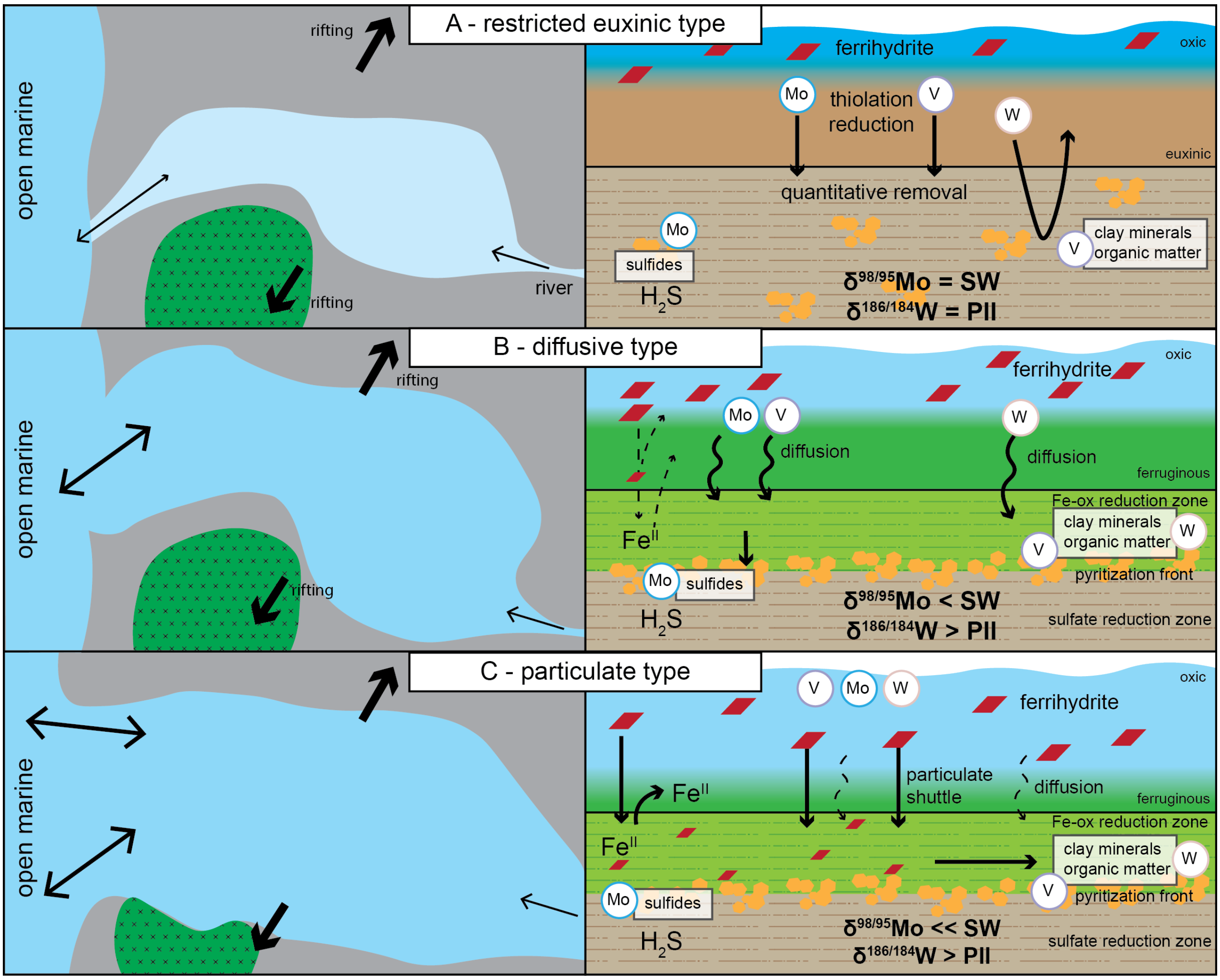

Figure 3.4: basinal and redox evolution model of the Onega paleobasin. The restricted euxinic type represent the depositional environments of the layers 1 and 2 in a Black Sea-like environment. The diffusive type represents the depositional environment of the layer 3, with Mo, V and W fluxes dominated by diffusion of RSE from the seawater. The particulate type represents the depositional environment of the layer 4, dominated by Fe-oxides shuttle (red symbols), leading to isotopically light $\delta^{98/95}$Mo values in the sediment.

3.4 A).

The layers 3 and 4 of the core 12AB reveal fractionated $\delta^{186/184}$W values and higher W concentrations than the underlying organic-rich layers 1 and 2. These signals strongly point toward non-euxinic depositional environments. As a result, their $\delta^{98/95}$Mo values are not representative of the one of the open ocean, contrary to the layer 1. Their Mo/Ti and V/Ti weight ratios spread alongside the complete spectrum of values for restricted basins and continental margins OMZ (Bennett and Canfield, 2020). Modern continental margins OMZ show significant variations in their Mo and V authigenic enrichments intensity. For example, the Peruvian margin sediments deposited within the OMZ are characterized by higher Mo and

V enrichments than the ones of the Gulf of California OMZ (Böning et al., 2004; Brumsack, 1989), even though they both have a large access to the open ocean RSE reservoir. These two OMZs have different mode of supply of Mo and V to the sediment, the so-called particulate and diffusive fluxes (Eroglu et al., 2020; Scholz et al., 2011; Scholz et al., 2019; Scholz et al., 2017). Particulate shuttling of Mn-Fe oxides is responsible for efficient scavenging of Mo, V and W in modern marine environments (Kurzweil et al., 2021; Scholz et al., 2011). Denitrification and Mn-oxide reduction already occur in the water column at the OMZ, leaving Fe-oxides as the main carrier of RSE to the sediments (Böning et al., 2004; Scholz et al., 2011; Scholz et al., 2017). Once deposited in the sediment Fe-oxides are reduced in the Fe-oxide reduction zone, with Fe^{II} refluxed to the above water column and Mo, V and W oxyanions released to the sediments pore water (Figure 3.4 B and C).

Molybdenum has a high affinity for sulfides and organic matter, while V and W mostly adsorbs onto clay minerals and organic matter (Ripley et al., 1990; Sen Tuna and Braida, 2014; Tuna et al., 2012; Vorlicek et al., 2004). The adsorption of Mo_4^{2-} and WO_4^{2-} to Fe-oxides favors the removal of the lighter over the heavier isotopes from the solution, with equilibrium isotopic fractionations $\varepsilon^{98/95}Mo_{(dissolved-adsorbed)}$ ranging from +0.83 ±0.60 ‰ for magnetite, +1.11 ±0.15 ‰ for ferrihydrite and +2.19 ±0.54 ‰ for hematite, and an equilibrium isotopic fractionation $\varepsilon^{186/184}W_{(dissolved-adsorbed)}$ of +0.51 ±0.06 ‰ for ferrihydrite (Goldberg et al., 2009; Kashiwabara et al., 2017). As a result, modern sediments of the Peruvian OMZ – where the supply of Mo is controlled by ferric oxide drawdown – are characterized by high Mo enrichments (< 101 µg.g^{-1}) and a light $\delta^{98/95}$Mo value of +1.32 ±0.17 ‰ that reflects the equilibrium isotope fractionation of adsorbed Mo on ferrihydrite to modern seawater with $\delta^{98/95}$Mo a value of +2.3 ‰ (Scholz et al., 2011; Scholz et al., 2017).

Modern redox stratified basins reveal conservative open marine-like $\delta^{98/95}$Mo values in the water column from the surface, across the redoxcline and towards bottom waters (Noordmann et al., 2015). As a result, the diffusive-controlled Guaymas OMZ (Gulf of California) is characterized by a $\delta^{98/95}$Mo value close to the one of seawater, with an average value of +1.93 ±0.32 ‰ (2SD) (Eroglu et al., 2020). However, such diffusive-controlled depositional settings are characterized by moderate Mo and V enrichments (<19 µg.g^{-1} and <133 µg.g^{-1}, respectively) (Brumsack, 1989; Eroglu et al., 2020).

As such, the global decrease in $\delta^{98/95}$Mo values from the layer 1 (+1.54 ±0.41 ‰; n=3), to the layer 3 (+1.13 ±0.38 ‰; 2SD; n=7) to the layer 4 (+0.54 ±0.38 ‰ 2SD; n=7) cannot be interpreted as changes in the oxygenation state of the global ocean and atmosphere system, but rather by changes in the delivery mode of Mo to the sediment. We propose a two-component mixing model for the $\delta^{98/95}$Mo values of the layers 3 and 4, with a diffuse component (characterized by an $\delta^{98/95}$Mo of +1.544 ‰, average $\delta^{98/95}$Mo value of the euxinic interval of the layer 1) and particulate component (dominated by ferrihydrite with an $\delta^{98/95}$Mo value ∼1.11 ‰ lighter that the one of the contemporaneous seawater). This model is based on the premise that the $\delta^{98/95}$Mo value of the ocean did not change over the course of the deposition of the layers 3 and 4. Using this model, we suggest that the Mo delivery of the layer 3 (+1.132 ±0.385 ‰; 2SD; n=7) was dominated by diffusion (63 %), while the one of the layer 4 (+0.542 ±0.381; 2SD; n=7) was dominated by particulate fluxes (90 %).

The recent study of Kurzweil et al. (2021) revealed non-conservative dissolved W isotopic compositions in the water column of the redox-stratified Landsort Deep (LD1, deepest basin of the Baltic Sea). The surface waters are typified by $\delta^{186/184}$W values spanning from +0.615 ‰ to +0.638 ‰ associated with dissolved W concentrations (72 to 73 pM), both exceeding the ones of the open ocean (+0.55 ‰; ∼50 pM) (Fujiwara et al., 2020; Kurzweil et al., 2021). The redoxcline between oxidized and euxinic water masses is marked by a heavy $\delta^{186/184}$W value of +0.810 ‰ with 232 pM of W, as a result of dissolution and re-precipitation of Mn-oxides, characterized by relatively light $\delta^{186/184}$W values from +0.096 to +0.335 ‰. Finally, the euxinic bottom waters have constants $\delta^{186/184}$W values and concentrations with averages of +0.414 ±0.008 ‰ and 164 ±11 nM, respectively (n=7) (Kurzweil et al., 2021). As such, the behavior of W in a the water column of a redox stratified basin is influenced by local redox and oxide cycling, contrary to Mo who behaves conservatively (Noordmann et al., 2015).

In the case of the redox stratified Onega paleobasin, the water column $\delta^{186/184}$W value might have fluctuated at depth, and likely particulate transport of W to the bottom waters or to the porewater of sediments favored light W isotopes. Tungsten efficiently adsorbs onto clay minerals and organic matter (Sen Tuna and Braida, 2014; Tuna et al., 2012), but no study so far investigated the potentially associated isotopic fractionation. Still, bond-strength theory predicts that isotopically light W would be favored in the adsorbed phase. Then, it can be expected that (1) the bottom waters bellow the redoxcline were enriched in isotopically light W that diffused to the sediment porewaters and quantitatively adsorbed onto clay minerals and organic matter, and/or (2) an isotopic fractionation favored isotopically light W during WO_4^{2-} adsorption onto clay minerals and organic matter. As such, it can be expected that the spread of $\delta^{186/184}$W values typically ranging from +0.063 ‰ to +0.285 ‰ observed in the layers 3 and 4 (with the exception of the 51.23 m sample) does not represent the $\delta^{186/184}$W value of the Paleoproterozoic open ocean.

The sample taken at a depth of 51.23 m is characterized by the heaviest W isotopic composition measured in the 12AB core with $\delta^{186/184}$W of +0.536 ±0.018 ‰ (2SE), with the lowest W concentrations of the layer 4 (2.651 µg.g^{-1}) and low Mo/Ti and V/Ti weight ratios. Likely, layer 4 deposited below an OMZ-like environment, with oxic, hypoxic or ferruginous water masses which did not efficiently accumulate diffusive-sourced Mo and V due to non-euxinic porewaters. On the other hand, W is easily removed from solution with adsorption to clay minerals and organic matter, and has the potential to authigenically enrich hypoxic sediment surfaces or deeper depositional environments dominated by ferruginous sediments (Dellwig et al., 2019; Roué et al., 2021). If such W sourced from the open ocean and was quantitatively removed to the sediment, then it might be possible that this heavy $\delta^{186/184}$W value closely mirrors the open ocean seawater signal prevalent at this time of the Paleoproterozoic.

3.5.3 Atmosphere – ocean chemistry changes

The $\delta^{186/184}$W value of the modern open ocean with an isotopic composition of ~0.55 ‰ results from efficient Mn-oxides cycling (Fujiwara et al., 2020; Kurzweil et al., 2021). The adsorption of WO_4^{2-} onto Mn and Fe-oxides is associated with inner-sphere complexing resulting in similar equilibrium isotopic fractionations $\varepsilon^{186/184}W_{dissolved–adsorbed}$ of +0.59 and +0.51 ‰, respectively (Kashiwabara et al., 2017). The offset between the PII range (-0.010 to +0.097 ‰) and the value of sample 51.23 m in layer 4 (+0.536 ‰) represent the equilibrium isotopic fractionation of WO_4^{2-} onto either Mn or Fe-oxides. On the other hand, the isotopic fractionation factor of molybdate onto Fe-oxides is much lower, 1.11 ±0.15 ‰ (Goldberg et al., 2009).

As such, combined Mo and W isotope systematics in marine sediments enable to distinguish between Mn-oxides or Fe-oxides dominated oxide cycling in ancient times. Per example, euxinic marine sediments from the Sengoma Argillite Formation (Bostwana) deposited at 2.15 Ga during the Lomagundi-Jatuli Event are characterized with $\delta^{98/95}$Mo values from 0.00 to +2.21 ‰ (in NIST +0.25), similar to that of the modern ocean, and points towards Mn-oxides control onto the seawater $\delta^{98/95}$Mo value (Asael et al., 2018; Barling et al., 2001). If the heaviest value of the Sengoma Argillite Formation represents the global ocean $\delta^{98/95}$Mo value, then the decrease in $\delta^{98/95}$Mo values observed from 2.15 to 2.0 Ga represent a drop in redox

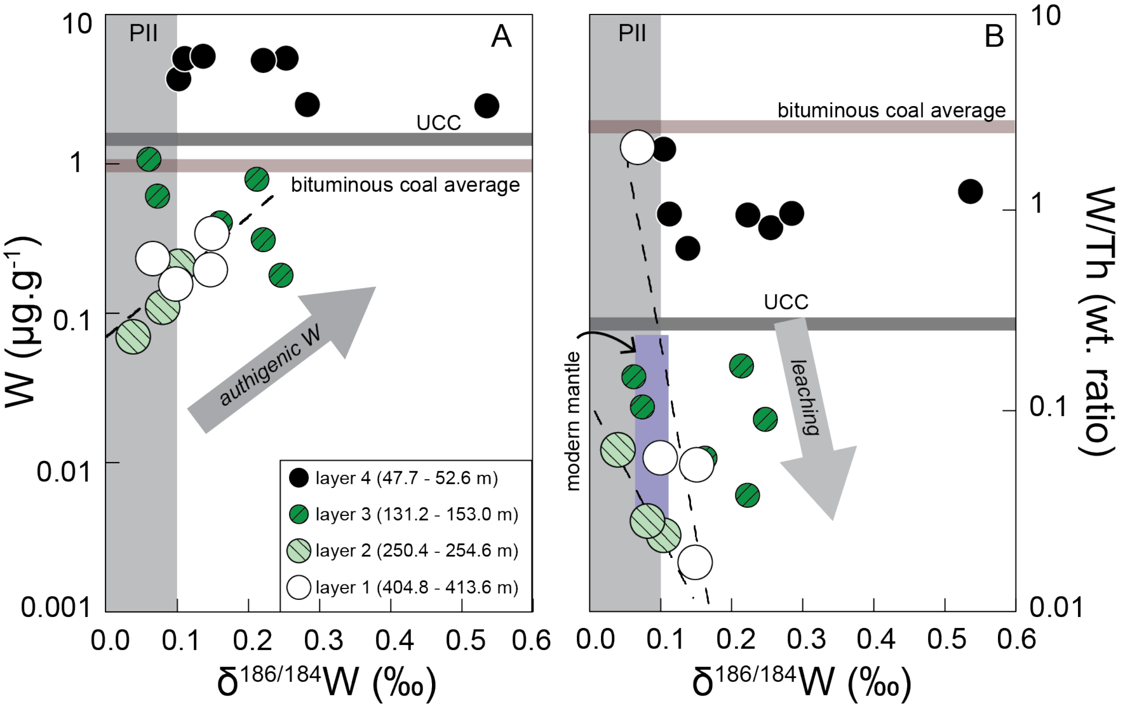

Figure 3.5: $\delta^{186/184}$W values space W concentrations (A) and W/Th weight ratios (B). The bituminous coal average (brown zone) values source from Ketris and Yudovich (2009), the UCC (dark gray) values source from Rudnick and Gao (2014), the PII (Precambrian Igneous Inventory) $\delta^{186/184}$W values originate from Roué et al. (2021), the modern mantle W/Th ratios and $\delta^{186/184}$W values from König et al. (2011) and Kurzweil et al. (2019), respectively. The 2SD of the measurement session for W was of 0.015 ‰ (n=16) on NIST 3163.

potential of the global ocean, not enabling the persistence of Mn-oxides.

However, such heavy $\delta^{98/95}$Mo value has been reported for only one sample, while the rest of the $\delta^{98/95}$Mo data set is typified by values bellow +1.70 ‰. If the global ocean had a Mo isotopic composition of +1.7 ‰ during the deposition of the 2.15 Ga Sengoma Argillite Fm., then the redox state of the ocean remained stable between the LJE and the Shunga Event, with a Fe-oxide control onto the seawater $\delta^{98/95}$Mo value.

3.5.4 Alteration by magmatic intrusions

The W concentrations of the samples from layers 1 and 2 are extremely low (0.004 to 0.246 µg.g^{-1}) compared to the UCC (1.9 µg.g^{-1}; Rudnick and Gao (2014)). An explanation could lie in the dilution of W in the sediment by the injection of W-depleted oil, but would imply the addition of very large volumes of hydrocarbons. Alternatively, W may have been removed from the organic-rich mudstones by hydrothermal fluids originating from the frequent gabbroic intrusions below the Zaonega Fm. (Melezhik et al., 2012b).

Previous studies reported a significant change in the structural order of the organic matter associated with variations in $\delta^{13}C_{org}$ at contact with the thick gabbro intrusion found at depths from 484 to 414 m in core 12AB, where temperatures might have reached up to ~400 °C (Qu et al., 2012; Qu et al., 2020). Tungsten is strongly fluid mobile and the W/Th weight ratio of igneous rocks is typically used as a marker for fluid mobilization during magma generation or during metamorphism, using a modern mantle reference W/Th value of 0.090 to 0.24 (König et al., 2011; Kurzweil et al., 2020; Mazza et al., 2020).

The study of Osvald et al. (2021) mimicked a natural geothermal reservoir and observed the leaching of W from pure W-minerals such as scheelite ($CaWO_4$) and/or ferberite ($FeWO_4$), over the course of 1 to 1.5 h, at temperatures ranging from 200 to 300 °C and pressures of 250 bars under a flow of deionized water. The collected leachates yielded W concentrations from 1 to 182 µg.g^{-1}, with a tendency in higher concentrations in scheelite. These experiments focused on pure-W minerals using fluids with circumneutral pH and likely are not representative of natural hydrothermal alteration of magmatic rocks, but still confirm that W can be mobilized at a simulated depth of 2.5-3 km in an average geothermal field.

In the case of this study, the representation of W/Th ratios combined with $\delta^{186/184}W$ values of the organic-rich mudstones (Figure 3.5) show negative non-linear correlations for the samples of layers 1 and 2 (R^2=0.96 and R^2=0.74, respectively). The apparent loss of W (indicated as decreasing W/Th ratios) is associated with slightly increasing $\delta^{186/184}W$ values for both these layers. In case of the layer 1, the massive 70 m thick gabbro intrusion (484-414 m) heated the overlying soft sediments at their contact and potentially induced the leaching of isotopically light W from the organic-rich sediments by hydrothermal fluids, while insoluble Th remained in the sediment. This hypothesis might explain why the samples further away from the intrusion are less depleted in W. Unfortunately, the change in structural order of the organic matter and associated $\delta^{13}C_{org}$ values were so far not investigated for sediments of the layer 2. The very narrow range in $\delta^{186/184}W$ values and W/Th ratios agree well with the ranges reported for unaltered igneous rocks, and as such cannot be regarded as strong evidence for hydrothermal alteration (König et al., 2011; Kurzweil et al., 2019).

3.6 Summary and conclusion

The 2.22 to 2.06 Ga Lomagundi-Jatuli carbonate carbon isotope excursion is considered recording an atmospheric oxygen overshoot (Bekker and Holland, 2012; Karhu and Holland, 1996), followed by a strong atmospheric deoxygenation towards stable oxygen concentrations of 0.001

to 0.1 PAL for the so-called Boring Billion (Daines et al., 2017; Gilleaudeau et al., 2016; Ossa Ossa et al., 2018a; Planavsky et al., 2014b; Scott et al., 2014). Still, the marine sediments of the Zaonega Fm. postdating the Lomagundi-Jatuli event revealed the highest RSE concentrations and fractionated $\delta^{98/95}$Mo and δ^{238}U values recorded until the Neoproterozoic, and strongly point towards well-oxygenated oceans (Asael et al., 2013; Mänd et al., 2020).

In this study, we show that the high concentrations of RSE and associated variations in $\delta^{98/95}$Mo and $\delta^{186/184}$W values are related to basin-scale processes during the deposition of the Zaonega Fm. We propose that the high Mo, V and W concentrations of layer 4 are related to efficient particle shuttling. The data of this study report one of the heaviest $\delta^{98/95}$Mo value measured for Paleoproterozoic euxinic shales with +1.736 ±0.034 ‰ (2SE), similarly to other studies who reported values of +1.49 ‰ (Mänd et al., 2020), +1.4 ‰ (Canfield et al., 2013) and +1.45 ‰ (Asael et al., 2018), but significantly heavier than the value of +0.67 ‰ from Asael et al. (2013).

We conclude that Fe-oxides were controlling Mo and W cycling in the 2.0 Ga Onega paleobasin, in a similar intensity as the modern Mn-cycling. The decrease in $\delta^{98/95}$Mo values of the core 12AB do not represent changes in the redox state of the global ocean, but rather changes in the delivery mode of RSE to the sediment. The organic-rich shales of this study illustrate the use of combined Mo and W concentrations and stable isotopes as a potentially strong tool for paleoenvironmental reconstitution of ancient marine basins.

Further investigations should focus on combined Mo and W signals in euxinic and non-euxinic marine sediments deposited during the Lomagundi-Jaluti Event in order to decipher the evolution of the redox state of the ocean before the Boring Billion, and whether the Shunga Event was indeed a drop in atmospheric content.

Chapter 4

Stable W isotopes behaviour during anoxic continental weathering: evidence from two paleosols profiles of the 2.77 Ga Mt Roe Basalt

4.1 Introduction

Tungsten (W) is the 74^{th} element of the periodic table, and is classified in the group 6 of elements with molybdenum (Mo) and chromium (Cr). Tungsten is a low level trace element in crustal rocks but is more concentrated in the upper continental crust (UCC) with an average of 1.9 µg.g^{-1} (Rudnick and Gao, 2014) compared to the depleted mantle with 12 ng.g^{-1} (König et al., 2011). Tungsten and thorium (Th) both behave as highly incompatible lithophile elements during mantle melting, giving the primitive mantle and mafic rocks an expected conservative W/Th weight ratio between 0.15 to 0.19 (Arevalo Jr and McDonough, 2008), 0.040 to 0.23 (König et al., 2011), while the UCC has a W/Th weight ratio of 0.181 (Rudnick and Gao, 2014). However, W is selectively more enriched in hydrothermal fluids than Th during metasomatism or subduction, resulting in a large spread of W/Th values exceeding the one of the mantle in metamorphic igneous rocks and arc-lavas (Kurzweil et al., 2020; Mazza et al., 2020). As a result, W/Th weight ratios of igneous rocks is commonly used to track alteration processes (e.g. metasomatism) and fluid influence in magmatic melts (e.g. W secondary enrichments in subduction zones) (Babechuk et al., 2010; König et al., 2011; Kurzweil et al., 2020; Mazza et al., 2020; Tusch et al., 2019).

Tungsten exhibits a fluid-mobile behavior in surface environments and is present in solution in the W^{6+} oxidation state as tungstate (WO_4^{2-}) under a large Eh-pH range (Takeno, 2005). The average dissolved world riverine flux of W is estimated at 0.54 nM, eight times lower that the one of Mo with 4.4 nM (Viers et al., 2009). Pokrovsky and Schott (2002) reported a linear correlation of W and Fe content in the inorganic Fe-colloidal fraction of modern rivers, likely accounting for the W discharge to the oceans dominated by the particulate phase (90 %; Viers et al. (2009)). The dissolved W concentration in the modern ocean is estimated between 53-66 pM (Sohrin et al., 1987) and 49 to 54 pM (Kurzweil et al., 2021). Similarly as Mo, U, V and Cr, dissolved W is particle reactive and efficiently adsorbs onto oxides, clay minerals and organic matter (Kashiwabara et al., 2017; Kashiwabara et al., 2013; Kashiwabara et al., 2010; Sen Tuna and Braida, 2014; Tuna et al., 2012).

Recently, Kurzweil et al. (2021) and Fujiwara et al. (2020) reported the $\delta^{186/184}$W value of the open ocean to be homogenous with a value from +0.543 ± 0.046 ‰ to +0.55 ± 0.12 ‰, respectively, which is significantly larger than the estimated bedrock $\delta^{186/184}$W range (-0.010 to +0.110 ‰). However, the riverine-influenced surface of the South Chinese Sea – with a $\delta^{186/184}$W value of +0.445 ‰ – is characterized by a lighter W isotopic composition that of the open ocean (Kurzweil et al., 2021). This relatively low $\delta^{186/184}$W value likely reflect mixing between isotopically heavy seawater with lighter riverine W, as observed for Mo (Archer and Vance, 2008), but can also be related to release of adsorbed W onto Mn-Fe oxides and/or atmospheric W input (Kurzweil et al., 2021).

The recent study of Roué et al. (2021) reported authigenic W enrichments and $\delta^{186/184}$W values above crustal background in 3.47 to 2.5 Ga marine shales. They concluded that such signals require sources for dissolved W to the ocean as early as 3.47 Ga, most likely from weathering of continental surfaces with contributions from hydrothermal inputs. However, modern and past processes of W removal from bedrock, continental W transfer (groundwater versus riverine fluxes) and their associated $\delta^{186/184}$W values have yet to be determined.

Numerous studies focused on element mobility and associated stable isotopic fractionation during weathering, using modern and ancient lithified weathering profiles (Babechuk et al., 2017; Babechuk et al., 2019; Baronas et al., 2020; Greaney et al., 2021; Rudnick et al., 2004; Wang et al., 2018; Wille et al., 2018). Generally, the main processes involved in the isotopic fractionation are (1) mineral control on isotopic compositions, and/or (2) preferential release of light/heavy isotopes and/or (3) interactions of dissolved elements with surrounding oxides, organic matter and clay minerals. During the entire Archean eon, paleosols do not generally preserve evidence for redox-sensitive element mobility that is induced by pore water oxygen. Tungsten, however, may be solubilized at lower Eh than most other redox-sensitive elements

(Mo, U, Cr, Fe, S) (Takeno, 2005). As such, there is basis to further evaluate W behavior in other paleosols, which preserve the end-product of a potential W source to the oceans on the ancient Earth.

Babechuk et al. (2015) reported intense loss of W during the incipient to intermediate stages in the oxic weathering of the 65-67 Ma Deccan Trap basalt in India. This confirms that chemical weathering solubilizes W, and is consistent with the soluble budget documented in rivers and groundwaters (Johannesson et al., 2013; Johannesson et al., 2000; Pokrovsky and Schott, 2002; Viers et al., 2009). However, contradictory signals for W mobility were reported in the Precambrian paleosol record. First Murakami et al. (2016) postulated that there is a temporal record of increasing W loss in oxic (post-GOE) paleosols relative to anoxic (pre-GOE) paleosols based on data from the ca. 2.2 Ga Gaborone and ca. 2.45 Ga Cooper Lake paleosols, respectively. However, a detailed analysis of the Cooper Lake paleosol by Babechuk et al. (2019) revealed that there was no firm information regarding the chemical weathering behavior of W because W concentrations were consistent with re-enrichment during later metasomatic alteration.

Here, the behavior of W under weathering should be investigated in pre-GOE paleosol profiles altered under unequivocal anoxic conditions and with significant W concentrations. The 2.77 Ga Mt Roe paleosol profiles are one of the oldest occurrences of ancient weathered surfaces and are very important source of information regarding anoxic weathering conditions of the Neoarchean (Macfarlane et al., 1994a; MacFarlane et al., 1994b; Teitler et al., 2015; Yang et al., 2002). In this study we investigate W concentrations and $\delta^{186/184}$W values of samples from two paleosol profiles of the ABDP-6 drill core. We further explore the interrelation of W with other elements in order to understand the processes of W removal from igneous rocks and its' partial retention in clay minerals. We highlight the implications of dissolved W inputs under anoxic weathering and how it influenced the early W cycling in oceans.

4.2 Geological context and material

The 2.77 Ga Mt. Roe Basalt sequence forms the base of the Fortescue Group, Pilbara craton, and has been interpreted as continental flood basalts that covered up to 200,000 km^2 (Arndt et al., 1991; Blake, 1993). It consists of a thick sequence of ultramafic to felsic volcanic rocks with minor sediments. The chemical composition of the basalts shows significant evidence of crustal contamination from an Eo- to Paleoarchean crust, with evolved Nd isotopes, enrichments in incompatible elements (Th, LREE) and the presence of 3,308 ±138 Ma old zircons xenocrysts (Mole et al., 2018; Nelson et al., 1992).

The Mt. Roe Basalt lays at the base of the Fortescue Group and is mostly exposed throughout the northern and southwestern part of the Pilbara Craton. The deposition of the Mt. Roe Basalt initiated between 2763 ±13 Ma and 2775 ±10 Ma (zircon U-Pb; Arndt et al. (1991)), and is capped by the 2768 ±16 Ma Spinaway Porphyry (Pidgeon, 1984) and 2756 ±8 Ma Hardey Fm (Arndt et al., 1991). The total thickness of the Mt. Roe Basalt reaches up to 2.5 km (Blake, 1993). The most dominant facies of the Mt. Roe Basalt consists of subaerial basaltic lavas, with minor basaltic andesite flows, pillow lavas, tuff, sedimentary successions, hyaloclastite and epiclastic rocks (Blake, 1993; Thorne and Trendall, 2001). The subaerial basaltic lavas can be separated in two categories depending on their thickness, dominated by massive (2-78 m) amygdaloidal basalts and minor thin (0.1-3.0 m) Pahoehoe flows (Blake, 1993). The emplacement of these basaltic flows was punctuated by quiescent time intervals which enabled the surfaces of the fresh basalts to be altered under an anoxic atmosphere, as shown by the presence of multiple inter-basaltic paleosol profiles throughout the Mt. Roe Basalt Formation.

The Mt. Roe #1 and #2 paleosol profiles are well documented weathered profiles reported throughout the Pilbara Craton (Macfarlane et al., 1994a; MacFarlane et al., 1994b; Macfarlane and Holland, 1991). Both paleosols developed on amygdaloidal subaerial flows but differ from each other based in their directly overlying units, which are lacustrine sedimentary rocks for the Mt. Roe #1 and basalt flows for the Mt. Roe #2. The base of the paleosols profiles consists in approximatively 6 meters of a thick chlorite section (Fe^{2+} rich) which transition to 10 meters of an upper sericite-rich section (Macfarlane and Holland, 1991). The original basaltic texture is sometimes preserved with some plagioclase and clinopyroxene, but most of the primary minerals have been replaced by pseudomorphs like sericite, kaolinite, chlorite, rutile and phosphate minerals (Macfarlane et al., 1994a). The weathering of ferromagnesian minerals produced chlorite and zeolites clay minerals, while further weathering of these second end products produced sericite. The zonation of the paleosols profiles into sericite and chlorite sections are interpreted as a result of combined chemical weathering intensity and compaction of the upper part during diagenesis (Macfarlane et al., 1994a).

The samples measured in this study originate from the ABDP-6 drillcore (Archean Biosphere Drilling Project) with further details outlined in Babechuk et al. (in prep). Two separate paleosols profiles of the Mt Roe Basalt occur at respective depths of 123 to 146 m (shallow profile) and 277 to 290 m (deep profile). Both paleosol profiles are similarly organized and developed on superposed massive amygdaloid basaltic flows, with the exception of a thin sedimentary layer deposited between two basalt flows in the shallow profile at depth of 131 m. The two paleosol profiles are composed of a basal chlorite section with thicknesses of approximately 10 m for the shallow profile and 13 m for the deep profile. The chlorite sections are directly overlaid by the sericite sections with thicknesses of 7 m for the shallow profile and 5 m for the deep profile. Then, the shallow profile is directly covered by 3 m of a mixture of sediment and volcanic rocks, 1 m of sandstone and 30 m of shales, while the deep profile is covered by less than 0.5 m of sandstone and 25 m of shale with minor siltstone and sandstone.

The 21 core samples used in this study cover both profiles, starting from the parent basalt into the weathered basalt section (chlorite and sericite sections). A few marine shale samples overlying the weathered units were previously measured for W isotopes and are reported by Roué et al. (2021).

4.3 Methods

The sample powders were prepared without tungsten carbide. Major and trace elements data are reported by Babechuk et al. (in prep) using the same sample powder aliquots used for W isotopes determination in this study. Major elements were measured either on XRF, or with an iCAP-Qc® quadrupole ICP-MS (after table top digestion).

All materials (PFA beakers, centrifuge tubes) were carefully cleaned with HCl, HNO_3 and HF before use. All acids (HCl, HNO_3, HF) were distilled once with Savillex DST-4000 sub-boiling Teflon stills.

Between 80 and 130 mg (60 to 150 ng total W) of sample powder was mixed with a ^{180}W-^{183}W double-spike to reach a 3:2 sample to spike W ratio. The spiked samples were then digested in closed PFA beakers with 2 ml of concentrated HF-HNO_3 (3:1) on a hotplate at 85 °C for 48h. After drying, the samples were refluxed with concentrated 4 ml 9 M HCl for 48 h at 130 °C to dissolve potential fluorides. Finally, the samples were taken up in 10 ml 1 M HCl.

The method for W purification is detailed in Tusch et al. (2019) and Kurzweil et al. (2018). Briefly, the samples dissolved in 10 ml of 1 M HCl + 1 %v H_2O_2 were centrifuged for 10 minutes at 5,000 rpm prior to loading onto the first separation columns containing 10 ml of Biorad AG 50W-X8 (200-400 mesh). The samples were directly collected and further rinsed with an extra 15 ml of 1 M HCl. These 25 ml sample aliquots were then directly loaded onto the second column containing 2 ml of Biorad AG1-x8 (100-200 mesh). Residual matrix elements were further rinsed off the resin with 10 ml 1 M HCl + 1 %v H_2O_2 and 5 ml 2 M HF, before sample W was finally collected with 15 mL 3M HNO_3-0.2 M HF. The samples were dried down and treated twice with 100 µL of concentrated $HNO_3 + H_2O_2$ to remove potential resin residues. The samples were fluxed with 2 ml 6 M HCl and put on a hotplate at 100 °C for a few hours. The samples were finally loaded onto the third column containing 0.7 ml TEVA resin B and collected with 4 ml 6 M and 6 ml 4 M HCl.

The purified samples were once again taken up in concentrated HNO_3-H_2O_2 twice to destroy potential resin residues. Prior to measurements, the samples were taken up with few µL of concentrated HF and HNO_3 in order to efficiently mobilize W from the dry pellet. Adequate amounts of H_2O were then added to the samples to reach a final concentration of 0.56 M HNO_3– 0.24 M HF in a volume of 1 mL, and centrifuged.

Stable W isotopic compositions of the samples were measured on a ThermoFisher Scientific NeptunePlus MC-ICP-MS hosted at the Isotope Geochemistry facilities of the University of Tübingen. Because of yield variability, pre-concentration measurements were carried on aliquots (50 µL) of the sample solution with a dilution factor of 10. The W concentrations of the mother solutions were then adjusted to match the one of the standards to precisely 30 ng.g^{-1} of total (sample+spike) tungsten.

Stable W isotopic data are reported normalized to NIST 3163 and presented in the delta notation according to the equation 4.1:

$$\delta^{186/184}W = [(^{186}W/^{184}W)_{sample})/(^{186}W/^{184}W)_{NIST\ 3163}) - 1] * 1000 \tag{4.1}$$

The average $\delta^{186/184}$W values and 2SD reproducibilities of the NIST 3163 and our in-house Alfa Aesar solution standard during the course of this study were of 0.000 ±0.008 ‰ (2SD, n=10) and +0.051 ±0.014 ‰ (2SD, n=6), respectively. Single measurements of OU-6 (slate powder, split 8/31) and BCR-2 (3223) rock reference materials yielded $\delta^{186/184}$W values of +0.101 ±0.016 ‰ and +0.049 ±0.013 ‰ (both in-run 2 SE uncertainties), in good agreement with the values reported by Krabbe et al. (2017), Kurzweil et al. (2019) and Roue et al. (2021). The total procedure W blank was 124 pg and can be considered negligible to the amount of 60 to 180 ng of processed sample W.

Table 4.1: Shallow profile major elements concentrations and alteration indexes

		parent basalt		chlorite zone				sericite zone				
sample depht (m)		123.77	124.65	125.88	129.96	130.58	132.37	133.68	137.57	138.54	143.94	145.68
Measurement method		XRF	XRF	XRF	XRF	iCAP	XRF	XRF	XRF	XRF	XRF	XRF
SiO_2	wt. %	43.22	48.56	61.64	47.64		43.22	59.84	55.28	55.53	52.26	50.09
TiO_2	”	2.76	2.49	1.68	2.41	1.33	1.44	1.20	0.98	1.13	1.30	1.38
Al_2O_3	”	35.93	31.37	21.74	31.26	15.32	17.78	13.40	11.83	13.95	14.90	15.90
Fe_2O_3(T)	”	0.47	0.48	1.79	2.76	2.87	16.42	9.65	8.72	9.73	10.90	10.83
MnO	”	0.09	0.08	0.08	0.10	0.02	0.25	0.20	0.31	0.22	0.21	0.17
MgO	”	0.37	0.39	0.49	1.25	0.90	9.01	6.24	4.96	5.49	5.36	5.84
CaO	”	1.45	1.31	1.85	1.37	1.55	2.51	2.06	7.51	4.27	4.06	4.50
Na_2O	”	0.59	0.62	0.37	0.42	0.13	0.07	0.09	0.91	1.62	5.01	4.86
K_2O	”	9.50	8.49	5.82	8.17	3.51	1.12	1.46	0.97	1.05	0.13	0.12
P_2O5	”	1.08	1.00	1.37	1.00	0.98	1.15	0.97	0.79	0.91	1.01	1.07
LOI	”	4.90	4.70	4.17	3.67		6.03	4.32	7.73	5.23	4.03	4.40
Sum (%)		100.58	100.45	100.98	100.16		99.56	99.69	100.51	99.68	99.41	99.85
SiO_2/TiO_2	wt. ratio	15.66	19.51	36.76	19.73		30.1	49.7	56.29	49.31	40.36	36.38
Al_2O_3/TiO_2	”	13.02	12.6	12.97	12.95	11.55	12.38	11.13	12.04	12.39	11.51	11.55
Fe_2O_3(T)/TiO_2	”	0.17	0.19	1.07	1.14	2.16	11.44	8.01	8.88	8.64	8.42	7.86
MnO/TiO_2	”	0.03	0.03	0.05	0.04	0.01	0.17	0.17	0.31	0.19	0.16	0.12
MgO/TiO_2	”	0.13	0.16	0.29	0.52	0.68	6.28	5.18	5.05	4.87	4.14	4.24
CaO/TiO_2	”	0.53	0.52	1.1	0.57	1.17	1.75	1.71	7.65	3.8	3.13	3.27
Na_2O/TiO_2	”	0.21	0.25	0.22	0.17	0.1	0.05	0.07	0.93	1.44	3.87	3.53
K_2O/TiO_2	”	3.44	3.41	3.47	3.38	2.64	0.78	1.21	0.99	0.93	0.1	0.09
P_2O_5/TiO_2	”	0.39	0.4	0.82	0.41	0.74	0.8	0.81	0.8	0.8	0.78	0.77
Al/Si	mol ratio	0.98	0.76	0.42	0.77		0.48	0.26	0.25	0.3	0.34	0.37
CIA		72.13	71.37	67.92	72.25	69.20	75.15	71.01	42.19	54.66	48.61	49.37
PIA		87.69	86.71	79.56	87.62	79.21	78.02	75.22	41.56	55.12	48.60	49.37
MIA[R]		70.41	69.34	63.24	64.86	58.37	31.22	32.82	25.63	30.58	29.12	29.50

4.4 Results

It has thoroughly been documented in previous studies that the Mt. McRoe paleosols have been affected by multiple alteration events prior to and after burial (Macfarlane et al., 1994a; Macfarlane and Holland, 1991; Yang et al., 2002). Alteration often results in mass loss and increased volume, while burial may compact altered rocks and soils (Brimhall and Dietrich, 1987). All of these processes can artificially increase/decrease element concentrations and it is common practice to use a mass balance strategy that assumes an element to be fully immobile. Here, Ti is selected. As evaluated further by Babechuk et al. (in prep), Ti was immobile along with several other elements (Al, Nb, Ta, Zr, Hf) across all of the alteration events. Here, the TiO_2 content from the major elements determination results is used to normalize major elements and elemental Ti (ICPMS) concentrations to normalize trace elements. The space of TiO_2 (major element data) and Ti (trace element data) of the paleosol samples determined for W isotopic compositions revealed a linear positive correlation with a R^2 of 0.98 (n=21) (not presented).

Table 4.2: Deep profile major elements concentrations and alteration indexes

		parent basalt		chlorite zone				sericite zone			
sample depht (m)		277.37	278.56	279.04	281.09	282.13	283.48	286.42	290.02	297.00	299.70
Measurement method		iCAP	iCAP	XRF	iCAP	iCAP	XRF	XRF	iCAP	XRF	XRF
SiO_2	wt. %			60.29			51.40	47.86		45.57	49.58
TiO_2	”	2.32	2.02	2.17	3.26	1.82	1.39	2.16	1.51	1.62	1.73
Al_2O_3	”	24.35	18.00	22.79	33.01	19.18	16.52	19.88	14.67	15.91	17.55
Fe_2O_3(T)	”	1.13	1.37	1.18	0.39	14.68	19.16	11.15	7.16	12.00	10.04
MnO	”	0.00	0.00	0.10	0.00	0.06	0.17	0.20	0.13	0.31	0.19
MgO	”	0.12	0.18	0.36	0.22	2.13	4.20	4.92	3.75	5.11	4.72
CaO	”	0.84	0.80	1.26	0.35	0.86	0.63	2.66	2.48	7.41	4.59
Na_2O	”	0.14	0.09	0.35	0.19	0.08	0.18	0.13	2.35	2.08	4.33
K_2O	”	6.07	4.60	6.59	7.64	3.70	1.54	3.89	1.68	1.30	0.89
P_2O5	”	0.66	0.69	0.90	0.29	0.62	0.44	0.81	0.52	0.62	0.66
LOI	”			3.52			4.65	5.05		7.37	4.81
Sum (%)				100.04			100.12	99.78		100.25	100.16
SiO_2/TiO_2	wt. ratio			27.81			37.06	22.14		28.22	28.69
Al_2O_3/TiO_2	”	10.50	8.92	10.51	10.14	10.51	11.91	9.19	9.71	9.85	10.15
Fe_2O_3(T)/TiO_2	”	0.49	0.68	0.54	0.12	8.05	13.82	5.16	4.74	7.43	5.81
MnO/TiO_2	”	0.00	0.00	0.05	0.00	0.03	0.12	0.09	0.08	0.19	0.11
MgO/TiO_2	”	0.05	0.09	0.17	0.07	1.17	3.03	2.27	2.48	3.17	2.73
CaO/TiO_2	”	0.36	0.40	0.58	0.11	0.47	0.45	1.23	1.64	4.59	2.65
Na_2O/TiO_2	”	0.06	0.05	0.16	0.06	0.04	0.13	0.06	1.56	1.29	2.50
K_2O/TiO_2	”	2.62	2.28	3.04	2.35	2.03	1.11	1.80	1.11	0.80	0.52
P_2O_5/TiO_2	”	0.28	0.34	0.41	0.09	0.34	0.32	0.37	0.34	0.38	0.38
Al/Si	mol ratio			0.45			0.38	0.49		0.41	0.42
CIA		74.53	73.20	69.50	78.18	77.11	84.15	68.22	58.97	46.52	51.66
PIA		91.02	88.99	84.52	96.33	89.97	91.12	75.63	60.52	46.20	51.76
MIA[R]		72.25	69.48	66.15	76.70	48.37	38.87	40.81	37.67	29.03	33.54

The major and trace elements of the respective profiles are listed in tables 4.1, 4.2, 4.3 and 4.4. The W stable isotopic compositions of the paleosol samples are listed in table 4.5. The major and trace elements data of the two paleosol profiles are similarly distributed, and as such are presented as one composite weathering profile.

4.4.1 Major elements

Iron is one of the element of interest in paleosols studies, as the mobility of Fe depends on its redox state (soluble Fe^{2+} versus insoluble Fe^{3+}), and its depletion from ancient paleosols helped tracking the oxygenation of the atmosphere (Prasad and Roscoe, 1996; Rye and Holland, 1998). The Fe_2O_3/TiO_2 weight ratios of the profiles range from 0.12 to 13.82. The parent basalts have a homogenous Fe_2O_3/TiO_2 ratio with an average of 7.38 ±2.24 (2SD, n=4). The chlorite section samples show a wider scatter of Fe_2O_3/TiO_2 ratios from 4.74 up to 13.82 (Figure 4.1). The Fe_2O_3/TiO_2 ratios of the sericite section range from 2.16 to 0.12, with a trend in decreasing ratios upward.

The MgO/TiO$_2$ weight ratios of the paleosol samples follows similar trends as the ones of Fe$_2$O$_3$/TiO$_2$, with values ranging from 2.73 to 4.24 in the parent basalt, 1.17 to 6.28 in the chlorite sections and 0.68 to 0.05 in the sericite sections.

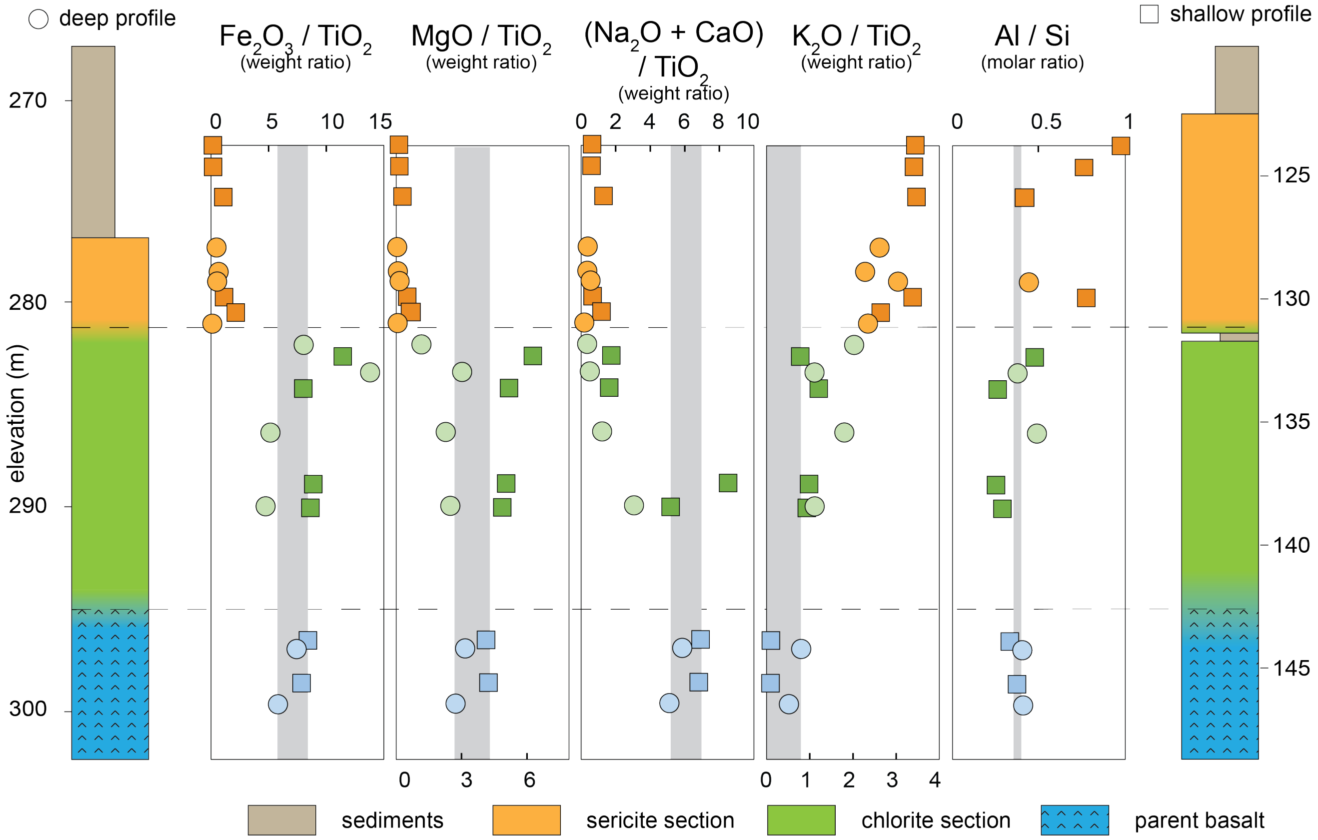

Figure 4.1: stratigraphic columns and major elements distribution (normalized to TiO$_2$ concentrations) of the two weathered profiles from the ABDP-6 core. The unweathered, chlorite and sericite units of the two paleosols profiles are correlated with the dotted lines. Note the different scales for the deep profile (left) and shallow profile (right). The shadow areas on the plots represent the average ±2SD of the various ratios of the combined unweathered basalts.

The Na$_2$O/TiO$_2$ and CaO/TiO$_2$ weight ratios are good indicators for plagioclase alteration. Their ratios range from 0.04 to 3.87 and 0.11 to 7.65, respectively. They display the same patterns with decreasing ratios upward, except for one high CaO/TiO$_2$ ratio of 7.65 in the chlorite section of the shallow profile. They are represented as combined (Na$_2$O + CaO) normalized to TiO$_2$ in the figures and discussion.

The K$_2$O/TiO$_2$ weight ratios are indicators for secondary K enrichment by metasomatism (Macfarlane and Holland, 1991). The K$_2$O/TiO$_2$ weight ratios of the paleosol profiles of this study range from 0.09 to 3.47. The parent basalt of the deep profile has lower K$_2$O/TiO$_2$ content (0.09 to 0.010) than the shallow profile (0.52 to 0.80). The K$_2$O/TiO$_2$ ratios linearly

Table 4.3: Trace elements concentrations of the shallow paleosol profile

		parent basalt		chlorite zone				sericite zone				
sample depth (m)		123.77	124.65	125.88	129.96	130.58	132.37	133.68	137.57	138.54	143.94	145.68
Li	µg/g	1.63	1.17	2.24	10.55	7.60	84.66	57.00	41.44	45.15	21.21	23.53
Be	”	2.82	3.04	2.28	3.45	2.30	1.31	1.33	1.67	1.61	1.51	1.64
Sc	”	56.63	57.21	34.28	47.28	26.77	27.66	23.35	19.73	22.49	26.79	27.20
Ti	”	16,075	15,662	9,749	13,896	7,413	8,485	7,009	5,754	6,611	7,247	7,960
V	”	502.96	488.31	296.08	423.30	227.99	323.26	200.38	166.88	193.64	214.87	221.84
Cr	”	722.55	702.87	487.19	633.28	304.39	364.56	300.79	226.37	290.47	295.27	369.56
Co	”	6.27	5.07	79.23	20.69	50.06	46.69	28.62	28.53	28.58	31.73	30.54
Ni	”	101.78	76.96	194.27	98.00	185.98	149.83	86.54	84.34	88.91	92.87	91.14
Cu	”	38.73	24.66	45.10	20.74	54.25	21.22	20.29	22.43	8.88	28.25	21.57
Zn	”	204.05	463.74	57.09	470.67	362.23	138.60	86.09	79.10	85.39	92.82	105.01
Ga	”	38.45	41.26	26.16	36.21	16.90	22.37	15.46	14.83	17.19	18.46	15.66
As	”	5.58	4.18	24.58	8.15	21.18	3.18	2.45	3.29	2.82	3.22	2.88
Rb	”	279.50	261.27	159.23	229.66	120.67	38.15	51.98	35.54	39.68	3.89	3.77
Sr	”	278.12	301.57	217.44	193.04	136.75	78.68	49.07	284.65	364.98	1,170	1,234
Y	”	79.86	70.52	35.70	66.45	32.70	32.43	29.19	25.76	26.59	31.75	29.92
Zr	”	482.64	470.85	290.64	414.45	233.36	251.27	204.81	165.96	190.22	210.94	226.41
Nb	”	26.30	25.33	15.62	22.05	12.68	13.80	11.23	9.11	10.46	11.46	12.64
Mo	”	0.88	1.28	2.11	1.66	1.79	1.98	0.53	1.04	0.62	0.44	0.61
Cd	”	0.19	0.33	0.24	0.43	0.36	0.11	0.08	0.10	0.10	0.13	0.13
Sn	”	2.91	2.94	1.63	1.95	1.68	0.64	1.66	1.02	0.81	1.12	0.80
Sb	”	0.03	0.03	0.10	0.05	0.48	0.06	0.08	0.33	0.04	0.19	0.12
Cs	”	4.65	4.37	3.34	4.06	3.94	0.98	1.31	0.81	0.90	0.25	0.25
Ba	”	3,594	3,152	2,005	3,465	1,617	490.07	681.23	516.08	520.88	312.28	481.24
La	”	300.85	281.35	237.90	231.10	96.96	193.84	161.35	148.88	157.55	232.67	188.47
Ce	”	615.68	575.15	471.56	454.57	206.14	380.07	321.75	295.85	315.29	430.71	382.27
Pr	”	71.36	64.84	53.00	51.20	24.49	42.04	36.51	33.63	35.29	45.60	42.84
Nd	”	255.74	223.67	190.76	185.93	91.88	150.25	129.33	118.99	123.43	155.96	148.82
Sm	”	34.11	28.25	26.06	27.35	14.39	19.33	17.46	15.76	15.84	19.74	19.10
Eu	”	8.31	6.28	3.53	5.49	3.29	7.34	5.62	4.84	2.32	5.01	4.34
Gd	”	24.76	21.16	14.35	19.78	10.09	11.35	10.98	9.31	9.47	11.94	11.20
Tb	”	3.11	2.74	1.58	2.34	1.24	1.28	1.29	1.09	1.12	1.39	1.32
Dy	”	16.03	14.16	7.58	11.88	6.49	6.32	6.22	5.28	5.52	6.71	6.29
Y	”	79.86	70.52	35.70	66.45	32.70	32.43	29.19	25.76	26.59	31.75	29.92
Ho	”	3.02	2.68	1.41	2.35	1.25	1.23	1.11	0.98	1.05	1.22	1.18
Er	”	7.67	6.67	3.73	6.25	3.23	3.33	2.81	2.52	2.73	3.10	3.08
Tm	”	1.06	0.92	0.55	0.88	0.45	0.49	0.39	0.36	0.39	0.45	0.44
Yb	”	6.32	5.53	3.46	5.30	2.73	3.13	2.44	2.23	2.46	2.78	2.81
Lu	”	0.90	0.78	0.50	0.76	0.38	0.47	0.35	0.33	0.36	0.41	0.41
Hf	”	10.78	10.46	6.48	9.22	5.11	5.54	4.56	3.73	4.27	4.73	5.05
Ta	”	1.22	1.18	0.74	1.03	0.56	0.63	0.51	0.42	0.48	0.53	0.57
W	”	1.59	0.98	1.06	0.71	1.04	1.77	1.05	0.96	1.21	1.52	1.77
Tl	ng/g	2.14	2.07	1.32	1.78	1.11	0.32	0.38	0.24	0.27	0.03	0.02
Pb	µg/g	11.75	10.32	29.95	4.61	38.28	11.82	36.44	36.76	17.21	62.99	28.08
Th	”	31.75	32.06	19.52	27.86	14.70	16.63	13.51	11.07	12.77	14.19	15.60
U	”	4.87	4.78	2.90	4.11	2.37	2.44	2.07	1.67	1.92	2.24	2.32
τ_{Ti}^{W}		-0.54	-0.71	-0.50	-0.76	-0.35	-0.03	-0.31	-0.23	-0.15	-0.03	0.03

Table 4.4: Trace elements concentrations of the deep paleosol profile

		parent basalt		chlorite zone				sericite zone			
sample depth (m)		277.37	278.56	279.04	281.09	282.13	283.48	286.42	290.02	297.00	299.70
Li	µg/g	0.66	0.55	0.73	0.68	15.22	26.59	25.47	18.65	25.32	24.61
Be	”	2.09	2.20	3.01	3.44	2.45	1.83	4.15	2.91	2.21	2.61
Sc	”	31.87	22.08	29.03	43.06	25.49	15.00	26.72	19.32	20.44	19.60
Ti	”	13,344	10,451	12,966	19,152	11,604	7,955	12,550	9,123	9,446	10,104
V	”	249.72	187.84	245.02	354.34	216.48	154.90	227.54	156.03	175.30	177.45
Cr	”	266.26	201.46	261.63	382.40	241.35	157.70	257.94	173.46	183.40	201.31
Co	”	123.16	43.80	28.25	1.15	45.46	44.93	33.53	20.70	31.66	30.51
Ni	”	297.00	153.21	117.48	4.16	124.17	129.28	83.50	53.76	65.47	70.81
Cu	”	126.62	18.99	24.65	2.17	27.29	23.01	29.76	23.59	35.74	26.72
Zn	”	327.47	155.98	209.64	47.46	134.82	251.79	139.35	111.19	124.66	101.86
Ga	”	30.36	23.33	30.76	43.95	29.34	21.64	27.57	15.43	22.94	18.27
As	”	38.37	0.68	2.20	2.21	0.56	0.98	2.05	1.27	7.25	6.17
Rb	”	191.10	140.13	185.59	301.00	128.44	47.37	138.16	63.40	49.33	34.46
Sr	”	69.95	48.17	62.46	78.31	47.91	35.33	66.25	409.16	396.94	785.34
Y	”	117.76	47.23	65.23	94.20	60.41	35.71	65.15	41.48	44.06	47.84
Zr	”	635.70	491.72	624.61	928.33	557.70	387.07	598.57	414.73	446.63	474.36
Nb	”	26.66	21.26	26.31	39.48	24.12	16.49	25.60	18.22	19.17	20.57
Mo	”	3.32	1.86	3.34	5.54	2.05	2.14	6.45	0.58	0.65	0.20
Cd	”	0.40	0.23	0.34	0.33	0.24	0.26	0.30	0.25	0.21	0.22
Sn	”	3.39	2.43	3.08	5.85	1.38	0.70	2.80	2.26	2.06	1.28
Sb	”	0.33	0.09	0.11	0.06	0.08	0.09	0.19	0.06	0.14	0.01
Cs	”	3.05	3.90	5.24	3.61	2.15	1.66	4.02	1.62	1.59	1.07
Ba	”	1,517	1,270	1,585	2,471	981.59	474.74	1,987	951.19	742.76	521.65
La	”	136.92	55.46	86.13	329.54	51.11	31.87	58.25	84.85	75.72	77.01
Ce	”	298.10	121.95	184.97	621.10	114.53	65.24	150.61	176.97	169.99	158.66
Pr	”	34.67	14.71	22.00	68.74	14.04	8.26	21.59	20.06	20.55	18.92
Nd	”	128.28	57.22	84.19	245.32	54.72	33.58	91.16	73.55	78.45	72.16
Sm	”	22.09	11.00	16.70	36.91	10.60	6.39	17.62	12.34	14.06	12.82
Eu	”	5.26	1.63	2.43	3.86	1.22	1.19	7.40	3.54	2.82	2.75
Gd	”	22.11	9.73	14.36	24.16	11.07	6.07	14.62	9.99	11.31	10.46
Tb	”	3.50	1.46	2.09	3.11	1.80	0.91	2.07	1.42	1.56	1.54
Dy	”	20.97	8.58	12.06	17.44	11.07	5.78	11.85	8.04	8.67	8.93
Y	”	117.76	47.23	65.23	94.20	60.41	35.71	65.15	41.48	44.06	47.84
Ho	”	4.29	1.77	2.47	3.60	2.29	1.33	2.46	1.62	1.74	1.84
Er	”	11.80	4.88	6.70	9.79	6.13	4.00	6.80	4.42	4.70	5.07
Tm	”	1.74	0.71	0.97	1.39	0.88	0.62	1.01	0.66	0.70	0.75
Yb	”	11.05	4.46	6.04	8.60	5.38	4.05	6.36	4.10	4.40	4.67
Lu	”	1.61	0.65	0.88	1.25	0.79	0.62	0.94	0.60	0.64	0.69
Hf	”	14.86	11.49	14.39	21.53	12.81	8.91	13.92	9.64	10.43	11.00
Ta	”	1.40	1.09	1.34	2.02	1.19	0.83	1.30	0.93	0.98	1.05
W	”	0.90	1.38	1.17	1.21	1.49	0.87	1.79	1.46	1.52	2.29
Tl	ng/g	1.38	0.99	1.34	2.04	0.92	0.36	0.93	0.41	0.32	0.23
Pb	µg/g	36.55	10.14	19.20	16.97	14.47	14.80	24.14	19.80	16.17	22.42
Th	”	14.47	11.04	14.03	21.38	12.41	8.82	13.28	9.35	9.98	10.59
U	”	2.42	1.83	2.28	3.43	2.03	1.43	2.21	1.54	1.65	1.72
τ_{Ti}^{W}		-0.65	-0.32	-0.54	-0.67	-0.34	-0.43	-0.26	-0.17	-0.17	0.17

increase upwards in the stratigraphy of the two paleosol profiles, starting from the base of the chlorite to the top of the sericite section.

Most of the SiO_2 content of the two paleosol profiles was not measured due to the specificities of the major element data acquisition (glass bead for XRF measurements versus silicate digestion method for ICPMS measurements). The Al_2O_3/SiO_2 weight ratios available indicate a homogeneous value of 0.33 ±0.06 for both parent basalts (2SD, n=4). The chlorite sections Al_2O_3/SiO_2 values are similar to the underlying parent basalt body, with values ranging from 0.21 to 0.41. The Al_2O_3/SiO_2 values steadily increase from 0.35 from 0.35 in the lowermost sections of the profiles towards 0.83 in the sericite sections.

Many indexes were developed in order to monitor the alteration of minerals in igneous rocks. All of the alteration indexes presented here are calculated with molecular abundances. The silicate-bound Ca (CaO*) cannot be calculated from the bulk CaO abundance due to missing total inorganic C content data. As such, all indexes of alteration are uncorrected from the carbonate-bound Ca data.

The most commonly used index of alteration is the CIA (chemical index of alteration, equation 4.2, Nesbitt and Young (1982)) which relies on Al_2O_3, NaO, CaO and K_2O molecular contents to efficiently track plagioclase alteration. However, the CIA does not correct for secondary addition of K via metasomatism and should thus only be used on well characterized samples. The PIA (plagioclase index of alteration, equation 4.3) is a better fit to monitor primary weathering as it does circumvent influences of metasomatic K_2O content on underestimating extent of initial feldspar alteration (Fedo et al., 1995). Babechuk et al. (2014) introduced the MIA (mafic index of alteration) as a better index of alteration for mafic weathered profiles, separated into oxic (MIA (O)) or reducing (MIA (R), equation 4.4) alteration indexes, based on the redox-dependent behaviour of Fe. Both consider the molecular contents in Al_2O_3, Fe_2O_3, MgO, CaO* and Na_2O of mafic rocks to calculate the % loss of elements, which does not include K_2O content (MIA (R) -K). The MIA(R)-K fits in the case of this study as it does account for removal of Fe^{2+} under anoxic conditions and is depleted from the upper part of the profile. The MIA(R)-K values are also expected to increase where soluble Fe^{2+} mobilized from the upper portions of the profiles infiltrated and was incorporated in the secondary products of the deeper part of a profile.

Figure 4.2 presents the CIA, PIA and MIA(R)-K of the two paleosol profiles investigated in this study.

$$CIA = 100 * [Al_2O_3/(Al_2O_3 + CaO + Na_2O + K_2O)] \tag{4.2}$$

$$PIA = 100 * [(Al_2O_3 - K_2O)/(Al_2O_3 + CaO + Na_2O - K_2O)] \tag{4.3}$$

$$MIA_{(R)} = 100 * [Al_2O_3/(Al_2O_3 + Fe_2O_3 + MgO + CaO + Na_2O + K_2O)] \tag{4.4}$$

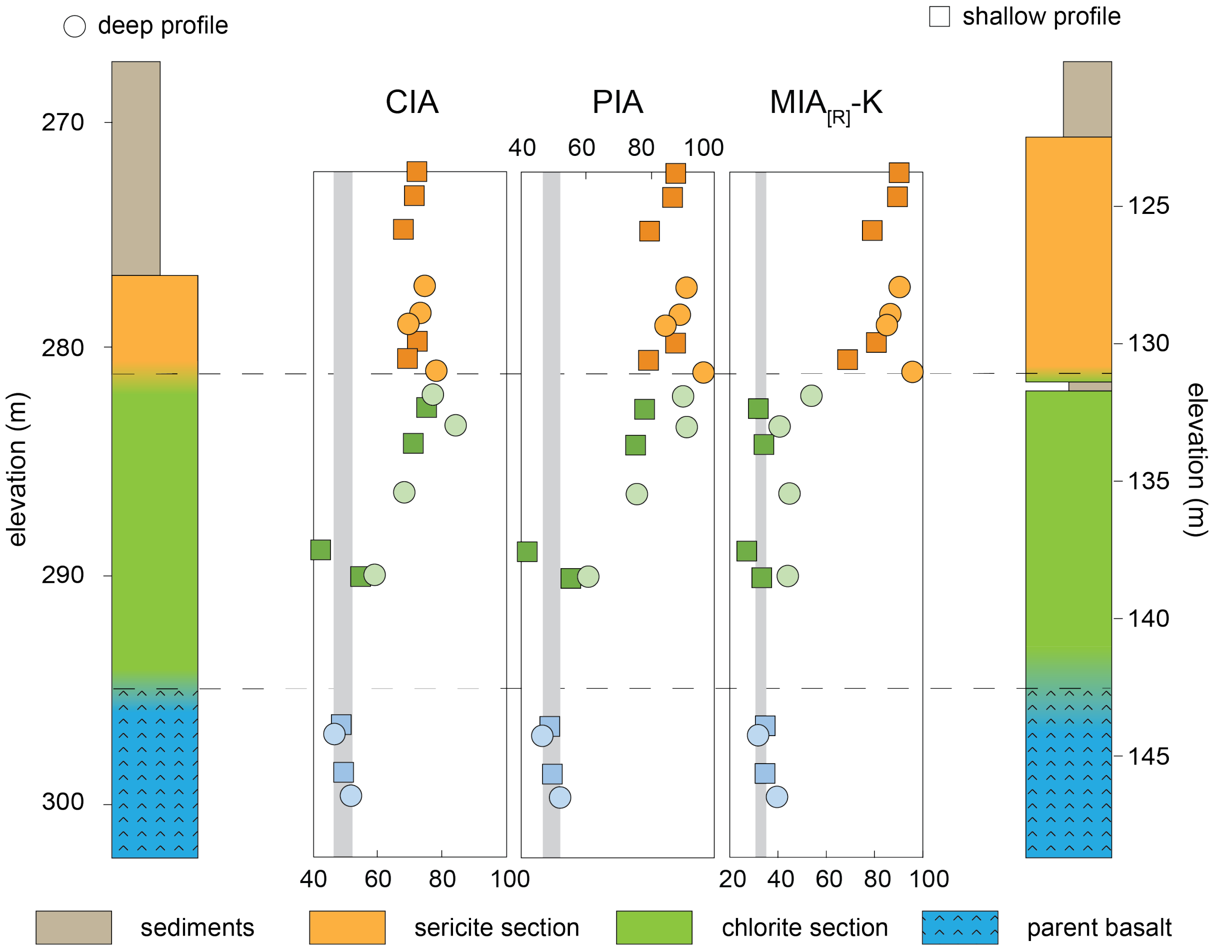

Figure 4.2: alteration indexes (CIA, PIA and MIA(R)-K) of the two paleosol profiles investigated in this study. The gray shadings represent the average ±2sd of the CIA, PIA and MIA[R]-K values of the combined parent basalts.

The CIA values of the paleosol profiles range from 42.19 to 84.15. The parent basalts have a CIA average value of 49.04 ±4.25 (2sd). The CIA values then increase upward in the chlorite sections with values from 42.19 at the bottom towards a maximum value of 84.15 close to the contact with the sericite section. All sericite section samples have very similar CIA values with an average of 72.03 ±6.21 regardless of their stratigraphic position.

The PIA values of the paleosol samples range from 41.56 to 96.33. The PIA values of the altered basalt linearly increase from the bottom of the chlorite sections towards the upper part of the sericite sections with a R^2 value of 0.69 for both profiles.

The MIA(R) – K values range from 27.12 towards 95.78. The parent basalts have an average value of 35.27 ±6.50. The chlorite sections MIA(R) – K values span from 27.12 to 53.99, and the sericite ones from 69.90 to 95.78.

4.4.2 Tungsten concentration and stable isotopes

The W concentrations of the samples range from 0.76 to 2.31 µg.g^{-1} in both profiles (Table 4.5). The parent basalts have the highest W concentrations from 1.64 to 2.31 µg.g^{-1}. The W concentrations of the weathered paleosol samples steadily decrease toward the top of both profiles. The mobility of W during weathering is quantified with τ_{Ti}^{W} values, using Ti as an immobile element and W/Ti weight ratios of 0.00020 ±0.00002 (n=2) and 0.00023 ±0.00008 (n=2) as the averages of the unweathered basalts for the deep and shallow profiles, respectively (equation 4.5).

$$\tau_{Ti}^{W} = \frac{(W/Ti)_{sample}}{(W/Ti)_{average\ parent\ basalt}} - 1 \tag{4.5}$$

The τ_{Ti}^{W} values of the unweathered parent basalt range from -0.14 to +0.03, the τ_{Ti}^{W} of the chlorite sections from -0.02 to -0.45 and the ones from the sericite sections from -0.36 to -0.67.

The residual W concentrations are calculated using the equation 4.6. The residual W concentrations range from 0.40 to 2.10 µg.g^{-1} in both profiles, with a trend in decreasing content upward (Figure 3).

$$W_{residual} = \frac{(W/Ti)_{sample}}{(W/Ti)_{average\ parent\ basalt}} * W_{average\ parent\ basalt} \tag{4.6}$$

The W/Th weight ratios of the parent basalts of the paleosol profiles are 0.12 and 0.11 in the shallow profile, and 0.16 and 0.22 in the deeper profile.

The $\delta^{186/184}$W values of the paleosols range from -0.061 ‰ to +0.095 ‰ (Table 4.5). The parent basalt samples have a narrow range in $\delta^{186/184}$W from +0.071 ‰ to +0.093 ‰, with an overall average to +0.081 ±0.019 ‰ (n=4, 2sd). The $\delta^{186/184}$W values of the two chlorite sections linearly decrease upwards, starting from parent basalt-like values of +0.095 ‰ at the base of the chlorite section towards -0.019 ‰ at the middle of the sericite section. The $\delta^{186/184}$W values of the upper sericite section of the shallow profile increases towards $\delta^{186/184}$W value of +0.015 ‰. One outliner from these general trends is found at a depth of 278.56 m in the deep profile with a $\delta^{186/184}$W value of +0.077 ‰.

Table 4.5: W stable isotopic composition of the paleosols profiles

sample depth [m]		$\delta^{186/184}$W [permill]	2SE	W [ppm]
shallow profile				
123.77	sericite zone	0.015	0.02	1.59
124.65	sericite zone	0.001	0.01	0.98
125.88	sericite zone	-0.061	0.01	1.06
129.96	sericite zone	-0.019	0.03	0.71
130.58	sericite zone	-0.002	0.02	1.04
132.37	chlorite zone	0.041	0.01	1.77
133.68	chlorite zone	0.055	0.02	1.05
137.57	chlorite zone	0.075	0.02	0.96
138.54	chlorite zone	0.095	0.02	1.22
143.94	parent basalt	0.084	0.02	1.53
145.68	parent basalt	0.078	0.02	1.77
deep profile				
277.37	sericite zone	-0.001	0.02	0.90
278.56	sericite zone	0.077	0.02	1.38
279.04	sericite zone	0.010	0.01	1.17
281.09	sericite zone	0.020	0.01	1.21
282.13	chlorite zone	0.006	0.01	1.49
283.48	chlorite zone	0.011	0.01	0.87
286.42	chlorite zone	0.050	0.01	1.79
290.02	chlorite zone	0.068	0.01	1.47
297.00	parent basalt	0.071	0.01	1.52
299.70	parent basalt	0.093	0.01	2.29

4.5 Discussion

The following discussion aims at (1) characterizing the parent basalt chemical and mineralogical properties, (2) deciphering the alteration steps which led to the chemical and mineralogical composition observed in the paleosol profiles, (3) understanding the behavior of W and its $\delta^{186/184}$W values in an anoxic weathering setting.

4.5.1 Parent basalt properties

The Mt. Roe Basalt formed from LIP emplacement with a magmatic source enriched in incompatible elements derived from crustal contamination (Mole et al., 2018; Nelson et al., 1992). The parent basalts of this study are almost ∼150 times more enriched in W compared to the 2.7 Ga komatiite and komatiitic basalt from the Belingwe Greenstone Belt with W concentrations of 0.016 and 0.019 µg.g^{-1}, respectively (Roué et al., 2021). The W/Th weight ratios of the parent basalt from the shallow paleosol profile (0.11 to 0.12) are lower than the ones measured in the deeper profile (0.16 to 0.21), but are still consistent with the range of W/Th

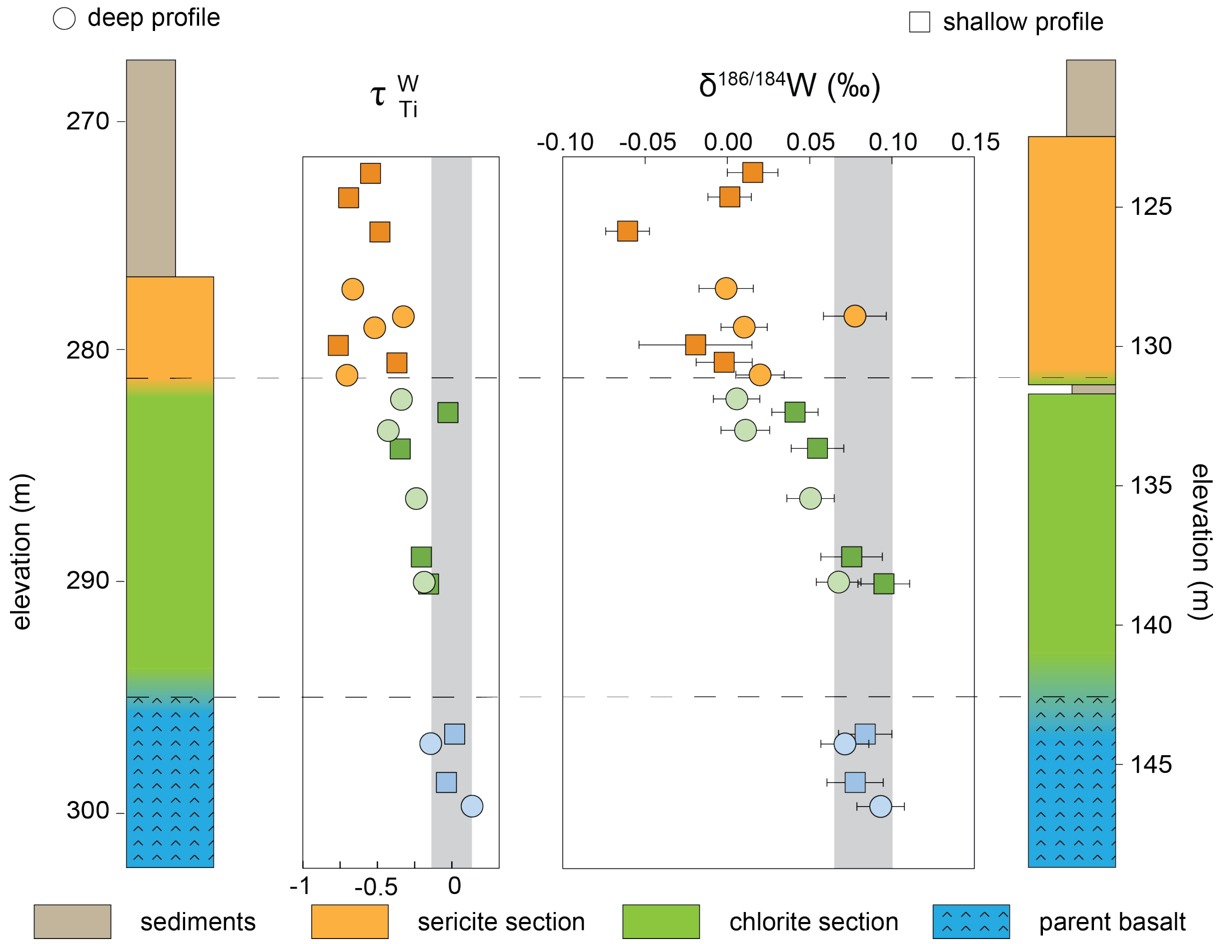

Figure 4.3: τ_{Ti}^{W} and $\delta^{186/184}$W values of the shallow and deep profiles. The brown shadings represent the range of τ_{Ti}^{W} and $\delta^{186/184}$W values for the parent basalt of both profiles. The horizontal error bars represent the 2SE of each measurement.

values reported for modern OIBs and MORBs (0.040 to 0.24; Babechuk et al. (2010); König et al. (2011)).

Little is known about the mineral host of W in mafic-ultramafic volcanic rocks. The oxygen fugacity of the mantle was proposed to increase from -4.5 QFM at 3.0 Ga to -3 ~ -3.2 at 2.7 Ga (Aulbach et al., 2019), but likely remained significantly lower than the ones of the modern mantle (-1.25 to +0.5 QFM; Aeolus Lee et al. (2005)). O'Neill et al. (2008) demonstrated that W is present as W^{6+} in silicate melts at 1400 °C, even at the extremely low oxygen fugacity expected of the Archean mantle (fO_2 of -12, QFM = -4.5; Aulbach et al. (2019)), which contrast to the results of the earlier study of Ertel et al. (1996). Fonseca et al. (2014) investigated the partition coefficients of W^{6+} between clinopyroxene, orthopyroxene, olivine, plagioclase and silicate melt under various oxygen fugacity levels. These experiments revealed increasing compatibility of W^{6+} with decreasing oxygen fugacity. However, the partition coefficients between mineral and silicate melt do not exceed 10^{-2} for QFM values of -4 and overall indicate that W^{6+} is highly incompatible, regardless on the oxygen fugacity (Fonseca et al., 2014). In situ trace element determination of modern Kilauea Iki lava lake samples revealed that W behaves as a lithophile element during magmatic differentiation and is found enriched in the glass fraction (up to 2.51 µg.g^{-1}) compared to sulfides (partition coefficients sulfide/glass $\leq$ 0.10), while olivine and augite do not host detectable W (Greaney et al., 2017). The study of W concentration and distribution determinations in Eoarchean ultramafic rocks (metakomatiite, amphibolite, lithospheric mantle, layered body) revealed high W concentration in secondary minerals and grain-boundary assemblages, and as well in so-called cryptic W nuggets minerals (Liu et al., 2016). These ultramafic rocks were altered by metamorphic-induced transport and W re-distribution as indicated by their wide range of W/Th weight ratios (0.0047 to 13.9), and are not representative of W distribution in ancient igneous rocks. Conclusively, W was likely hosted in the glass fraction of the Mt Roe Basalt as W^{6+}.

The average $\delta^{186/184}$W of both parent basalts is +0.081 ±0.019 ‰ (2SD, n=4), in perfect agreement with the values for MORBs of +0.088 ±0.017 ‰ (2SD, n=8) and modern OIBs of +0.084 ±0.019 ‰ (2SD, n= 17) published by Kurzweil et al. (2019), and two 2.7 Ga old komatiite (+0.070 ±0.008 ‰, 2SE) and komatiitic basalt (+0.096 ±0.008 ‰, 2SE) samples reported by by Roué et al. (2021) for. The similar $\delta^{186/184}$W values of the unweathered Mt Roe Basalt compared to other $\delta^{186/184}$W values published for mafic rocks indicates that the crustal contamination during the genesis of the Mt Roe Basalt did not significantly alter its stable W isotopic composition.

4.5.2 Primary versus secondary alteration chemical signals

The Mt. Roe paleosols record multiple stages of alteration in their paragenesis. First, anoxic subaerial weathering altered the Mt. Roe basaltic flows during and after their emplacement, with the paleosols marking prolonged episodes of thick weathering profile development during longer time intervals between volcanic eruptions. Subaerial weathering was accompanied by replacement of primary minerals (inferred to be primarily plagiclase, pyroxene and olivine) with secondary products that varied depending on the depth/intensity of weathering. Repeated flooding of the deep paleosol surfaces with fresh- or marine water led to the deposition of sandstone or shale, while the shallow paleosol profile is covered by volcaniclastic sediments. The flooding of the paleosol profiles may have further influenced their chemical and mineralogical compositions by secondary enrichments W sourcing from the overlying water column. Finally, deeper burial and later metasomatism and metamorphism modified the profiles primarily by enriching them in K (and other alkali elements). The end of K-enrichment is placed by a Rb-Sr isochron age at 2,168 ±10 Ma based on the co-enrichment of Rb with K (Macfarlane and Holland (1991)). Mineralogically, the latter events are evident by sericitization of smectite and kaolinite minerals (illite-muscovite formation). The influence of each of these events on the chemical composition of the profiles of this study may be responsible of the variations in $\delta^{186/184}$W values observed.

Primary alteration

The iron content distribution of the two paleosols profiles investigated in this study is similar to that of other pre-GOE paleosols (Prasad and Roscoe, 1996). Iron and magnesium in basalts are mostly contained in clinopyroxene and to lesser amounts in olivine and their content in paleosols is thus a direct proxy for ferromagnesian minerals alteration. Dehouck et al. (2014) investigated the alteration of forsteritic olivine grains in solution under a CO_2-rich atmosphere and reported the release of mineral-bound Fe and Mg into solution within hours. However, the Fe and Mg concentrations in the solutions started decreasing after 15-31 days, indicating the formation of secondary Fe-Mg-rich phases, like smectite or vermiculite (most likely saponite). These secondary products are enriched in Al (+188 to +376 %), strongly depleted in K (-56 % to -77 %), Mg (-42 % to -76 %) and slightly depleted in Fe (-7 % to -50 %) compared to the initial olivine concentrations (Dehouck et al., 2014).

In the context of our study, the conservation of Fe in the chlorite sections of both Mt. Roe Basalt paleosols indicates that the Fe^{2+} release by alteration of ferromagnesian minerals formed Fe2+-bearing smectite clays (likely saponite). The parent basalt-like Fe_2O_3/Al_2O_3 and MgO/Al_2O_3 weight ratios of the chlorite units can result from alteration of ferromangnesian minerals, release of Fe and Mg, and formation of secondary products with quantitative incorporation of these elements. Alternatively, the alteration of the basalt removed Fe and Mg from the profiles and later re-enrichments with parent basalt-like and even greater Fe and Mg content. Laboratory experiments revealed that the formation of Fe-Mg clays is relatively slow (15 to 95 days, Dehouck et al. (2014)) compared to water turnover time, which means that the dissolved Fe would have remained in the pore water only under low fluxes or stagnant meteoritic water in a low porosity environment. On the other hand, the low Fe content of the sericite sections of the two profiles indicates a stronger and more dynamic intensity of chemical weathering with thorough alteration of ferromagnesian minerals and removal of soluble elements with meteoritic water fluxes. The close association of Fe and Mg contents in the sericite units supports the global agreement that the Mt. Roe Basalt's weathering occurred under anoxic conditions and removed Fe and Mg in their soluble form, as reduced Fe^{2+}.

The replacement of plagioclase ($NaAlSi_3O_8$ – $CaAl_2Si_2O_8$), likely to have been primarily anorthitic in the basalt, by kaolinite ($Al_2Si_2O_5(OH)_4$) can be monitored with the plagioclase index of alteration (PIA) that quantifies loss of Na and Ca relative to conservative Al. The increase in PIA values from the middle of the chlorite section upwards indicates that plagioclase was efficiently altered and replaced by secondary products. Plagioclase alteration into secondary products depends on the chemical weathering intensity under which silica is conserved or removed with fluids, creating variations in Al/Si molar ratio. For example, montmorillonite ($(Na,Ca)_{0.3}(Al,Mg)Si_4O_{10}(OH).2nH_2O$) forms after plagioclase and clinopyroxene under stagnant to low flow chemical weathering rates which enables partial conservation of Si, Na and Ca with an Al/Si mol. ratio of 0.25 . On the other hand, kaolinite ($Al_2Si_2O_5(OH)_4$, Al/Si = 1) and gibbsite ($Al(OH)_3$, Al/Si $\geq$ 1) formation require a moderate to high flow chemical weathering rate. To the best of our knowledge, no mineralogical composition has been published on the paleosol profiles of this study sourcing from drillcores of the Mt. Roe Basalt. However, Teitler et al. (2015) reported mineral abundances of outcrop samples of the MR #1, #2 and #3, dominated by 40-80 % of chlorite, 15-30 % of quartz, 7-25 % of sericite and 0-20 % of albite in the chlorite units. The sericite units are dominated by 50-90 % of Fe-sericite, 10-20 % of quartz, 5-35 % of berthierine and less that 1 % of Fe-smectite.

Without precise mineralogical composition, the Al/Si molar ratios of the paleosol samples can be used as a first order approximation of the alteration intensity at various depth. Unfortunately, the SiO_2 content of many samples has not been determined due to the specifications of the sample preparation for major element measurements (XRF versus ICPMS). The Al/Si molar ratios range from 0.34 to 0.41 in the parent basalt body section and remain similar in the chlorite sections with values of 0.25 to 0.49 (Figure 4.1). The conservation of the SiO_2 content indicates that the secondary product was likely smectite group mineral, like montmorillonite. Then, the Al/Si values steadily increase from 0.42 towards 0.98 in the sericite section, indicating a loss of Si likely due to a moderate to high flow weathering regime. These observations points toward gibbsite - kaolinite formation in the sericite section and montmorillonite formation deeper in the chlorite sections of the two paleosol profiles.

The chlorite sections of both profiles were altered under low flow chemical weathering rates, as indicated by the distribution of Fe content, Al/Si mol. ratios and the lower PIA and MIA$_{[R]}$-K values (Figure 4.1 and 4.2). The sericite sections were altered under high to moderate flow rates and removal of Fe, Na and Ca from primary minerals was near-complete. As such, the weathering intensity was likely related to the paleosol porosity and meteoric fluids residence time which varied along the profiles.

The graphical representation of τ_{Ti}^{W} against $\delta^{186/184}$W values display a linear decrease with a R^2 of 0.56, and indicates that the loss of W from the profile was accompanied with an isotopic fractionation. The most plausible explanation is linked to the weathering event itself, but other processes such as flooding and metasomatism cannot be excluded.

Flooding of the profiles

The subaerial alteration of the two basalt flows was interrupted by the flooding of the platform and might have influenced the W content and isotopic concentration of the paleosols. If WO_4^{2-} from the overlying water masses diffused and re-enriched to the paleosol profiles, then the τ_{Ti}^{W} values and the $\delta^{186/184}$W values of the affected samples would drift from the linear trend observed for the lower part of the profiles. Figure 3 presents the τ_{Ti}^{W}, calculated with Ti and the parent basalt average W concentrations, alongside the $\delta^{186/184}$W value of the samples in an elevation (m) space. The samples on top of the deep paleosol profile display increases in residual W concentration associated with $\delta^{186/184}$W values from -0.061 up to +0.015 ‰. This observation testifies for secondary W enrichments, per example under immersed conditions such as lakes or marine waters. We speculate that the $\delta^{186/184}$W values and W concentrations of the upper part of the paleosol profiles initially followed the linear trend in decreasing W content and associated light $\delta^{186/184}$W values. Upon the flooding of the profiles, surrounding dissolved W was able to penetrated the profiles and was incorporated the paleosols. The $\delta^{186/184}$W value of the overlying water was likely heavier than the original $\delta^{186/184}$W value of the residual W so that a small proportion of secondary W enrichments could strongly modify the bulk $\delta^{186/184}$W value of the upper part of the paleosols, even though the increase in τ_{Ti}^{W} values is not significant (Figure 4.3).

Metasomatism event

The transition from burial diagenesis to lithification to low-grade metamorphism of the paleosol were progressive and are thus difficult to separate from each other. The Rb-Sr isochron of 2,168 ±9.7 Ma of the sericite unit indicates the last fixation/closure of Rb in micas (Macfarlane and

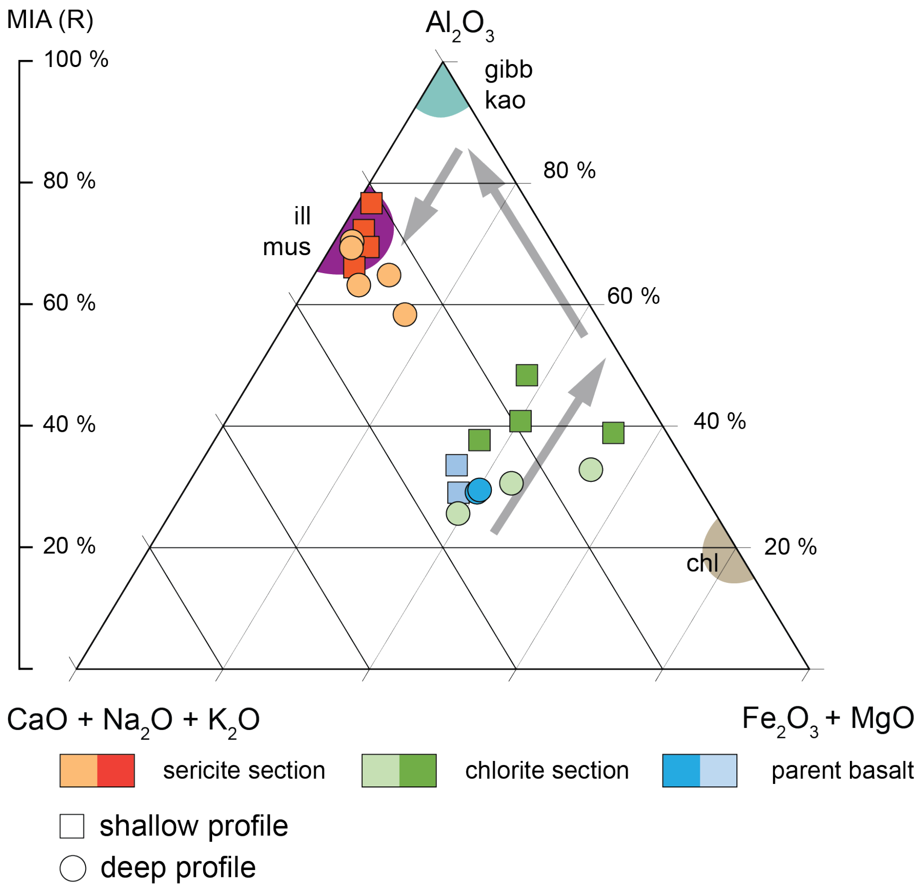

Figure 4.4: ternary diagram of basalt alteration with A (Al_2O_3) – CNK ($CaO+NaO_2+ K_2O$) – FM (Fe_2O_3 + MgO) space and $MIA_{(R)}$ values. The arrows represent the effects of weathering onto the chemical and mineralogical compositions of the paleosol samples compared to the unweathered parent basalt (blue).

Holland, 1991). The mineralogical assemblage of the upper part of the profiles transitioned from a kaolinite-gibbsite dominated towards an illite and muscovite dominated composition (Macfarlane et al., 1994a). This secondary enrichment in K is visible in the sericite sections of the two drill cores with a decrease in CIA values (Figure 3) and in the ternary A (Al_2O_3) – CNK ($CaO+NaO_2+ K_2O$) – FM (Fe_2O_3 + MgO) space (Figure 4.4) (Fedo et al., 1995). However, the chlorite sections of the two drill cores have lower secondary enrichment in K, likely due to more restricted contact with metasomatic fluids and less advanced weathering of alkali element bearing minerals.

Figure 4.4 presents the A-CNK-FM plot of the two paleosol profiles and illustrates the succession of alteration steps that the two paleosol profiles went through. The parent basalts plot in the non-weathered are of this plot with pristine ferromagnesian and plagioclase minerals. The chlorite section samples show a mixed composition between unweathered basalt, chlorite and kaolinite-gibbsite endmembers. The sericite section samples are homogenously located on the illite-muscovite endmember, with a few samples indicating a minor influence of chlorite. The plot demonstrates that the chlorite section samples' mineralogical composition evolved upwards from a non-altered composition to a mineralogical composition composed of chlorite and kaolinite/gibbsite associated with a loss of Ca and Na, but with the conservation of the Fe and Mg into secondary minerals. The sericite section samples were likely primary altered to kaolinite and gibbsite clay minerals, which were transformed during the metasomatic event by the secondary addition of K and production of illite and muscovite.

4.5.3 W isotopes in paleosols profiles

The processes which mobilized W into solution and preferentially removed heavy W isotopes from the paleosol profiles are difficult to constrain, because of the lack of information about W behavior in igneous rocks, such as identification of the main W hosting minerals in basaltic rock and its coordination in their crystal structure.

The parent basalts are typically more enriched in W than the sericite and chlorite weathered sections. The τ_{Ti}^{W} values indicate that decreasing W concentrations in the weathered basalt are associated with decreasing $\delta^{186/184}$W values in both profiles. Interestingly, $\delta^{186/184}$W values of both chlorite sections positively correlate with (CaO+NaO$_2$)/TiO$_2$ and Sr/Ti weight ratios (Figure 4.5). These observations lead to two potential hypothesis: (1) plagioclase was a major host of W and partially released heavy W isotopes during breakdown (2) or secondary products of plagioclase alteration preferentially adsorbed isotopically light dissolved W from the pore water.

The first hypothesis is based on the premise that W was incorporated in the structure of plagioclase, and preferentially heavy W isotopes were released alongside Ca, Na and Sr during alteration. However, this hypothesis is not supported by the partition coefficients measured by Fonseca et al. (2014) between plagioclase and silicate melt. The fact that W is not efficiently incorporated in the structure of major basaltic minerals (Fonseca et al., 2014) indicates that W is likely hosted in accessory minerals and/or in the microcrystalline matrix surrounding them. Unfortunately, no available data of LA-ICPMS mapping of W distribution in non-altered basalt is available.

The second hypothesis is based on W adsorption onto plagioclase secondary breakdown products such as kaolinite, gibbsite, illite and muscovite. Dissolved W have previously shown strong affinity for Mn-Fe oxides with an associated isotopic fractionation (Kashiwabara et al.,

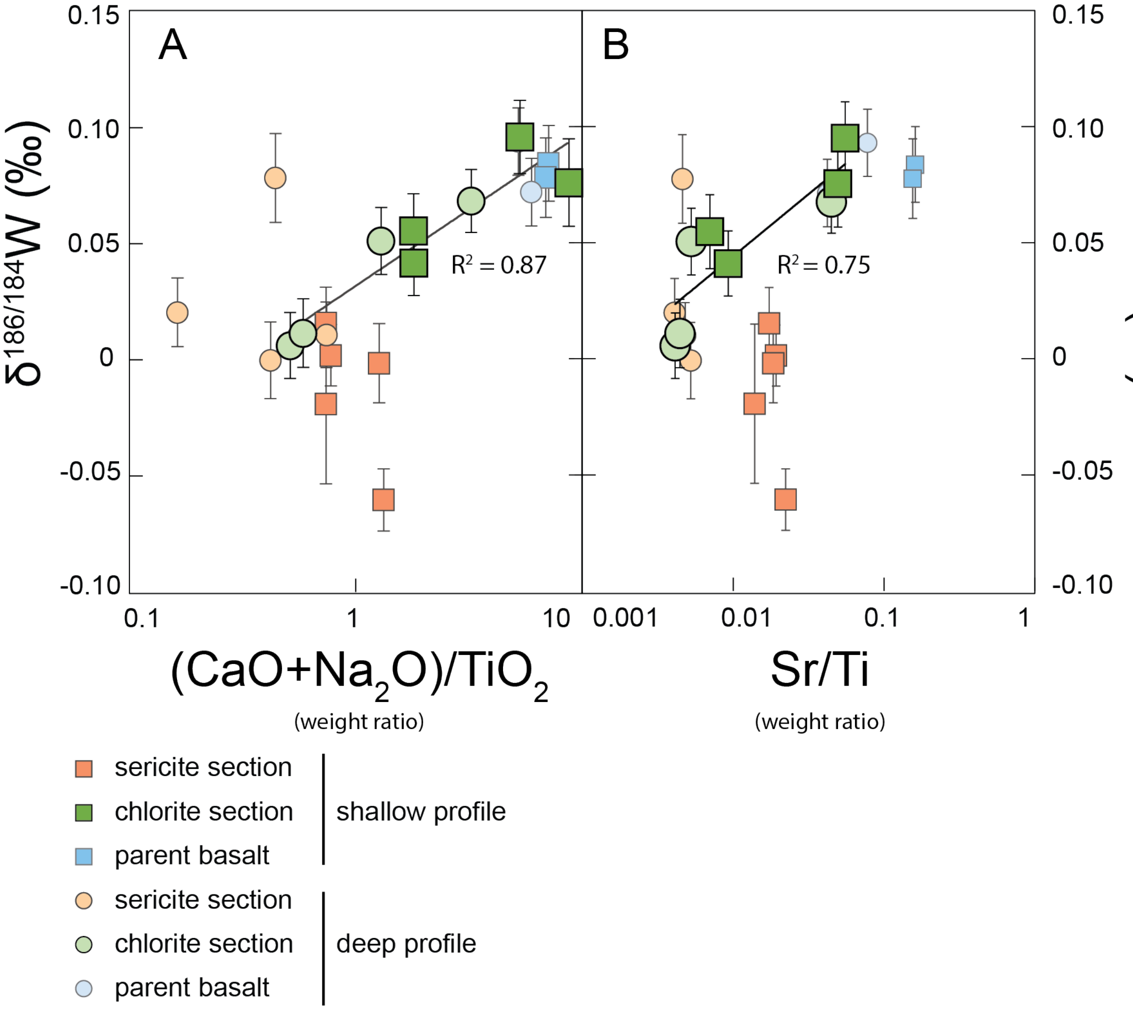

Figure 4.5: Ca/Ti, Na2O/Ti and Sr/Ti as plagioclase alteration indexes. The exponential trends (filled lines) were calculated using the data of the combined chlorite units of the two profiles, highlighted from the sericite units and parent basalts. The vertical error bars represent the 2SE of each measurement.

2017; Kashiwabara et al., 2010). Figure 6 presents the results of two studies investigating the adsorption of WO_4^{2-} onto clay minerals (kaolinite, illite and montmorillonite) at various pH (Iwai and Hashimoto, 2017; Sen Tuna and Braida, 2014). The results of these studies are highly sensitive to the conditions of the experiments such as the concentrations of dissolved W and of clays and oxides, temperature, ionic strength of the solution, time, and should be taken cautiously. For example, Sen Tuna and Braida (2014) reported ~15 % of W adsorption onto montmorillonite at a pH between of 5 and 7, while Iwai and Hashimoto (2017) reported adsorption rates close to 0 for the same mineral and pH range. The WO_4^{2-} adsorption onto kaolinite, montmorillonite and illite measured by Sen Tuna and Braida (2014) are very similar at a pH below 7, indicating similar adsorption processes of W onto these clays. Tungstate adsorption onto gibbsite is near quantitative under a pH of 5, and remains strong at neutral pH (∼50 %) (Iwai and Hashimoto, 2017).

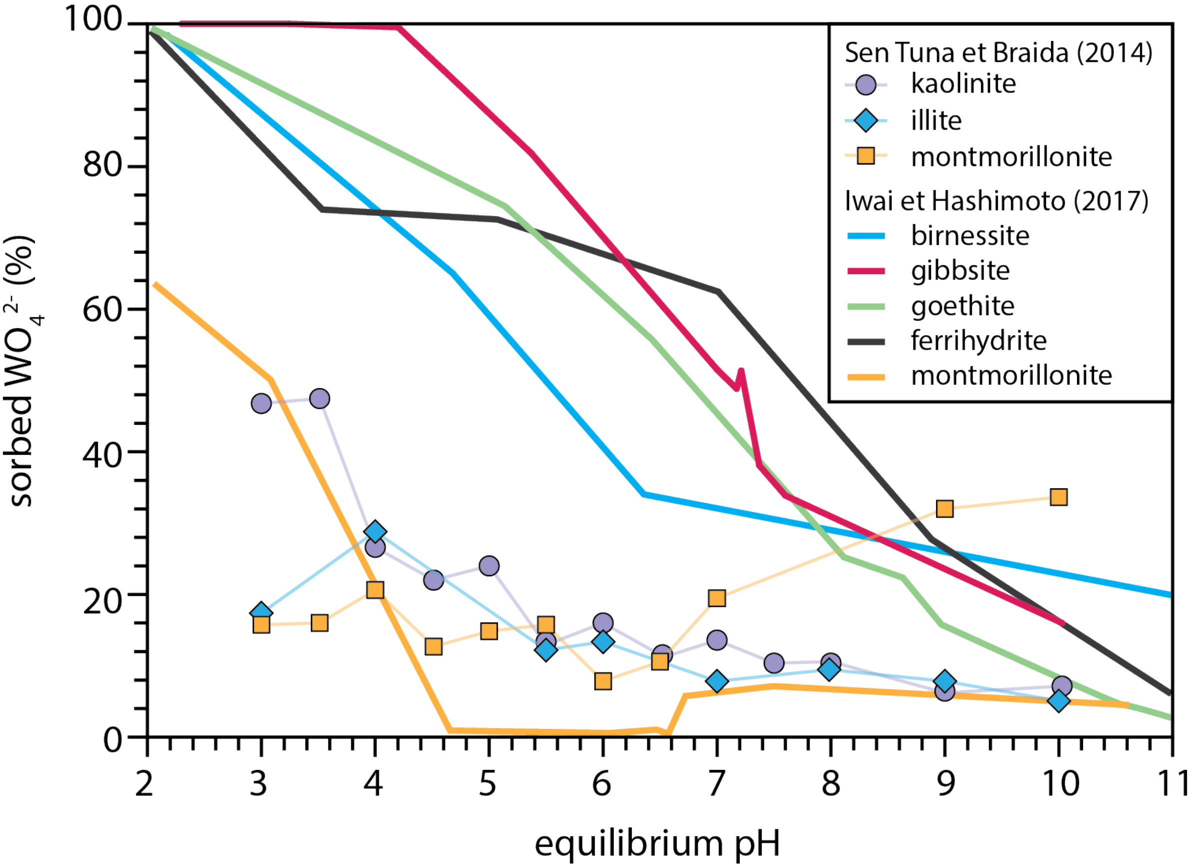

Figure 4.6: WO_4^{2-} adsorption onto clay and oxides. The data from Iwai et Hashimoto (2017) is represented as filled lines instead of the data points representation of the original publication for simplification. The WO_4^{2-} concentrations used for the experiments of Sen Tuna et Braida (2014) were of 150 µg.g^{-1} (kaolinite, illite, monmorillonite) for 10 g.L^{-1} (or 10,000 µg.g^{-1}) of reactant. The experiments lasted 7 days at 23.5 ±1 °C. The WO_4^{2-} concentrations used for the experiments of Iwai et Hashimoto (2017) were of 273 µM (= 50.2 µg.g^{-1}) (gibbsite, ferrihydrite. goethite), 54 µM (=9.9 µg.g^{-1}) (birnessite) and 27 µM (=5.0 µg.g^{-1}) (montmorillonite) for 1 g.L^{-1} - 1000 µg.g^{-1} of reactant. The experiments lasted 24 h at 25 °C.

Hur and Reeder (2016) studied dissolved W adsorption onto boehmite (γ-AlOOH) and reported a change in coordination from dissolved tetrahedral WO_4^{2-} to adsorbed distorted octahedral W. Similar observations were previously reported by Kashiwabara et al. (2013) for W adsorption onto birnessite and ferrihydrite. Bond strength models predict that heavy isotopes tend to concentrate in phases with stiffer bounds which are characterized by lower coordination number and higher valence state (Schauble, 2004), resulting in a isotopic fractionation between dissolved and adsorbed phases. Kashiwabara et al. (2017) confirmed this theory by reporting isotopic fractionations of $\varepsilon^{186/184}W_{solution\ adsorbed} = +0.59 \pm 0.14$ and $+0.51 \pm 0.06$ during dissolved WO_4^{2-} adsorption onto birnessite and ferrihydrite, respectively. The investigation of the coordination state of adsorbed WO_4^{2-} onto clay minerals such as montmorillonite and kaolinite has yet to be determined, but the similar pattern of gibbsite, birnessite and ferrihydrite adsorption envelopes might be caused by similar adsorption processes involving inner-sphere complexation (Kashiwabara et al., 2013).

The trends observed in τ_{Ti}^{W} and $\delta^{186/184}$W values cannot be explained with solely chemical weathering. The fact that $\delta^{186/184}$W values correlate with potential secondary products signals such as montmorillonite, kaolinite indicates potential retention of W in clay minerals in the paleosol profile. As such, we propose a model for Mt Roe Basalt weathering based on the premises that (1) W was fully removed from its mineral host, (2) had the same $\delta^{186/184}$W value as the parent basalt, (3) and adsorbed onto secondary minerals (with an associated isotopic fractionation).

As outlined before, W was not incorporated in a major mineral phase and might have been enriched in disseminated minor minerals phases like oxides, or distributed in the matrix. Superficial and intense chemical weathering started from the deposition of the Mt. Roe Basalt subaerial magmatic flows. The weathering horizons infiltrated the non-altered underlying basalts and progressively invaded downwards in the profiles with the alteration of minerals in the order of olivine > glass = plagioclase > clinopyroxene (Nesbitt and Wilson, 1992). The superficial weathering produced abundance of kaolinite and smectite, which were sericitized during later low grade metamorphism. We speculate that mineral-bound W was (near-) quantitatively mobilized by these fluids as WO_4^{2-} with an isotopic composition indistinguishable from that of the parent basalt. As predicted by the bond-strength theory (Urey, 1947), preferentially light dissolved W was adsorbed onto the surrounding secondary clay minerals leading to an isotopic fractionation between adsorbed and dissolved W. As observed in Figure 4.3, the bottom parts of the chlorite sections from the two drill cores have similar τ_{Ti}^{W} and $\delta^{186/184}$W values as the ones of the underlying parent basalts. However, these samples have slightly higher CIA values (54.7 to 59.0 %) than the unweathered parent basalts (46.5 to 51.7 %), indicating the beginning of early alteration. Under such conditions, W either remained mineral-bound, or was partially hydrolyzed and quantitatively adsorbed onto secondary mineral products. However, whichever process was at work , it obviously did not result in resolvable isotopic fractionation from the original W isotopic composition of the parent basalt (see $\delta^{186/184}$W values of samples from the lower sericite zones in Figures 4.3 and 4.8).

Starting from the upper part the chlorite sections the CIA and PIA values of the samples show stronger and near complete alteration of the major minerals. These parts of the profiles are characterized by a linear decrease in τ_{Ti}^{W} and $\delta^{186/184}$W values. Such isotopically light residual W likely is not mineral bound but rather suggests incomplete adsorption of previously mineral-bound and now fully liberated and dissolved WO_4^{2-} onto secondary clay minerals. The dynamic weathering regime in the upper part of the weathered profiles would had limited the interaction time between dissolved W and secondary minerals. As such, the porosity of the soil profiles and the velocity of fluid exchanges at various depths most probably were important factors, which controlled the proportion of adsorbed W and thus the $\delta^{186/184}$W values throughout the profiles.

Another potential explanation for the variations in τ_{Ti}^{W} and $\delta^{186/184}$W values with depth might be a pore water pH gradient in the paleosol profiles. As seen in Figure 4.6, the proportions of adsorbed W onto clay minerals depend on the ambient pH, with a general trend of increased adsorption at decreasing pH (Iwai and Hashimoto, 2017; Sen Tuna and Braida, 2014). However, modern soils display the tendency of increasing pH in the pore water from the surface (pH 4.45; 50 cm deep) downwards (pH 6.4; 205 cm deep) (Pogge von Strandmann et al., 2012). A modern-like pH decrease from top to bottom in our Neoarchean paleosol profiles would thus not have promoted the observed W isotopic trends.

An equilibrium isotopic fractionation represent the partitioning at thermodynamic equilibrium of isotopes between two phases. In this study, equilibrium isotope fractionation between dissolved and adsorbed W can be determined if the rate of isotopic exchange is relatively slower than the rate of separation of these two phases with water renewal during weathering. However, if the removal of dissolved W from the system is faster than the rate of isotopic exchange, , then the resulting isotopic fractionation can be described with a Rayleigh distillation model, or an open system. The Figure 4.7 represents two types of adsorption processes, with (1) fractionation in a closed system with reversible reaction and (2) an equilibrium isotopic fractionation in an open system with limited interaction between dissolved and adsorbed W.

In the two cases, dissolved and adsorbed W are related to one other by the fractionation factor $\alpha_{dissolved/adsorbed}$ throughout the range of adsorption with a value of 1.0000126, following Equation 4.7 using the initial values $\delta^{186/184}W_{dissolved\ 0}$ of +0.081 ‰ and $\delta^{186/184}W_{adsorbed\ 0}$ of -0.045 ‰ (determined by linear regression).

$$\alpha_{dissolved/adsorbed} = (\delta^{186/184}W_{dissolved\ 0} + 1000)/(\delta^{186/184}W_{adsorbed\ 0} + 1000) \qquad (4.7)$$

The isotopic fractionation $\varepsilon_{dissolved/adsorbed}$ is defined as:

$$\varepsilon_{dissolved/adsorbed} = (\alpha_{dissolved/adsorbed} - 1) * 1000 \tag{4.8}$$

The two solid black curves on Figure 4.7 represent liquid and adsorbed $\delta^{186/184}$W values following equations 4.9 and 4.10, with F$_{adsorbed}$ representing the fraction of adsorbed W.

$$\delta^{186/184}W_{dissolved} = \delta^{186/184}W_{dissolved\ 0} + F_{adsorbed} * (\alpha_{dissolved/adsorbed} - 1) \tag{4.9}$$

$$\delta^{186/184}W_{adsorbed} = \delta^{186/184}W_{dissolved\ 0} - (1 - F_{adsorbed}) * (\alpha_{dissolved/adsorbed} - 1) \tag{4.10}$$

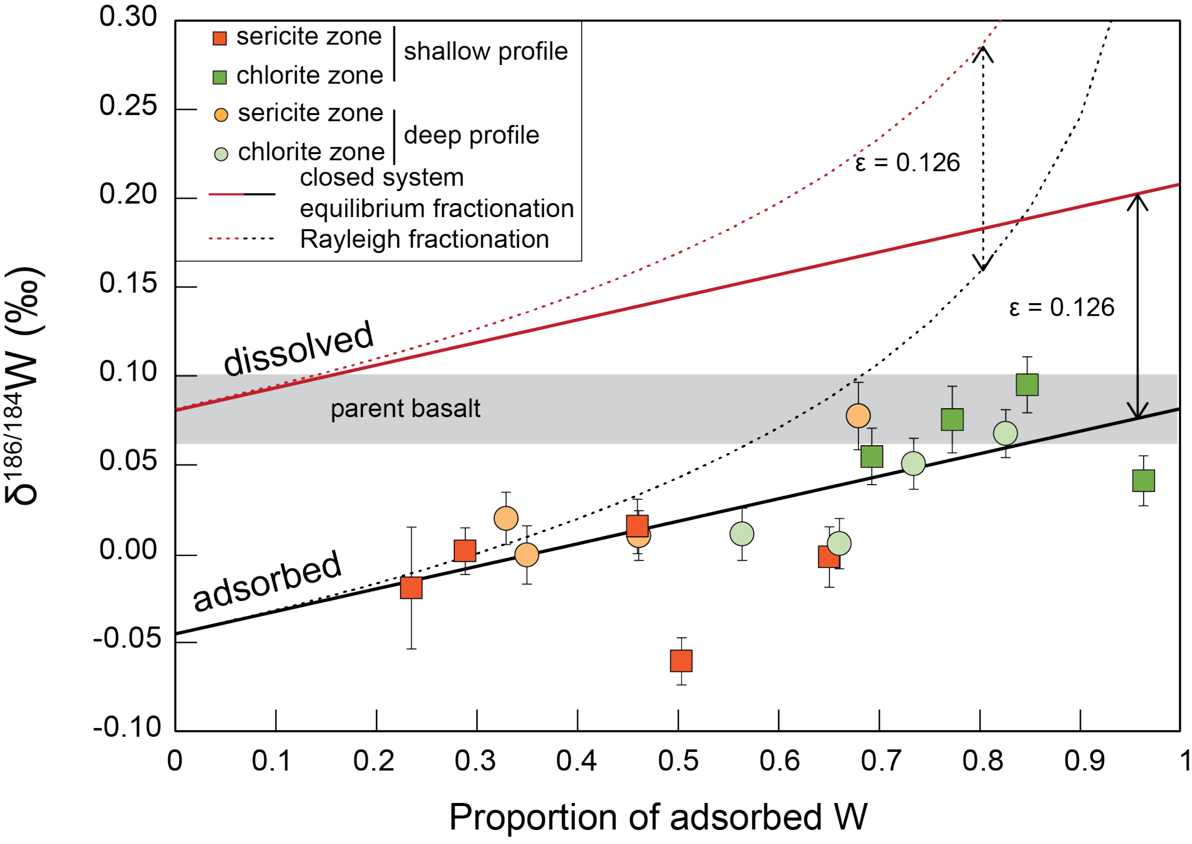

Figure 4.7: W isotopes fractionation model during weathering. The parent basalt $\delta^{186/184}$W average value is of +0.081 ±0.019 ‰ (n=4) and is calculated with both parent basalt $\delta^{186/184}$W values. The vertical error bars represent the 2SE of each measurement.

In the case where the adsorption of W onto clay minerals is non-reversible and that dissolved W is being removed by alteration fluids, dissolved and adsorbed W do not interact anymore and the resulting isotopic fractionation follows a Rayleigh distillation model represented by the equations 4.11 and 4.12, with F representing the fraction of adsorbed W.

$$\delta^{186/184}W_{dissolved} = (1000 + \delta^{186/184}W_{dissolved\ 0}) * (1 - F_{adsorbed})^{(\alpha_{(dissolved/adsorbed)}-1)} - 1000 \quad (4.11)$$

$$\delta^{186/184}W_{adsorbed} = \frac{1000 + \delta^{186/184}W_{dissolved}}{\alpha_{dissolved/adsorbed}} - 1000 \quad (4.12)$$

The $\delta^{186/184}$W data distributions of the chlorite and sericite sections of the two profiles fit well to a closed system with equilibrium isotopic fractionation. The offset of 0.126 ‰ between adsorbed and dissolved W in this model is much lower to the ones reported for W adsorption onto Mn-Fe oxides (Kashiwabara et al., 2017), most probably because of outer-sphere complexation of W onto montmorillonite and kaolinite clay minerals.

In conclusion, we propose a weathering model where the $\delta^{186/184}$W values of basalt profiles weathered under an anoxic regime depend on the weathering intensity and water renewal rates at various depth (Figure 4.8). The alteration of primary minerals and formation of secondary products such as smectite, gibbsite and kaolinite are responsible for the removal of a proportion of relatively isotopically light dissolved W from the pore waters, associated with an equilibrium isotopic fractionation characterized by a factor of $\varepsilon = 0.126$ ‰.

4.5.4 Implications for W mobility at surfaces of ancient continents

The linear decrease in $\delta^{186/184}$W values and W/Ti weight ratios upwards indicates that the loss of W was proportional to the depth of the weathering profile. Using linear regression, we determine a loss of 2.91 % of W (in weight) associated with a decrease of 0.0043 % per meter of depth in a paleosol profile with a thickness of 22 m (Figure 4.9). With this model, we estimate an overall W loss of 29 % during weathering, while 71 % remained in the paleosol composite profile. We propose that the processes that fractionated W occurred in a close system with reversible reaction as presented in Figure 4.7. In such conditions, the isotopic fractionation between dissolved and adsorbed is constantly of $\varepsilon = 0.126$ ‰, regardless of the proportions of adsorbed W. Per example, for 50 % of W loss during weathering the residue $\delta^{186/184}$W value is of +0.052 ‰ then the dissolved W pool has an $\delta^{186/184}$W value is of +0.178 ‰. By combining the W concentration and $\delta^{186/184}$W values of the residual alongside a composite 22 m thick paleosol profile combining the $\delta^{186/184}$W values of the profiles, we determine that the average residual profile $\delta^{186/184}$W value is of +0.026 ‰, while the average W isotopic composition of the fluids is estimated at +0.175 ‰. This simple model does not include the potential loss of material by erosion, compaction and variations in weathering horizon. Still, this first order

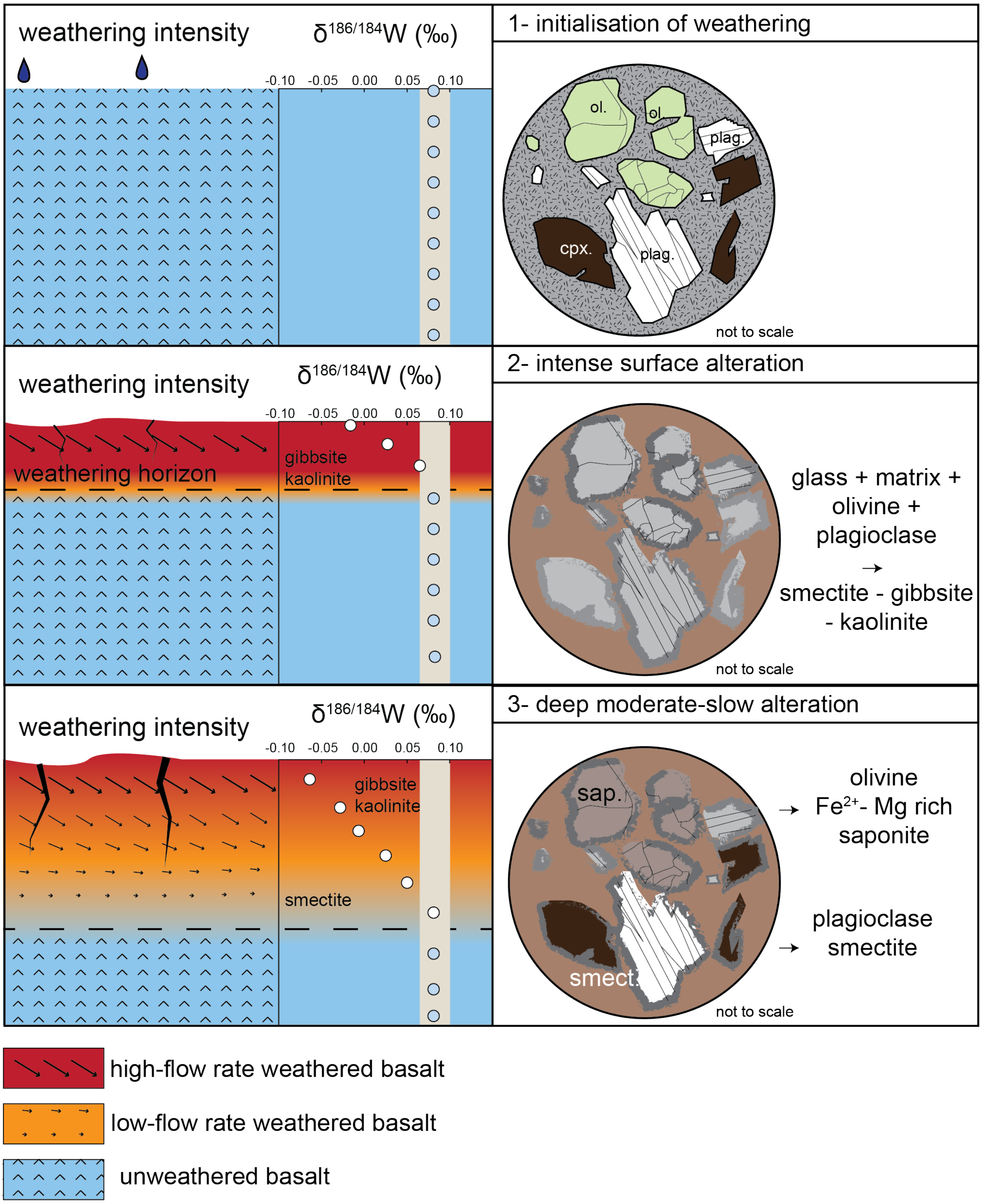

Figure 4.8: paleosol alteration model. 1) The unweathered parent basalt contains phenocrysts of plagioclase (plag.; ∼50 %), clinopyroxene (cpx.; ∼22 %), and olivine (ol.; ∼10 %) in an aphanitic matrix. The $\delta^{186/184}$W value of the parent basalt is homogenous throughout the basalt flows. 2) The surface of the parent basalt is exposed to high rate subaerial weathering and the primary minerals are altered to a mixture of smectite, gibbsite and kaolinite. Mineral-bound W is efficiently hydrolyzed and a relatively small proportion of preferentially light WO_4^{2-} is adsorbed onto secondary minerals, while the relatively heavy residual WO_4^{2-} is removed from the profile by ground- and/or surface water. 3) At greater depth, the low porosity and relatively long residence time of the meteoric fluids enable the formation of chlorite clay minerals like saponite (sap.) and the incorporation of Fe and Mg from the fluids. Increasing proportions of dissolved W are adsorbed onto the secondary productswith $\delta^{186/184}$W values approaching that of the parent basalt with increasing depth.

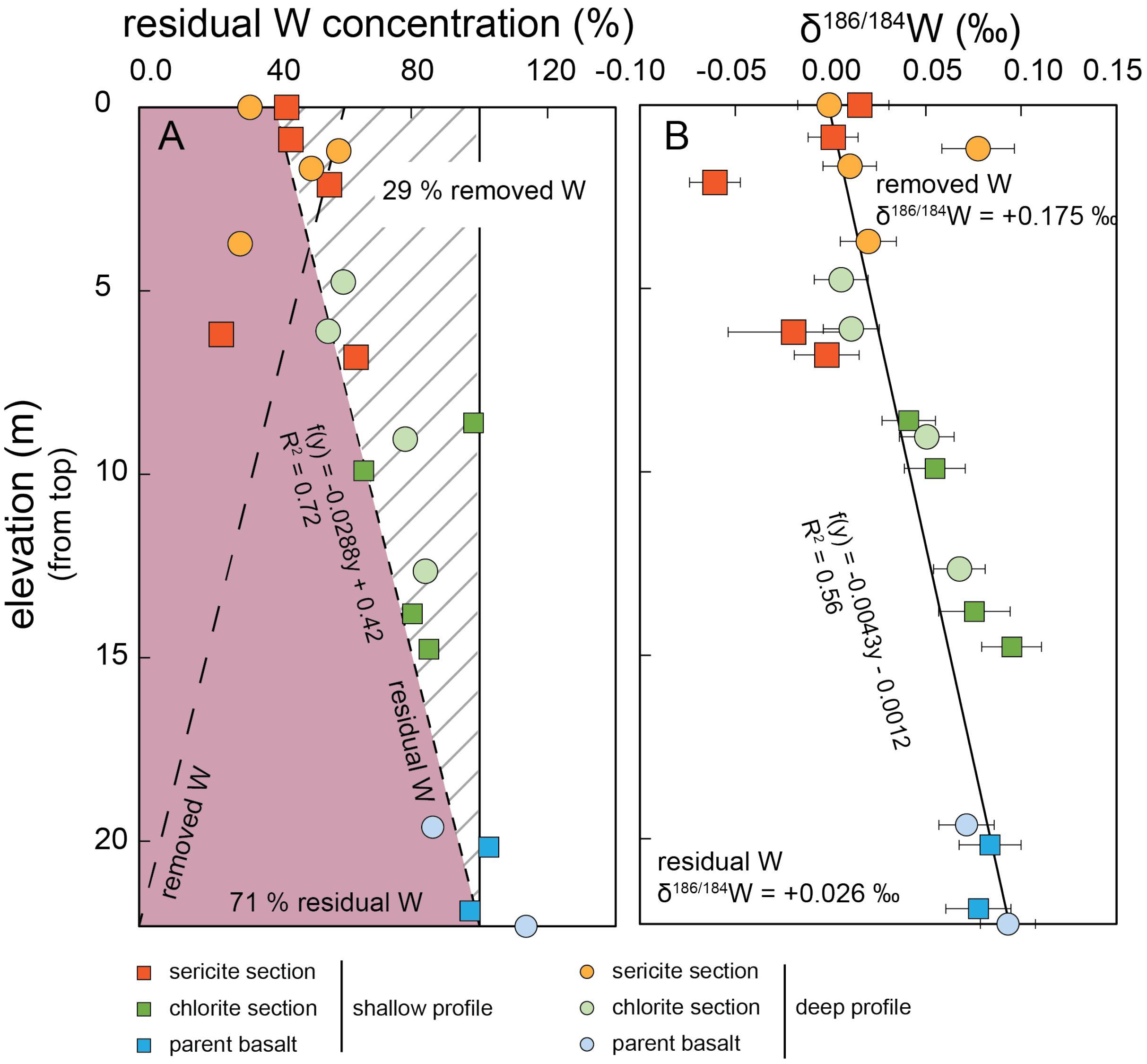

Figure 4.9: model of W loss and associated $\delta^{186/184}$W values during weathering. The lines represent the calculated linear decrease in W concentrations and $\delta^{186/184}$W values upwards, while the circles and squares are the reported data the paleosol data. The model is based on a hypothetical weathering horizon of 22 m with W content and $\delta^{186/184}$W values similar than the ones reported for the combined shallow and deep paleosol profiles. The W concentrations of the basaltic flows prior to alteration are expected to be homogeneous and similar by the average W concentration of the parent basalts of both profiles.

approximation indicates that the removal of W from the paleosols profiles was associated with a significant isotopic fractionation compared to the range of $\delta^{186/184}$W values of the unweathered bedrock.

The average residual basalt's $\delta^{186/184}$W value still remains similar to the ones of modern and ancient igneous rocks, from -0.010 to +0.110 ‰ in $\delta^{186/184}$W (Krabbe et al., 2017; Kurzweil et al., 2019; Kurzweil et al., 2018; Mazza et al., 2020; Roué et al., 2021). This relatively narrow range in $\delta^{186/184}$W values indicates that magmatic differentiation does not influence the

$\delta^{186/184}$W value of igneous rocks. As such, the $\delta^{186/184}$W value of the weathered continental crust in the Neoarchean was likely not controlled by primary mineralogy but rather by weathering intensity and W affinity with secondary products. The more intense the weathering alters the exposed continental crust the more W is removed from the soils with a $\delta^{186/184}$W value narrowing towards the one of the igneous W's source. If the transport of WO_4^{2-} by surface fluids conserved its $\delta^{186/184}$W value without further adsorption processes, then the riverine input $\delta^{186/184}$W value of the Archean ocean was slightly heavier than the igneous inventory.

The study of marine shales deposited between the deep and shallow paleosol profiles (267.7 m) and after the flooding of the shallow profile (85.3 – 173.5 m) of the ABDP-6 core show $\delta^{186/184}$W values from +0.098 to +0.167 ‰, while slightly younger marine shales from the 2.76 Ga ABDP-3 core from Hardey F. show $\delta^{186/184}$W values from +0.119 to +0.164 ‰ (Roué et al., 2021). The $\delta^{186/184}$W values of the core 2.77 Ga ABDP-6 previously revealed exponential mixing trends between detrital ($\delta^{186/184}$W value from -0.010 to +0.097 ‰) and authigenic ($\delta^{186/184}$W value of +0.170 ‰) endmembers (Roué et al., 2021). Such isotopically W authigenic component was interpreted to source from an isotopically heavy seawater. If the process of adsorption of WO_4^{2-} in marine sediments is near-quantitative, then the maximum $\delta^{186/184}$W value observed in the ABDP-3 and ABDP-6 core reveal a seawater $\delta^{186/184}$W value controlled by continental input based on the Mt. Roe Basalt weathered profiles, and not by Fe-Mn cycling as proposed before. On the other hand, if the process of WO_4^{2-} adsorption onto clay minerals and organic matter is non-quantitative and associated with a hypothetical $\varepsilon = 0.126$ ‰, then it can be expected that the seawater was significantly heavier that the $\delta^{186/184}$W value recorded in the marine shale record at 2.76-2.77 Ga.

The Archean weathering mode and W retention is soils were likely very different from the modern ones. No study investigated the $\delta^{186/184}$W value of a modern soil profile so far, but Tuna et al. (2012) and Sen Tuna and Braida (2014) reported efficient retention of W to organic matter rich soil (Pahokee peat) in much higher rates than the ones of kaolinite, montmorillonite and illite. As such, the process of weathering of igneous rocks in the Archean was likely very different from the modern ones which likely retain WO_4^{2-} in organic matter-rich soils. Moreover, the growth of continental landscape between 3.0 to 2.7 Ga must have influenced greatly the rates of W subaerial weathering (Liu and He, 2021). We propose that the increase in $\delta^{186/184}$W values from the 3.47 Ga (+0.028 to +0.132 ‰) to 2.94 Ga (+0.024 to +0.177 ‰) marine shales from the Pilbara Craton marks the shift from an hydrothermal-dominated towards a subaerial anoxic weathering-dominated input of W to the ocean.

4.6 Conclusion

This study presents the first data set of $\delta^{186/184}$W values in a Precambrian paleosol, as well as the first isotopic fractionation documented for W during chemical weathering. Not only does this study indicate that dissolved W could have been delivered from continental masses as early as 2.77 Ga, it also highlights that its removal from soil profiles was associated with an isotopic fractionation. This study furthermore focuses on the interaction between dissolved W and clay minerals, and its potential influence on the W cycling on land and aqueous environments. Significantly more research about modern W cycling in aqueous reservoirs is needed to fully understand the similarities and differences to the Archean environment.

The offset between modern seawater and igneous rocks clearly reflects that the W marine cycling is dominated by Mn-Fe oxides sink (Fujiwara et al., 2020; Kashiwabara et al., 2017; Kurzweil et al., 2021). It can be expected that W cycling in the Archean ocean was dominated by Fe-oxides sink in shallow and oxidized environments. However, clay minerals and organic matter controlled the W drawdown in the open ocean, potentially with an isotopic fractionation between dissolved and adsorbed W similar to the one measured in this study. This observation questions the use of $\delta^{186/184}$W values in shale as a direct proxy for the seawater $\delta^{186/184}$W value, and thus for the global ocean redox state. Then, the W isotopic composition of the seawater likely changed when the redox potential of the open ocean increased starting 2.7 Ga (Kurzweil et al., 2015; Ostrander et al., 2020) to become dominated by Fe-Mn oxides shuttling, even in more distal environments (e.g. Mt Rae Shale, 2.5 Ga, Anbar et al. (2007)). Similarly, the GOE must have influenced the processes of W removal from soils and the stronger W retention in soils with oxides. Finally, the colonialization of continental surfaces by a significant of biomasses further impacted the W input to the ocean due to efficient retention of W in organic rich soils as observed today (Tuna et al., 2012).

Chapter 5

W stable isotopes in carbonates: leaching, chemical separation and preliminary results

5.1 Highlights

- Trace elements concentrations in carbonates leachates are highly variable
- JDo-1 and JLs-1 are suitable carbonate reference materials for monitoring W separation procedures
- W from carbonate matrices and W from double-spike efficiently equilibrate in HCl and HNO_3
- Modern Bahamas carbonates $\delta^{186/184}$W values do not mirror the seawater $\delta^{186/184}$W signature
- Terrestrial 2.05 Ga hydrothermal carbonates reveal crustal-like $\delta^{186/184}$W values and high W concentrations
- Marine carbonates $\delta^{186/184}$W values range from the detrital background signatures towards $\delta^{186/184}$W values up to +0.329 ‰
- Open ocean carbonates deposited in deep environments might efficently record the seawater $\delta^{186/184}$W value, while the ones deposited in shallow to restricted environments might record riverine $\delta^{186/184}$W values and/or local draw-down of W with particles and oxides to the sediment

5.2 Introduction

The carbonated-rock record has proven to efficiently record the seawater REE+Y pattern, and is used as a sedimentary archive for reconstructing the past ocean oxygenation state. More recently the determination of non-conventional stable isotopic compositions of molybdenum (Mo), zinc (Zn), uranium (U), and chromium (Cr) in carbonates provided a valuable contribution to a better understanding of the redox evolution of the atmosphere and ocean system through time (Bonnand et al., 2013; Bonnand et al., 2011; Chen et al., 2018; Eroglu et al., 2015; Frei et al., 2011; Gaspers et al., 2020; Rodler et al., 2016; Thoby et al., 2019; Voegelin et al., 2010; Voegelin et al., 2009; Von Blanckenburg et al., 2008; Zhang et al., 2020).

A leaching procedure is commonly used to separate the carbonate matrix from the detrital component, prior to trace element determination and/or separation chemistry for isotopic composition determination. But the type of acid used (hydrochloric (HCl), nitric (HNO_3) and acetic (HAc)), temperature and reaction time change from study to study. The effects of these differences on trace elements concentrations (mostly REE+Y patterns) were thoroughly investigated (Rongemaille et al., 2011; Tostevin et al., 2016), but very few focused on leaching methods for the purpose of isotopic composition determination (Clarkson et al., 2020; Tissot et al., 2018).

Carbonate samples tend to be heterogenous, and the trace element determination of a large sample load is more representative than a small powder aliquot. However, the use of nitric acid on a high sample mass (in the gram range) led to the formation of a nitric-based gel, extremely hard to dry, while acetic acid introduces organic components in the sample causing potential interferences during measurement. This is mostly why weak HCl is used for leaching carbonate prior to separation chemistry in most studies where the concentration of the element of interest is low (Bonnand et al., 2011; Thoby et al., 2019; Voegelin et al., 2009).

The high variability in leaching techniques complicates the comparison of trace element data and reported isotopic ratios from a study to another. The differences in leaching methods bear the potential to induce highly variable trace elements concentrations, various contributions from the detrital component, and potential adsorption-desorption effects. As a result, the isotopic composition of the same carbonate sample might vary depending on the leaching method. No studies so far have focused on the trace element composition of the same carbonate reference standard leached with different acids with the objective to measure isotopic ratios. Per example, Clarkson et al. (2020) investigated the effect of reductive cleaning combined with different leaching methods (acetic, hydrochloric or nitric acid with various acid strength) on the stable Mo and U isotopic compositions of carbonate-rich sediments. However, the samples used for that study were composed of 61 to 70 % of carbonate matrix only, with the remaining 39 to 30 % composed of oxides and detrital related minerals. They do not represent pure carbonate matrixes with low detrital-sourced content. Still, the stable U isotopic compositions of these samples were not affected by the type of acid used, time and reducing cleaning, whist their stable Mo isotopic compositions widely vary from the UCC to the modern seawater $\delta^{98/95}$Mo value. That study highly the influence of Mn-coating and clay minerals on $\delta^{98/95}$Mo values.

In this study, the trace elements concentrations of various rock reference materials leached with the three most used leaching procedures (HNO_3, HCl, HAc) are reported in order to select a method generating high W yields (compared to the bulk W concentrations) with the lowest detrital contribution.

This chapter is divided in three parts. First, the distribution of trace elements concentrations (with a focus on W) of four carbonate rock reference materials (two limestones and two dolomites) was investigated after leaching with HCl, HNO_3 and HAc for two days. Then, two rock reference materials (one limestone, one dolomite) were selected as monitor rock standards for stable W isotopic determination. Tests were carried on W sample-spike equilibration of carbonate matrices spiked in HCl or HNO_3, and the W separation procedure on the selected rock reference materials with high sample loads. Finally, the $\delta^{186/184}$W values in natural modern to Mesoarchean carbonates were measured, their potential as a proxy for the redox state of the ocean was tested.

5.3 Leaching experiments

Here, we compare the trace elements distribution of four pure carbonate rock standards used as reference materials, targeting the best method for carbonate matrix leaching prior to W separation. First, the effect of various acids (HCl, HNO_3, HAc and HF-HNO_3) on the trace elements concentrations and their reproducibilities were investigated. Then, we used the concentrations of Th, Zr and Ti as representatives of the detrital component contribution, and calculated the proportions of authigenically-sourced W in each carbonate reference material.

Four carbonate reference materials were used for this study: the JLs-1 (limestone,

Table 5.1: stochiometric volumes of acid for leaching of limestones and dolomites

	HCl 3 M	HNO_3 5%v	HAc 5 M
Limestone (M=100 g/mol)			
0.5 g	3.33 mL	9 mL	2 mL
1 g	6.66 mL	18 mL	4 mL
Dolomite (M=136 g/mol)			
0.5 g	4.90 mL	13.36 mL	2.72 mL
1 g	10.80 mL	26.72 mL	5.44 mL

split 3 position 92-3) and JDo-1 (dolomite, split 1 position 61) were obtained from the Japan Geological survey, and the ECRM 752-1 (or CRM-BCR 393, lot 3151) and ERCM 782-1 (lot 0662) were obtained from the British chemical standard certified reference materials.

The carbonate reference materials were leached and bulk digested (with table-top technique) for trace elements determination, using 30, 100, 500 and 1,000 mg of sample weight.

5.3.1 Methods

Leaching procedure

Each step of the experiment (sample weights, aliquots, dilutions) was gravimetrically measured for higher accuracy.

The carbonate reference material powders were scaled into 50 mL pre-cleaned centrifuge tubes and suspended in 2 mL of H_2O to prevent strong effusion and sample loss before the drop wise addition of the respective acids. The carbonate samples are leached with appropriate volumes of acid to ensure the full dissolution of the carbonate fraction, but avoiding excess acid (Table 5.1).

The carbonates powders were leached for 2 days at room temperature and regularly remobilized to avoid deposition of carbonate powder at the bottom of the centrifuge tube. After two days, the tubes were centrifuged 10 min at 4,000 rpm. An aliquot of the supernatant was carefully taken out and transferred to a cleaned PFA beaker.

The aliquots were dried down at 85°C. Upon dryness and cooling, the carbonate pellets were refluxed using concentrated nitric acid (14.5 M), with volumes of 100 µL (HCl-HNO_3 leachates) and 200 µL (HAc leachates), respectively. The samples were dried down at 85°C on a hotplate. The conversion was repeated with a volume of 100 µL and dried again. The carbonate leachates were diluted in 10 mL of 2 %v/v HNO_3. This stage dilution factor reaches approximately 100.

In parallel, total digests were performed on 30-100 mg of each bulk rock reference material powders weighed in pre-cleaned PFA beakers. First, 5% HNO_3 was added drop wise to the carbonate powders, and left to react at room temperature for a few hours. Then, 2 mL of concentrated HF-HNO_3 (3:1) were added to the samples and were left to react in closed beakers on a hotplate for 48 h at 85 °C. The digested samples were dried down, and taken up twice in 2 mL HCl 9 M at 120 °C for 48 h on a hotplate to dissolve the abundant fluorides. The dried samples were then converted to nitric form twice using 200 µL of concentrated HNO_3. Finally, the samples were dissolved in 10 mL of 2 % HNO_3.

Dilution - measurements

Scaled aliquots of $\sim$ 1 mL of the carbonate leachates and total digests were taken out and mixed with 9 mL of internal standard composed of ^{6}Li (3 ng.g^{-1}), In ($\sim$1 ng.g^{-1}), Re ($\sim$1 ng.g^{-1}) and Bi ($\sim$1 ng.g^{-1}) in 2 % HNO_3 following the method published by Eggins et al. (1997). The final dilution factor reaches $\sim$ 1,000 to 5,000.

Forty-two trace elements were measured on an iCap-Qc ICP-MS at the university of Tübingen. Raw intensities were externally corrected using internal standard signals, monitoring standards (every 5 samples measurements), pure and procedure acid blanks. The corresponding trace elements concentrations were calculated using a rock calibration of W2a with dilution factors of 10k, 20k, 40k, 100k and 200k to enable low concentrated elements to be comprised in the range of the calibration curve (e.g. W, Mo, Th).

5.3.2 Results and discussion

The concentrations of the HAc, HCl and HNO_3 blanks were low and represent only a maximum of 0.0002 % of the total Cr, 0.001 % of the total Mo, 0.003 % of the total W and negligible U and Zn.

The different leaching procedures induced different concentrations in trace elements for the same carbonate reference material, and pose the problem to check for the precision of the measurements. Moreover, the very few data available to compare this data set in the literature were reported on fully digested carbonate reference material samples, and some did not report the whole spectrum of trace element concentrations (Jochum et al., 2005). Here, we compare the trace elements of the leachates to the ones of the bulk digested rock reference materials, used as proxies for the absolute initial trace elements concentrations of the original samples.

The results are presented in the scatter plots of trace elements concentrations of the Figure 5.1, normalized to that of the bulk digested aliquots.

Detrital sourced elements

In general, HCl and HNO_3 and leachates contain a higher concentration of detrital related elements for both limestones and dolomites. Acetic acid leachates are globally less contaminated by the detrital component and present the lowest Ti, Zr and Th concentrations measured from all samples (Tables 5.3, 5.4, 5.5 and 5.6).

The Th concentrations of the JLs-1 and JDo-1 leachates are close to the ones of the bulk digested aliquots and indicate than the host of Th in these carbonate rock reference materials is easily leached out from the detrital component in the first 2 days. As such, the calculation of authigenic concentrations of elements in carbonate leachates using Th can induce large errors and unrepresentative results. Zirconium or Ti should preferentially be used as proxies for the detrital component to monitor the W, Mo, Zn and Cr enrichments.

REE+Y concentrations and extended patterns

The HCl and HNO_3 leachates of the rock reference materials JDo-1 and JLs-1 yielded in REE+Y concentrations indistinguishable than that of the bulk digested (Figure 5.1). The samples leached with HAc are less concentrated in REE+Y, but similar shapes to the bulk one when normalized to the PAAS (Figure 5.2).

However, the rock refenence material ECRM 782-1 and ECRM 752-1 have lower REE+Y concentrations compared to that of the bulk concentrations, especially in the light-REE. As a result, the extended REE+Y pattern of these two rock reference materials show slight depletion in LREE compared to the bulk patterns, especially for the rock reference material ECRM 782-1.

In conclusion, the yields of REE+Y concentrations in leachates compared to the bulk are highly variable from a rock reference material to another. Still, the Jdo-1 and JLs-1 rock reference material reveal consistency in REE+Y concentrations between all HCl and HNO_3 leachates compared to the bulk concentrations.

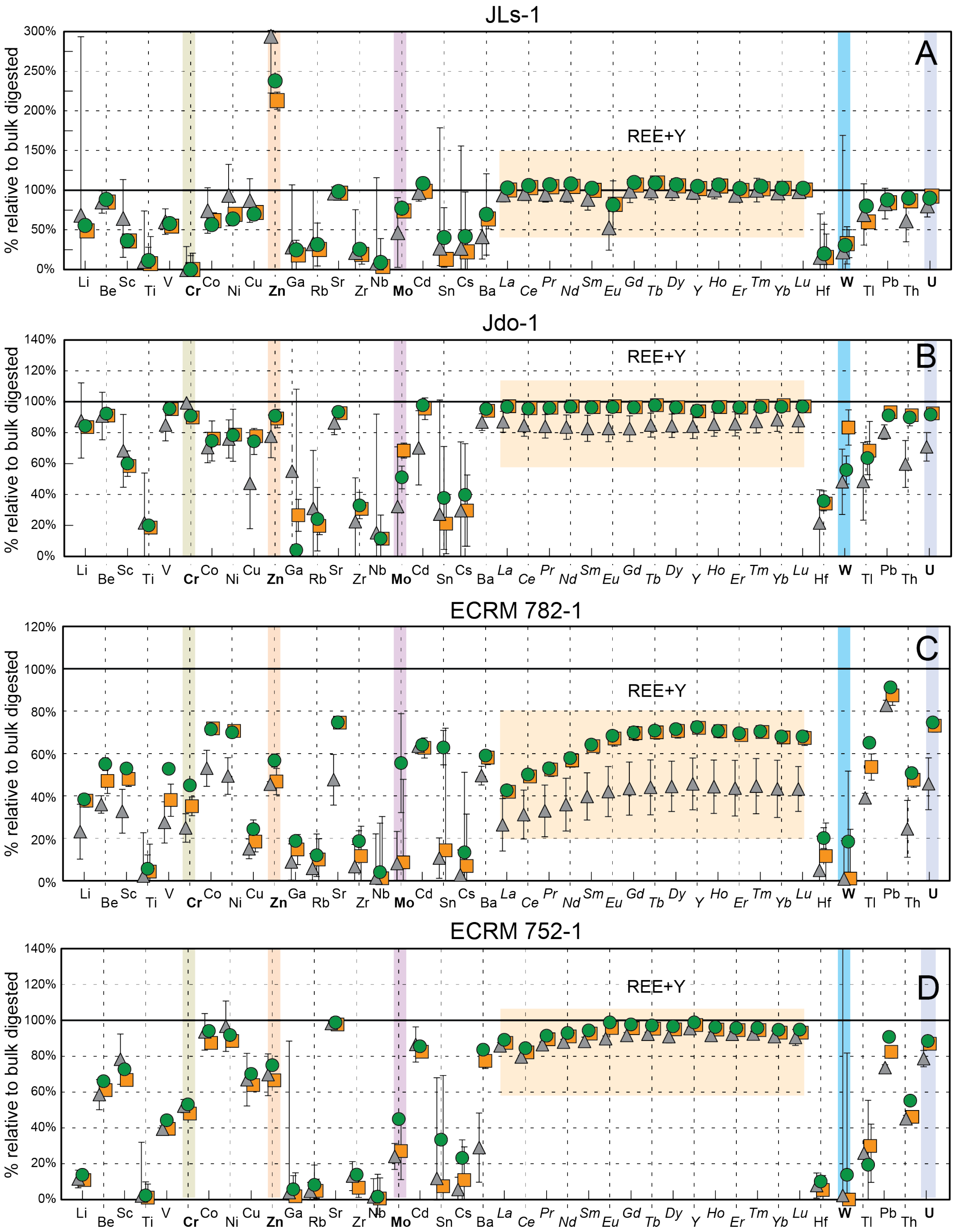

Figure 5.1: scatter plots of the average trace elements concentrations (vertical error bars are 1SD) of each type of leachate normalized to the bulk concentrations. Green circles represent HCl 3 M leachates, orange squares represent 5 % HNO_3 leachates, gray triangles represent HAc 5 M leachates. Horizontal black line represent the bulk concentrations. Emphasis is put on Cr, Zn, Mo, W, U and REE+Y elements with colorful arrays.

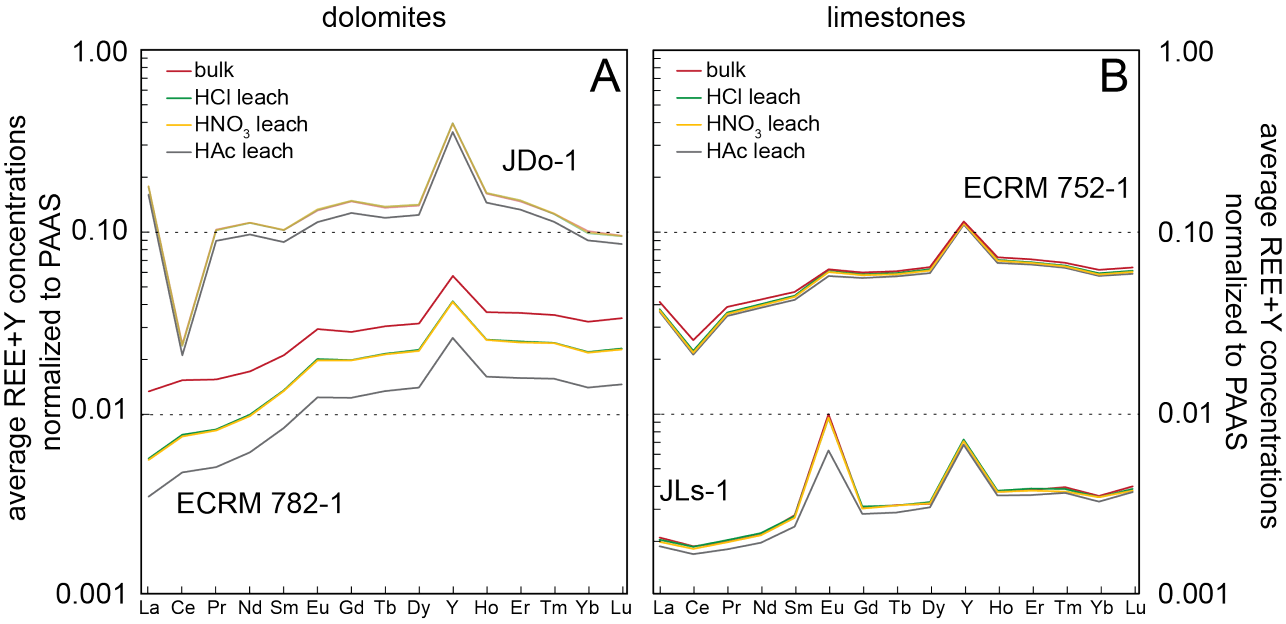

Figure 5.2: extended REE+Y patterns of the four carbonate reference material investigated in this study. REE+Y values of the PAAS originate from Pourmand et al. (2012).

W concentrations in carbonate leachates

The W concentrations in the leachates are typically lower than the ones of the bulk digested carbonates reference materials (Tables 5.3, 5.4, 5.5 and 5.6 and Figure 5.3), but the variability in W concentrations are independent from their lithology type (dolomite-limestone) and acid used.

The bulk JLs-1 rock reference material revealed a W concentration of 188.07 ng.g^{-1}, while W concentrations of the leachates decrease in the order of HNO_3 (61.54 ±5.44 ng.g^{-1}, 1SD, n=2), HCl (53.41 ±8.53 ng.g^{-1}, 1SD, n=3) and HAc (42.18 ±30.92 ng.g^{-1}, 1SD, n=10).

The bulk JDo-1 rock reference material has a W concentration of 282.63 ng.g^{-1}, while the leachates has W concentrations averages of 235.61 ±26.93 ng.g^{-1} (1SD, n=2) for HNO_3 leachates, 157.96 ±14.24 ng.g^{-1} (1SD, n=3) for HCl leachates and 136.27 ±28.77 ng.g^{-1} (1SD, n=6) for the HAc ones.

Surprisingly, the bulk digested aliquots of the ECRM 782-1 revealed extremely variable W concentrations from 25.83 to 295.45 ng.g^{-1}, with an average of 134.83 ±125.18 (1SD, n=7), while the HNO_3 and HAc leachates do not yield more than 1.49 ng.g^{-1} and 1.11 ng.g^{-1}, respectively. On the contrary, the HCl leachates revealed W concentrations from 18.99 to 30.68 ng.g^{-1}.

Similarly, the W concentrations of the HCl, HNO_3 and HAc leachates of the rock reference material ECRM 752-1 range from 3.59 ng.g^{-1} down to bellow detection limit, while

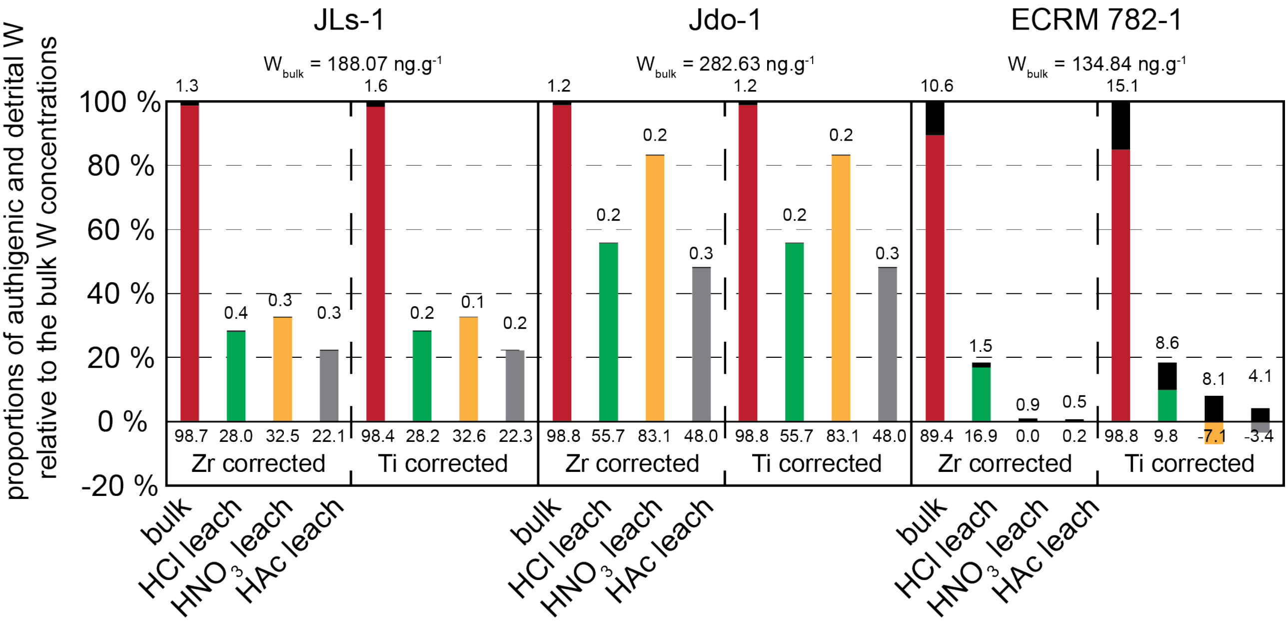

Figure 5.3: stacked column diagram of W concentrations in the leachates of carbonate reference materials JLs-1, Jdo-1 and ECRM 782-1 relative to the bulk digested. Black areas represent the detrital contribution to the total W in the samples calculated with the equation 5.1. The carbonate reference material ERCM 752.1 is not represented.

the bulk digested samples are characterized by a relatively homogenous W concentration of 17.56 ±1.52 ng.g^{-1} (1SD, n=3).

The contrasts in the HNO_3 and HAc leachates of the ECRM 782-1 and ECRM 752-1 rock reference materials compared to the HCl one are questioning, and indicates that only HCl 3 M mobilized W from the carbonate matrix.

Because the Th contents of the leachates are very high, the Ti and Zr concentrations are used to monitor the proportions of detrital-sourced W in the leachates. Based on the assumption that Ti, Zr and detrital W are leached from the detrital component in the same rates, the equation 5.1 enables to calculate the detrital W content of each leachate, using the UCC values from Rudnick et al. (2014).

$$W_{detrital} = Ti \times (W_{UCC}/Ti_{UCC}) \tag{5.1}$$

The results are plotted in Figure 5.3, relative to total W in bulk and leachates of the JLs-1, JDo-1 and ECRM 782-1. Globally, the HCl and HNO_3 leachates yield higher W concentrations in JDo-1 and JLs-1 compared to HAc ones, with minor contribution of detrital sourced W. On the other hand, the rock standard ECRM 752-1 revealed non-existent to negative authigenic W in the leachates associated a high proportion of calculated detrital-W in the leachates and in the bulk digested aliquots, indicating that W enrichments factors calculations are not appropriate for this rock reference material. The stacked column data of the carbonate reference material ECRM-752-1 is not represented due to its low W content.

The proportions of detrital sourced-W in all leachates of the JLs-1 and JDo-1 reference materials are very low and can be considered negligible. On the other hand, the carbonate reference material ECRM 782-1 bulk digested aliquots revealed very high contributions of detrital-W between 10.6 to 15.1 % of the total W.

5.3.3 Conclusions

Based on W concentrations and reproducibilities, only JLs-1 and JDo-1 standards are considered suitable monitoring rock standards for trace elements with the purpose of W isotope determination. The W concentrations in the leachates of these two rock reference materials range from 50 to 170 ng.g^{-1} and are representative of natural abundance of W in carbonates. The W yields in the leachates are relatively low, but enough for W chemical separation and isotopic composition determination.

Preliminary trace elements on carbonates from the 2.39 Ga Mooidraai Fm. revealed W concentrations as low as 20 ng.g^{-1}, requiring sample powder amounts for W isotope determination exceeding 1 g. As a result, a leaching step in 3 M HCl will be preferred for simplifying the process of large amount of sample powders and reducing the amount of acid used and conversion steps. Moreover, leaching carbonate powders with 3 M HCl has the advantage to shorten the sample preparation time and use of acid prior to loading onto the first column of the W separation chemistry in hydrochloric form.

However, the use of HCl for leaching is only relevant if sample-W and double spike-W can equilibrate in hydrochloric-acid based solutions. All previously reported $\delta^{186/184}$W values of sedimentary rocks in the literature were obtained with sample-spike equilibration during the digestion step in concentrated HF-HNO$_3$. No other study yet investigated sample-spike equilibration in HNO$_3$ or HCl solutions. As such, testing whether leachate-W and double spike-W can equilibrate in other acids than concentrated HF-HNO$_3$ is necessary.

5.4 Spike and sample W equilibration tests

This section focuses on the equilibration of carbonate W with double spike in both HCl and HNO_3 prior to separation chemistry. The aim of the following experiments was to test if W from carbonate sample and ^{180}W-^{183}W could equilibrate in HCl in order to simplify the leaching and separation chemistry for $\delta^{186/184}W$ determination.

5.4.1 Spike and sample W equilibration

Only two modern pure carbonate samples from the Bahamas were previously determined for W isotopic composition due to their high authigenic W concentrations (> 300 ng.g^{-1}) enabling bulk digestion of small sample aliquots. However, such carbonates are not representative of ancient ones which are silicified, have very low W concentrations (< 50 ng.g^{-1}) and require high sample amounts for a single W isotopic composition determination.

As such, one of the previously described Bahamas W-rich carbonates was diluted with a W-poor silicified Precambrian carbonate powder to replicate high sample loads and ancient matrix, but with a known $\delta^{186/184}W$ value.

5.4.2 Sample preparation

The hybrid carbonate sample is composed of a modern carbonate sample from the Bahamas as a W source with 485 ng.g^{-1} of W and a $\delta^{186/184}W$ value of $+0.193 \pm 0.010$ ‰ (2SE) previously determined on a bulk digested powder aliquot, and a silicified 2.39 Ga carbonate matrix sample from depth 205.65 m of the core NB-72, intersecting the Mooidraai Fm. (Transvaal Supergroup, South Africa) with a W concentration of 19 ng.g^{-1}. The Bahamas and Mooidraai carbonates powders were mixed with a ratio of 2:5 in weight, respectively. The target was to yield 10 times more W from the known Bahamas sample than from the silicified ancient sample.

Fourteen hybrid carbonates and 4 powders aliquots of each rock reference material JDo-1 and JLs-1 were prepared for the W equilibration experiments.

Between 0.2 and 1.5 g of carbonate powders were combined in 50 mL centrifuge tubes and covered with few mL of H_2O. Then, the carbonate powders were leached with the addition of drop wise HCl 6 M until reaching a theorical neutral solution. The carbonates powders were leached at room temperature and regularly resuspended. After two days, the samples were centrifuged and the supernatant were transferred to PFA beakers.

Equilibration in nitric acid: the samples for the nitric experiments were dried down and converted to nitric form with 2 mL of concentrated HNO_3. The samples were dried down, fluxed in 10 mL 5 M HNO_3 and spiked with adequates volumes of ^{180}W-^{183}W double spike. The samples were left to equilibrate in closed beakers on a hotplate at 100 °C for two days. Then, the samples were dried down and reconverted to HCl twice with concentrated HCl, and dried down again.

Equilibration in hydrochloric acid: the supernatants of the samples for the HCl experiments were directly diluted with the addition of 3 mL 6 M HCl and spiked with the ^{180}W-^{183}W double spike. The solutions stayed in closed beakers on a hotplate for 2 days at 100 °C and were dried down.

All spiked W samples were dissolved in 1.67 mL of HCl 6 M and put a few hours in a sonic bath to ensure full dissolution of the carbonate pellets. Then, 100 µM of concentrated H_2O_2 were added to the samples to digest potential organic matter and stayed at room temperature overnight. Finally, a volume of 8.23 mL of H_2O was added to the samples to yield a final volume of 10 mL and molarity of 1 M HCl. The samples were left overnight on a hotplate at 100 °C.

W chemistry

The chemistry protocol is identical to the one described by Kurzweil et al. (2018), with higher volumes of cationic resin in the first column (with 15 mL instead of 5 mL) than used for shales and paleosols in the previous chapters, in order to optimize the separation of W from high loads of carbonate matrix.

The samples in 10 mL of 1 M HCl were cooled down and 100 µL of H_2O_2 conc. was added to yield a concentration of 1 M HCl + 1 %v H_2O_2. The samples were transferred to 15 mL pre-cleaned centrifuge tubes and centrifuged 10 min at 5,000 rpm prior to loading onto the first column of W separation chemistry (15 mL of Biorad AG 50-W 100-200 mesh). The samples were directly collected with an extra 15 mL of HCl 1M + 1 %v H_2O_2.

Then, the samples were directly loaded onto the second column (2mL Biorad AG1x8 100-200 mesh) and rinsed with 1 M HCl + 1 % H_2O_2, 2 M HF, and were collected in 15 mL of HNO_3-HF. The W fractions were dried down and treated twice with concentrated HNO_3-H_2O_2 to digest the resin residues. Finally, the samples were fluxed in 6 M HCl and loaded onto the third column (2 mL TEVA resin), rinsed with 1 mL HCl and collected with 6 M and 4 M HCl.

Table 5.2: $\delta^{186/184}$W values of the carbonate samples measured in this study

Samples	$\delta^{186/184}$**W** ‰	2SE	yield	sample load (mg)
Hybrid sample, equilibration in HNO_3	0.183	0.013	40 %	205
	0.170	0.014	44 %	301
	0.191	0.014	53 %	502
	0.182	0.012	46 %	501
	0.192	0.013	57 %	707
	0.184	0.013	52 %	1,001
	0.192	0.016	54 %	1,505
Hybrid sample, equilibration in HCl	0.196	0.013	40 %	200
	0.190	0.015	29 %	301
	0.181	0.012	51 %	505
	0.185	0.013	51 %	508
	0.172	0.015	50 %	749
	0.193	0.014	37 %	1,028
	0.202	0.015	40 %	1,005
JDo-1, equilibration in HNO_3 (1)	0.063	0.018	33 %	144
JDo-1, equilibration in HNO_3 (2)	0.062	0.018	34 %	173
JDo-1, equilibration in HCl (1)	0.067	0.017	31 %	139
JDo-1, equilibration in HCl (2)	0.065	0.019	35 %	139
JLs-1, equilibration in HNO_3 (1)	0.039	0.020	43 %	175
JLs-1, equilibration in HNO_3 (2)	0.029	0.020	51 %	172
JLs-1, equilibration in HCl (2)	0.026	0.018	71 %	174
JLs-1, equilibration in HCl (2)	0.081	0.024	39 %	134

The collected fractions were dried down and treated with concentrated HNO_3-H_2O_2 to digest resin residues.

The samples were finally converted to the analyte solution of 0.56 M HNO_3 – 0.24 M HF, prior to measurement on MC-ICPMS NeptunePlus at the facilities of the University of Tübingen. The reference solutions NIST 3163 and in-house Alfa Aesar yielded $\delta^{186/184}$W values of 0.000 ±0.020 ‰ (2SD, n=20) and +0.056 ±0.021 ‰ (2SD, n=17) during the measurement session. The total procedure blanks yielded W concentrations of 135 to 140 pg.

Results

The hybrid samples, regardless of the acid used for equilibration, revealed a homogeneous $\delta^{186/184}$W average value of +0.185 ±0.018 ‰ (2SD, n=14), similar within uncertainty to the $\delta^{186/184}$W value of the modern Bahamas carbonate of +0.193 ±0.010 ‰ (2SE) previously determined on a bulk digested powder aliquot (Figure 5.4, Table 5.2).

The JDo-1 (dolomite) rock reference material yielded an average $\delta^{186/184}$W value of

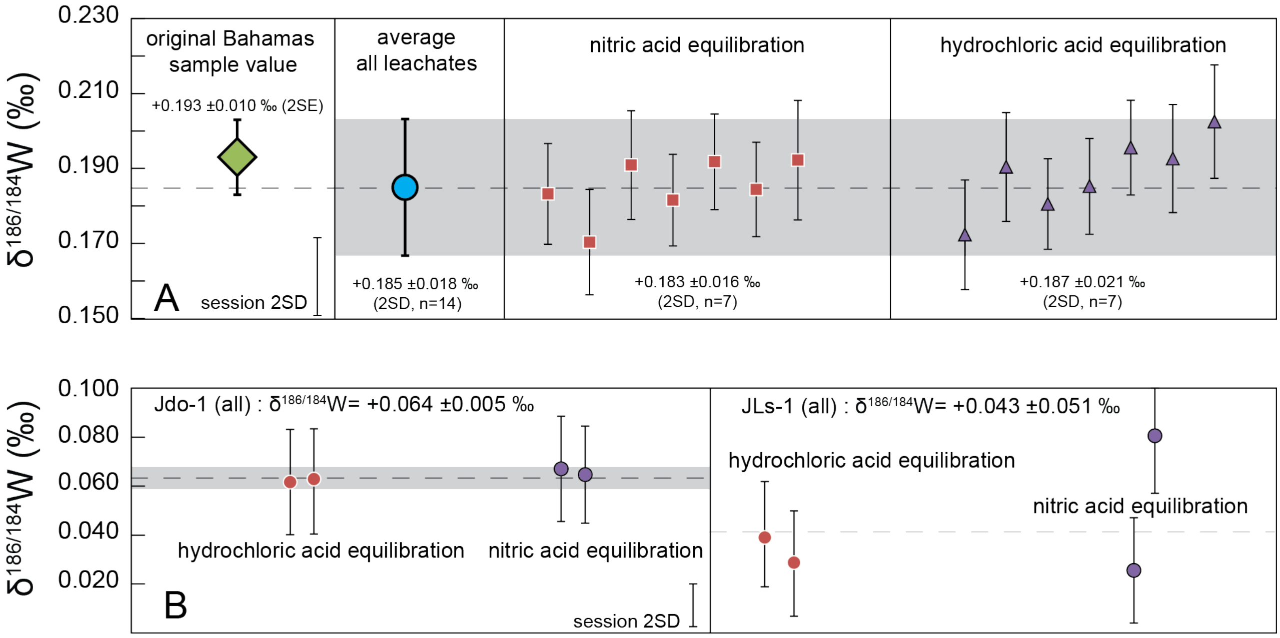

Figure 5.4: $\delta^{186/184}$W values of a) hydrib samples and b) rock reference materials JDo-1 and JLs-1.

+0.064 ±0.005 ‰ (2SD, n=4) for both equilibration method combined (Figure 5.4). The W concentrations of JDo-1 determined with MC-ICPMS concentrations ranged from 136.19 to 153.99 ng.g^{-1}.

The JLs-1 (limestone) rock reference material revealed an average $\delta^{186/184}$W value of +0.043 ±0.051 ‰ (2SD, n=4) (Figure 5.4). The W concentrations of JLs-1 determined with MC-ICPMS concentrations ranged from 47.92 to 59.00 ng.g^{-1}.

The W chemistry yields range from 31 to 57 %, regardless on the amount of sample processed. The variability of yields already showed to have no influence on the $\delta^{186/184}$W values of shales and igneous rocks (see section 2.6.4). Still, improvement of the chemical separation or more frequent replacement of the cationic resin might be required to increase the W chemical yields.

5.4.3 Conclusions

Carbonate-W and double-spike-W equilibration efficiency was investigated in both HCl and HNO_3 solutions. Shortly:

- Sample-spike equilibration can be done with HCl or HNO_3
- The blanks represent less than 0.5 % of the total W (135 to 140 pg).
- JDo-1 rock reference material seems more homogeneous than JLs-1.

Conclusively, the preferred protocol for leaching carbonate samples prior to the W separation chemistry is based on one single HCl leach on large sample material amounts (> 1 g) for both trace elements and W isotopic composition determination. After leaching 2 days in 3 M HCl, an aliquot of the leached samples is taken out and prepared for trace element determination. As such, accurate addition of W double spike to the samples in HCl prior to chemistry enable to target an ideal sample-spike ratio.

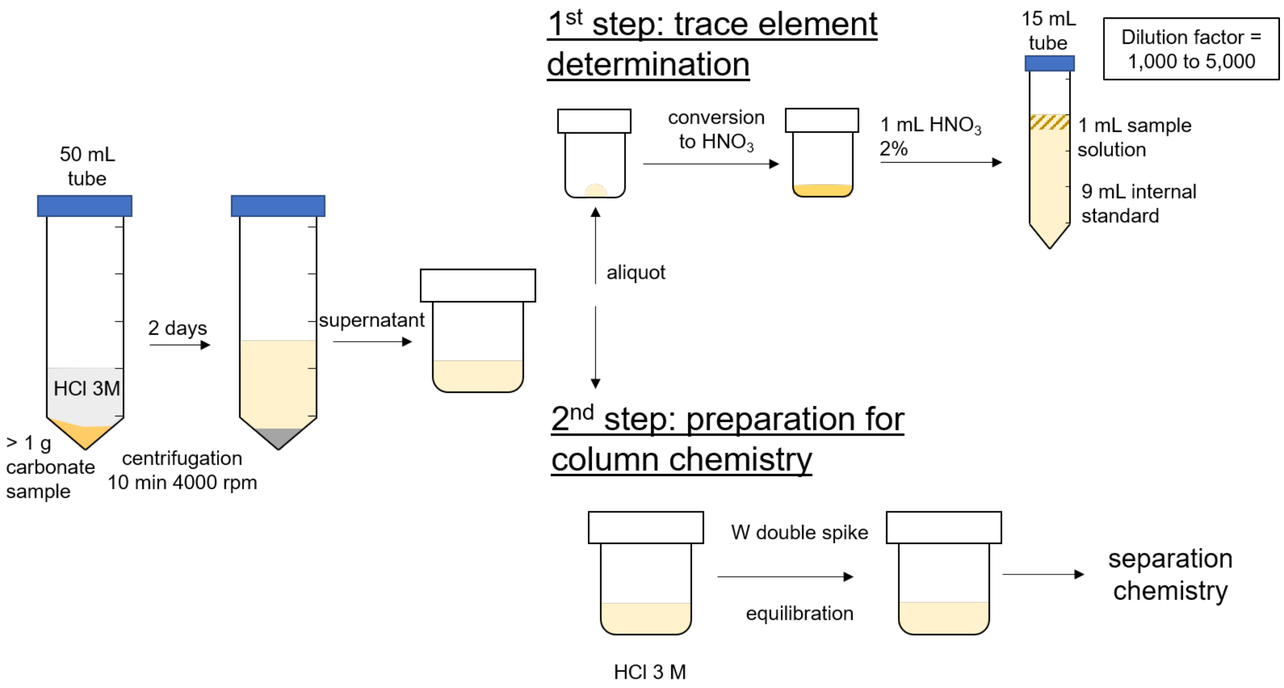

Figure 5.5: simplified procedure for leaching of carbonate matrix prior to W separation chemistry .

5.5 Carbonates $\delta^{186/184}$W values through time: preliminary data and potential for future work

This section is a preliminary survey of the W isotopes in carbonates with two main targets: testing whether modern carbonates $\delta^{186/184}$W values mirror the one of the open ocean, and if ancient carbonates $\delta^{186/184}$W enables to track the redox state of the ocean through time.

Various carbonate samples deposited in marine and continental settings up to 2.39 Ga ago were processed for W isotope determination following the HCl leaching protocol described previously, with the exceptions of two modern Bahamas carbonates which were bulk digested and measured for $\delta^{186/184}$W at an early stage of this thesis project.

5.5.1 Samples

Modern carbonates from Bahamas

Surface carbonate sands were collected from the Bahamas archipelago from shallow, open marine settings. Their carbonate sands are dominated by aragonitic grains, with minor magnesian calcite grains. Sample BD was collected in 2013 from Big Darby Island (approximate sample location 23.856032 N, 76.226015 W). Sample EL was collected in 2017 from Eleuthera Island (approximate location 24.619114 N, 76.145534 W).

Core 5A travertines

The core 5A from the FAR-DEEP project (Fennoscandian Arctic Russia- Drilling Early Earth Project, International Continental Scientific Drilling Program ICDP) intersects the 2,058 ±2 Ma Kuetsjärvi Sedimentary Formation in the Pechenga Greenstone belt (GSB) (5.6). This formation records the end of the Lomagundi Jatuli Event with $\delta^{13}C_{carb}$ values of +6 ‰ to +9 ‰ across the marine sedimentary units (Melezhik et al., 2007). The travertines of the core 5A of the Penchenga GSB formed as thermal, autochthonous and volcanic-related travertines (Melezhik and Fallick, 2001). The shape of the travertines mounts and laminas indicates that they formed on a flat short-term active spring under an arid to semi-arid climate, most likely on a coastal plain. Then, as the activity of the springs decreased an eventually stopped, the surfaces of the travertines were dissolved, coated by silica and buried under sub-aerial, red silty sandstones (Melezhik and Fallick, 2001). The original estimated $\delta^{13}C_{carb}$ of the travertines is of -6.0 ‰

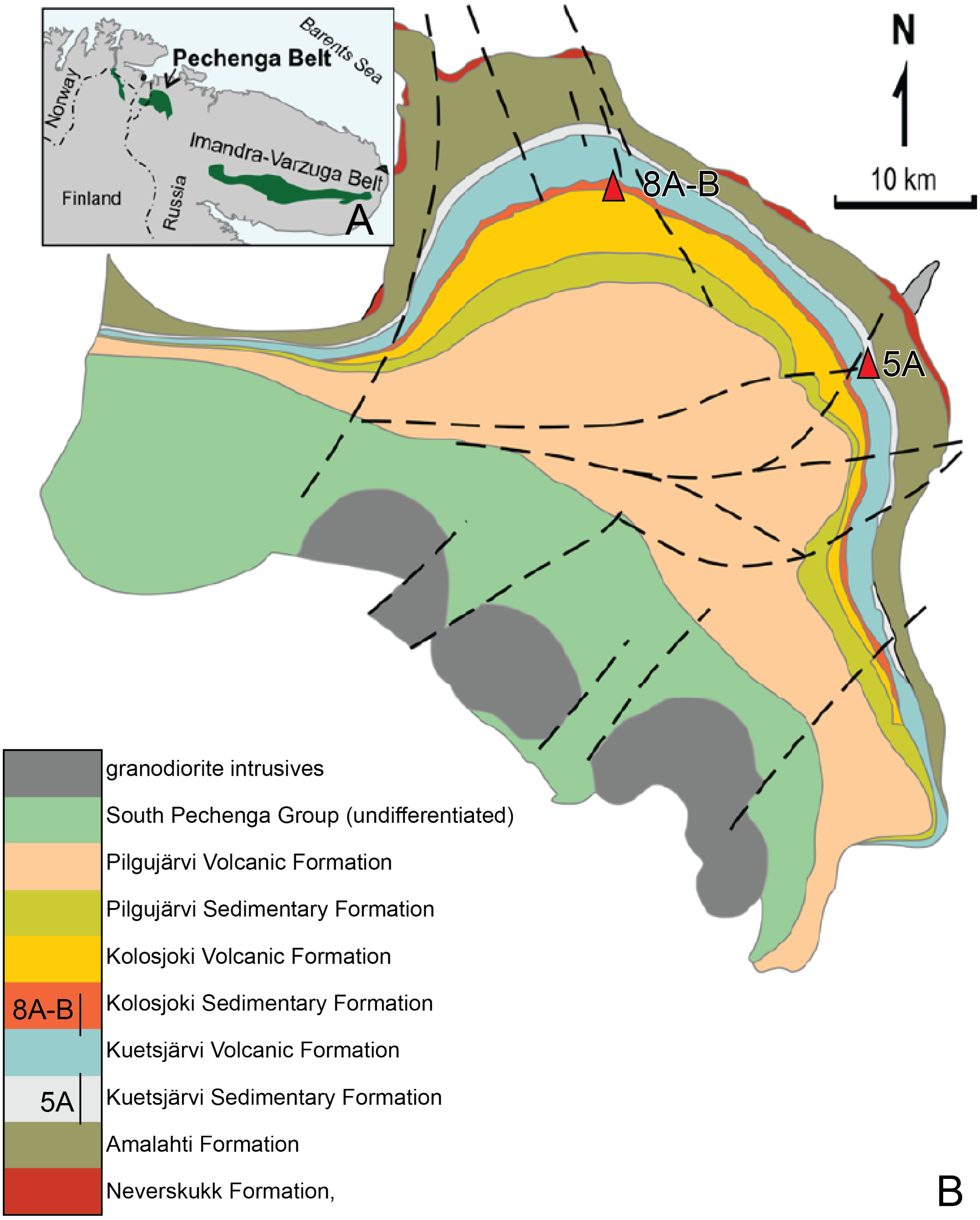

Figure 5.6: a) location of the Pechenga Greenstone belt. b) simplified geological map of the Pechenga Group, with localisation of the cores 8A-B and 5A (modified from Melezhic et al. (2012) and Joosu et al. (2016)).

and points toward volcanic-sourced CO_2 (Melezhik and Fallick, 2001).

The core 5A is thoroughly described in Melezhik et al. (2012). Briefly, two intervals of dolomite units are reported in this core, with the Lower (92-52.17 m) and Upper (40.3-57 m) Dolostone members. The Lower Dolostone member is dominated by dolarenites, sparry dolostones and micritic dolostones. Numerous occurences of travertines crusts, veinlets and small mounts are recorded. Two travertine samples (56.83 and 77.53 m) were sampled from this interval. The Upper Dolostone member is characterized by a diversity of lithologies, with dolostones, limestones, dolarenite, calcarenite, stromatolitic dolostones, travertines, shales, siltstones and sandstones. These units display desiccation figures, dissolution cavities and encrusting of travertines, indicating a shallow to subaerial depositional environment. The thickness of travertine crusts from the Upper Dolostone member range from millimetric to tens of centimeters. Two travertine samples (28.17 and 56.83 m) were sampled from this interval.

Core 8B marine carbonates

The 2.055 ±2.3 Ma Kolosjoki Sedimentary Formation in Penchenga GSB overlays the Kuestsjärvi Sedimentary and Volcanic Formations (Martin et al., 2013), and show $\delta^{13}C_{carb}$ values typical of post Lomagundi Jatuli Event (average $\delta^{13}C_{carb}$ of $+1.9 \pm 0.3$ ‰ Melezhik et al. (2007)). The Formation consists in volcaniclastic red beds, haematite-rich lithofacies, and marine carbonates.

The core 8B of the (FAR-DEEP) intersect the lower part of the Kolosjoki Sedimentary Formation (5.6). The samples investigated here originate from the Dolostone member, a 40 m thick unit composed of calstic, microsparitic and stromatolitic dolostones (Melezhik et al., 2012). This sedimentary unit deposited in a shallow marine environment, with occurrence of oolites, oncolites, microbial lamination and stromatolites. Several episodes of subaerial exposures were recorded with the occurrence of karsts, carbonate breccias and travertines/tufa deposits. The lower part of the Dolostone member is intensively silicified (SiO_2 from 17 to 48 %).

Mooidraai Formation marine carbonates

The 2.394 ±26 Ma Mooidraai Dolomite Formation belongs to the Postmasburg Group, upper Transvaal Supergroup, and is found in the Prieska Bain and Ghaap Plateau in South Africa. It deposited above the Hotazel Formation and is unconformably overlaid by the Olifantschoek Group (Bau et al., 1999). The Mooidraai Formation experienced early diagenesis (dolomitization) followed by silicification at temperatures from 120 and 150 °C, sealing the system and protecting the primary isotopic composition of the micritic dolomite (Bau et al., 1999). The Mooidraai Fm. represents the end-member of chemical precipitation that produced the cyclic Mn-Fe rich Hotazel Fm. sequence (Tsikos et al., 2001). The REE+Y signatures of the Mooidraai Fm. are comparable to the one of the modern-day seawater, but without Ce anomaly, which were interpreted as a return of marine anoxia after the deposition of the Hotazel Fm. (Bau and Alexander, 2006).

The Mooidraai samples used in this study originate from the exploration drill core MP-72, South Africa, with the courtesy of the Hotazel Manganese Mines© and BHP© companies. Six carbonate lithologies were identified based on the detailed facies analysis of Kunzmann et al. (2014), representing six depositional environments (Figure 5.7) .

The transition from the Hotazel to Mooidraai Formations is found at depth of 304.34 m. The lower part of the Mooidraai Fm. in the core MP-72 is typified by 10 meters of microbialamine. Microbialamine is composed of centi- to decametric- thick massive dolarenite alternated with millimetric crinkly and undulating microbial laminae. Dispersed fenestrae and bird eyes can be found. The microbialamine facies formed in shallow – subtidal – lagoonal environments.

A massive slope breccia of 22 m lies over the microbialamine facies starting from 293.5 m. The clast-supported breccia is composed of polygenic and poorly sorted clasts, from angular to subrounded. Still, the clasts are composed of lithofacies types typical of the Mooidraai F., suggesting an intraformation origin. Few layers of rythmite clasts intercalate with breccia layers, pointing towards a substorm wave base origin.

A thick uniform carbonate-greenalite-magnetite lithofacies is found from 265.4 to 228.7 m and is dominated by laminated rythmite and few massive dololutite, with 8 m of regularly laminated jaspelite from 249.6 to 241.6 m (see picture B and C in Figure 5.7). A few syn-sedimentary deformations occur in this unit. This section of the Mooidraai Fm. deposited in foreslope to platform margin depositional settings, characterized by gravital collapse and storm-reworking, remobilizing the sediment as homogenous layers of massive dololutite. The iron-rich unit of the Mooidraai core MP72 consists in alternation of dark red hematite-rich carbonate with few fine dark laminations of magnetite. Some irregular contacts and asymmetric bedding indicate the influence of currents or storms in the depositional environment. The upper part of the carbonate-greenalite-magnetite lithofacies is dominated by rythmite (see picture A in

Figure 5.7).

The transition from the rythmites to the overlying stromatolites and microbialaminite deposits is gradual. This lithofacies is characterized by alternation of undulating and crinkly microbial laminae, and by massive stromatolitic domes at the uppermost part. These sediments deposited in supratidal and upper intertidal environments.

The rest of the Mooidraai Fm. has been eroded and covered by modern soil. Still, the sequence observed in the core MP-72 is similar to the full sequences reported by Kunzmann et al. (2014), indicating that most of the Mooidraai Fm. was conserved in the core. Globally, the sedimentary sequences observed in this core recorded a transgressive-regressive cycle, similarly to the ones observed in the underlying Hotazel Fm.

5.5.2 Methods

Between 100 mg to 2 g of carbonate powder (excluding the modern carbonates from the Bahamas archipelago) were scaled in 50 mL centrifuge tubes and leached with 3 M HCl for two days. Upon dissolution of the carbonate matrix, the samples were centrifuged and the supernatant transferred to PFA beakers. A solution aliquot from 35 to 200 µL was taken out of the solution and dried down. The mother solutions were dried down and stored.

The aliquots were converted twice to nitric acid form with 100 µL and 200 µL. The aliquots were diluted to reach a dilution factor of 1,000 to 3,000 and measured for trace element composition determination.

Adequate amounts of W double spike (in HNO_3 -HF) were added to the dried samples and immediately evaporated on a hot plate at 85 °C. The dried spiked samples were refluxed in 4 mL of 9 M HCl and left on a hotplate to equilibrate at 120 °C for 24 h. The Bahamas carbonates were bulk digested during an early stage of the PhD in 2019.

Finally, the samples were dried down and processed for W separation chemistry as detailed in the section 5.4.2.

The collected W fractions were measured on the NeptunePlus MC-ICPMS. The measurement session of the leachates yielded $\delta^{186/184}$W values of 0.000 ±0.019 ‰ (2SD, n=8) on NIST 3163 and of +0.048 ±0.017 ‰ (2SD, n=6) on the Alfa Aesar monitoring solution. The measurement session of the bulk digested Bahamas samples yielded $\delta^{186/184}$W values of 0.000 ±0.018 ‰ (2SD, n=27) on NIST 3163 and of +0.055 ±0.022 ‰ (2SD, n=15) on the Alfa Aesar monitoring solution. Two leached rock reference material JLs-1 yielded $\delta^{186/184}$W values

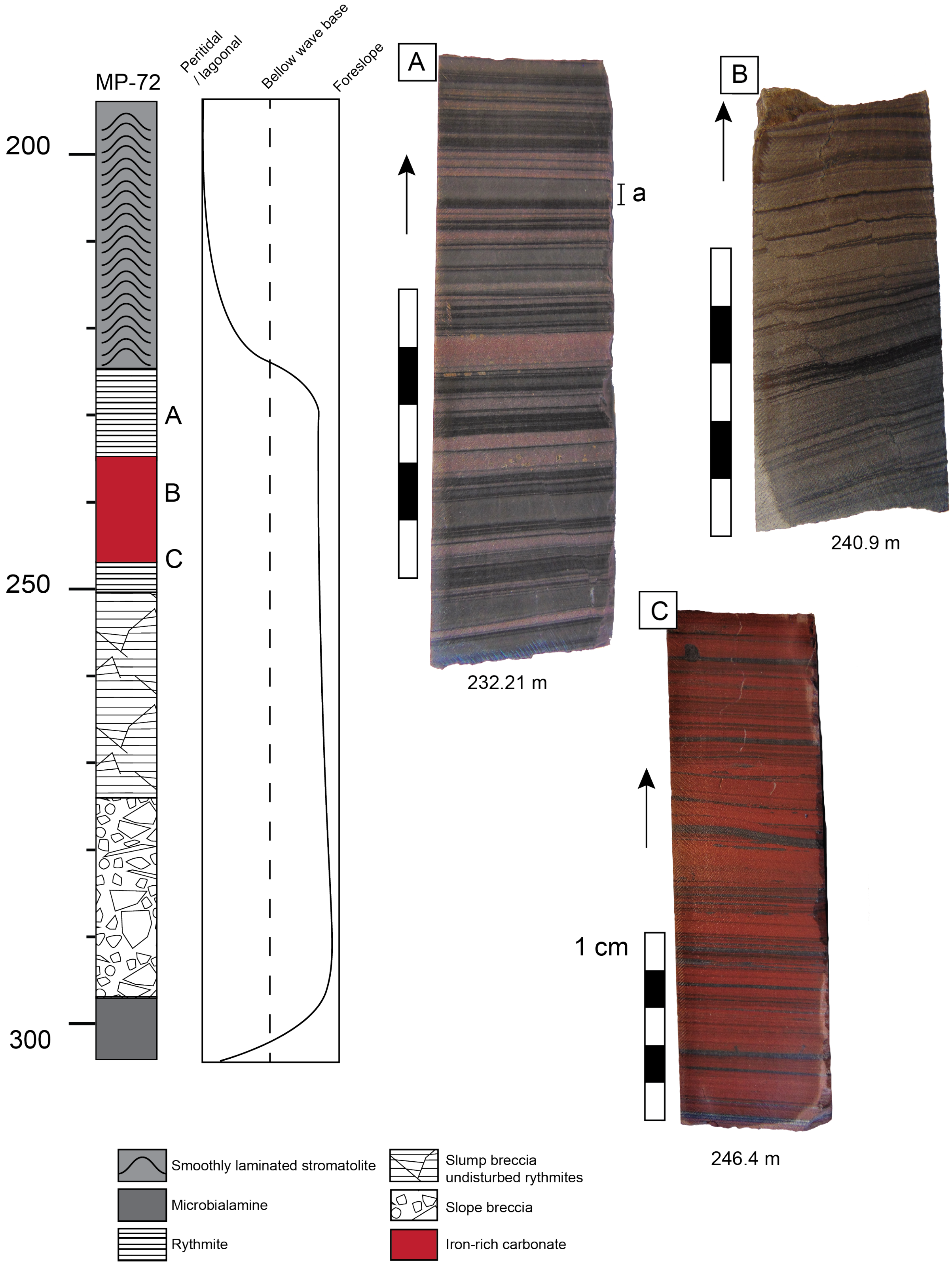

Figure 5.7: simplified lithological description and reconstructed depositional environment of the Mooidraai Fm. intersected in the core MP-72. Pictures A represents a carbonate bearing rythmite with jaspelite-rich intervals with few disseminated mm-pyrite nodules. Picture B represents an Fe-poor carbonate of the carbonate-greenalite-magnetite sequence, with few small-scale syn-sedimentary deformations. Picture C represents a jaspelite-rich sample, characterized by a very high W concentration of 1.6 µg.g^{-1}.

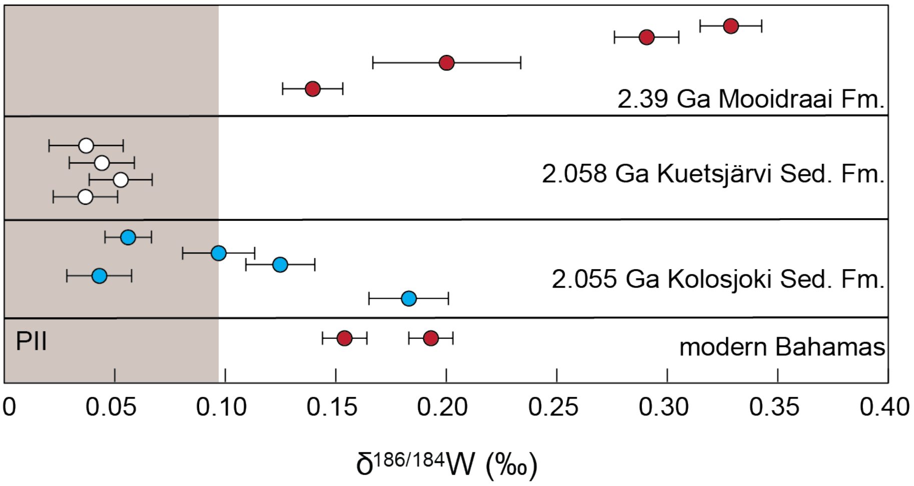

Figure 5.8: overview of the range of $\delta^{186/184}$W measured on carbonates in this study. Horizontal error bars represent the 2SE of each sample. Red circles represent open marine carbonates, blue circles represent shallow to restricted marine environments, white circles represent continental carbonates

of +0.050 ±0.015 ‰ and +0.049 ±0.014 ‰, and W concentrations of 50 and 169 ng.g^{-1} for the leached (ancient carbonates) and bulk digested (Bahamas carbonates session) powder aliquots, respectively. The leached rock reference material JDo-1 revealed a $\delta^{186/184}$W value of +0.029 ±0.014‰, lower than the average $\delta^{186/184}$W of +0.064 ±0.005 ‰ with a W concentration of 141 ng.g^{-1} reported in section 5.4.2. The W concentrations of the blanks were of 38 and 44 pg. Overall, the yields ranged from 46 to 80 %.

5.5.3 Results and discussion

Modern carbonates versus open ocean $\delta^{186/184}$W values

The bulk-digested modern Bahamas carbonates BD and EL yielded $\delta^{186/184}$W values of +0.154 ±0.10 ‰ (2SE) and +0.193 ±0.10 ‰ (2SE) with concentrations of 317 and 485 ng.g^{-1} (MC-ICPMS determined), respectively.

These values are significantly lighter than that of the open modern ocean (Fujiwara et al., 2020; Kurzweil et al., 2021). The influence of isotopically light W from the detrital component onto the bulk $\delta^{186/184}$W values of these two samples cannot be excluded, but the variations in W concentrations between acetic acid leachates (Herrmann et al., non-published; table 5.7) and bulk digested sample powders appears to be related rather to sample heterogeneity rather that detrital W contamination.

The $\delta^{98/95}$Mo values of non-skeletal carbonates are expected to mirror the one of the open ocean (Voegelin et al., 2009), but published modern (< 1 Ma) carbonate Mo data reveal a very large spread of $\delta^{98/95}$Mo values from +0.007 to +2.42 ‰ (see Thoby et al. (2019) and references therein). Such variations in $\delta^{98/95}$Mo values can source from detrital input of Mo, delivery mode of Mo to the sediment and early diagenesis processes. The latter is responsible for the seawater-like $\delta^{98/95}$Mo value of modern carbonates from the Bahamas archipelago deposited with euxinic porewater (50-100 µM H_2S), while carbonates with lower H_2S levels (<11 µM) yielded $\delta^{98/95}$Mo values ∼1.0 to 1.2 ‰ lighter than that of the open ocean (Romaniello et al., 2016).

Dissolved W is not prone to authigenically enrich the authigenic component of euxinic sediments, and is refluxed to the water column during early diagenesis and associated reductive dissolution of Mn-Fe oxides in the pore-water of modern estuarine sediments (Mohajerin et al., 2016). The observation of high W (317 and 485 ng.g^{-1}) but low Mo concentrations (41 to 61 ng.g^{-1}) indicates that likely the surface sands investigated here deposited with non-euxinic porewater. Tungstate and molybdate can be delivered to the sedimentary-water column interface with particles (oxides, organic matter, clay minerals), and incorporate the authigenic fraction of the sediment. Such transport mechanism can be responsible for the high W concentrations and for the relatively light $\delta^{186/184}$W values of the Bahamas sediments, yielding similar $\delta^{186/184}$W values than a Fe-Mn crust from the modern Pacific ocean with an average $\delta^{186/184}$W value of +0.154 ±0.013 ‰ (2SD, n= 6) (Kurzweil et al., 2018).

This short survey demonstrates that the $\delta^{186/184}$W values of marine carbonates do not necessarily mirrors the one of the open ocean, but might reflect the delivery mode of W to the sediment and/or diagenesis processes. Robust reconstitution of the ocean redox state with the use of W stable isotopes in the carbonate archive requires more knowledge about W isotopes in modern carbonates. Ideal targets for future work are represented by marine carbonates with lower W concentrations, mostly sourcing from diffusion of WO_4^{2-} from the water column with higher potential to mirror the seawater $\delta^{186/184}$W value.

Continental signals

The core 5A travertines samples (n=4) revealed $\delta^{186/184}$W values ranging from +0.037 to +0.053 ‰, with W concentrations from 4.650 to 22.940 µg.g^{-1}. Travertines are continental carbonates originating from CO2-saturated groundwater degassing upon contact with the atmosphere, leading to the deposition of successions of carbonated crusts or mounts. The core 5A recorded the occurrence of basaltic flows above, under and within the Kuetsjärvi Sedimentary

Formation, indicating that these sediments deposited in a zone of high thermal gradient and intense hydrothermal circulation. Per example, signs of post-magmatic alteration are found in the abnormally KO_2-rich (6.3 wt. %) ferropicrite body found in the core 5A (92-97 m) between the two Dolostone members of the Kuetsjärvi Sedimentary Formation (Melezhik et al., 2013).

The experiments of Osvald et al. (2021) revealed that W-minerals were very efficiently leached in an artificial geothermal system, whose leachates yielded W concentrations from 1-182 µg.g^{-1}, in good agreement with modern travertines from Central Anatolia characterized with high W concentrations from 4.4 to 19.0 µg.g^{-1} (Temiz et al., 2021).

The source of such W in the core 5A travertines has not yet been constrained, but the chemical signals points towards igneous rocks as a W source. The representation of W (4.07 to 18.61 µg.g^{-1}) and cobalt (Co, 3.87 to 17.87 µg.g^{-1}) concentrations space revealed a very strong positive linear correlation (R^2=0.90, n=5, not represented), and implies that W and Co were conservatively removed and transported to the surface by hydrothermal fluids. Carbonates are usually depleted in Co (average of 0.1 µg.g^{-1}; Krauskopf and Bird (1995)), while ultramafic, mafic and granite igneous rocks show an average Co content usually exceeding 41 µg.g^{-1} (Dehaine et al., 2021). Little is known about Co during hydrothermal alteration, but acid hydrothermal fluids (273 to 355 °C) from the Pacific east rise were found 3 to 4 order of magnitude more enriched in Co than the initial basalt (Von Damm et al., 1985). Similarly, W concentrations are up to five orders of magnitude higher in hydrothermal fields (210 to 123,000 pM) than the modern seawater (0.54 pM) (Kishida et al., 2004). As such, it is more likely that the high Co and W concentrations in the travertine samples of the core 5A sourced from leached igneous rocks, rather than sediments. Finally, the homogeneous average $\delta^{186/184}$W value of the travertines (+0.043 ±0.015 ‰; 2SD; n=4) is comprised in the Precambrian igneous inventory $\delta^{186/184}$W range (-0.010 to +0.097 ‰). This short investigation of W isotopes in travertines reveal that continental hydrothermal input might be an important flux of W to the ocean, with an $\delta^{186/184}$W value reflecting the ones of the rock sources.

Shallow marine stromatolitic carbonates

The shallow marine carbonates (n=5) of the core 8B revealed $\delta^{186/184}$W values from +0.043 to +0.183 ‰, with W concentrations from 13 to 166 ng.g^{-1}.

The space of 1/W concentrations and $\delta^{186/184}$W values (not represented) reveals a strong positive trend (linear R^2 of 0.98, n=5) and indicates that the core 8B stromatolites are composed of two endmembers, one with a relatively heavy $\delta^{186/184}$W value of +0.183 ‰ with low W concentration of 12.42 ng.g^{-1}, and one with a low $\delta^{186/184}$W value of 0.043 ‰ but with ten times higher W concentration of 150.91 ng.g^{-1}.

Three W sources are expected in such depositional environment, (1) marine , with a heavy $\delta^{186/184}$W value and low W concentration, (2) riverine, of unknown $\delta^{186/184}$W value, (3) and detrital, with a $\delta^{186/184}$W value from -0.010 to +0.097 ‰ and relatively high W concentration.

The mixing of detrital and authigenic W is a plausible explanation for the correlation between $\delta^{186/184}$W values and W concentrations. However, the heaviest $\delta^{186/184}$W value measured (+0.183 ‰ ±0.018 ‰, 2SE) is also associated with the highest Th (186 ng.g^{-1}) and Ti (2.64 µg.g^{-1}) concentrations measured for this sample set, and do not agree with the common agreement that detrital sourced W is associated with crustal $\delta^{186/184}$W values from -0.010 to +0.097 ‰.

In this short study, two mechanisms for the variations in W concentrations and $\delta^{186/184}$W values in these samples are proposed, with (1) early diagenesis processes in the stromatolite mat, and (2) mixing trends between riverine and continental hydrothermal-sourced W.

Stromatolitic mats are microenvironments whose microbial communities, pH, dissolved O_2 and H_2S content vary in depth (Dupraz and Visscher, 2005). As a result, the distribution of transition metals and metalloids in stromatolites depends on the type of depositional environment and in-situ chemical conditions of the porewaters. The study of the 3.48 Ga Dresser Fm. marine stromatolites revealed association of Zn, Co and Ni with organic-rich nano-porous pyrite, with large vertical heterogeneity (Baumgartner et al., 2020).

Similarly, we report linear positive correlations between Ni and Co (R^2=0.99, n=7), Ni and Zn (R^2=0.77, n=7), Co and Zn (R^2=0.79, n=7) in the leachates of the core 8B stromatolites (not represented). These three elements negatively correlate with W concentrations, but positively with the $\delta^{186/184}$W values of the five carbonates samples (Figure 5.9). As such, the processes that enriched the stromatolites in Co, Ni, and Zn did not enable significant enrichments of W, such as euxinic porewater. On the other hand, the samples with higher W concentrations deposited under conditions than efficiently drew down WO_4^{2-} from the water column or porewater, but did not accumulate Co, Ni and Zn.

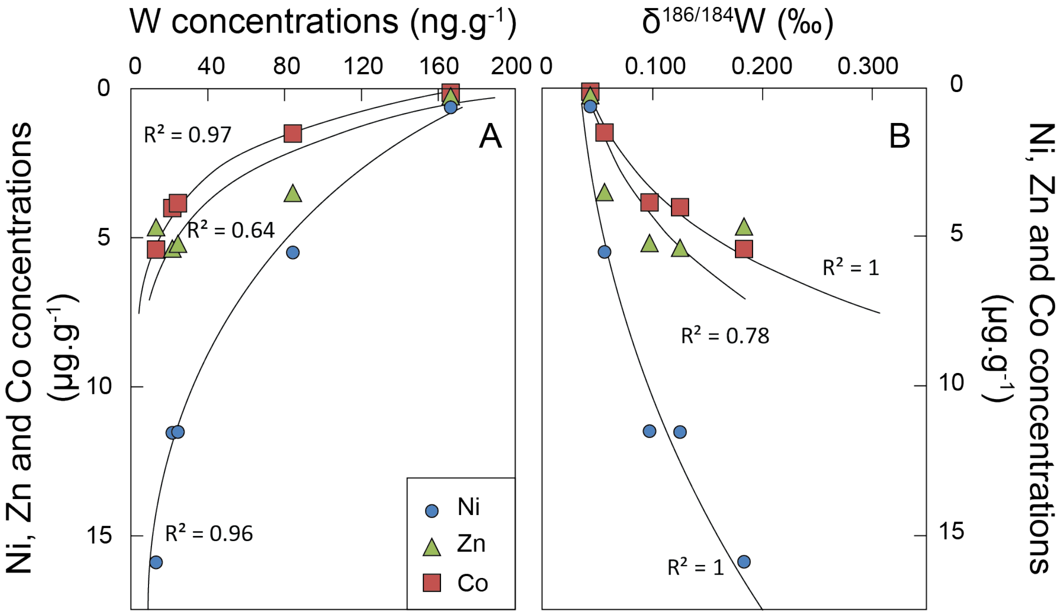

Figure 5.9: Co, Ni and Zn concentrations space W concentrations (A) and $\delta^{186/184}$W values (B) of the shallow marine stromatolites of the core 8B. Trendlines are exponential.

Carbonate $\delta^{186/184}$W record during the early stages of the GOE

The core MP-72 of the Mooidraai Formation revealed $\delta^{186/184}$W values from +0.140 to +0.329 ‰, with W concentrations from 41 to 1,773 ng.g^{-1}. The Y/Ho weight ratios of these carbonates leachates range from 47.76 to 63.55. Interestingly, the Y/Ho ratios decrease upwards in the stratigraphy, alongside the change of water depth.

The sedimentology of the core MP-72 reveal a progressive marine regression, from a foreslope to a lagoonal to peritidal depositional environment. Associated with the change in sea level, the $\delta^{186/184}$W values of the carbonate formation decrease upwards, starting from +0.329 to +0.291 ‰ in deep settings, towards lighter $\delta^{186/184}$W values at the coastal depositional environment upwards in the core.

The change in $\delta^{186/184}$W values with decreasing water depth indicates that likely the $\delta^{186/184}$W value of carbonates deposited in shallow environments do not mirror the one of the global ocean. Likely, the carbonate sample from the foreslope (262.4 m) with a $\delta^{186/184}$W value of +0.329 ±0.014 ‰ is closer to the one of the open ocean, while carbonates deposited in shallow environments recorded other processes, such as adsorption onto organic matter, early diagenesis, Mn-Fe oxides precipitation in the carbonates, etc. The jaspelite-rich carbonate of depht 262.4 m revealed similar $\delta^{186/184}$W values that surroundings carbonates, but with high W concentrations. As such, it is possible that the removal of tungstate from the seawater to iron-rich sediments is quantitative. The study of $\delta^{186/184}$W values in the iron-rich sediments of

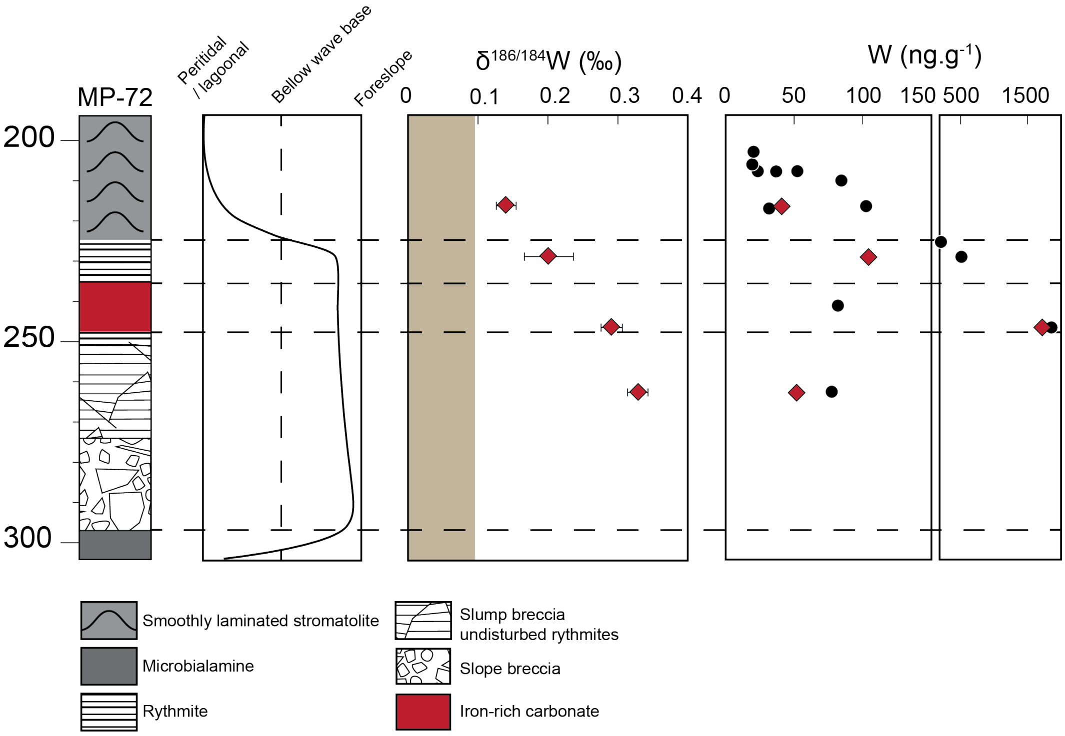

Figure 5.10: stable W isotopic composition of the Mooidraai Fm. intersected by the core MP-72. Red circles represent $\delta^{186/184}$W and W concentrations obtained on leachates, black circles represent W concentrations measured on bulk digests. The W concentrations of these samples are plotted in two difference spaces with different scales.

the underlying Hotazel Fm. may provide informations about the W cycling prior to the GOE.

Conclusively, carbonates deposited in deeper environments are more likely to record the $\delta^{186/184}$W value of the open ocean compared to shallower carbonates.

Interestingly, these carbonates deposited during the early stages of the GOE, and reveal isotopically heavy $\delta^{186/184}$W values, likely due to efficient draw-down of isotopically light W with oxides in shallow environments. The investigation of the stable W isotopic composition of the underlying Hotazel Fm. Fe and Mn-rich marine sediments combined with higher resolution sampling in the Mooidraai Fm. has the potential to track the earliest changes in the cycling of W associated with the rise of molecular oxygen.

5.5.4 Conclusions

The carbonates investigated in this Chapter revealed a large spread of $\delta^{186/184}$W values. General conclusions can be drawn from these preliminary data :

- The $\delta^{186/184}$W values of modern carbonates were lower than the one of the modern seawater, and indicates that the delivery mode of dissolved W to the carbonate porewaters might influence its $\delta^{186/184}$W value.

- The W concentrations and $\delta^{186/184}$W values of travertines highlights the role of hydrothermalism to the supply of W to the riverine and ocean systems. The proportions of hydrothermal and ground water inputs of W might be exceeding the respective ones of Mo.
- Stromatolitic carbonates likely do not mirror the $\delta^{186/184}$W value of the open ocean, but rather early diagenetic processes.
- The $\delta^{186/184}$W values of Precambrian marine carbonates vary depending on their depositional environment. Globally, shallow environments reveal ligher $\delta^{186/184}$W values, originating from adsorption processes or from light $\delta^{186/184}$W inputs from the continents. Deeper depositional settings revealed heavier $\delta^{186/184}$W values associated with low W concentrations (typically below 100 ng.g^{-1}), and might represent the stable W isotopic composition of the ferruginous open ocean.

Future research : next studies should focus of modern carbonates from various depositonal environments and hydrographical conditions (open, restricted, various bioproductivity levels, currents, waves, etc) to test for their ability to mirror the modern $\delta^{186/184}$W ocean value.

The modern W inputs to the ocean (hydrothermal systems, groundwaters, rivers, eolian) should be carefully constrained to ensure a better understanding of the modern and ancient W cycling in aqueous environments.

Then, higher resolution investigation of $\delta^{186/184}$W values of Precambrian marine carbonates deposited in deep to shallow environments and comparison to the $\delta^{98/95}$Mo carbonate record might enable to track the earliest changes in the ocean-atmosphere system.

Table 5.3: JLs-1 rock reference material trace element concentrations in bulk and leachates 1/4

(ng.g^{-1})	Li	Be	Sc	Ti	V	Cr	Co	Ni	Cu	Zn	Ga	Rb
certified values	200		31	11,990	3,590	3,370	83	362	268	3,190	100	180
table top	**77.91**	**14.61**	**241.05**	**6,098**	**3,486**	**3,255**	**955.55**	**8,377**	**971.91**	**781**	**29.19**	**128.95**
HAc 5 M												
(n=10)	28.58	12.23	187.99	579.11	2,104	1,342	809.90	9,570	964.90	2,304	8.57	38.74
	33.45	12.72	171.93	752.96	2,254	1,432	805.15	9,433	976.44	2,190	12.54	46.45
	111.21	13.00	148.26	864.62	2,163	1,431	612.35	5,892	769.97	2,288	10.31	57.63
	202.54	12.01	134.94	942.22	2,202	1,473	554.76	6,212	675.09	2,103	12.01	64.63
	49.57	13.92	175.56	684.64	2,393	1,605	685.82	7,363	815.97	4,540	10.76	56.72
	30.88	12.24	182.46	488.32	2,006	1,581	871.35	8,954	999.94	2,214	7.02	35.08
	1.58	13.04	192.65	765.66	2,127	1,690	747.03	9,066	882.29	2,041	7.66	41.08
	8.41	13.07	178.14	571.62	2,125	1,715	756.33	9,200	904.70	1,966	8.05	35.53
	34.12	11.11	90.21	351.18	1,848	1,137	628.14	6,283	709.59	1,699	3.21	23.27
	34.45	11.23	92.25	357.06	1,851	1,149	646.10	6,553	760.78	1,621	3.22	22.67
average	**53.48**	**12.46**	**155.44**	**635.74**	**2,107**	**1,455**	**711.69**	**7,852**	**845.97**	**2,296**	**8.33**	**42.18**
1SD	60.15	0.87	38.13	201.94	169.69	202.81	101.96	1,523	116.13	821.68	3.26	14.21
RSD (%)	112%	7%	25%	32%	8%	14%	14%	19%	14%	36%	39%	34%
yield (%)	69%	85%	64%	10%	60%	45%	74%	94%	87%	294%	29%	33%
HCl 3 M												
(n=3)	44.98	14.05	128.55	693.49	2,229	1,661	761.39	8,771	914.55	1,422	12.20	51.06
	43.91	13.20	89.38	735.74	2,042	1,441	543.96	5,312	700.00	1,840	7.60	44.67
	42.95	12.67	87.22	653.73	2,006	1,428	541.54	5,399	660.24	1,871	6.98	36.84
average	**43.95**	**13.31**	**101.72**	**694.32**	**2,092**	**1,510**	**615.63**	**6,494**	**758.26**	**1,711**	**8.92**	**44.19**
1SD	1.02	0.70	23.27	41.01	119.67	130.75	126.24	1,973	136.80	250.84	2.85	7.12
RSD (%)	2%	5%	23%	6%	6%	9%	21%	30%	18%	15%	32%	16%
yield (%)	56%	91%	42%	11%	60%	46%	64%	78%	78%	219%	31%	34%
HNO_3 5%												
(n=2)	38.41	12.53	85.41	516.98	1,913	1,153	568.48	5,703	689.88	1,725	5.48	33.41
	37.49	12.37	88.44	405.43	1,916	1,141	610.08	5,967	709.21	1,598	5.33	32.26
average	**37.95**	**12.45**	**86.92**	**461.21**	**1,915**	**1,147**	**589.28**	**5,835**	**699.54**	**1,661**	**5.41**	**32.84**
1SD	0.65	0.11	2.15	78.88	2.01	8.36	29.42	186.54	13.67	89.45	0.11	0.81
RSD (%)	2%	1%	2%	17%	0%	1%	5%	3%	2%	5%	2%	2%
yield (%)	49%	85%	36%	8%	55%	35%	62%	70%	72%	213%	19%	25%

Table 5.3 continued 2/4

(ng.g^{-1})	Sr	Zr	Nb	Mo	Cd	Sn	Cs	Ba	La	Ce	Pr
certified values	295,000	4,190	1,000	500	159	80	20	476,000	153	521	32
table top	**306,603**	**251.21**	**22.25**	**71.62**	**81.35**	**8.49**	**19.28**	**497,643**	**92.40**	**161.67**	**20.11**
HAc 5 M											
(n=10)	306,397	47.23	1.99	32.35	80.33	3.36	3.61	231,261	92.20	164.53	20.33
	295,461	53.20	2.23	25.35	71.20	3.39	6.23	211,717	86.69	152.74	18.59
	274,841	53.64	2.82	35.81	80.94	<0.001	9.42	201,812	82.34	147.10	18.28
	276,724	53.49	3.73	40.09	80.73	3.61	10.40	202,678	83.54	149.08	18.51
	302,915	75.50	2.91	50.31	79.51	5.25	8.86	244,438	91.90	163.48	20.64
	293,244	63.96	1.21	31.75	82.78	0.21	3.28	220,279	86.19	156.53	18.77
	305,609	66.33	1.33	33.03	82.42	0.73	3.47	228,198	91.36	162.09	19.91
	305,351	64.22	1.30	27.32	84.05	3.17	3.41	213,127	90.83	160.21	19.49
	297,977	32.06	0.67	26.70	75.10	1.43	1.49	157,339	83.51	148.15	18.15
	299,134	30.16	0.75	32.23	73.23	1.82	1.75	157,435	83.84	148.73	18.24
average	**295,765**	**53.98**	**1.90**	**33.49**	**79.03**	**2.30**	**5.19**	**206,828**	**87.24**	**155.26**	**19.09**
1SD	11,431	14.59	1.02	7.37	4.34	1.72	3.29	29,143	3.96	6.92	0.93
RSD (%)	4%	27%	54%	22%	5%	75%	63%	14%	5%	4%	5%
yield (%)	96%	21%	9%	47%	97%	27%	27%	42%	94%	96%	95%
HCl 3 M											
(n=3)	305,506	74.92	1.52	133.45	83.22	12.02	10.81	310,341	94.18	167.91	21.21
	302,269	63.61	2.23	53.84	88.75	3.89	9.61	408,801	96.11	172.56	21.71
	300,702	64.63	1.80	56.90	87.83	2.97	6.43	283,512	94.21	170.11	21.37
average	**302,826**	**67.72**	**1.85**	**81.40**	**86.60**	**6.29**	**8.95**	**334,218**	**94.83**	**170.19**	**21.43**
1SD	2,450	6.26	0.36	45.10	2.96	4.98	2.26	65,969	1.11	2.33	0.26
RSD (%)	1%	9%	19%	55%	3%	79%	25%	20%	1%	1%	1%
yield (%)	99%	27%	8%	114%	106%	74%	46%	67%	103%	105%	107%
HNO_3 5%											
(n=2)	296,360	50.47	0.87	52.15	81.49	1.10	4.72	332,289	93.09	168.04	21.06
	293,596	46.23	0.86	53.80	79.10	1.09	3.88	304,111	92.54	166.43	20.97
average	**294,978**	**48.35**	**0.86**	**52.97**	**80.30**	**1.09**	**4.30**	**318,200**	**92.81**	**167.23**	**21.02**
1SD	1,954	3.00	0.01	1.17	1.68	0.01	0.59	19,925	0.39	1.14	0.07
RSD (%)	1%	6%	1%	2%	2%	1%	14%	6%	0%	1%	0%
yield (%)	96%	19%	4%	74%	99%	13%	22%	64%	100%	103%	104%

Table 5.3 continued 3/4

(ng.g^{-1})	Nd	Sm	Eu	Gd	Tb	Dy	Y	Ho	Er	Tm	Yb	Lu
certified values	136	135	7	30	4	28	223	5	14	2	16	22
table top	**80.87**	**19.79**	**16.32**	**18.44**	**2.76**	**17.62**	**214.38**	**4.06**	**12.76**	**1.81**	**11.11**	**1.81**
HAc 5 M												
(n =10)	81.15	18.64	7.39	19.26	3.00	19.13	223.59	4.20	11.71	2.03	11.14	1.83
	76.31	16.47	7.00	17.68	2.76	16.84	206.42	4.02	12.49	1.76	10.12	1.80
	73.06	17.29	7.28	16.36	2.50	16.25	195.61	3.81	11.68	1.58	10.17	1.72
	75.26	16.85	7.89	16.83	2.66	16.83	197.28	3.82	11.44	1.69	10.49	1.66
	83.36	19.82	10.53	19.68	2.91	18.83	217.24	4.29	12.50	1.92	11.30	1.82
	75.03	16.63	8.81	18.85	2.68	18.31	211.78	4.05	12.02	1.90	10.40	1.91
	78.65	18.86	10.14	20.20	2.85	17.25	217.73	4.26	12.03	1.94	11.15	1.83
	78.52	18.14	9.48	19.17	2.79	18.75	217.06	4.49	12.22	1.74	11.11	1.75
	72.51	16.60	8.73	17.35	2.64	16.60	202.28	3.90	11.91	1.75	10.92	1.74
	72.38	16.45	8.91	17.16	2.62	16.67	202.80	3.92	11.66	1.83	10.76	1.76
average	**76.62**	**17.58**	**8.62**	**18.25**	**2.74**	**17.54**	**209.18**	**4.08**	**11.97**	**1.81**	**10.76**	**1.78**
1SD	3.74	1.21	1.22	1.33	0.15	1.09	9.64	0.23	0.36	0.13	0.43	0.07
RSD (%)	5%	7%	14%	7%	6%	6%	5%	6%	3%	7%	4%	4%
yield (%)	95%	89%	53%	99%	99%	100%	98%	100%	94%	100%	97%	98%
HCl 3 M												
(n=3)	85.81	20.02	13.00	19.87	2.92	18.55	220.20	4.32	12.90	1.91	11.09	1.79
	86.46	20.65	14.76	20.47	3.02	19.00	225.41	4.35	13.08	1.92	11.51	1.87
	88.37	19.90	11.90	20.02	3.01	18.71	224.09	4.33	13.05	1.88	11.28	1.83
average	**86.88**	**20.19**	**13.22**	**20.12**	**2.98**	**18.75**	**223.23**	**4.33**	**13.01**	**1.90**	**11.30**	**1.83**
1SD	1.33	0.41	1.44	0.32	0.05	0.23	2.71	0.02	0.09	0.02	0.21	0.04
RSD (%)	2%	2%	11%	2%	2%	1%	1%	0%	1%	1%	2%	2%
yield (%)	107%	102%	81%	109%	108%	106%	104%	107%	102%	105%	102%	101%
HNO_3 5%												
(n=2)	85.02	19.83	13.43	19.83	3.02	18.66	220.15	4.30	12.83	1.84	11.39	1.82
	84.65	19.71	13.42	19.50	3.01	18.53	217.15	4.26	12.65	1.84	11.34	1.81
average	**84.83**	**19.77**	**13.43**	**19.66**	**3.01**	**18.59**	**218.65**	**4.28**	**12.74**	**1.84**	**11.37**	**1.81**
1SD	0.26	0.08	<0.001	0.24	0.01	0.10	2.12	0.03	0.13	<0.001	0.03	<0.001
RSD (%)	0%	0%	0%	1%	0%	1%	1%	1%	1%	0%	0%	0%
yield (%)	105%	100%	82%	107%	109%	106%	102%	105%	100%	102%	102%	100%

Table 5.3 continued 4/4

(ng.g^{-1})	Hf	Ta	W	Tl	Pb ges	Th	U	Y/Ho	Ce*	Pr*	Eu*
certified values	126	14	210	3	700	29	1,750		$_{PAAS}$	$_{PAAS}$	$_{PAAS}$
table top	**5.01**	**2.30**	**188.07**	**2.81**	**158.29**	**18.87**	**2,011**	**52.80**	**0.90**	**0.89**	**4.53**
HAc 5 M											
(n=10)	0.72	0.16	25.50	2.02	129.93	12.54	1,728	53.19	0.92	0.92	2.06
	0.94	0.20	40.38	2.14	129.85	11.49	1,623	51.30	0.92	0.97	2.16
	0.94	0.27	85.06	2.26	118.08	12.13	1,558	51.40	0.91	0.91	2.30
	1.01	0.27	95.56	2.24	125.20	12.16	1,559	51.67	0.91	0.94	2.48
	1.07	0.11	74.85	2.44	134.25	14.06	1,764	50.67	0.90	0.91	2.83
	0.69	0.08	22.77	2.03	126.78	11.12	1,621	52.23	0.94	0.94	2.62
	0.65	0.01	24.92	1.89	131.00	12.57	1,701	51.14	0.92	0.90	2.74
	0.82	<0.001	24.59	1.84	165.91	11.88	1,711	48.31	0.92	0.92	2.69
	0.48	0.08	13.80	1.36	127.71	9.30	1,499	51.92	0.92	0.93	2.72
	0.47	0.08	14.33	1.29	127.99	8.92	1,409	51.75	0.92	0.93	2.81
average	**0.78**	**0.13**	**42.18**	**1.95**	**131.67**	**11.62**	**1,617**	**51.36**	**0.92**	**0.93**	**2.54**
1SD	0.21	0.10	30.92	0.38	12.76	1.54	112.48	1.27	0.01	0.02	0.28
RSD (%)	27%	77%	73%	19%	10%	13%	7%	2%	1%	2%	11%
yield (%)	16%	6%	22%	69%	83%	62%	80%	97%	101%	104%	56%
HCl 3 M											
(n=3)	1.14	0.04	45.22	2.31	146.26	17.04	1,888	51.01	0.91	0.92	3.45
	1.13	0.09	62.25	2.24	139.73	17.19	1,821	51.80	0.91	0.90	3.80
	0.87	0.06	52.74	2.27	138.39	16.89	1,798	51.78	0.91	0.95	3.16
average	**1.05**	**0.06**	**53.41**	**2.27**	**141.46**	**17.04**	**1,836**	**51.53**	**0.91**	**0.92**	**3.47**
1SD	0.15	0.03	8.53	0.03	4.21	0.15	46.64	0.45	<0.001	0.02	0.32
RSD (%)	15%	43%	16%	2%	3%	1%	3%	0%	0%	4%	13%
yield (%)	21%	3%	28%	81%	89%	90%	91%	98%	101%	104%	77%
HNO_3 5%											
(n=2)	0.85	0.16	65.39	1.73	134.03	16.53	1,864	51.18	0.91	0.92	3.59
	0.69	0.06	57.70	1.65	132.47	16.21	1,863	51.00	0.91	0.92	3.63
average	**0.77**	**0.11**	**61.54**	**1.69**	**133.25**	**16.37**	**1,863**	**51.09**	**0.91**	**0.92**	**3.61**
1SD	0.11	0.07	5.44	0.06	1.10	0.23	1.18	0.13	<0.001	<0.001	0.03
RSD (%)	15%	63%	9%	3%	1%	1%	0%	0%	0%	0%	1%
yield (%)	15%	5%	33%	60%	84%	87%	93%	97%	101%	103%	80%

Table 5.4: Jdo-1 rock reference material trace element concentrations in bulk and leachates 1/4

(ng.g^{-1})	Li	Be	Sc	Ti	V	Cr	Co	Ni	Cu	Zn	Ga	Rb
certified values	400		136	8,000	3,140	7,930	168	2,900	1,410	35,400	100	1,750
table top	**564.72**	**23.37**	**336.52**	**6,690**	**3,703**	**8,228**	**693.25**	**7,522**	**2,242**	**30,935**	**14.23**	**84.56**
Hac 5 M												
(n =10)	409.40	20.77	258.50	1,415	3,209	8,155	535.45	6,623	973.08	24,525	25.55	36.14
	597.77	27.06	269.10	2,294	3,650	8,197	540.52	5,999	1,323	28,202	1.16	29.75
	685.63	18.11	225.64	1,280	3,135	8,155	437.75	5,598	901.18	23,812	6.51	23.73
	483.18	22.63	293.26	1,608	3,224	8,197	514.81	6,191	1,546	27,033	9.47	37.38
	420.42	19.71	174.42	1,026	3,017	8,155	470.66	5,156	888.27	20,883	1.70	14.82
	382.30	18.99	158.07	1,069	2,654	8,197	432.40	4,697	722.83	19,700	2.64	15.62
average	**496.45**	**21.21**	**229.83**	**1449**	**3,148**	**8,176**	**488.60**	**5,711**	**1,059**	**24,026**	**7.84**	**26.24**
1SD	120.51	3.26	54.08	467.55	323.22	22.61	48.26	706.48	310.19	3,328	9.25	9.84
RSD (%)	24%	15%	24%	32%	10%	0%	10%	12%	29%	14%	118%	37%
yield (%)	88%	91%	68%	22%	85%	99%	70%	76%	47%	78%	55%	31%
HCl 3 M												
(n=3)	472.00	21.44	221.17	1368	3,539	7,463	595.05	7,038	1,806	28,377	<0.001	24.71
	483.16	21.39	192.06	1361	3,520	7,519	471.83	5,238	1,669	28,141	0.54	20.02
	473.76	21.96	192.75	1299	3,557	7,462	486.38	5,413	1,526	27,854	1.20	16.35
average	**476.30**	**21.60**	**201.99**	**1342**	**3,539**	**7,481**	**517.75**	**5,896**	**1,667**	**28,124**	**0.58**	**20.36**
1SD	6.00	0.31	16.61	37.54	18.48	32.75	67.33	992.66	140.10	261.72	0.60	4.19
RSD (%)	1%	1%	8%	3%	1%	0%	13%	17%	8%	1%	104%	21%
yield (%)	84%	92%	60%	20%	96%	91%	75%	78%	74%	91%	4%	24%
HNO_3 5%												
(n=2)	478.14	20.95	198.70	1259	3,561	7,474	531.69	5,998	1,754	28,753	4.05	17.26
	465.86	21.62	194.30	1229	3,493	7,304	523.73	5,847	1,730	26,422	3.50	15.96
average	**472.00**	**21.29**	**196.50**	**1244**	**3,527**	**7,389**	**527.71**	**5,922**	**1,742**	**27,588**	**3.77**	**16.61**
1SD	8.68	0.48	3.11	21.03	48.14	121.64	5.62	106.46	17.09	1,648	0.39	0.92
RSD (%)	2%	2%	2%	2%	1%	2%	1%	2%	1%	6%	10%	6%
yield (%)	84%	91%	58%	19%	95%	90%	76%	79%	78%	89%	27%	20%

Table 5.4 continued 2/4

(ng.g^{-1})	Sr	Zr	Nb	Mo	Cd	Sn	Cs	Ba	La	Ce	Pr
certified values	116,000	6,210	400	780	644	100	70	6,140	7,930	2,490	956
table top	**128,459**	**546.60**	**44.57**	**232.22**	**309.66**	**16.38**	**4.73**	**6,477**	**8,203**	**2,192**	**1,081**
Hac 5 M											
(n =10)	108,131	159.60	16.09	75.97	206.45	8.04	1.81	5,461	6,973	1,827	894.04
	126,465	137.21	5.37	55.64	288.12	0.06	1.39	6,172	7,989	2,089	1,025
	109,434	111.91	3.66	55.70	231.43	3.30	1.33	5,371	6,994	1,826	894.61
	111,467	160.58	9.85	115.94	258.47	4.93	2.36	5,535	7,318	1,911	946.83
	108,668	84.15	2.49	102.99	168.90	2.11	0.69	5,784	7,018	1,808	872.31
	101,147	84.53	3.50	43.86	151.65	8.38	0.81	5,428	6,562	1,692	822.21
average	**110,885**	**122.99**	**6.83**	**75.02**	**217.50**	**4.47**	**1.40**	**5,625**	**7,142**	**1,859**	**909.10**
1SD	8,396	34.83	5.23	28.90	52.31	3.31	0.62	304	480	133	69.44
RSD (%)	8%	28%	77%	39%	24%	74%	45%	5%	7%	7%	8%
yield (%)	86%	23%	15%	32%	70%	27%	30%	87%	87%	85%	84%
HCl 3 M											
(n=3)	122,895	196.26	5.93	128.61	290.94	8.44	2.35	6,109	7,884	2,088	1,029
	118,621	177.69	5.09	114.40	312.88	5.75	2.12	6,246	7,961	2,098	1,042
	118,939	165.67	4.37	112.86	304.53	4.39	1.17	6,173	7,957	2,098	1,041
average	**120,152**	**179.88**	**5.13**	**118.62**	**302.78**	**6.19**	**1.88**	**6,176**	**7,934**	**2,095**	**1,037**
1SD	2,381	15.41	0.78	8.69	11.07	2.06	0.62	69	43	6	7.55
RSD (%)	2%	9%	15%	7%	4%	33%	33%	1%	1%	0%	1%
yield (%)	94%	33%	12%	51%	98%	38%	40%	95%	97%	96%	96%
HNO_3 5%											
(n=2)	120,315	172.36	5.17	164.38	310.58	3.94	1.63	6,206	8,059	2,124	1,052
	117,528	163.14	5.03	153.44	281.29	2.98	1.18	5,990	7,875	2,075	1,027
average	**118,922**	**167.75**	**5.10**	**158.91**	**295.93**	**3.46**	**1.40**	**6,098**	**7,967**	**2,099**	**1,040**
1SD	1,970	6.53	0.10	7.74	20.71	0.67	0.32	153	130	34	18.03
RSD (%)	2%	4%	2%	5%	7%	19%	23%	3%	2%	2%	2%
yield (%)	93%	31%	11%	68%	96%	21%	30%	94%	97%	96%	96%

Table 5.4 continued 3/4

(ng.g^{-1})	Nd	Sm	Eu	Gd	Tb	Dy	Y	Ho	Er	Tm	Yb
certified values	5,250	788	176	1,300	116	814	10,300	420	500	59	323
table top	**4,326**	**731.78**	**166.70**	**930.76**	**125.50**	**781.69**	**11,468**	**178.62**	**476.19**	**58.69**	**306.14**
Hac 5 M											
(n =10)	3,560	596.37	133.04	753.56	104.62	649.46	9,468	150.24	404.73	50.10	263.14
	4,072	685.36	157.27	868.66	119.81	745.11	10,955	173.09	464.16	57.83	305.55
	3,567	604.36	136.01	764.22	106.03	648.91	9,550	151.83	399.39	51.34	266.32
	3,801	639.61	145.75	810.96	111.52	683.51	9,944	156.62	415.72	51.95	276.52
	3,459	572.61	132.17	734.39	102.25	642.35	9,348	148.29	398.36	50.35	268.00
	3,251	538.51	123.60	683.80	95.37	595.68	8,653	136.49	367.18	45.92	244.02
average	**3,618**	**606.14**	**137.97**	**769.26**	**106.60**	**660.84**	**9,653**	**152.76**	**408.26**	**51.25**	**270.59**
1SD	284.67	51.37	11.84	63.89	8.34	49.95	763.87	12.00	31.80	3.86	20.22
RSD (%)	8%	8%	9%	8%	8%	8%	8%	8%	8%	8%	7%
yield (%)	84%	83%	83%	83%	85%	85%	84%	86%	86%	87%	88%
HCl 3 M											
(n=3)	4,109	695.17	157.12	885.63	119.29	738.34	10,951	168.50	449.69	54.83	286.95
	4,239	712.92	164.12	902.94	124.89	762.81	10,721	174.96	465.02	57.65	302.29
	4,212	706.86	161.94	901.48	123.91	758.91	10,741	173.82	463.11	57.42	299.78
average	**4,187**	**704.98**	**161.06**	**896.68**	**122.69**	**753.35**	**10,804**	**172.42**	**459.28**	**56.64**	**296.34**
1SD	69.04	9.02	3.58	9.60	2.99	13.15	127.80	3.45	8.36	1.57	8.23
RSD (%)	2%	1%	2%	1%	2%	2%	1%	2%	2%	3%	3%
yield (%)	97%	96%	97%	96%	98%	96%	94%	97%	96%	97%	97%
HNO$_3$ 5%											
(n=2)	4,249	714.18	164.05	907.78	124.33	763.93	10,853	174.59	464.87	57.75	303.53
	4,143	699.05	159.82	887.15	121.17	743.96	10,661	170.24	451.77	56.51	295.38
average	**4,196**	**706.61**	**161.94**	**897.46**	**122.75**	**753.94**	**10,757**	**172.41**	**458.32**	**57.13**	**299.46**
1SD	75.16	10.70	2.99	14.59	2.24	14.12	135.77	3.08	9.27	0.88	5.77
RSD (%)	2%	2%	2%	2%	2%	2%	1%	2%	2%	2%	2%
yield (%)	97%	97%	97%	96%	98%	96%	94%	97%	96%	97%	98%

Table 5.4 continued 4/4

(ng.g^{-1})	Lu	Hf	Ta	W	Tl	Pb ges	Th	U	Y/Ho	Ce*	Pr*	Eu*
certified values	49	90	9	260	3	950	43	858	25	*PAAS*	*PAAS*	*PAAS*
table top	**42.94**	**11.56**	**1.91**	**282.63**	**2.11**	**442.81**	**50.44**	**1,003**	**64**	**0.17**	**1.09**	1.05
Hac 5 M												
(n =10)	37.04	2.66	0.53	150.69	1.14	341.60	31.78	714	63.02	0.169	1.092	1.036
	43.13	2.66	0.24	154.72	1.07	371.41	32.80	794	63.29	0.169	1.088	1.064
	37.46	1.95	<0.001	154.46	0.98	340.96	28.39	685	62.90	0.169	1.086	1.045
	37.67	3.43	<0.001	159.14	1.44	377.00	36.93	778	63.49	0.168	1.094	1.056
	37.08	2.17	<0.001	100.33	0.79	363.85	26.58	672	63.04	0.168	1.096	1.063
	34.06	2.14	<0.001	98.27	0.73	341.49	24.42	621	63.40	0.168	1.094	1.063
average	**37.74**	**2.50**	**0.13**	**136.27**	**1.02**	**356.05**	**30.15**	**711**	**63.19**	**0.169**	**1.092**	**1.055**
1SD	2.95	0.54	0.22	28.77	0.26	16.64	4.57	66	0.24	0.001	0.004	0.011
RSD (%)	8%	21%	170%	21%	25%	5%	15%	9%	0%	0%	0%	1%
yield (%)	88%	22%	7%	48%	49%	80%	60%	71%	98%	99%	100%	100%
HCl 3 M												
(n=3)	40.08	4.37	<0.001	143.74	1.18	401.65	46.03	901				
	42.60	4.21	<0.001	172.23	1.44	405.04	47.25	940	61.28	0.169	1.101	1.068
	42.21	3.85	<0.001	157.90	1.42	403.78	42.58	920	61.79	0.169	1.100	1.058
average	**41.63**	**4.14**	**0.00**	**157.96**	**1.34**	**403.49**	**45.29**	**920**	**61.53**	**0.169**	**1.101**	**1.063**
1SD	1.35	0.27	0.00	14.24	0.14	1.71	2.42	20	0.36	0.000	0.001	0.007
RSD (%)	3%	6%		9%	11%	0%	5%	2%	1%	0%	0%	1%
yield (%)	97%	36%	0%	56%	64%	91%	90%	92%	96%	99%	101%	101%
HNO$_3$ 5%												
(n=2)	42.26	4.06	<0.001	254.65	1.64	421.42	46.67	947	62.16	0.169	1.098	1.063
	41.10	3.85	<0.001	216.57	1.25	404.27	45.40	908	62.62	0.169	1.095	1.059
average	**41.68**	**3.95**	**0.00**	**235.61**	**1.44**	**412.85**	**46.03**	**927**	**62.39**	**0.169**	**1.097**	**1.061**
1SD	0.82	0.15	0.00	26.93	0.27	12.13	0.89	28	0.33	0.000	0.002	0.003
RSD (%)	2%	4%		11%	19%	3%	2%	3%	1%	0%	0%	0%
yield (%)	97%	34%	0%	83%	68%	93%	91%	92%	97%	99%	101%	101%

Table 5.5: ECRM 782-1 rock reference material trace element concentrations in bulk and leachates 1/4

$(ng.g^{-1})$	Li	Be	Sc	Ti	V	Cr	Co	Ni	Cu	Zn	Ga
certified values				18,740		4,588		3,143		53,022	
table top	3,155.82	48.98	236.72	26,592	1,447	4,218	2,552	6,157	2,616	55,075	152.38
(n=7)	9,685.82	75.92	450.34	38,539	2,247	7,330	3,914	8,131	12,027	103,779	209.80
	12,653.46	78.29	494.03	39,808	2,210	6,868	4,029	8,710	14,498	103,042	216.12
	3,161.25	47.87	202.86	27,856	1,385	4,272	2,370	4,540	2,733	61,220	135.53
	3,223.51	48.99	204.61	27,568	1,380	4,202	2,388	4,496	2,798	59,070	136.18
	11,160.09	82.11	333.93	42,108	2,197	7,154	3,838	7,071	11,344	99,252	225.26
	11,233.83	88.24	331.97	42,626	2,213	7,137	3,852	7,062	11,441	100,050	217.48
average	**7,753.40**	**67.20**	**322.06**	**35,014**	**1,868**	**5,883**	**3,278**	**6,595**	**8,208**	**83,070**	**184.68**
1SD	4,362.90	17.80	116.59	7,318	435	1,552	791	1,638	5,243	23,148	41.14
RSD (%)	56%	26%	36%	21%	23%	26%	24%	25%	64%	28%	22%
HAc 5 M											
(n=2)	1,960.90	24.87	113.17	863	548	1,533	1,844	3,456	1,272	38,128	17.27
	1,631.86	23.46	97.73	644	478	1,393	1,635	3,057	1,190	37,501	15.30
average	**1,796.38**	**24.17**	**105.45**	**753**	**513**	**1,463**	**1,740**	**3,256**	**1,231**	**37,815**	**16.29**
1SD	232.67	1.00	10.92	154	50	99	148	282	57	443	1.39
RSD (%)	13%	4%	10%	21%	10%	7%	9%	9%	5%	1%	9%
yield (%)	23%	36%	33%	2%	27%	25%	53%	49%	15%	46%	9%
HCl 3 M											
(n=2)	2,962.14	37.76	171.95	2,064	969	2,593	2,319	4,567	2,054	48,138	34.85
	2,984.38	36.16	168.64	1,882	1,003	2,694	2,361	4,659	1,931	46,073	34.35
average	**2,973.26**	**36.96**	**170.30**	**1,973**	**986**	**2,644**	**2,340**	**4,613**	**1,992**	**47,105**	**34.60**
1SD	15.73	1.13	2.34	129	24	71	30	65	87	1,460	0.35
RSD (%)	1%	3%	1%	7%	2%	3%	1%	1%	4%	3%	1%
yield (%)	38%	55%	53%	6%	53%	45%	71%	70%	24%	57%	19%
HNO_3 5%											
(n=2)	2,988.25	32.96	158.55	1,629	748	2,132	2,398	4,723	1,559	40,567	28.44
	2,862.22	30.30	150.72	1,355	672	2,002	2,309	4,592	1,457	37,151	25.73
average	**2,925.24**	**31.63**	**154.63**	**1,492**	**710**	**2,067**	**2,354**	**4,657**	**1,508**	**38,859**	**27.08**
1SD	89.12	1.88	5.54	194	54	92	63	93	72.26	2,416	1.92
RSD (%)	3%	6%	4%	13%	8%	4%	3%	2%	5%	6%	7%
yield (%)	38%	47%	48%	4%	38%	35%	72%	71%	18%	47%	15%

Table 5.5 continued 2/4

$(ng.g^{-1})$	Rb	Sr	Zr	Nb	Mo	Cd	Sn	Cs	Ba	La	Ce
certified values									6,270		
table top	890.20	25,533	816.76	89.35	163.52	220.20	97.11	58.65	8,015	433.96	993.44
(n=7)	1,422.67	37,623	1,399	147.54	257.72	411.30	134.17	87.19	12,079	645.69	1,471
	1,527.28	37,843	1,229	143.34	126.71	406.51	127.63	90.88	12,059	655.00	1,502
	837.45	24,423	791.89	94.25	113.50	277.41	75.30	56.15	7,832	420.70	970.35
	838.24	24,467	800.80	95.04	114.37	288.15	88.47	56.77	7,941	424.97	978.94
	1,582.17	37,836	1,323	149.68	191.28	443.55	125.58	93.30	13,570	732.48	1,650
	1,603.92	37,985	1,335	148.38	184.03	441.48	122.85	92.93	13,528	736.84	1,653
average	**1,243.13**	**32,244**	**1,099**	**123.94**	**164.45**	**355.51**	**110.16**	**76.55**	**10,718**	**578.52**	**1,317**
1SD	367.69	6,966	281.60	29.17	52.17	91.10	22.86	18.24	2,678	146.35	321.82
RSD (%)	30%	22%	26%	24%	32%	26%	21%	24%	25%	25%	24%
HAc 5 M											
(n=2)	75.26	16,664	78.55	1.73	14.77	226.00	12.51	2.23	5,479	165.77	444.68
	68.21	14,062	67.71	1.28	11.91	225.42	10.93	1.89	5,149	139.06	377.46
average	**71.73**	**15,363**	**73.13**	**1.51**	**13.34**	**225.71**	**11.72**	**2.06**	**5,314**	**152.41**	**411.07**
1SD	4.98	1,840	7.66	0.31	2.02	0.41	1.12	0.24	234	18.89	47.53
RSD (%)	7%	12%	10%	21%	15%	0%	10%	12%	4%	12%	12%
yield (%)	6%	48%	7%	1%	8%	63%	11%	3%	50%	26%	31%
HCl 3 M											
(n=2)	159.53	23,857	211.78	5.78	106.27	227.90	73.13	12.91	6,270	247.24	660.33
	138.48	24,320	197.52	4.15	76.21	227.74	65.20	7.46	6,386	245.96	659.74
average	**149.01**	**24,089**	**204.65**	**4.96**	**91.24**	**227.82**	**69.17**	**10.18**	**6,328**	**246.60**	**660.03**
1SD	14.88	328	10.09	1.15	21.26	0.11	5.61	3.85	82	0.91	0.42
RSD (%)	10%	1%	5%	23%	23%	0%	8%	38%	1%	0%	0%
yield (%)	12%	75%	19%	4%	55%	64%	63%	13%	59%	43%	50%
HNO_3 5%											
(n=2)	132.60	24,502	139.37	1.65	18.07	230.28	22.11	6.18	6,368	246.47	660.16
	115.49	23,549	113.99	1.09	10.22	215.29	9.29	4.35	6,078	238.04	634.27
average	**124.04**	**24,026**	**126.68**	**1.37**	**14.14**	**222.79**	**15.70**	**5.27**	**6,223**	**242.25**	**647.22**
1SD	12.10	674	17.95	0.40	5.55	10.60	9.06	1.29	205	5.96	18.31
RSD (%)	10%	3%	14%	29%	39%	5%	58%	25%	3%	2%	3%
yield (%)	10%	75%	12%	1%	9%	63%	14%	7%	58%	42%	49%

Table 5.5 continued 3/4

($ng.g^{-1}$)	Pr	Nd	Sm	Eu	Gd	Tb	Dy	Y	Ho	Er	Tm	Yb
certified values												
table top	115.61	471.63	108.21	26.95	128.17	19.94	125.64	1,197	28.45	82.16	11.74	71.03
(n=7)	170.55	711.81	161.30	39.80	193.96	30.41	187.47	1,771	42.86	127.18	17.84	108.30
	173.80	716.23	160.63	40.39	192.83	30.33	189.74	1,794	44.28	127.94	18.14	111.99
	112.90	463.63	104.79	26.21	126.34	20.04	125.36	1,164	28.17	81.50	11.60	70.64
	114.54	467.33	106.79	26.75	129.09	20.00	127.45	1,163	28.65	81.59	11.92	71.94
	192.65	765.63	173.38	40.92	199.17	31.56	191.29	1,794	43.64	127.59	18.06	113.38
	192.53	770.88	172.26	41.90	196.43	31.92	195.85	1,801	43.76	127.13	18.28	113.23
average	**153.23**	**623.88**	**141.05**	**34.70**	**166.57**	**26.31**	**163.26**	**1,526**	**37.12**	**107.87**	**15.37**	**94.36**
1SD	37.33	147.95	32.61	7.57	36.27	5.94	34.81	329.18	8.14	24.44	3.38	21.73
RSD (%)	24%	24%	23%	22%	22%	23%	21%	22%	22%	23%	22%	23%
HAc 5 M												
(n=2)	54.80	243.67	60.47	15.81	78.79	12.65	78.72	757.37	17.93	51.48	7.49	44.82
	46.10	204.24	51.64	13.37	66.00	10.53	66.51	636.87	14.99	42.74	6.23	37.00
average	**50.45**	**223.96**	**56.06**	**14.59**	**72.40**	**11.59**	**72.62**	**697.12**	**16.46**	**47.11**	**6.86**	**40.91**
1SD	6.15	27.88	6.25	1.73	9.04	1.50	8.63	85.20	2.07	6.18	0.90	5.53
RSD (%)	12%	12%	11%	12%	12%	13%	12%	12%	13%	13%	13%	14%
yield (%)	33%	36%	40%	42%	43%	44%	44%	46%	44%	44%	45%	43%
HCl 3 M												
(n=2)	81.32	361.22	90.59	23.60	115.87	18.52	116.24	1,098	26.10	74.55	10.77	64.33
	81.11	359.95	90.36	23.84	117.17	18.72	117.20	1,115	26.40	75.53	10.89	64.11
average	**81.22**	**360.59**	**90.47**	**23.72**	**116.52**	**18.62**	**116.72**	**1,107**	**26.25**	**75.04**	**10.83**	**64.22**
1SD	0.15	0.90	0.17	0.17	0.92	0.14	0.67	11.76	0.21	0.69	0.08	0.15
RSD (%)	0%	0%	0%	1%	1%	1%	1%	1%	1%	1%	1%	0%
yield (%)	53%	58%	64%	68%	70%	71%	71%	72%	71%	70%	70%	68%
HNO_3 5%												
(n=2)	82.09	361.52	91.07	23.88	118.57	18.81	117.92	1,121	26.75	75.56	10.91	64.77
	78.47	345.79	87.81	22.70	113.05	18.00	112.56	1,079	25.60	72.54	10.66	62.72
average	**80.28**	**353.66**	**89.44**	**23.29**	**115.81**	**18.41**	**115.24**	**1,100**	**26.17**	**74.05**	**10.78**	**63.74**
1SD	2.56	11.12	2.31	0.84	3.90	0.57	3.79	30.25	0.81	2.14	0.18	1.45
RSD (%)	3%	3%	3%	4%	3%	3%	3%	3%	3%	3%	2%	2%
yield (%)	52%	57%	63%	67%	70%	70%	71%	72%	71%	69%	70%	68%

Table 5.5 continued 4/4

(ng.g-1)	Lu	Hf	Ta	W	Tl	Pb ges	Th	U	Y/Ho	Ce*	Pr*	Eu*
certified values						25,064				PAAS	PAAS	PAAS
table top	10.79	19.74	5.14	58.66	8.73	27,487	96.69	610.90	42.09	1.07	0.93	1.20
(n=7)	17.16	28.84	10.73	202.10	6.48		133.08	870.77	41.33	1.07	0.95	1.18
	16.87	30.31	8.74	41.32	6.96		135.97	850.12	40.51	1.07	0.95	1.20
	10.96	19.34	5.48	26.12	10.24		94.95	619.42	41.32	1.07	0.94	1.19
	10.90	19.64	5.55	25.83	10.68		94.37	611.60	40.60	1.07	0.93	1.19
	16.89	33.03	10.58	295.45	6.60		165.99	889.80	41.11	1.06	0.93	1.16
	17.00	35.30	11.26	294.35	6.40		163.30	893.74	41.16	1.06	0.94	1.20
average	**14.37**	**26.60**	**8.21**	**134.83**	**8.01**	**27,487**	**126.34**	**763.76**	**41.16**	**1.06**	**0.94**	**1.19**
1SD	3.26	6.88	2.75	125.18	1.86		31.53	140.86	0.52	0.01	0.01	0.02
RSD (%)	23%	26%	34%	93%	23%		25%	18%	1%	1%	1%	1%
HAc 5 M												
(n=2)	6.68	1.45	0.03	1.11	3.08	23,134	33.82	379.64	42.25	1.11	0.92	1.19
	5.75	1.16	<0.001	0.86	3.18	22,350	27.97	319.29	42.47	1.12	0.91	1.19
average	**6.22**	**1.30**	**0.01**	**0.99**	**3.13**	**22,742**	**30.89**	**349.47**	**42.36**	**1.11**	**0.91**	**1.19**
1SD	0.66	0.21	0.02	0.18	0.07	554.13	4.14	42.68	0.16	0.01	0.01	<0.001
RSD (%)	11%	16%	141%	18%	2%	2%	13%	12%	0%	1%	1%	0%
yield (%)	43%	5%	0%	1%	39%	83%	24%	46%	103%	104%	97%	100%
HCl 3 M												
(n=2)	9.77	5.52	0.05	30.68	5.30	25,020	64.28	567.82	42.08	1.10	0.91	1.20
	9.79	5.15	0.01	18.99	5.13	25,108	63.88	572.59	42.22	1.11	0.91	1.21
average	**9.78**	**5.34**	**0.03**	**24.84**	**5.21**	**25,064**	**64.08**	**570.21**	**42.15**	**1.11**	**0.91**	**1.20**
1SD	0.01	0.26	0.03	8.27	0.12	62.18	0.28	3.37	0.10	<0.001	<0.001	<0.001
RSD (%)	0%	5%	105%	33%	2%	0%	0%	1%	0%	0%	0%	0%
yield (%)	68%	20%	0%	18%	65%	91%	51%	75%	102%	104%	97%	101%
HNO_3 5%												
(n=2)	9.91	3.42	0.01	1.49	4.49	24,835	61.64	570.35	41.93	1.10	0.91	1.20
	9.44	2.74	<0.001	1.07	4.11	23,238	58.64	546.81	42.13	1.10	0.90	1.19
average	**9.67**	**3.08**	**0.00**	**1.28**	**4.30**	**24,036**	**60.14**	**558.58**	**42.03**	**1.10**	**0.91**	**1.19**
1SD	0.33	0.48	0.01	0.30	0.27	1,130	2.12	16.65	0.15	<0.001	<0.001	0.01
RSD (%)	3%	16%	141%	23%	6%	5%	4%	3%	0%	0%	0%	1%
yield (%)	67%	12%	0%	1%	54%	87%	48%	73%	102%	103%	97%	100%

Table 5.6: ECRM 752-1 rock reference material trace element concentrations in bulk and leachates 1/4

(ng.g-1)	Li	Be	Sc	Ti	V	Cr	Co	Ni	Cu	Zn	Ga	Rb
certified values				50,000								
table top	1,114	40.18	436.93	42,143	3,039	4,234	1,147	10,174	1,723	3,288	148.08	929.33
	1,223	43.43	437.02	52,609	3,278	4,452	910.26	8,677	1,660	4,021	156.05	914.26
	1,249	44.55	432.46	52,299	3,272	4,379	899.29	8,420	1,646	1,779	156.51	918.48
average	**1,195**	**42.72**	**435.47**	**49,017**	**3,196**	**4,355**	**985.43**	**9,090**	**1,676**	**3,029**	**153.55**	**920.69**
1SD	71.86	2.27	2.61	5,955	136.14	110.73	139.81	947.21	41.28	1,143	4.74	7.77
RSD (%)	6%	5%	1%	12%	4%	3%	14%	10%	2%	38%	3%	1%
HAc 5 M												
(n=3)	144.88	27.43	396.17	785.49	1,281	2,368	1,030	10,221	1,311	2,394	11.70	44.68
	132.43	23.65	314.14	1,324	1,243	2,226	869.93	8,134	1,033	1,981	3.26	40.78
	134.11	23.94	312.30	847.36	1,237	2,219	865.71	8,025	1,020	1,956	2.82	41.42
average	**137.14**	**25.00**	**340.87**	**985.63**	**1,254**	**2,271**	**922.05**	**8,794**	**1,121**	**2,110**	**5.92**	**42.29**
1SD	6.76	2.10	47.90	294.70	23.76	83.98	93.95	1,237	164.41	246.02	5.01	2.09
RSD (%)	5%	8%	14%	30%	2%	4%	10%	14%	15%	12%	85%	5%
yield (%)	11%	59%	78%	2%	39%	52%	94%	97%	67%	70%	4%	5%
HCl 3 M												
(n=2)	167.88	28.71	318.13	1,172	1,406	2,282	915.11	8,206	1,156	2,285	9.16	81.37
	161.72	27.69	314.73	1,053	1,417	2,337	938.45	8,479	1,194	2,255	8.22	69.58
average	**164.80**	**28.20**	**316.43**	**1,113**	**1,412**	**2,309**	**926.78**	**8,342**	**1,175**	**2,270**	**8.69**	**75.47**
1SD	8.71	1.44	4.82	168.89	16.45	78.65	33.00	386.26	54.30	42.44	1.33	16.66
RSD (%)	5%	5%	2%	15%	1%	3%	4%	5%	5%	2%	15%	22%
yield (%)	14%	66%	73%	2%	44%	53%	94%	92%	70%	75%	6%	8%
HNO_3 5%												
(n=2)	129.55	26.12	292.33	534.56	1,270	2,088	859.20	8,095	1,076	2,000	2.53	46.35
	129.61	26.05	288.32	480.31	1,254	2,083	862.06	7,989	1,063	2,026	3.04	42.23
average	**129.58**	**26.08**	**290.32**	**507.43**	**1,262**	**2,086**	**860.63**	**8,042**	**1,070**	**2,013**	**2.78**	**44.29**
1SD	0.04	0.05	2.84	38.36	11.58	3.56	2.02	74.48	9.03	18.46	0.37	2.92
RSD (%)	0%	0%	1%	8%	1%	0%	0%	1%	1%	1%	13%	7%
yield (%)	11%	61%	67%	1%	39%	48%	87%	88%	64%	66%	2%	5%

Table 5.6 continued 2/4

(ng.g-1)	Sr	Zr	Nb	Mo	Cd	Sn	Cs	Ba	La	Ce	Pr
certified values	160,000	2,400		65.00				53,000			
table top	159,597	1,592	145.34	81.73	294.54	44.83	112.21	51,839	1,424	1,503	300.82
	163,654	1,719	190.56	80.69	380.20	38.02	111.60	65,664	1,525	1,663	319.86
	164,222	1,719	190.44	82.19	397.69	46.25	113.38	66,524	1,543	1,684	324.32
average	**162,491**	**1,677**	**175.44**	**81.54**	**357.48**	**43.03**	**112.40**	**61,342**	**1,497**	**1,617**	**315.00**
1SD	2,522	73.03	26.07	0.77	55.20	4.40	0.90	8,242	63.69	98.94	12.48
RSD (%)	2%	4%	15%	1%	15%	10%	1%	13%	4%	6%	4%
HAc 5 M											
(n=3)	157,832	240.13	2.36	18.09	344.25	8.35	6.75	20,100	1,255	1,280	267.82
	160,680	213.10	2.88	20.89	293.53	3.27	5.92	19,422	1,301	1,296	275.21
	160,297	206.75	2.54	19.84	290.01	3.59	6.16	13,849	1,295	1,284	273.55
average	**159,603**	**219.99**	**2.60**	**19.61**	**309.26**	**5.07**	**6.28**	**17,791**	**1,284**	**1,287**	**272.19**
1SD	1,546	17.73	0.27	1.41	30.35	2.85	0.43	3,430	24.78	8.07	3.88
RSD (%)	1%	8%	10%	7%	10%	56%	7%	19%	2%	1%	1%
yield (%)	98%	13%	1%	24%	87%	12%	6%	29%	86%	80%	86%
HCl 3 M											
(n=2)	160,704	236.97	3.16	36.67	308.98	14.48	27.92	51,427	1,337	1,367	289.06
	160,497	228.09	2.42	36.55	302.02	14.27	24.20	51,070	1,331	1,362	286.78
average	**160,600**	**232.53**	**2.79**	**36.61**	**305.50**	**14.37**	**26.06**	**51,249**	**1,334**	**1,365**	**287.92**
1SD	293.73	12.56	1.04	0.18	9.84	0.30	5.26	504.56	8.71	7.64	3.22
RSD (%)	0%	5%	37%	0%	3%	2%	20%	1%	1%	1%	1%
yield (%)	99%	14%	2%	45%	85%	33%	23%	84%	89%	84%	91%
HNO_3 5%)											
(n=2)	159,481	113.37	0.92	24.49	295.86	4.59	13.77	48,815	1,312	1,332	282.57
	157,916	105.13	1.08	19.54	293.75	1.80	10.58	45,998	1,305	1,321	280.30
average	**158,698**	**109.25**	**1.00**	**22.02**	**294.80**	**3.20**	**12.18**	**47,407**	**1,308**	**1,327**	**281.44**
1SD	1,107	5.83	0.11	3.50	1.49	1.97	2.25	1,991	4.76	7.80	1.60
RSD (%)	1%	5%	11%	16%	1%	62%	19%	4%	0%	1%	1%
yield (%)	98%	7%	1%	27%	82%	7%	11%	77%	87%	82%	89%

Table 5.6 continued 3/4

(ng.g-1) certified values	Nd	Sm	Eu	Gd	Tb	Dy	Y	Ho	Er	Tm	Yb
table top	1,234	259.08	65.21	309.62	45.99	295.56	3,074	68.40	192.09	26.37	156.83
	1,328	275.22	68.86	325.78	49.37	315.61	3,354	72.72	205.22	28.67	171.51
	1,338	276.26	70.78	334.39	50.29	316.87	3,372	73.21	208.69	29.18	174.18
average	**1,300**	**270.19**	**68.28**	**323.26**	**48.55**	**309.35**	**3,267**	**71.44**	**202.00**	**28.08**	**167.51**
1SD	57.15	9.63	2.83	12.58	2.26	11.95	166.86	2.65	8.76	1.50	9.34
RSD (%)	4%	4%	4%	4%	5%	4%	5%	4%	4%	5%	6%
HAc 5 M											
(n=3)	1,123	231.95	60.17	290.50	44.24	269.91	3,089	63.99	183.21	25.50	146.76
	1,157	241.93	61.85	299.43	45.14	287.01	3,138	66.33	188.43	26.32	155.74
	1,146	241.27	61.81	298.26	45.03	286.63	3,118	65.87	187.26	25.98	154.33
average	**1,142**	**238.38**	**61.28**	**296.06**	**44.80**	**281.18**	**3,115**	**65.40**	**186.30**	**25.93**	**152.28**
1SD	17.26	5.58	0.96	4.85	0.49	9.76	24.99	1.24	2.74	0.42	4.83
RSD (%)	2%	2%	2%	2%	1%	3%	1%	2%	1%	2%	3%
yield (%)	88%	88%	90%	92%	92%	91%	95%	92%	92%	92%	91%
HCl 3 M											
(n=2)	1,211	255.03	67.71	316.34	47.39	300.14	3,226	69.03	193.44	27.09	158.89
	1,203	254.56	67.18	314.71	46.86	297.60	3,231	68.40	192.99	26.65	158.41
average	**1,207**	**254.79**	**67.44**	**315.52**	**47.12**	**298.87**	**3,229**	**68.71**	**193.22**	**26.87**	**158.65**
1SD	11.41	0.65	0.75	2.30	0.75	3.59	6.42	0.90	0.63	0.62	0.68
RSD (%)	1%	0%	1%	1%	2%	1%	0%	1%	0%	2%	0%
yield (%)	93%	94%	99%	98%	97%	97%	99%	96%	96%	96%	95%
HNO$_3$ 5%)											
(n=2)	1,185	251.20	65.63	308.42	46.47	295.33	3,187	67.85	191.81	26.60	155.88
	1,181	248.74	65.02	309.31	46.02	291.99	3,167	67.61	189.97	26.50	155.86
average	**1,183**	**249.97**	**65.32**	**308.86**	**46.24**	**293.66**	**3,177**	**67.73**	**190.89**	**26.55**	**155.87**
1SD	2.94	1.73	0.43	0.63	0.31	2.36	14.34	0.17	1.30	0.07	0.02
RSD (%)	0%	1%	1%	0%	1%	1%	0%	0%	1%	0%	0%
yield (%)	91%	93%	96%	96%	95%	95%	97%	95%	95%	95%	93%

Table 5.6 continued 4/4

(ng.g-1) certified values	Lu	Hf	Ta	W	Tl	Pb ges	Th	U	Y/Ho	Ce* PAAS	Pr* PAAS	Eu* PAAS
table top	23.84	32.77	8.57	15.99	9.24	1,714	108.05	568	44.95	0.55	0.98	1.21
	25.62	35.17	11.66	19.03	11.31		118.30	573	46.12	0.57	1.00	1.21
	26.69	35.17	11.94	17.64	11.71		118.67	573	46.06	0.57	0.99	1.22
average	**25.38**	**34.37**	**10.72**	**17.56**	**10.75**		**115.01**	**571**	**45.71**	**0.57**	**0.99**	**1.21**
1SD	1.44	1.39	1.87	1.52	1.33		6.03	2.71	0.66	0.01	0.01	0.01
RSD (%)	6%	4%	17%	9%	12%		5%	0%	1%	2%	1%	1%
HAc 5 M												
(n=3)	21.80	2.47	0.23	1.17	3.30		52.83	425	48.26	0.53	1.00	1.20
	23.78	2.77	<d.l.	<d.l.	2.57	1,275.37	51.69	461	47.31	0.52	1.00	1.20
	23.26	2.82	<d.l.	<d.l.	2.47	1,246.49	50.85	461	47.33	0.52	0.99	1.21
average	**22.95**	**2.69**		**0.39**	**2.78**	**1,261**	**51.79**	**449**	**47.64**	**0.52**	**1.00**	**1.20**
1SD	1.03	0.19		0.68	0.45	20.42	0.99	20.59	0.54	0.01	0.01	<0.001
RSD (%)	4%	7%		173%	16%	2%	2%	5%	1%	1%	1%	0%
yield (%)	90%	8%		2%	26%	74%	45%	79%	104%	93%	100%	99%
HCl 3 M												
(n=2)	24.21	3.51	<d.l.	3.59	1.56	1,560	64.78	508	46.74	0.53	0.99	1.25
	23.92	3.41	<d.l.	1.26	2.61	1,551	62.04	502	47.24	0.53	0.99	1.24
average	**24.06**	**3.46**		**2.42**	**2.09**	**1,556**	**63.41**	**505**	**46.99**	**0.53**	**0.99**	**1.24**
1SD	0.42	0.14		3.29	1.50	13.72	3.88	8.43	0.71	<0.001	<0.001	0.01
RSD (%)	2%	4%		136%	72%	1%	6%	2%	2%	0%	0%	1%
yield (%)	95%	10%		14%	19%	91%	55%	88%	103%	94%	100%	103%
HNO$_3$ 5%)												
(n=2)	23.63	1.94	<d.l.	<d.l.	3.22	1,376	52.82	500	46.97	0.53	0.99	1.23
	23.64	1.73	<d.l.	<d.l.	3.20	1,446	53.33	493	46.83	0.53	0.99	1.23
average	**23.64**	**1.83**			**3.21**	**1,411**	**53.07**	**496**	**46.90**	**0.53**	**0.99**	**1.23**
1SD	0.01	0.15			0.01	50.00	0.37	5.28	0.09	<0.001	<0.001	0.01
RSD (%)	0%	8%			0%	4%	1%	1%	0%	0%	0%	0%
yield (%)	93%	5%			30%	82%	46%	87%	103%	93%	100%	101%

Table 5.7: MC-ICPMS and iCAP-Qc® quadrupole ICP-MS data of the carbonates investigated in this study

	MC-ICMPS data				iCAP-Qc® quadrupole ICP-MS data ($ng.g^{-1}$)								
sample ID	$\delta^{186/184}$W	2SE	W ($ng.g^{-1}$)	yield	W	W §	Ti	Co	Ni	Zn	Mo	Th	Y/Ho
modern Bahamas carbonates													
BD	0.154	0.010	317 §	80%	497 *								
EL	0.193	0.010	485 §	80%	284 *								
8B (2.06 Ga): stromatolitic dolostones													
67.79					4.01		430	2,197	5,419	4,249	4.19	5	40.59
76.47	0.056	0.011	84	54%	81.35		287	1,500	5,500	3,499	112.86	2	47.89
83.94	0.183	0.018	13	60%	12.42		2,684	5,399	15,884	4,652	45.51	186	28.85
84.1					17.76		4,733	7,539	21,594	7,099	72.71	302	29.44
85.59	0.043	0.015	166	49%	150.91		1,163	131	627	255.43	35.60	8	31.55
86.85	0.125	0.016	22	59%	23.15		642	4,007	11,540	5,360	150.87	6	41.82
87.0	0.097	0.016	24	62%	25.44		636	3,842	11,511	5,199	80.03	5	42.44
5A (2.05 Ga): travertines													
28.17	0.037	0.015	4,650	48%	4,073		11,556	3,874	5,410	4,352	21.66	384	27.68
31.63	0.053	0.014	14,144	46%	11,500		36,367	7,652	6,516	5,902	14.41	1,314	26.98
32.76					10,665		29,544	8,010	3,944	3,728	2.07	1,542	25.50
56.83	0.044	0.015	10,249	53%	9,732		30,892	5,931	5,661	9,448	11.32	486	29.44
77.53	0.037	0.017	22,940	48%	18,611		27,886	17,873	4,682	5,156	109.18	977	29.41
MP-72 (2.39 Ga): Mooidraai marine carbonates													
198.37					94.76	771	790	350	1,432	3,548	169.17	20	47.76
216.055	0.140	0.014	41	81%	59.40	103	1,386	623	2,742	4,310	89.87	39	52.40
228.685	0.200	0.033	104	62%	103.77	511	5,578	1,832	3,086	17,885	142.31	168	45.25
240.89					26.59	82	1812	1923	3,896	8,890	17.94	178	55.21
246.29	0.291	0.015	1,773	52%	1,647	1,861	21,296	10,819	4,416	11,611	91.27	237	54.87
262.4	0.329	0.014	52	59%	53.61	77	2141	2039	4,566	2,739	26.39	41	63.55

Most of the data originate from carbonates leached with 3 M HCl, with the expections of § for W concentrations measured on bulk digests and * for W concentrations measured on HAc leachates

Chapter 6

Conclusions and outlook

This dissertation aimed at defining the potential and limits of the stable W isotope systematics as a proxy for the redox state of ancient oceans. Three main research topics were successfully approached : (1) tracking the evolution of the $\delta^{186/184}$W values in open marine sediments deposited under ferruginous conditions, (2) aim at constraining the potential inputs of W to the ocean during the Precambrian, such as anoxic weathering or hydrothermal and (3) measure carbonates $\delta^{186/184}$W values and compare the signals with the ones of open ocean shales.

6.1 Summary

The chapters 2 and 3 investigated sediments deposited in marine environments from 3.47 to 2.0 Ga and revealed a spread of $\delta^{186/184}$W values from the PII-range towards authigenic-W with a heavy $\delta^{186/184}$W value as early as 3.47 Ga, reaching up to modern-like seawater $\delta^{186/184}$W value at 2.0 Ga. The results of the chapter 2 and 3 imply early mobility of W in oceans as early as 3.47 Ga.

The chapter 4 focused of 2.7 Ga paleosols developed on basaltic flows during subaerial anoxic weathering revealed that preferentially light W readily adsorbed onto clay minerals, while preferentially heavy W isotopes were removed with fluids leading to an estimated riverine $\delta^{186/184}$W value of +0.174 ‰ at 2.77 Ga.

Experiments were then conducted on various carbonates reference materials in order to establish a protocol for $\delta^{186/184}$W determination of carbonate matrices. Then, carbonates from various depositional settings and age were processed for $\delta^{186/184}$W determination and revealed large $\delta^{186/184}$W variations. Continental hydrothermal carbonates (travertines) yielded

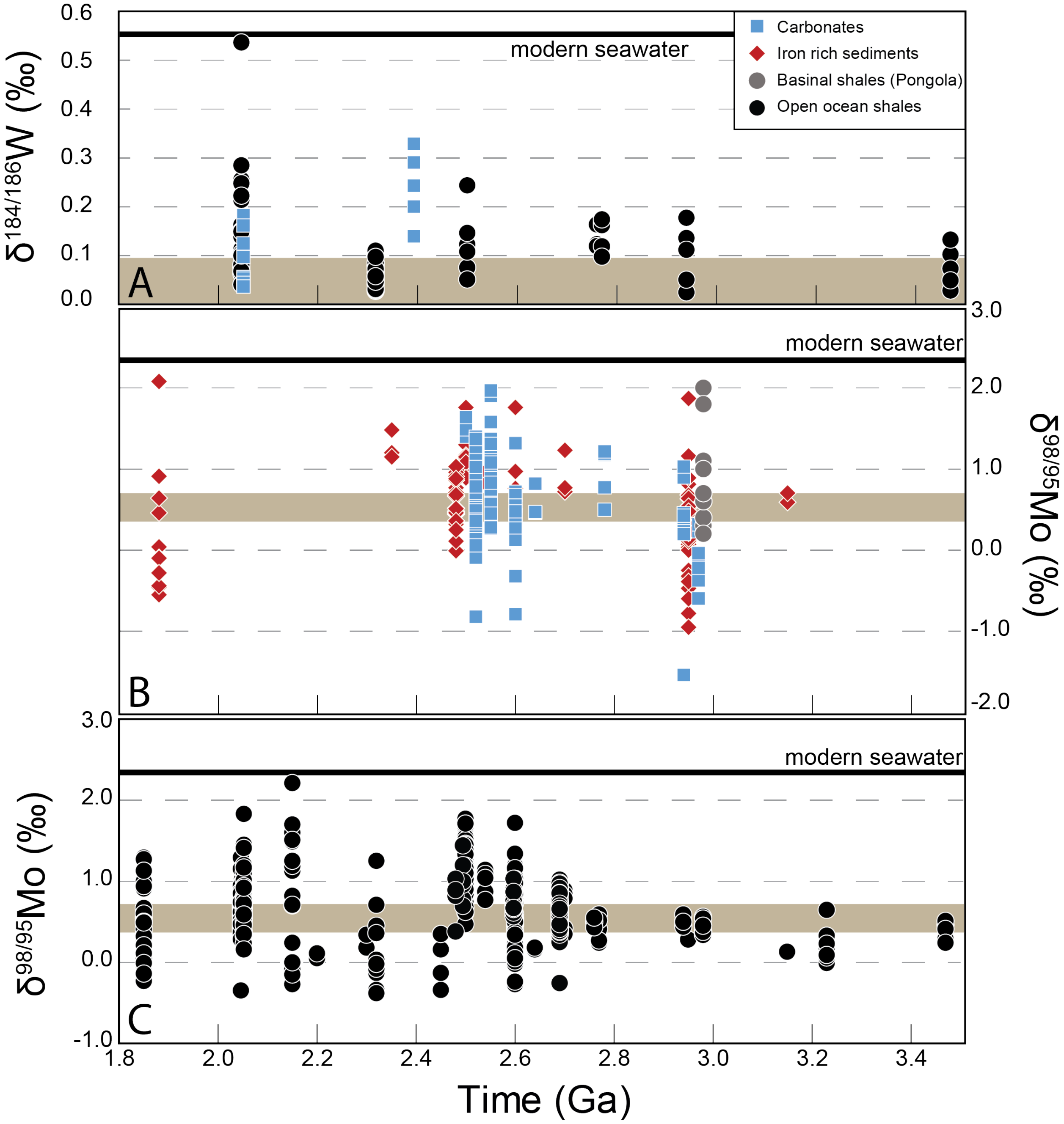

Figure 6.1: W and Mo stable isotopes variations from the Paleoarchean to the Paleoproterozoic. A: combined shallow, terresterial and marine $\delta^{186/184}$W signals Modern seawater value originates from from Fujiwara et al. (2020) and Kurzweil et al. (2021). B: shallow environments $\delta^{98/95}$Mo values. Data set originate from the compilation of Thoby et al. (2019) modern seawater value from Barling et al. (2001). C: open environment shale $\delta^{98/95}$Mo record. Data originate from Thoby et al. (2019), Ostrander et al., (2020) and Asael et al. (2018).

a very narrow $\delta^{186/184}$W range from +0.037 to +0.053 ‰ associated with very high W concentrations (4.1 to 18.6 µg.g^{-1}). These results indicate that W is efficiently leached with high-temperature hydrothermal fluids in continental settings, preserving the $\delta^{186/184}$W value of the source rock (igneous in this case). As such, the inputs of W to the Precambrian oceans were controlled by the proportions of riverine (low W concentrations with $\delta^{186/184}$W value of +0.174 ‰) and hydrothermal fluids (higher W concentrations, $\delta^{186/184}$W value mirroring the one of the W source). Carbonates deposited in deep environments revealed heavier $\delta^{186/184}$W values than shallow ones (e.g. Mooidraai Fm.), pointing towards diagenetic processes in shallow environments and retention of isotopically light W in such depositional environments.

6.2 Global model

- Pre-3.0 Ga oceans: W inputs were rather dominated by hydrothermal fluids with a PII-like $\delta^{186/184}$W value, due to the limited surface of the exposed continental crust in the Meso- to Paleoarchean (Liu and He, 2021). This hypothesis is supported by the low $\delta^{186/184}$W range observed in 3.47 Ga shales, with values ranging from +0.028 ‰ to +0.132 ‰, potentially reflecting mixing components between detrital and authigenic W from the seawater.

  The absence of authigenic Mo enrichments and associated $\delta^{98/95}$Mo values in marine shales indicates that the inputs of Mo to the ocean were non-existent or too little to efficiently shift Mo concentrations or $\delta^{98/95}$Mo values of open ocean shales, and/or that the redox potentials of the open ocean were too reducing for the persistence of MoO_4^{2-} in such environments.

- 3.0 to 2.7 Ga: the contribution of riverine W increased between 3.0 to 2.7 Ga, pushing the seawater to a hypothetical $\delta^{186/184}$W value of +0.174 ‰. Sedimentary archive from shallow or restricted marine environments revealed on-going oxide cycling, as shown with fractionated $\delta^{98/95}$Mo values (Figure 6.2 B), while open ocean sediments do not show $\delta^{98/95}$Mo values exceeding the detrital background range. Such difference between two depositional environments can be explained by a strong redoxcline separating a highly reducing ocean (Eh<-0.4 V) to less reducing (Eh>-0.4 V) shallow to restricted environments.

- 2.7 to 2.5 Ga: The open ocean sedimentary archive revealed fractioned $\delta^{98/95}$Mo values starting from 2.7 Ga (Ostrander et al., 2020), but the first significant enrichments in Mo concentrations occurred at 2.5 Ga in the Mt Roe Shale euxinic intervals (Anbar et al., 2007). Marine shales from underlying Wittenoom Fm. and Mt Sylvia Fm. revealed similar mixed PII to riverine inputs W signals, with $\delta^{186/184}$W values from +0.051 to +0.146 ‰, while a non-euxinic shale sample from the Mt McRae Shale yielded a heavier $\delta^{186/184}$W value of +0.246 ‰. Such changes in the $\delta^{186/184}$W value of marine shales might be associated with increasing scavenging of isotopically light W in oxic depositional settings during the so-called whiff of oxygen.

- 2.5 to 2.3 Ga: Marine shales deposited in the lead-up, during and the wake of the GOE revealed crustal $\delta^{186/184}$W values, most likely due to euxinic depositional environment limiting the extend of authigenic W enrichments. However, open marine carbonates of the Mooidraai Fm. yielded fractionated $\delta^{186/184}$W values reaching up to +0.329 ‰. As such, if the $\delta^{186/184}$W value measured in the Mt. McRae Shale represent the $\delta^{186/184}$W signature of the 2.5 Ga ocean, then the GOE is likely associated with an increase in seawater $\delta^{186/184}$W value.

- 2.0 Ga: Marine shales of the Zaonega Fm. deposited at the termination of the GOE are typified with $\delta^{186/184}$W values ranging from +0.041 to +0.536 ‰ and $\delta^{98/95}$Mo values from +0.325 to +1.736 ‰. The offsets between the heaviest $\delta^{186/184}$W and $\delta^{98/95}$Mo values to their respective detrital background mirrors the isotopic fractionation factor measured for WO_4^{2-} and MoO_4^{2-} adsorption onto Fe-oxides (ferrihydrite) (Goldberg et al., 2009; Kashiwabara et al., 2017). Such findings indicate that the seawater W and Mo isotopic compositions were controlled by Fe-oxides drawdown rather than Mn-oxides.

6.3 Outlook

Still, too little is known about the processes of W incorporation in marine sediments under anoxic conditions, and whether an isotopic fractionation is involved. To better understand the implications of these results, future studies could address:

- Refining the evolution of $\delta^{186/184}$W values in marine shales and carbonates with more measurements of marine sediments deposited between 2.0 to 2.7 Ga

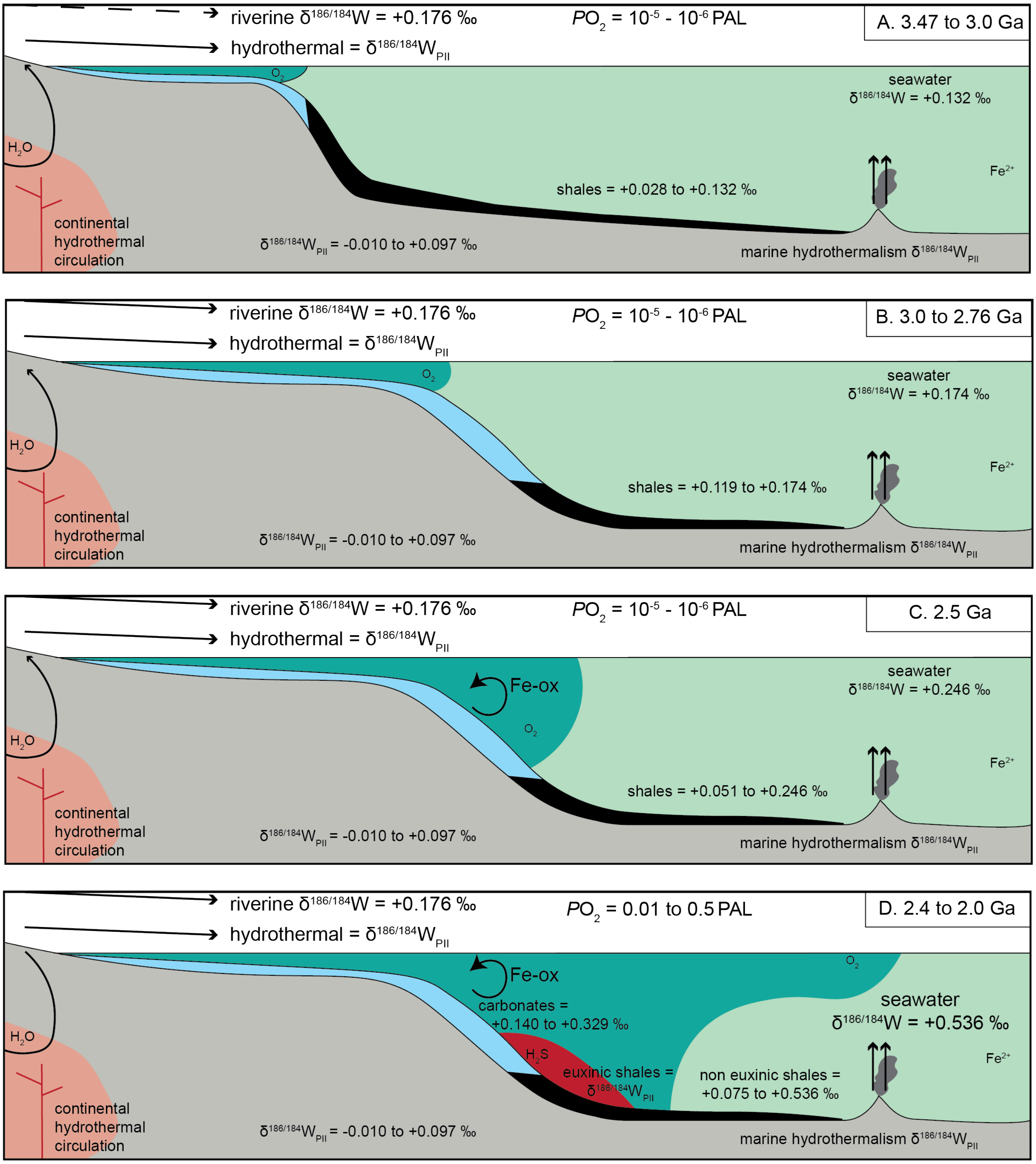

Figure 6.2: Global model of the evolution of redox state of the ocean with W and Mo isotopes.

- Adsorption experiments of tungstate onto organic matter and clay minerals
- Experimental weathering of Mt Roe Basalt samples under anoxic atmosphere and measurement of leachates and residues
- Measurement of post-GOE paleosols and tracing oxic weathering processes

References

Abraham, K., Barling, J., Siebert, C., Belshaw, N., Gall, L. and Halliday, A.N. (2015) Determination of mass-dependent variations in tungsten stable isotope compositions of geological reference materials by double-spike and MC-ICPMS. J Anal Atom Spectrom 30, 2334-2342.

Adelson, J.M., Helz, G.R. and Miller, C.V. (2001) Reconstructing the rise of recent coastal anoxia; molybdenum in Chesapeake Bay sediments. Geochim. Cosmochim. Acta 65, 237-252.

Aeolus Lee, C.-T., Leeman, W.P., Canil, D. and Li, Z.-X.A. (2005) Similar V/Sc Systematics in MORB and Arc Basalts: Implications for the Oxygen Fugacities of their Mantle Source Regions. J. Petrol. 46, 2313-2336.

Albani, A.E., Bengtson, S., Canfield, D.E., Bekker, A., Macchiarelli, R., Mazurier, A., Hammarlund, E.U., Boulvais, P., Dupuy, J.-J., Fontaine, C., Fürsich, F.T., Gauthier-Lafaye, F., Janvier, P., Javaux, E., Ossa, F.O., Pierson-Wickmann, A.-C., Riboulleau, A., Sardini, P., Vachard, D., Whitehouse, M. and Meunier, A. (2010) Large colonial organisms with coordinated growth in oxygenated environments 2.1 Gyr ago. Nature 466, 100-104.

Albut, G., Babechuk, M.G., Kleinhanns, I.C., Benger, M., Beukes, N.J., Steinhilber, B., Smith, A.J.B., Kruger, S.J. and Schoenberg, R. (2018) Modern rather than Mesoarchaean oxidative weathering responsible for the heavy stable Cr isotopic signatures of the 2.95 Ga old Ijzermijn iron formation (South Africa). Geochim. Cosmochim. Acta 228, 157-189.

Albut, G., Kamber, B.S., Bruske, A., Beukes, N.J., Smith, A.J.B. and Schoenberg, R. (2019) Modern weathering in outcrop samples versus ancient paleoredox information in drill core samples from a Mesoarchaean marine oxygen oasis in Pongola Supergroup, South Africa. Geochim. Cosmochim. Acta 265, 330-353.

Algeo, T.J. and Lyons, T.W. (2006) Mo-total organic carbon covariation in modern anoxic marine environments: Implications for analysis of paleoredox and paleohydrographic conditions. Paleoceanogr. 21.

Anbar, A.D., Duan, Y., Lyons, T.W., Arnold, G.L., Kendall, B., Creaser, R.A., Kaufman, A.J., Gordon, G.W., Scott, C., Garvin, J. and Buick, R. (2007) A whiff of oxygen before the great oxidation event? Science 317, 1903-1906.

Anbar, A.D. and Holland, H. (1992) The photochemistry of manganese and the origin of banded iron formations. Geochim. Cosmochim. Acta 56, 2595-2603.

Anbar, A.D. and Rouxel, O. (2007) Metal stable isotopes in paleoceanography. Annu. Rev. Earth Planet. Sci. 35, 717-746.

Archer, C. and Vance, D. (2008) The isotopic signature of the global riverine molybdenum flux and anoxia in the ancient oceans. Nat. Geosci. 1, 597-600.

Arevalo Jr, R. and McDonough, W.F. (2008) Tungsten geochemistry and implications for understanding the Earth's interior. Earth Planet. Sci. Lett. 272, 656-665.

Arndt, N.T. (1991) High Ni in Archean tholeiites. Tectonophysics 187, 411-419.

Arndt, N.T., Nelson, D.R., Compston, W., Trendall, A.F. and Thorne, A.M. (1991) The age of the Fortescue Group, Hamersley Basin, Western Australia, from ion microprobe zircon U-Pb results. Aust. J. Earth Sci. 38, 261-281.

Arnold, G.L., Anbar, A., Barling, J. and Lyons, T. (2004) Molybdenum isotope evidence for widespread anoxia in mid-Proterozoic oceans. Science 304, 87-90.

Asael, D., Rouxel, O., Poulton, S.W., Lyons, T.W. and Bekker, A. (2018) Molybdenum record from black shales indicates oscillating atmospheric oxygen levels in the early Paleoproterozoic. Am. J. Sci. 318, 275-299.

Asael, D., Tissot, F.L.H., Reinhard, C.T., Rouxel, O., Dauphas, N., Lyons, T.W., Ponzevera, E., Liorzou, C. and Chéron, S. (2013) Coupled molybdenum, iron and uranium stable isotopes as oceanic paleoredox proxies during the Paleoproterozoic Shunga Event. Chem. Geol. 362, 193-210.

Aulbach, S., Woodland, A.B., Stern, R.A., Vasilyev, P., Heaman, L.M. and Viljoen, K.S. (2019) Evidence for a dominantly reducing Archaean ambient mantle from two redox proxies, and low oxygen fugacity of deeply subducted oceanic crust. Scientific Reports 9, 20190.

Babechuk, M., Widdowson, M. and Kamber, B. (2014) Quantifying chemical weathering intensity and trace element release from two contrasting basalt profiles, Deccan Traps, India. Chem. Geol. 363, 56-75.

Babechuk, M.G., Kamber, B.S., Greig, A., Canil, D. and Kodolányi, J. (2010) The behaviour of tungsten during mantle melting revisited with implications for planetary differentiation time scales. Geochim. Cosmochim. Acta 74, 1448-1470.

Babechuk, M.G., Kleinhanns, I.C., Reitter, E. and Schoenberg, R. (2018) Kinetic stable Cr isotopic fractionation between aqueous Cr (III)-Cl-H_2O complexes at 25° C: implications for Cr (III) mobility and isotopic variations in modern and ancient natural systems. Geochim. Cosmochim. Acta 222, 383-405.

Babechuk, M.G., Kleinhanns, I.C. and Schoenberg, R. (2017) Chromium geochemistry of the ca. 1.85 Ga Flin Flon paleosol. Geobiology 15, 30-50.

Babechuk, M.G., Weimar, N.E., Kleinhanns, I.C., Eroglu, S., Swanner, E.D., Kenny, G.G., Kamber, B.S. and Schoenberg, R. (2019) Pervasively anoxic surface conditions at the onset of the Great Oxidation Event: New multi-proxy constraints from the Cooper Lake paleosol. Precambrian Res. 323, 126-163.

Babechuk, M.G., Widdowson, M., Murphy, M. and Kamber, B.S. (2015) A combined Y/Ho, high field strength element (HFSE) and Nd isotope perspective on basalt weathering, Deccan Traps, India. Chem. Geol. 396, 25-41.

Bakakas Mayika, K., Moussavou, M., Prave, A.R., Lepland, A., Mbina, M. and Kirsimäe, K. (2020) The Paleoproterozoic Francevillian succession of Gabon and the Lomagundi-Jatuli event. Geol.

Barling, J. and Anbar, A.D. (2004) Molybdenum isotope fractionation during adsorption by manganese oxides. Earth Planet. Sci. Lett. 217, 315-329.

Barling, J., Arnold, G.L. and Anbar, A.D. (2001) Natural mass-dependent variations in the isotopic composition of molybdenum. Earth Planet. Sci. Lett. 193, 447-457.

Baronas, J.J., West, A.J., Burton, K.W., Hammond, D.E., Opfergelt, S., Pogge von Strandmann, P.A.E., James, R.H. and Rouxel, O.J. (2020) Ge and Si Isotope Behavior During Intense Tropical Weathering and Ecosystem Cycling. Global Biogeochemical Cycles 34, e2019GB006522.

Bau, M. and Alexander, B. (2006) Preservation of primary REE patterns without Ce anomaly during dolomitization of Mid-Paleoproterozoic limestone and the potential re-establishment of marine anoxia immediately after the "Great Oxidation Event". S Afr J Geol 109, 81-86.

Bau, M., Romer, R.L., Lüders, V. and Beukes, N.J. (1999) Pb, O, and C isotopes in silicified Mooidraai dolomite (Transvaal Supergroup, South Africa): implications for the composition of Paleoproterozoic seawater and 'dating' the increase of oxygen in the Precambrian atmosphere. Earth Planet. Sci. Lett. 174, 43-57.

Bauer, K.W., Gueguen, B., Cole, D.B., Francois, R., Kallmeyer, J., Planavsky, N. and Crowe, S.A. (2018a) Chromium isotope fractionation in ferruginous sediments. Geochim. Cosmochim. Acta 223, 198-215.

Bauer, S., Conrad, S. and Ingri, J. (2018b) Geochemistry of tungsten and molybdenum during freshwater transport and estuarine mixing. Appl. Geochem. 93, 36-48.

Baumgartner, R.J., Van Kranendonk, M.J., Pagès, A., Fiorentini, M.L., Wacey, D. and Ryan, C. (2020) Accumulation of transition metals and metalloids in sulfidized stromatolites of the 3.48 billion–year–old Dresser Formation, Pilbara Craton. Precambrian Res. 337, 105534.

Becking, L.G.M.B., Kaplan, I.R. and Moore, D. (1960) Limits of the Natural Environment in Terms of pH and Oxidation-Reduction Potentials. The Journal of Geology 68, 243-284.

Bekker, A. and Holland, H.D. (2012) Oxygen overshoot and recovery during the early Paleoproterozoic. Earth Planet. Sci. Lett. 317-318, 295-304.

Bekker, A., Holland, H.D., Wang, P.L., Rumble, D., 3rd, Stein, H.J., Hannah, J.L., Coetzee, L.L. and Beukes, N.J. (2004) Dating the rise of atmospheric oxygen. Nature 427, 117-120.

Bekker, A., Karhu, J.A., Eriksson, K.A. and Kaufman, A.J. (2003) Chemostratigraphy of Paleoproterozoic carbonate successions of the Wyoming Craton: tectonic forcing of biogeochemical change? Precambrian Res. 120, 279-325.

Bellefroid, E.J., Hood, A.v.S., Hoffman, P.F., Thomas, M.D., Reinhard, C.T. and Planavsky, N.J. (2018) Constraints on Paleoproterozoic atmospheric oxygen levels. Proc. Natl. Acad. Sci. 115, 8104-8109.

Bennett, W.W. and Canfield, D.E. (2020) Redox-sensitive trace metals as paleoredox proxies: A review and analysis of data from modern sediments. Earth-Sci Rev 204, 103175.

Blake, T.S. (1993) Late Archaean crustal extension, sedimentary basin formation, flood basalt volcanism and continental rifting: the Nullagine and Mount Jope Supersequences, Western Australia. Precambrian Res. 60, 185-241.

Blättler, C., Claire, M., Prave, A.R., Kirsimäe, K., Higgins, J., Medvedev, P., Romashkin, A., Rychanchik, D., Zerkle, A.L. and Paiste, K. (2018) Two-billion-year-old evaporites capture Earth's great oxidation. Science 360, 320-323.

Bolhar, R., Van Kranendonk, M.J. and Kamber, B.S. (2005) A trace element study of siderite–jasper banded iron formation in the 3.45Ga Warrawoona Group, Pilbara Craton—Formation from hydrothermal fluids and shallow seawater. Precambrian Res. 137, 93-114.

Bolhar, R., Woodhead, J.D. and Hergt, J.M. (2003) Continental setting inferred for emplacement of the 2.9–2.7 Ga Belingwe Greenstone Belt, Zimbabwe. Geol. 31, 295-298.

Böning, P., Brumsack, H.-J., Böttcher, M.E., Schnetger, B., Kriete, C., Kallmeyer, J. and Borchers, S.L. (2004) Geochemistry of Peruvian near-surface sediments. Geochim. Cosmochim. Acta 68, 4429-4451.

Bonnand, P., James, R., Parkinson, I., Connelly, D. and Fairchild, I. (2013) The chromium isotopic composition of seawater and marine carbonates. Earth Planet. Sci. Lett. 382, 10-20.

Bonnand, P., Parkinson, I.J., James, R.H., Karjalainen, A.-M. and Fehr, M.A. (2011) Accurate and precise determination of stable Cr isotope compositions in carbonates by double spike MC-ICP-MS. J Anal Atom Spectrom 26, 528-535.

Borchers, S.L., Schnetger, B., Böning, P. and Brumsack, H.-J. (2005) Geochemical signatures of the Namibian diatom belt: Perennial upwelling and intermittent anoxia. Geochem. Geophys. Geosyst. 6.

Bosco-Santos, A., Gilhooly, W.P., Fouskas, F., Fabricio-Silva, W. and Oliveira, E.P. (2020) Euxinia in the Neoarchean: The starting point for early oxygenation in a Brazilian Craton. Precambrian Res. 341, 105655.

Breton, T. and Quitte, G. (2014) High-precision measurements of tungsten stable isotopes and application to earth sciences. J Anal Atom Spectrom 29, 2284-2293.

Brimhall, G.H. and Dietrich, W.E. (1987) Constitutive mass balance relations between chemical composition, volume, density, porosity, and strain in metasomatic hydrochemical systems: Results on weathering and pedogenesis. Geochim. Cosmochim. Acta 51, 567-587.

Brumsack, H.-J. (1989) Geochemistry of recent TOC-rich sediments from the Gulf of California and the Black Sea. Geologische Rundschau 78, 851-882.

Brüske, A., Martin, A.N., Rammensee, P., Eroglu, S., Lazarov, M., Albut, G., Schuth, S., Aulbach, S., Schoenberg, R., Beukes, N., Hofmann, A., Nägler, T. and Weyer, S. (2020a) The onset of oxidative weathering traced by uranium isotopes. Precambrian Res. 338, 105583.

Brüske, A., Weyer, S., Zhao, M.Y., Planavsky, N.J., Wegwerth, A., Neubert, N., Dellwig, O., Lau, K.V. and Lyons, T.W. (2020b) Correlated molybdenum and uranium isotope signatures in modern anoxic sediments: Implications for their use as paleo-redox proxy. Geochim.

Cosmochim. Acta 270, 449-474.

Calvert, S.E. and Pedersen, T.F. (1993) Geochemistry of Recent oxic and anoxic marine sediments: Implications for the geological record. Mar. Geol. 113, 67-88.

Canfield, D.E. (1998) A new model for Proterozoic ocean chemistry. Nature 396, 450-453.

Canfield, D.E., Habicht, K.S. and Thamdrup, B. (2000) The Archean sulfur cycle and the early history of atmospheric oxygen. Science 288, 658-661.

Canfield, D.E., Ngombi-Pemba, L., Hammarlund, E.U., Bengtson, S., Chaussidon, M., Gauthier-Lafaye, F., Meunier, A., Riboulleau, A., Rollion-Bard, C. and Rouxel, O. (2013) Oxygen dynamics in the aftermath of the Great Oxidation of Earth's atmosphere. Proc. Natl. Acad. Sci. 110, 16736-16741.

Canfield, D.E., Poulton, S.W., Knoll, A.H., Narbonne, G.M., Ross, G., Goldberg, T. and Strauss, H. (2008) Ferruginous conditions dominated later neoproterozoic deep-water chemistry. Science 321, 949-952.

Canfield, D.E. and Raiswell, R. (1999) The evolution of the sulfur cycle. Am. J. Sci. 299, 697-723.

Catling, D.C. and Zahnle, K.J. (2020) The Archean atmosphere. Science Advances 6, eaax1420.

Chauvel, C., Dupré, B. and Arndt, N. (1993) Pb and Nd isotopic correlation in Belingwe komatiites and basalts, The geology of the Belingwe Greenstone Belt, Zimbabwe. A study of the evolution of Archaean continental crust, pp. 167-174.

Che, X.D., Linnen, R.L., Wang, R.C., Aseri, A. and Thibault, Y. (2013) Tungsten solubility in evolved granitic melts: An evaluation of magmatic wolframite. Geochim. Cosmochim. Acta 106, 84-98.

Chen, K., Rudnick, R.L., Wang, Z., Tang, M., Gaschnig, R.M., Zou, Z., He, T., Hu, Z. and Liu, Y. (2020) How mafic was the Archean upper continental crust? Insights from Cu and Ag in ancient glacial diamictites. Geochim. Cosmochim. Acta.

Chen, X., Romaniello, S.J., Herrmann, A.D., Hardisty, D., Gill, B.C. and Anbar, A.D. (2018) Diagenetic effects on uranium isotope fractionation in carbonate sediments from the Bahamas. Geochim. Cosmochim. Acta 237, 294-311.

Clarkson, M.O., Müsing, K., Andersen, M.B. and Vance, D. (2020) Examining pelagic carbonate-rich sediments as an archive for authigenic uranium and molybdenum isotopes using reductive cleaning and leaching experiments. Chem. Geol. 539, 119412.

Coetzee, L.L. (2001) Genetic stratigraphy of the Paleoproterozoic Pretoria Group in the western

Transvaal. University of Johannesburg.

Cole, D.B., Reinhard, C.T., Wang, X., Gueguen, B., Halverson, G.P., Gibson, T., Hodgskiss, M.S.W., McKenzie, N.R., Lyons, T.W. and Planavsky, N.J. (2016) A shale-hosted Cr isotope record of low atmospheric oxygen during the Proterozoic. Geol. 44, 555-558.

Condie, K.C. (1993) Chemical-Composition and Evolution of the Upper Continental-Crust - Contrasting Results from Surface Samples and Shales. Chem. Geol. 104, 1-37.

Črne, A., Melezhik, V., Prave, A., Lepland, A., Romashkin, A., Rychanchik, D., Hanski, E. and Luo, Z.-Y. (2013) Zaonega Formation: FAR-DEEP Holes 12A and 12B, and neighbouring quarries. Frontiers in Earth Sciences 7, 946-1007.

Crowe, S.A., Døssing, L.N., Beukes, N.J., Bau, M., Kruger, S.J., Frei, R. and Canfield, D.E. (2013) Atmospheric oxygenation three billion years ago. Nature 501, 535-538.

Crusius, J., Calvert, S., Pedersen, T. and Sage, D. (1996) Rhenium and molybdenum enrichments in sediments as indicators of oxic, suboxic and sulfidic conditions of deposition. Earth Planet. Sci. Lett. 145, 65-78.

Cui, M. and Johannesson, K.H. (2017) Comparison of tungstate and tetrathiotungstate adsorption onto pyrite. Chem. Geol. 464, 57-68.

Cui, M., Luther, G.W. and Gomes, M. (2021) Cycling of W and Mo species in natural sulfidic waters and their sorption mechanisms on MnO_2 and implications for paired W and Mo records as a redox proxy. Geochim. Cosmochim. Acta 295, 24-48.

Cui, M., Mohajerin, T.J., Adebayo, S., Datta, S. and Johannesson, K.H. (2020) Investigation of tungstate thiolation reaction kinetics and sedimentary molybdenum/tungsten enrichments: Implication for tungsten speciation in sulfidic waters and possible applications for paleoredox studies. Geochim. Cosmochim. Acta.

Czaja, A.D., Johnson, C.M., Roden, E.E., Beard, B.L., Voegelin, A.R., Nägler, T.F., Beukes, N.J. and Wille, M. (2012) Evidence for free oxygen in the Neoarchean ocean based on coupled iron–molybdenum isotope fractionation. Geochim. Cosmochim. Acta 86, 118-137.

Dahl, T.W., Anbar, A.D., Gordon, G.W., Rosing, M.T., Frei, R. and Canfield, D.E. (2010) The behavior of molybdenum and its isotopes across the chemocline and in the sediments of sulfidic Lake Cadagno, Switzerland. Geochim. Cosmochim. Acta 74, 144-163.

Daines, S.J., Mills, B.J.W. and Lenton, T.M. (2017) Atmospheric oxygen regulation at low Proterozoic levels by incomplete oxidative weathering of sedimentary organic carbon.

Nature Communications 8, 14379.

Dauphas, N. and Pourmand, A. (2011) Hf–W–Th evidence for rapid growth of Mars and its status as a planetary embryo. Nature 473, 489-492.

Daye, M., Klepac-Ceraj, V., Pajusalu, M., Rowland, S., Farrell-Sherman, A., Beukes, N., Tamura, N., Fournier, G. and Bosak, T. (2019) Light-driven anaerobic microbial oxidation of manganese. Nature 576, 311-314.

De Ronde, C.E. and Kamo, S.L. (2000) An Archean arc-arc collisional event: a short-lived (ca 3 Myr) episode, Weltevreden area, Barberton greenstone belt, South Africa. J. Afr. Earth. Sci. 30, 219-248.

Dehaine, Q., Tijsseling, L.T., Glass, H.J., Törmänen, T. and Butcher, A.R. (2021) Geometallurgy of cobalt ores: A review. Minerals Engineering 160, 106656.

Dehouck, E., Gaudin, A., Mangold, N., Lajaunie, L., Dauzères, A., Grauby, O. and Le Menn, E. (2014) Weathering of olivine under CO_2 atmosphere: A martian perspective. Geochim. Cosmochim. Acta 135, 170-189.

Dellwig, O., Beck, M., Lemke, A., Lunau, M., Kolditz, K., Schnetger, B. and Brumsack, H.-J. (2007) Non-conservative behaviour of molybdenum in coastal waters: Coupling geochemical, biological, and sedimentological processes. Geochim. Cosmochim. Acta 71, 2745-2761.

Dellwig, O., Wegwerth, A., Schnetger, B., Schulz, H. and Arz, H.W. (2019) Dissimilar behaviors of the geochemical twins W and Mo in hypoxic-euxinic marine basins. Earth-Sci Rev 193, 1-23.

Dermatas, D., Braida, W., Christodoulatos, C., Strigul, N., Panikov, N., Los, M. and Larson, S. (2004) Solubility, Sorption, and Soil Respiration Effects of Tungsten and Tungsten Alloys. Environ. Forensics 5, 5-13.

Dickson, A.J., Idiz, E., Porcelli, D. and van den Boorn, S.H. (2020) The influence of thermal maturity on the stable isotope compositions and concentrations of molybdenum, zinc and cadmium in organic-rich marine mudrocks. Geochim. Cosmochim. Acta 287, 205-220.

Duan, Y., Anbar, A.D., Arnold, G.L., Lyons, T.W., Gordon, G.W. and Kendall, B. (2010) Molybdenum isotope evidence for mild environmental oxygenation before the Great Oxidation Event. Geochim. Cosmochim. Acta 74, 6655-6668.

Dupraz, C. and Visscher, P.T. (2005) Microbial lithification in marine stromatolites and hypersaline mats. Trends in Microbiology 13, 429-438.

Eggins, S., Woodhead, J., Kinsley, L., Mortimer, G., Sylvester, P., McCulloch, M., Hergt, J. and Handler, M. (1997) A simple method for the precise determination of $\geq$ 40 trace elements in geological samples by ICPMS using enriched isotope internal standardisation. Chem. Geol. 134, 311-326.

Eickmann, B., Hofmann, A., Wille, M., Bui, T.H., Wing, B.A. and Schoenberg, R. (2018) Isotopic evidence for oxygenated Mesoarchaean shallow oceans. Nat. Geosci. 11, 133-138.

Emerson, S.R. and Huested, S.S. (1991) Ocean anoxia and the concentrations of molybdenum and vanadium in seawater. Mar. Chem. 34, 177-196.

Erickson, B.E. and Helz, G.R. (2000) Molybdenum(VI) speciation in sulfidic waters:: Stability and lability of thiomolybdates. Geochim. Cosmochim. Acta 64, 1149-1158.

Eroglu, S., Schoenberg, R., Wille, M., Beukes, N. and Taubald, H. (2015) Geochemical stratigraphy, sedimentology, and Mo isotope systematics of the ca. 2.58-2.50 Ga-old Transvaal Supergroup carbonate platform, South Africa. Precambrian Res. 266, 27-46.

Eroglu, S., Scholz, F., Frank, M. and Siebert, C. (2020) Influence of particulate versus diffusive molybdenum supply mechanisms on the molybdenum isotope composition of continental margin sediments. Geochim. Cosmochim. Acta 273, 51-69.

Ertel, W., O'Neill, H.S.C., Dingwell, D.B. and Spettel, B. (1996) Solubility of tungsten in a haplobasaltic melt as a function of temperature and oxygen fugacity. Geochim. Cosmochim. Acta 60, 1171-1180.

Farkaš, J., Chrastný, V., Novák, M., Čadkova, E., Pašava, J., Chakrabarti, R., Jacobsen, S.B., Ackerman, L. and Bullen, T.D. (2013) Chromium isotope variations ($\delta^{53/52}$Cr) in mantle-derived sources and their weathering products: Implications for environmental studies and the evolution of $\delta^{53/52}$Cr in the Earth's mantle over geologic time. Geochim. Cosmochim. Acta 123, 74-92.

Farquhar, J., Bao, H. and Thiemens, M. (2000) Atmospheric influence of Earth's earliest sulfur cycle. Science 289, 756-759.

Fedo, C.M., Wayne Nesbitt, H. and Young, G.M. (1995) Unraveling the effects of potassium metasomatism in sedimentary rocks and paleosols, with implications for paleoweathering conditions and provenance. Geol. 23, 921-924.

Firdaus, M.L., Norisuye, K., Nakagawa, Y., Nakatsuka, S. and Sohrin, Y. (2008) Dissolved and labile particulate zr, hf, nb, ta, mo and W in the western North Pacific Ocean. J. Oceanogr. 64, 247-257.

Fonseca, R.O., Mallmann, G., Sprung, P., Sommer, J.E., Heuser, A., Speelmanns, I.M. and Blanchard, H. (2014) Redox controls on tungsten and uranium crystal/silicate melt partitioning and implications for the U/W and Th/W ratio of the lunar mantle. Earth Planet. Sci. Lett. 404, 1-13.

Frank, A.B., Klaebe, R.M. and Frei, R. (2019) Fractionation Behavior of Chromium Isotopes during the Sorption of Cr (VI) on Kaolin and its Implications for Using Black Shales as a Paleoredox Archive. Geochem. Geophys. Geosyst. 20, 2290-2302.

Frei, R., Gaucher, C., Døssing, L.N. and Sial, A.N. (2011) Chromium isotopes in carbonates — A tracer for climate change and for reconstructing the redox state of ancient seawater. Earth Planet. Sci. Lett. 312, 114-125.

Frei, R., Gaucher, C., Poulton, S.W. and Canfield, D.E. (2009) Fluctuations in Precambrian atmospheric oxygenation recorded by chromium isotopes. Nature 461, 250-253.

Freymuth, H., Vils, F., Willbold, M., Taylor, R.N. and Elliott, T. (2015) Molybdenum mobility and isotopic fractionation during subduction at the Mariana arc. Earth Planet. Sci. Lett. 432, 176-186.

Fuchs, S., Williams-Jones, A.E., Jackson, S.E. and Przybylowicz, W.J. (2016) Metal distribution in pyrobitumen of the Carbon Leader Reef, Witwatersrand Supergroup, South Africa: Evidence for liquid hydrocarbon ore fluids. Chem. Geol. 426, 45-59.

Fujiwara, Y., Tsujisaka, M., Takano, S. and Sohrin, Y. (2020) Determination of the tungsten isotope composition in seawater: The first vertical profile from the western North Pacific Ocean. Chem. Geol. 555, 119835.

Gaillardet, J., Viers, J. and Dupré, B. (2014) 7.7 - Trace Elements in River Waters A2 - Holland, Heinrich D, in: Turekian, K.K. (Ed.), Treatise on Geochemistry (Second Edition). Elsevier, Oxford, pp. 195-235.

Gaschnig, R.M., Rudnick, R.L., McDonough, W.F., Kaufman, A.J., Hu, Z. and Gao, S. (2014) Onset of oxidative weathering of continents recorded in the geochemistry of ancient glacial diamictites. Earth Planet. Sci. Lett. 408, 87-99.

Gaschnig, R.M., Rudnick, R.L., McDonough, W.F., Kaufman, A.J., Valley, J.W., Hu, Z., Gao, S. and Beck, M.L. (2016) Compositional evolution of the upper continental crust through time, as constrained by ancient glacial diamictites. Geochim. Cosmochim. Acta 186, 316-343.

Gaspers, N., Magna, T. and Ackerman, L. (2020) Molybdenum mass fractions and stable isotope compositions of sedimentary carbonate and silicate reference materials. Geostand. Geoanal. Res. 44, 363-374.

Ghosh, R. (2020) Authigenic precipitation of ferric oxyhydroxides and greenalite in Archean oceans. Chem. Geol. 552, 119777.

Gilleaudeau, G.J., Frei, R., Kaufman, A., Kah, L., Azmy, K., Bartley, J., Chernyavskiy, P. and Knoll, A.H. (2016) Oxygenation of the mid-Proterozoic atmosphere: clues from chromium isotopes in carbonates. Geochem. Perspect. Lett.

Gilleaudeau, G.J., Romaniello, S.J., Luo, G., Kaufman, A.J., Zhang, F., Klaebe, R.M., Kah, L.C., Azmy, K., Bartley, J.K., Zheng, W., Knoll, A.H. and Anbar, A.D. (2019) Uranium isotope evidence for limited euxinia in mid-Proterozoic oceans. Earth Planet. Sci. Lett. 521, 150-157.

Gilleaudeau, G.J., Sahoo, S.K., Ostrander, C.M., Owens, J.D., Poulton, S.W., Lyons, T.W. and Anbar, A.D. (2020) Molybdenum isotope and trace metal signals in an iron-rich Mesoproterozoic ocean: A snapshot from the Vindhyan Basin, India. Precambrian Res. 343, 105718.

Goldberg, T., Archer, C., Vance, D. and Poulton, S.W. (2009) Mo isotope fractionation during adsorption to Fe (oxyhydr)oxides. Geochim. Cosmochim. Acta 73, 6502-6516.

Goldberg, T., Gordon, G., Izon, G., Archer, C., Pearce, C.R., McManus, J., Anbar, A.D. and Rehkämper, M. (2013) Resolution of inter-laboratory discrepancies in Mo isotope data: an intercalibration. J Anal Atom Spectrom 28, 724-735.

Greaney, A.T., Rudnick, R.L., Helz, R.T., Gaschnig, R.M., Piccoli, P.M. and Ash, R.D. (2017) The behavior of chalcophile elements during magmatic differentiation as observed in Kilauea Iki lava lake, Hawaii. Geochim. Cosmochim. Acta 210, 71-96.

Greaney, A.T., Rudnick, R.L., Romaniello, S.J., Johnson, A.C., Anbar, A.D. and Cummings, M.L. (2021) Assessing molybdenum isotope fractionation during continental weathering as recorded by weathering profiles in saprolites and bauxites. Chem. Geol. 566, 120103.

Greaney, A.T., Rudnick, R.L., Romaniello, S.J., Johnson, A.C., Gaschnig, R.M. and Anbar, A.D. (2020) Molybdenum isotope fractionation in glacial diamictites tracks the onset of oxidative weathering of the continental crust. Earth Planet. Sci. Lett. 534, 116083.

Greber, N.D. and Dauphas, N. (2019) The chemistry of fine-grained terrigenous sediments reveals a chemically evolved Paleoarchean emerged crust. Geochim. Cosmochim. Acta 255, 247-264.

Greber, N.D., Dauphas, N., Bekker, A., Ptáček, M.P., Bindeman, I.N. and Hofmann, A. (2017) Titanium isotopic evidence for felsic crust and plate tectonics 3.5 billion years ago. Science 357, 1271-1274.

Greber, N.D., Mäder, U. and Nägler, T.F. (2015a) Experimental dissolution of molybdenum-sulphides at low oxygen concentrations: A first-order approximation of late Archean atmospheric conditions. Earth Space Sci. 2, 173-180.

Greber, N.D., Puchtel, I.S., Nägler, T.F. and Mezger, K. (2015b) Komatiites constrain molybdenum isotope composition of the Earth's mantle. Earth Planet. Sci. Lett. 421, 129-138.

Greber, N.D., Siebert, C., Nägler, T.F. and Pettke, T. (2012) $\delta^{98/95}$Mo values and Molybdenum Concentration Data for NIST SRM 610, 612 and 3134: Towards a Common Protocol for Reporting Mo Data. Geostand. Geoanal. Res. 36, 291-300.

Gumsley, A.P., Chamberlain, K.R., Bleeker, W., Söderlund, U., de Kock, M.O., Larsson, E.R. and Bekker, A. (2017) Timing and tempo of the Great Oxidation Event. Proc. Natl. Acad. Sci. 114, 1811-1816.

Gustafsson, J.P. (2019) Vanadium geochemistry in the biogeosphere –speciation, solid-solution interactions, and ecotoxicity. Appl. Geochem. 102, 1-25.

Halevy, I. and Bachan, A. (2017) The geologic history of seawater pH. Science 355, 1069-1071.

Hannah, J.L., Bekker, A., Stein, H.J., Markey, R.J. and Holland, H.D. (2004) Primitive Os and 2316 Ma age for marine shale: implications for Paleoproterozoic glacial events and the rise of atmospheric oxygen. Earth Planet. Sci. Lett. 225, 43-52.

Hao, J., Knoll, A.H., Huang, F., Hazen, R.M. and Daniel, I. (2020) Cycling phosphorus on the Archean Earth: Part I. Continental weathering and riverine transport of phosphorus. Geochim. Cosmochim. Acta 273, 70-84.

Hawkesworth, C.J. and Kemp, A.I. (2006) Evolution of the continental crust. Nature 443, 811-817.

Hein, J.R. and Koschinsky, A. (2014) Deep-ocean ferromanganese crusts and nodules.

Helz, G.R., Miller, C.V., Charnock, J.M., Mosselmans, J.F.W., Pattrick, R.A.D., Garner, C.D. and Vaughan, D.J. (1996) Mechanism of molybdenum removal from the sea and its concentration in black shales: EXAFS evidence. Geochim. Cosmochim. Acta 60, 3631-3642.

Helz, G.R., Vorlicek, T.P. and Kahn, M.D. (2004) Molybdenum scavenging by iron monosulfide. Environ Sci Technol 38, 4263-4268.

Hessler, A.M. and Lowe, D.R. (2006) Weathering and sediment generation in the Archean: An integrated study of the evolution of siliciclastic sedimentary rocks of the 3.2Ga Moodies Group, Barberton Greenstone Belt, South Africa. Precambrian Res. 151, 185-210.

Hickman, A.H. (2012) Review of the Pilbara Craton and Fortescue Basin, Western Australia: Crustal evolution providing environments for early life. Isl. Arc 21, 1-31.

Hodgson, G.W. and Baker, B.L. (1957) Vanadium, nickel, and porphyrins in thermal geochemistry of petroleum. AAPG Bulletin 41, 2413-2426.

Hoffman, P.F. (2013) The Great Oxidation and a Siderian snowball Earth: MIF-S based correlation of Paleoproterozoic glacial epochs. Chem. Geol. 362, 143-156.

Holland, H.D. (1984) The chemical evolution of the atmosphere and oceans. Princeton University Press.

Holland, H.D. (2002) Volcanic gases, black smokers, and the great oxidation event. Geochim. Cosmochim. Acta 66, 3811-3826.

Homann, M., Sansjofre, P., Van Zuilen, M., Heubeck, C., Gong, J., Killingsworth, B., Foster, I.S., Airo, A., Van Kranendonk, M.J., Ader, M. and Lalonde, S.V. (2018) Microbial life and biogeochemical cycling on land 3,220 million years ago. Nat. Geosci. 11, 665-671.

Hur, H. and Reeder, R.J. (2016) Tungstate sorption mechanisms on boehmite: Systematic uptake studies and X-ray absorption spectroscopy analysis. J. Colloid Interface Sci. 461, 249-260.

Iwai, T. and Hashimoto, Y. (2017) Adsorption of tungstate (WO_4) on birnessite, ferrihydrite, gibbsite, goethite and montmorillonite as affected by pH and competitive phosphate (PO_4) and molybdate (MoO_4) oxyanions. App. Clay Sci. 143, 372-377.

Jochum, K.P., Nohl, U., Herwig, K., Lammel, E., Stoll, B. and Hofmann, A.W. (2005) GeoReM: A New Geochemical Database for Reference Materials and Isotopic Standards. Geostand. Geoanal. Res. 29, 333-338.

Johannesson, K.H., Dave, H.B., Mohajerin, T.J. and Datta, S. (2013) Controls on tungsten concentrations in groundwater flow systems: The role of adsorption, aquifer sediment Fe(III) oxide/oxyhydroxide content, and thiotungstate formation. Chem. Geol. 351, 76-94.

Johannesson, K.H., Lyons, W.B., Graham, E.Y. and Welch, K.A. (2000) Oxyanion Concentrations in Eastern Sierra Nevada Rivers – 3. Boron, Molybdenum, Vanadium, and Tungsten. Aquat. Geochem. 6, 19-46.

Johnson, A.C., Ostrander, C.M., Romaniello, S.J., Reinhard, C.T., Greaney, A.T., Lyons, T.W. and Anbar, A.D. (2021) Reconciling evidence of oxidative weathering and atmospheric anoxia on Archean Earth. Sci. Adv. 7, eabj0108.

Johnson, A.C., Romaniello, S.J., Reinhard, C.T., Gregory, D.D., Garcia-Robledo, E., Revsbech, N.P., Canfield, D.E., Lyons, T.W. and Anbar, A.D. (2019) Experimental determination of pyrite and molybdenite oxidation kinetics at nanomolar oxygen concentrations. Geochim. Cosmochim. Acta 249, 160-172.

Johnson, J.E., Gerpheide, A., Lamb, M.P. and Fischer, W.W. (2014) O_2 constraints from Paleoproterozoic detrital pyrite and uraninite. GSA Bulletin 126, 813-830.

Joosu, L., Lepland, A., Kreitsmann, T., Üpraus, K., Roberts, N.M.W., Paiste, P., Martin, A.P. and Kirsimäe, K. (2016) Petrography and the REE-composition of apatite in the Paleoproterozoic Pilgujärvi Sedimentary Formation, Pechenga Greenstone Belt, Russia. Geochim. Cosmochim. Acta 186, 135-153.

Kamo, S. and Davis, D. (1994) Reassessment of Archean crustal development in the Barberton Mountain Land, South Africa, based on U-Pb dating. Tectonics 13, 167-192.

Kappler, A., Pasquero, C., Konhauser, K.O. and Newman, D.K. (2005) Deposition of banded iron formations by anoxygenic phototrophic Fe (II)-oxidizing bacteria. Geol. 33, 865-868.

Karhu, J.A. and Holland, H.D. (1996) Carbon isotopes and the rise of atmospheric oxygen. Geol. 24, 867-870.

Karlstrom, K.E., Åhäll, K.-I., Harlan, S.S., Williams, M.L., McLelland, J. and Geissman, J.W. (2001) Long-lived (1.8–1.0 Ga) convergent orogen in southern Laurentia, its extensions to Australia and Baltica, and implications for refining Rodinia. Precambrian Res. 111, 5-30.

Kashiwabara, T., Kubo, S., Tanaka, M., Senda, R., Iizuka, T., Tanimizu, M. and Takahashi, Y. (2017) Stable isotope fractionation of tungsten during adsorption on Fe and Mn (oxyhydr) oxides. Geochim. Cosmochim. Acta 204, 52-67.

Kashiwabara, T., Takahashi, Y., Marcus, M.A., Uruga, T., Tanida, H., Terada, Y. and Usui, A. (2013) Tungsten species in natural ferromanganese oxides related to its different behavior from molybdenum in oxic ocean. Geochim. Cosmochim. Acta 106, 364-378.

Kashiwabara, T., Takahashi, Y., Tanimizu, M. and Usui, A. (2011) Molecular-scale mechanisms of distribution and isotopic fractionation of molybdenum between seawater and ferromanganese oxides. Geochim. Cosmochim. Acta 75, 5762-5784.

Kashiwabara, T., Takahashi, Y., Uruga, T., Tanida, H., Terada, Y., Niwa, Y. and Nomura, M. (2010) Speciation of tungsten in natural ferromanganese oxides using wavelength dispersive XAFS. Chem. Lett. 39, 870-871.

Kaufman, A.J., Knoll, A.H. and Narbonne, G.M. (1997) Isotopes, ice ages, and terminal Proterozoic earth history. Proc. Natl. Acad. Sci. 94, 6600-6605.

Kendall, B., Brennecka, G.A., Weyer, S. and Anbar, A.D. (2013) Uranium isotope fractionation suggests oxidative uranium mobilization at 2.50Ga. Chem. Geol. 362, 105-114.

Kendall, B., Dahl, T.W. and Anbar, A.D. (2017) The Stable Isotope Geochemistry of Molybdenum. Rev. Mineral. Geochem. 82, 683-732.

Kendall, B., Gordon, G.W., Poulton, S.W. and Anbar, A.D. (2011) Molybdenum isotope constraints on the extent of late Paleoproterozoic ocean euxinia. Earth Planet. Sci. Lett. 307, 450-460.

Kendall, B., Reinhard, C.T., Lyons, T.W., Kaufman, A.J., Poulton, S.W. and Anbar, A.D. (2010) Pervasive oxygenation along late Archaean ocean margins. Nat. Geosci. 3, 647-652.

Ketris, M.P. and Yudovich, Y.E. (2009) Estimations of Clarkes for Carbonaceous biolithes: World averages for trace element contents in black shales and coals. Int. J. Coal Geol. 78, 135-148.

Kipp, M.A., Lepland, A. and Buick, R. (2020) Redox fluctuations, trace metal enrichment and phosphogenesis in the 2.0 Ga Zaonega Formation. Precambrian Res. 343, 105716.

Kirschvink, J.L. (1992) Late Proterozoic low-latitude global glaciation: the snowball Earth.

Kishida, K., Sohrin, Y., Okamura, K. and Ishibashi, J.-i. (2004) Tungsten enriched in submarine hydrothermal fluids. Earth Planet. Sci. Lett. 222, 819-827.

Kleine, T., Münker, C., Mezger, K. and Palme, H. (2002) Rapid accretion and early core formation on asteroids and the terrestrial planets from Hf–W chronometry. Nature 418, 952-955.

Kleinhanns, I.C., Kramers, J.D. and Kamber, B.S. (2003) Importance of water for Archaean granitoid petrology: a comparative study of TTG and potassic granitoids from Barberton Mountain Land, South Africa. Contrib. Mineral. Petrol. 145, 377-389.

Knoll, A.H., Bergmann, K.D. and Strauss, J.V. (2016) Life: the first two billion years. Philosophical Transactions of the Royal Society B: Biological Sciences 371, 20150493.

Konhauser, K.O., Amskold, L., Lalonde, S.V., Posth, N.R., Kappler, A. and Anbar, A. (2007) Decoupling photochemical Fe(II) oxidation from shallow-water BIF deposition. Earth Planet. Sci. Lett. 258, 87-100.

Konhauser, K.O., Lalonde, S.V., Planavsky, N.J., Pecoits, E., Lyons, T.W., Mojzsis, S.J., Rouxel, O.J., Barley, M.E., Rosìere, C., Fralick, P.W., Kump, L.R. and Bekker, A. (2011) Aerobic bacterial pyrite oxidation and acid rock drainage during the Great Oxidation Event. Nature 478, 369-373.

König, S., Münker, C., Hohl, S., Paulick, H., Barth, A., Lagos, M., Pfänder, J. and Büchl, A. (2011) The Earth's tungsten budget during mantle melting and crust formation. Geochim. Cosmochim. Acta 75, 2119-2136.

Kowalski, N., Dellwig, O., Beck, M., Grawe, U., Neubert, N., Nagler, T.F., Badewien, T.H., Brumsack, H.J., van Beusekom, J.E.E. and Bottcher, M.E. (2013) Pelagic molybdenum concentration anomalies and the impact of sediment resuspension on the molybdenum budget in two tidal systems of the North Sea. Geochim. Cosmochim. Acta 119, 198-211.

Krabbe, N., Kruijer, T.S. and Kleine, T. (2017) Tungsten stable isotope compositions of terrestrial samples and meteorites determined by double spike MC-ICPMS. Chem. Geol. 450, 135-144.

Krauskopf, K. and Bird, D. (1995) Introduction to geochemistry.

Krissansen-Totton, J., Arney, G.N. and Catling, D.C. (2018) Constraining the climate and ocean pH of the early Earth with a geological carbon cycle model. Proc Natl Acad Sci U S A 115, 4105-4110.

Kruijer, T., Touboul, M., Fischer-Gödde, M., Bermingham, K., Walker, R. and Kleine, T. (2014) Protracted core formation and rapid accretion of protoplanets. Science 344, 1150-1154.

Kump, L.R., Junium, C., Arthur, M.A., Brasier, A., Fallick, A., Melezhik, V., Lepland, A., CČrne, A.E. and Luo, G. (2011) Isotopic Evidence for Massive Oxidation of Organic Matter Following the Great Oxidation Event. Science 334, 1694-1696.

Kunzendorf, H. and Glasby, G.P. (1992) Tungsten accumulation in Pacific ferromanganese deposits. Miner. Deposita 27, 147-152.

Kunzmann, M., Gutzmer, J., Beukes, N.J. and Halverson, G.P. (2014) Depositional environment and lithostratigraphy of the Paleoproterozoic Mooidraai Formation, Kalahari Maganese Field, South Africa. S Afr J Geol 117, 173-192.

Kurzweil, F., Archer, C., Wille, M., Schoenberg, R., Münker, C. and Dellwig, O. (2021) Redox control on the tungsten isotope composition of seawater. Proc. Natl. Acad. Sci., in press.

Kurzweil, F., Munker, C., Grupp, M., Braukmuller, N., Fechtner, L., Christian, M., Hohl, S.V. and Schoenberg, R. (2019) The stable tungsten isotope composition of modern igneous reservoirs. Geochim. Cosmochim. Acta 251, 176-191.

Kurzweil, F., Münker, C., Hoffmann, J.E., Tusch, J. and Schoenberg, R. (2020) Stable W isotope evidence for redistribution of homogeneous 182W anomalies in SW Greenland. Geochem. Perspect. Lett. 14, 53-57.

Kurzweil, F., Munker, C., Tusch, J. and Schoenberg, R. (2018) Accurate stable tungsten isotope measurements of natural samples using a W-180-W-183 double-spike. Chem. Geol. 476, 407-417.

Kurzweil, F., Wille, M., Gantert, N., Beukes, N.J. and Schoenberg, R. (2016) Manganese oxide shuttling in pre-GOE oceans – evidence from molybdenum and iron isotopes. Earth Planet. Sci. Lett. 452, 69-78.

Kurzweil, F., Wille, M., Schoenberg, R., Taubald, H. and Van Kranendonk, M.J. (2015) Continuously increasing δ^{98}Mo values in Neoarchean black shales and iron formations from the Hamersley Basin. Geochim. Cosmochim. Acta 164, 523-542.

Lahtinen, R., Garde, A.A. and Melezhik, V.A. (2008) Paleoproterozoic evolution of Fennoscandia and Greenland. Episodes 31, 20.

Lalonde, S.V. and Konhauser, K.O. (2015) Benthic perspective on Earth's oldest evidence for oxygenic photosynthesis. Proc. Natl. Acad. Sci. 112, 995-1000.

Langmuir, C.H. and Forsyth, D.W. (2007) Mantle melting beneath mid-ocean ridges. Oceanogr. 20, 78-89.

Large, R.R., Halpin, J.A., Danyushevsky, L.V., Maslennikov, V.V., Bull, S.W., Long, J.A., Gregory, D.D., Lounejeva, E., Lyons, T.W., Sack, P.J., McGoldrick, P.J. and Calver, C.R. (2014) Trace element content of sedimentary pyrite as a new proxy for deep-time ocean–atm. evolution. Earth Planet. Sci. Lett. 389, 209-220.

Lewan, M. and Maynard, J. (1982) Factors controlling enrichment of vanadium and nickel in the bitumen of organic sedimentary rocks. Geochim. Cosmochim. Acta 46, 2547-2560.

Lewan, M.D. (1984) Factors controlling the proportionality of vanadium to nickel in crude oils. Geochim. Cosmochim. Acta 48, 2231-2238.

Li, W., Czaja, A.D., Van Kranendonk, M.J., Beard, B.L., Roden, E.E. and Johnson, C.M. (2013) An anoxic, Fe(II)-rich, U-poor ocean 3.46 billion years ago. Geochim. Cosmochim. Acta 120, 65-79.

Liu, C.T. and He, Y.S. (2021) Rise of major subaerial landmasses about 3.0 to 2.7 billion years ago. Geochem. Perspect. Lett. 18, 1-5.

Liu, J., Touboul, M., Ishikawa, A., Walker, R.J. and Graham Pearson, D. (2016) Widespread tungsten isotope anomalies and W mobility in crustal and mantle rocks of the Eoarchean Saglek Block, northern Labrador, Canada: Implications for early Earth processes and W recycling. Earth Planet. Sci. Lett. 448, 13-23.

Liu, W., Hao, J., Elzinga, E.J., Piotrowiak, P., Nanda, V., Yee, N. and Falkowski, P.G. (2020) Anoxic photogeochemical oxidation of manganese carbonate yields manganese oxide. Proc. Natl. Acad. Sci. 117, 22698-22704.

Louis, A.D. and Stein, B.J. (1990) The chemical evolution of Precambrian seawater: evidence from REEs in banded iron formations. Geochim. Cosmochim. Acta 54, 2965-2977.

Lowe, D.R. and Byerly, G.R. (1999) Geologic evolution of the Barberton greenstone belt, South Africa. Geological Society of America.

Luo, G., Ono, S., Beukes, N.J., Wang, D.T., Xie, S. and Summons, R.E. (2016) Rapid oxygenation of Earth's atmosphere 2.33 billion years ago. Science advances 2, e1600134.

Lyons, T.W., Reinhard, C.T. and Planavsky, N.J. (2014) The rise of oxygen in Earth's early ocean and atmosphere. Nature 506, 307-315.

Macfarlane, A.W., Danielson, A. and Holland, H.D. (1994a) Geology and major and trace element chemistry of late Archean weathering profiles in the Fortescue Group, Western Australia: implications for atmospheric PO_2. Precambrian Res. 65, 297-317.

MacFarlane, A.W., Danielson, A., Holland, H.D. and Jacobsen, S.B. (1994b) REE chemistry and Sm-Nd systematics of late Archean weathering profiles in the Fortescue Group, Western Australia. Geochim. Cosmochim. Acta 58, 1777-1794.

Macfarlane, A.W. and Holland, H.D. (1991) The timing of alkali metasomatism in paleosols. Canadian Mineralogist 29, 1043-1050.

MacGregor, A. (1927) The problem of the Precambrian atmosphere, South African Journal of Science.

Mänd, K., Lalonde, S.V., Paiste, K., Thoby, M., Lumiste, K., Robbins, L.J., Kreitsmann, T., Romashkin, A.E., Kirsimäe, K. and Lepland, A. (2021) Iron Isotopes Reveal a Benthic Iron Shuttle in the Palaeoproterozoic Zaonega Formation: Basinal Restriction, Euxinia, and the Effect on Global Palaeoredox Proxies. Minerals 11, 368.

Mänd, K., Lalonde, S.V., Robbins, L.J., Thoby, M., Paiste, K., Kreitsmann, T., Paiste, P., Reinhard, C.T., Romashkin, A.E. and Planavsky, N.J. (2020) Palaeoproterozoic oxygenated oceans following the Lomagundi–Jatuli Event. Nat. Geosci. 13, 302-306.

Martin, A.P., Condon, D.J., Prave, A.R., Melezhik, V.A., Lepland, A. and Fallick, A.E. (2013) Dating the termination of the Palaeoproterozoic Lomagundi-Jatuli carbon isotopic event in the North Transfennoscandian Greenstone Belt. Precambrian Res. 224, 160-168.

Martin, A.P., Prave, A., Condon, D., Lepland, A., Fallick, A.E., Romashkin, A., Medvedev, P. and Rychanchik, D. (2015) Multiple Palaeoproterozoic carbon burial episodes and excursions. Earth Planet. Sci. Lett. 424, 226-236.

Mayer, A.J. and Wieser, M.E. (2014) The absolute isotopic composition and atomic weight of molybdenum in SRM 3134 using an isotopic double-spike. J Anal Atom Spectrom 29, 85-94.

Mazza, S.E., Stracke, A., Gill, J.B., Kimura, J.-I. and Kleine, T. (2020) Tracing dehydration and melting of the subducted slab with tungsten isotopes in arc lavas. Earth Planet. Sci. Lett. 530, 115942.

McCulloch, M.T. and Bennett, V.C. (1994) Progressive growth of the Earth's continental crust and depleted mantle: Geochemical constraints. Geochim. Cosmochim. Acta 58, 4717-4738.

McManus, J., Nägler, T.F., Siebert, C., Wheat, C.G. and Hammond, D.E. (2002) Oceanic molybdenum isotope fractionation: Diagenesis and hydrothermal ridge-flank alteration. Geochem. Geophys. Geosyst. 3, 1-9.

Melezhik, V., Prave, A.R., Hanski, E.J., Fallick, A.E., Lepland, A., Kump, L.R. and Strauss, H. (2012a) Reading the archive of earth's oxygenation: Volume 3: Global Events and the Fennoscandian Arctic Russia-Drilling Early Earth Project.

Melezhik, V.A. and Fallick, A.E. (2001) Palaeoproterozoic travertines of volcanic affiliation from a 13C-rich rift lake environment. Chem. Geol. 173, 293-312.

Melezhik, V.A., Fallick, A.E., Brasier, A.T. and Lepland, A. (2015) Carbonate deposition in the Palaeoproterozoic Onega basin from Fennoscandia: a spotlight on the transition from the Lomagundi-Jatuli to Shunga events. Earth-Sci Rev 147, 65-98.

Melezhik, V.A., Fallick, A.E., Filippov, M.M. and Larsen, O. (1999) Karelian shungite—an indication of 2.0-Ga-old metamorphosed oil-shale and generation of petroleum: geology, lithology and geochemistry. Earth-Sci Rev 47, 1-40.

Melezhik, V.A., Fallick, A.E., Filippov, M.M., Lepland, A., Rychanchik, D.V., Deines, Y.E., Medvedev, P.V., Romashkin, A.E. and Strauss, H. (2009) Petroleum surface oil seeps from a Palaeoproterozoic petrified giant oilfield. Terra Nova 21, 119-126.

Melezhik, V.A., Filippov, M.M. and Romashkin, A.E. (2004) A giant Palaeoproterozoic deposit of shungite in NW Russia: genesis and practical applications. Ore Geol. Rev. 24, 135-154.

Melezhik, V.A., Huhma, H., Condon, D.J., Fallick, A.E. and Whitehouse, M.J. (2007) Temporal constraints on the Paleoproterozoic Lomagundi-Jatuli carbon isotopic event. Geol. 35, 655-658.

Melezhik, V.A., Prave, A., Fallick, A.E., Hanski, E.J., Kump, L.R. and Strauss, H. (2012b) Reading the Archive of Earth's Oxygenation, Volume 2: The Core Archive of the Fennoscandian Arctic Russia – Drilling Early Earth Project.

Melezhik, V.A., Prave, A.R., Fallick, A.E., Hanski, E.J., Lepland, A., Kump, L.R. and Strauss, H. (2013) Reading the Archive of Earth's Oxygenation Volume 2: The Core Archive of the Fennoscandian Arctic Russia - Drilling Early Earth Project.

Miller, C.A., Peucker-Ehrenbrink, B., Walker, B.D. and Marcantonio, F. (2011) Re-assessing the surface cycling of molybdenum and rhenium. Geochim. Cosmochim. Acta 75, 7146-7179.

Mohajerin, T.J., Helz, G.R. and Johannesson, K.H. (2016) Tungsten-molybdenum fractionation in estuarine environments. Geochim. Cosmochim. Acta 177, 105-119.

Mohajerin, T.J., Helz, G.R., White, C.D. and Johannesson, K.H. (2014) Tungsten speciation in sulfidic waters: Determination of thiotungstate formation constants and modeling their distribution in natural waters. Geochim. Cosmochim. Acta 144, 157-172.

Mole, D.R., Barnes, S.J., Yao, Z., White, A.J.R., Maas, R. and Kirkland, C.L. (2018) The Archean Fortescue large igneous province: A result of komatiite contamination by a distinct Eo-Paleoarchean crust. Precambrian Res. 310, 365-390.

Moore, E.K., Hao, J., Spielman, S.J. and Yee, N. (2020) The evolving redox chemistry and bioavailability of vanadium in deep time. Geobiology 18, 127-138.

Morford, J.L. and Emerson, S. (1999) The geochemistry of redox sensitive trace metals in sediments. Geochim. Cosmochim. Acta 63, 1735-1750.

Muir, B., Andrunik, D., Hyla, J. and Bajda, T. (2017) The removal of molybdates and tungstates from aqueous solution by organo-smectites. Appl. Clay Sci. 136, 8-17.

Murakami, T., Matsuura, K. and Kanzaki, Y. (2016) Behaviors of trace elements in Neoarchean and Paleoproterozoic paleosols: Implications for atmospheric oxygen evolution and continental oxidative weathering. Geochim. Cosmochim. Acta 192, 203-219.

Nägler, T.F., Neubert, N., Böttcher, M.E., Dellwig, O. and Schnetger, B. (2011) Molybdenum isotope fractionation in pelagic euxinia: Evidence from the modern Black and Baltic Seas.

Chem. Geol. 289, 1-11.

Nägler, T.F., Siebert, C., Lüschen, H. and Böttcher, M.E. (2005) Sedimentary Mo isotope record across the Holocene fresh–brackish water transition of the Black Sea. Chem. Geol. 219, 283-295.

Neely, R.A., Gislason, S.R., Ólafsson, M., McCoy-West, A.J., Pearce, C.R. and Burton, K.W. (2018) Molybdenum isotope behaviour in groundwaters and terrestrial hydrothermal systems, Iceland. Earth Planet. Sci. Lett. 486, 108-118.

Nelson, D.R., Trendall, A.F., de Laeter, J.R., Grobler, N.J. and Fletcher, I.R. (1992) A comparative study of the geochemical and isotopic systematics of late archaean flood basalts from the pilbara and kaapvaal cratons. Precambrian Res. 54, 231-256.

Nesbitt, H. and Wilson, R. (1992) Recent chemical weathering of basalts. Am. J. Sci. 292, 740-777.

Nesbitt, H. and Young, G. (1982) Early Proterozoic climates and plate motions inferred from major element chemistry of lutites. Nature 299, 715-717.

Nisbet, E.G., Cheadle, M.J., Arndt, N.T. and Bickle, M.J. (1993) Constraining the potential temperature of the Archaean mantle: A review of the evidence from komatiites. Lithos 30, 291-307.

Nolte, N., Kleinhanns, I., Baero, W. and Hansen, B. (2011) Petrography and whole-rock geochemical characteristics of Västervik granitoids to syenitoids, southeast Sweden: constraints on petrogenesis and tectonic setting at the southern margin of the Svecofennian domain. GFF 133, 173-196.

Noordmann, J., Weyer, S., Montoya-Pino, C., Dellwig, O., Neubert, N., Eckert, S., Paetzel, M. and Böttcher, M.E. (2015) Uranium and molybdenum isotope systematics in modern euxinic basins: Case studies from the central Baltic Sea and the Kyllaren fjord (Norway). Chem. Geol. 396, 182-195.

O'Neill, H.S.C., Berry, A.J. and Eggins, S.M. (2008) The solubility and oxidation state of tungsten in silicate melts: Implications for the comparative chemistry of W and Mo in planetary differentiation processes. Chem. Geol. 255, 346-359.

Ojakangas, R.W., Marmo, J.S. and Heiskanen, K.I. (2001) Basin evolution of the Paleoproterozoic Karelian Supergroup of the Fennoscandian (Baltic) Shield. Sediment. Geol. 141-142, 255-285.

Ossa Ossa, F., Eickmann, B., Hofmann, A., Planavsky, N.J., Asael, D., Pambo, F. and Bekker,

A. (2018a) Two-step deoxygenation at the end of the Paleoproterozoic Lomagundi Event. Earth Planet. Sci. Lett. 486, 70-83.

Ossa Ossa, F., Hofmann, A., Vidal, O., Kramers, J.D., Belyanin, G. and Cavalazzi, B. (2016) Unusual manganese enrichment in the Mesoarchean Mozaan Group, Pongola Supergroup, South Africa. Precambrian Res. 281, 414-433.

Ossa Ossa, F., Hofmann, A., Wille, M., Spangenberg, J.E., Bekker, A., Poulton, S.W., Eickmann, B. and Schoenberg, R. (2018b) Aerobic iron and manganese cycling in a redox-stratified Mesoarchean epicontinental sea. Earth Planet. Sci. Lett. 500, 28-40.

Ostrander, C.M., Kendall, B., Olson, S.L., Lyons, T.W., Gordon, G.W., Romaniello, S.J., Zheng, W., Reinhard, C.T., Roy, M. and Anbar, A.D. (2020) An expanded shale δ^{98}Mo record permits recurrent shallow marine oxygenation during the Neoarchean. Chem. Geol. 532, 119391.

Ostrander, C.M., Nielsen, S.G., Owens, J.D., Kendall, B., Gordon, G.W., Romaniello, S.J. and Anbar, A.D. (2019) Fully oxygenated water columns over continental shelves before the Great Oxidation Event. Nat. Geosci. 12, 186-191.

Osvald, M., Kilpatrick, A., Rochelle, C.A., Szanyi, J., Raucsik, B., Medgyes, T. and Kóbor, B. (2021) Laboratory investigations of the physical parameters influencing the in situ leaching of tungsten. Geothermics 89, 101992.

Ovchinnikova, G.V., Kuznetsov, A.B., Melezhik, V.A., Gorokhov, I.M., Vasil'eva, I.M. and Gorokho- vskii, B.M. (2007) Pb-Pb age of Jatulian carbonate rocks: The Tulomozero Formation of southeast Karelia. Stratigr. Geol. Correl. 15, 359-372.

Paiste, K., Lepland, A., Zerkle, A., Kirsimäe, K., Izon, G., Patel, N., McLean, F., Kreitsmann, T., Mänd, K. and Bui, T. (2018) Multiple sulphur isotope records tracking basinal and global processes in the 1.98 Ga Zaonega Formation, NW Russia. Chem. Geol. 499, 151-164.

Paiste, K., Lepland, A., Zerkle, A.L., Kirsimäe, K., Kreitsmann, T., Mänd, K., Romashkin, A.E., Rychanchik, D.V. and Prave, A.R. (2020) Identifying global vs. basinal controls on Paleoproterozoic organic carbon and sulfur isotope records. Earth-Sci Rev 207, 103230.

Partin, C.A., Bekker, A., Planavsky, N.J., Scott, C.T., Gill, B.C., Li, C., Podkovyrov, V., Maslov, A., Konhauser, K.O., Lalonde, S.V., Love, G.D., Poulton, S.W. and Lyons, T.W. (2013) Large-scale fluctuations in Precambrian atmospheric and oceanic oxygen levels from the record of U in shales. Earth Planet. Sci. Lett. 369-370, 284-293.

Pavlov, A.A. and Kasting, J. (2002) Mass-independent fractionation of sulfur isotopes in Archean sediments: strong evidence for an anoxic Archean atmosphere. Astrobiol. 2, 27-41.

Petruzzelli, G. and Pedron, F. (2017) Tungstate adsorption onto Italian soils with different characteristics. Environ. Monit. Assess. 189, 379.

Petruzzelli, G. and Pedron, F. (2020) Adsorption, Desorption and Bioavailability of Tungstate in Mediterranean Soils. Soil Systems 4, 53.

Philippot, P., Ávila, J.N., Killingsworth, B.A., Tessalina, S., Baton, F., Caquineau, T., Muller, E., Pecoits, E., Cartigny, P., Lalonde, S.V., Ireland, T.R., Thomazo, C., van Kranendonk, M.J. and Busigny, V. (2018) Globally asynchronous sulphur isotope signals require redefinition of the Great Oxidation Event. Nature Communications 9, 2245.

Pidgeon, R.T. (1984) Geochronological constraints on early volcanic evolution of the Pilbara Block, Western Australia. Aust. J. Earth Sci. 31, 237-242.

Planavsky, N.J., Asael, D., Hofmann, A., Reinhard, C.T., Lalonde, S.V., Knudsen, A., Wang, X., Ossa Ossa, F., Pecoits, E., Smith, A.J.B., Beukes, N.J., Bekker, A., Johnson, T.M., Konhauser, K.O., Lyons, T.W. and Rouxel, O.J. (2014a) Evidence for oxygenic photosynthesis half a billion years before the Great Oxidation Event. Nat. Geosci. 7, 283-286.

Planavsky, N.J., McGoldrick, P., Scott, C.T., Li, C., Reinhard, C.T., Kelly, A.E., Chu, X., Bekker, A., Love, G.D. and Lyons, T.W. (2011) Widespread iron-rich conditions in the mid-Proterozoic ocean. Nature 477, 448-451.

Planavsky, N.J., Reinhard, C.T., Wang, X., Thomson, D., McGoldrick, P., Rainbird, R.H., Johnson, T., Fischer, W.W. and Lyons, T.W. (2014b) Earth history. Low mid-Proterozoic atmospheric oxygen levels and the delayed rise of animals. Science 346, 635-638.

Pogge von Strandmann, P.A.E., Opfergelt, S., Lai, Y.-J., Sigfússon, B., Gislason, S.R. and Burton, K.W. (2012) Lithium, magnesium and silicon isotope behaviour accompanying weathering in a basaltic soil and pore water profile in Iceland. Earth Planet. Sci. Lett. 339-340, 11-23.

Pokrovsky, O.S. and Schott, J. (2002) Iron colloids/organic matter associated transport of major and trace elements in small boreal rivers and their estuaries (NW Russia). Chem. Geol. 190, 141-179.

Poulson R.L., McManus, J., Severmann, S. and Berelson, W.M. (2009) Molybdenum behavior during early diagenesis: Insights from Mo isotopes. Geochem. Geophys. Geosyst. 10 Q06010

Poulson, R.L., Siebert, C., McManus, J. and Berelson, W.M. (2006) Authigenic molybdenum isotope signatures in marine sediments. Geol. 34, 617.

Poulton, S.W., Bekker, A., Cumming, V.M., Zerkle, A.L., Canfield, D.E. and Johnston, D.T. (2021) A 200-million-year delay in permanent atmospheric oxygenation. Nature 592, 232-236.

Poulton, S.W., Fralick, P.W. and Canfield, D.E. (2004) The transition to a sulphidic ocean approximately 1.84 billion years ago. Nature 431, 173-177.

Pourmand, A., Dauphas, N. and Ireland, T.J. (2012) A novel extraction chromatography and MC-ICP-MS technique for rapid analysis of REE, Sc and Y: Revising CI-chondrite and Post-Archean Australian Shale (PAAS) abundances. Chem. Geol. 291, 38-54.

Prasad, N. and Roscoe, S. (1996) Evidence of anoxic to oxic atmospheric change during 2.45-2.22 Ga from lower and upper sub-Huronian paleosols, Canada. Catena 27, 105-121.

Prave, A.R., Kirsimäe, K., Lepland, A., Fallick, A.E., Kreitsmann, T., Deines, Y.E., Romashkin, A.E., Rychanchik, D.V., Medvedev, P.V., Moussavou, M., Bakakas, K. and Hodgskiss, M.S.W. (2021) The grandest of them all: the Lomagundi–Jatuli Event and Earth's oxygenation. J. Geol. Soc., jgs2021-2036.

Puchtel, I., Arndt, N., Hofmann, A., Haase, K., Kröner, A., Kulikov, V., Kulikova, V., Garbe-Schönberg, C.-D. and Nemchin, A. (1998) Petrology of mafic lavas within the Onega plateau, central Karelia: evidence for 2.0 Ga plume-related continental crustal growth in the Baltic Shield. Contrib. Mineral. Petrol. 130, 134-153.

Puchtel, I., Brügmann, G. and Hofmann, A. (1999) Precise Re–Os mineral isochron and Pb–Nd–Os isotope systematics of a mafic–ultramafic sill in the 2.0 Ga Onega plateau (Baltic Shield). Earth Planet. Sci. Lett. 170, 447-461.

Qu, Y., Črne, A.E., Lepland, A. and van Zuilen, M.A. (2012) Methanotrophy in a Paleoproterozoic oil field ecosystem, Zaonega Formation, Karelia, Russia. Geobiology 10, 467-478.

Qu, Y., Lepland, A., van Zuilen, M.A., Whitehouse, M., Črne, A.E. and Fallick, A.E. (2018) Sample-scale carbon isotopic variability and diverse biomass in the Paleoproterozoic Zaonega Formation, Russia. Precambrian Res. 315, 222-231.

Qu, Y., van Zuilen, M.A. and Lepland, A. (2020) Hydrothermal circulation and oil migration at the root of the heterogeneous micro-structure of carbonaceous material in the 2.0 Ga Zaonega Formation, Onega Basin, Russia. Precambrian Res. 343, 105705.

Reinhard, C.T., Raiswell, R., Scott, C., Anbar, A.D. and Lyons, T.W. (2009) A late Archean sulfidic sea stimulated by early oxidative weathering of the continents. Science 326, 713-716.

Rino, S., Komiya, T., Windley, B.F., Katayama, I., Motoki, A. and Hirata, T. (2004) Major episodic increases of continental crustal growth determined from zircon ages of river sands; implications for mantle overturns in the Early Precambrian. Phys. Earth Planet. Inter. 146, 369-394.

Ripley, E.M., Shaffer, N.R. and Gilstrap, M.S. (1990) Distribution and geochemical characteristics of metal enrichment in the New Albany Shale (Devonian-Mississippian), Indiana. Econ Geol 85, 1790-1807.

Rodler, A.S., Hohl, S.V., Guo, Q. and Frei, R. (2016) Chromium isotope stratigraphy of Ediacaran cap dolostones, Doushantuo Formation, South China. Chem. Geol. 436, 24-34.

Romaniello, S.J., Herrmann, A.D. and Anbar, A.D. (2016) Syndepositional diagenetic control of molybdenum isotope variations in carbonate sediments from the Bahamas. Chem. Geol. 438, 84-90.

Rongemaille, E., Bayon, G., Pierre, C., Bollinger, C., Chu, N.C., Fouquet, Y., Riboulot, V. and Voisset, M. (2011) Rare earth elements in cold seep carbonates from the Niger delta. Chem. Geol. 286, 196-206.

Roué, L., Kurzweil, F., Wille, M., Wegwerth, A., Dellwig, O., Münker, C. and Schoenberg, R. (2021) Stable W and Mo isotopic evidence for increasing redox-potentials from the Paleoarchean towards the Paleoproterozoic deep Ocean. Geochim. Cosmochim. Acta 309, 366-387.

Rudnick, R.L. and Gao, S. (2014) 4.1 - Composition of the Continental Crust, in: Holland, H.D., Turekian, K.K. (Eds.), Treatise on Geochemistry (Second Edition). Elsevier, Oxford, pp. 1-51.

Rudnick, R.L., Tomascak, P.B., Njo, H.B. and Gardner, L.R. (2004) Extreme lithium isotopic fractionation during continental weathering revealed in saprolites from South Carolina. Chem. Geol. 212, 45-57.

Rye, R. and Holland, H.D. (1998) Paleosols and the evolution of atmospheric oxygen: a critical review. Am. J. Sci. 298, 621-672.

Sadiq, M. (1988) Thermodynamic solubility relationships of inorganic vanadium in the marine environment. Mar. Chem. 23, 87-96.

Satkoski, A.M., Beukes, N.J., Li, W., Beard, B.L. and Johnson, C.M. (2015) A redox-stratified ocean 3.2 billion years ago. Earth Planet. Sci. Lett. 430, 43-53.

Schauble, E.A. (2004) Applying stable isotope fractionation theory to new systems. Rev. Mineral. Geochem. 55, 65-111.

Scheiderich, K., Zerkle, A.L., Helz, G.R., Farquhar, J. and Walker, R.J. (2010) Molybdenum isotope, multiple sulfur isotope, and redox-sensitive element behavior in early Pleistocene Mediterranean sapropels. Chem. Geol. 279, 134-144.

Schlesinger, W.H., Klein, E.M. and Vengosh, A. (2017) Global biogeochemical cycle of vanadium. Proc. Natl. Acad. Sci. 114, E11092-E11100.

Schoenberg, R., Kamber, B.S., Collerson, K.D. and Moorbath, S. (2002) Tungsten isotope evidence from ∼3.8-Gyr metamorphosed sediments for early meteorite bombardment of the Earth. Nature 418, 403-405.

Scholz, F., Hensen, C., Noffke, A., Rohde, A., Liebetrau, V. and Wallmann, K. (2011) Early diagenesis of redox-sensitive trace metals in the Peru upwelling area – response to ENSO-related oxygen fluctuations in the water column. Geochim. Cosmochim. Acta 75, 7257-7276.

Scholz, F., Schmidt, M., Hensen, C., Eroglu, S., Geilert, S., Gutjahr, M. and Liebetrau, V. (2019) Shelf-to-basin iron shuttle in the Guaymas Basin, Gulf of California. Geochim. Cosmochim. Acta 261, 76-92.

Scholz, F., Siebert, C., Dale, A.W. and Frank, M. (2017) Intense molybdenum accumulation in sediments underneath a nitrogenous water column and implications for the reconstruction of paleo-redox conditions based on molybdenum isotopes. Geochim. Cosmochim. Acta 213, 400-417.

Scott, C., Lyons, T., Bekker, A., Shen, Y.-a., Poulton, S., Chu, X.-l. and Anbar, A. (2008) Tracing the stepwise oxygenation of the Proterozoic ocean. Nature 452, 456-459.

Scott, C. and Lyons, T.W. (2012) Contrasting molybdenum cycling and isotopic properties in euxinic versus non-euxinic sediments and sedimentary rocks: Refining the paleoproxies. Chem. Geol. 324-325, 19-27.

Scott, C., Slack, J.F. and Kelley, K.D. (2017) The hyper-enrichment of V and Zn in black shales of the Late Devonian-Early Mississippian Bakken Formation (USA). Chem. Geol. 452, 24-33.

Scott, C., Wing, B.A., Bekker, A., Planavsky, N.J., Medvedev, P., Bates, S.M., Yun, M. and Lyons, T.W. (2014) Pyrite multiple-sulfur isotope evidence for rapid expansion and contraction of the early Paleoproterozoic seawater sulfate reservoir. Earth Planet. Sci. Lett. 389, 95-104.

Sen Tuna, G. and Braida, W. (2014) Evaluation of the Adsorption of Mono- and Polytungstates onto Different Types of Clay Minerals and Pahokee Peat. Soil and Sediment Contamination: An International Journal 23, 838-849.

Sharp, Z. (2017) Principles of Stable Isotope Geochemistry, 2nd Edition.

Siebert, C., Kramers, J., Meisel, T., Morel, P. and Nägler, T.F. (2005) PGE, Re-Os, and Mo isotope systematics in Archean and early Proterozoic sedimentary systems as proxies for redox conditions of the early Earth. Geochim. Cosmochim. Acta 69, 1787-1801.

Siebert, C., Nagler, T.F., von Blanckenburg, F. and Kramers, J.D. (2003) Molybdenum isotope records as a potential new proxy for paleoceanography. Earth Planet. Sci. Lett. 211, 159-171.

Sindol, G.P., Babechuk, M.G., Petrus, J.A. and Kamber, B.S. (2020) New insights into Paleoproterozoic surficial conditions revealed by 1.85 Ga corestone-rich saprolith. Chem. Geol. 545, 119621.

Sohrin, Y., Fujishima, Y., Ueda, K., Akiyama, S., Mori, K., Hasegawa, H. and Matsui, M. (1998) Dissolved niobium and tantalum in the North Pacific. Geophys. Res. Lett. 25, 999-1002.

Sohrin, Y., Isshiki, K., Kuwamoto, T. and Nakayama, E. (1987) Tungsten in north Pacific waters. Mar. Chem. 22, 95-103.

Sorokin, Y.I. (1972) The bacterial population and the processes of hydrogen sulphide oxidation in the Black Sea. ICES J. Mar. Sci. 34, 423-454.

Swanner, E.D., Wu, W., Schoenberg, R., Byrne, J., Michel, F.M., Pan, Y. and Kappler, A. (2015) Fractionation of Fe isotopes during Fe(II) oxidation by a marine photoferrotroph is controlled by the formation of organic Fe-complexes and colloidal Fe fractions. Geochim. Cosmochim. Acta 165, 44-61.

Szalay, A. and Szilagyi, M. (1967) The association of vanadium with humic acids. Geochim. Cosmochim. Acta 31, 1-6.

Takeno, N. (2005) Atlas of Eh-pH diagrams Intercomparison of thermodynamic databases. . National Institute of Advanced Industrial Science and Technology.

Tang, M., Chen, K. and Rudnick, R.L. (2016) Archean upper crust transition from mafic to felsic marks the onset of plate tectonics. Science 351, 372-375.

Taylor, S.R. and McLennan, S.M. (1995) The geochemical evolution of the continental crust.

Rev. Geophys. 33, 241-265.

Teitler, Y., Philippot, P., Gérard, M., Le Hir, G., Fluteau, F. and Ader, M. (2015) Ubiquitous occurrence of basaltic-derived paleosols in the Late Archean Fortescue Group, Western Australia. Precambrian Res. 267, 1-27.

Temiz, U., Koçak, İ., Öksüz, N. and Akbay, S. (2021) Significance of neotectonic and paleoclimatic Late Pleistocene–Holocene travertine and origins: Balkayası, Avanos—Nevsehir, Central Anatolia/Turkey. International Journal of Earth Sciences 110, 2157-2177.

Thoby, M., Konhauser, K.O., Fralick, P.W., Altermann, W., Visscher, P.T. and Lalonde, S.V. (2019) Global importance of oxic molybdenum sinks prior to 2.6 Ga revealed by the Mo isotope composition of Precambrian carbonates. Geol. 47, 559-562.

Thorne, A. and Trendall, A.F. (2001) Geology of the Fortescue Group, Pilbara Craton, Western Australia. Geological Survey of Western Australia.

Tissot, B.P. and Welte, D.H. (1984) From Kerogen to Petroleum, Petroleum Formation and Occurrence. Springer Berlin Heidelberg, Berlin, Heidelberg, pp. 160-198.

Tissot, F.L.H., Chen, C., Go, B.M., Naziemiec, M., Healy, G., Bekker, A., Swart, P.K. and Dauphas, N. (2018) Controls of eustasy and diagenesis on the 238U/235U of carbonates and evolution of the seawater (234U/238U) during the last 1.4 Myr. Geochim. Cosmochim. Acta 242, 233-265.

Tossell, J.A. (2005) Calculating the partitioning of the isotopes of Mo between oxidic and sulfidic species in aqueous solution. Geochim. Cosmochim. Acta 69, 2981-2993.

Tostevin, R., Shields, G.A., Tarbuck, G.M., He, T., Clarkson, M.O. and Wood, R.A. (2016) Effective use of cerium anomalies as a redox proxy in carbonate-dominated marine settings. Chem. Geol. 438, 146-162.

Trendall, A.F. (2002) The Significance of Iron-Formation in the Precambrian Stratigraphic Record, Precambrian Sedimentary Environments, pp. 33-66.

Tsikos, H., Moore, J.M. and Harris, C. (2001) Geochemistry of the Palæoproterozoic Mooidraai Formation: Fe-rich limestone as end member of iron formation deposition, Kalahari Manganese Field, Transvaal Supergroup, South Africa. J. Afr. Earth. Sci. 32, 19-27.

Tsujisaka, M., Nishida, S., Takano, S., Murayama, M. and Sohrin, Y. (2020) Constraints on redox conditions in the Japan Sea in the last 47,000 years based on Mo and W as palaeoceanographic proxies. Geochem. J. 54, 351-363.

Tsujisaka, M., Takano, S., Murayama, M. and Sohrin, Y. (2019) Precise analysis of the concentrations and isotopic compositions of molybdenum and tungsten in geochemical reference materials. Anal. Chim. Acta.

Tuna, G.S., Braida, W., Ogundipe, A. and Strickland, D. (2012) Assessing tungsten transport in the vadose zone: from dissolution studies to soil columns. Chemosphere 86, 1001-1007.

Turner, D.R., Whitfield, M. and Dickson, A.G. (1981) The equilibrium speciation of dissolved components in freshwater and sea water at 25°C and 1 atm pressure. Geochim. Cosmochim. Acta 45, 855-881.

Tusch, J., Sprung, P., van de Löcht, J., Hoffmann, J.E., Boyd, A.J., Rosing, M.T. and Münker, C. (2019) Uniform 182W isotope compositions in Eoarchean rocks from the Isua region, SW Greenland: The role of early silicate differentiation and missing late veneer. Geochim. Cosmochim. Acta 257, 284-310.

Urey, H.C. (1947) The thermodynamic properties of isotopic substances. J. Chem. Soc., 562-581.

Vacquier, V. (1991) The origin of terrestrial heat flow. Geophys. J. Int. 106, 199-202.

Van Kranendonk, M.J., Hugh Smithies, R., Hickman, A.H. and Champion, D.C. (2007) Review: secular tectonic evolution of Archean continental crust: interplay between horizontal and vertical processes in the formation of the Pilbara Craton, Australia. Terra Nova 19, 1-38.

Viers, J., Dupre, B. and Gaillardet, J. (2009) Chemical composition of suspended sediments in World Rivers: New insights from a new database. Sci Total Environ 407, 853-868.

Voegelin, A.R., Nägler, T.F., Beukes, N.J. and Lacassie, J.P. (2010) Molybdenum isotopes in late Archean carbonate rocks: Implications for early Earth oxygenation. Precambrian Res. 182, 70-82.

Voegelin, A.R., Nägler, T.F., Samankassou, E. and Villa, I.M. (2009) Molybdenum isotopic composition of modern and Carboniferous carbonates. Chem. Geol. 265, 488-498.

Von Blanckenburg, F., Mamberti, M., Schoenberg, R., Kamber, B.S. and Webb, G.E. (2008) The iron isotope composition of microbial carbonate. Chem. Geol. 249, 113-128.

Von Damm, K.L., Edmond, J.M., Grant, B., Measures, C.I., Walden, B. and Weiss, R.F. (1985) Chemistry of submarine hydrothermal solutions at 21 °N, East Pacific Rise. Geochim. Cosmochim. Acta 49, 2197-2220.

Vorlicek, T.P., Kahn, M.D., Kasuya, Y. and Helz, G.R. (2004) Capture of molybdenum in pyrite-forming sediments: role of ligand-induced reduction by polysulfides 1. Geochim. Cosmochim. Acta 68, 547-556.

Walter, M.J. (1998) Melting of Garnet Peridotite and the Origin of Komatiite and Depleted

Lithosphere. J. Petrol. 39, 29-60.

Wang, Z., Ma, J., Li, J., Wei, G., Zeng, T., Li, L., Zhang, L., Deng, W., Xie, L. and Liu, Z. (2018) Fe (hydro) oxide controls Mo isotope fractionation during the weathering of granite. Geochim. Cosmochim. Acta 226, 1-17.

Wanty, R.B. and Goldhaber, M.B. (1992) Thermodynamics and kinetics of reactions involving vanadium in natural systems: Accumulation of vanadium in sedimentary rocks. Geochim. Cosmochim. Acta 56, 1471-1483.

Warke, M.R. and Schröder, S. (2018) Synsedimentary fault control on the deposition of the Duitschland Formation (South Africa): Implications for depositional settings, Paleoproterozoic stratigraphic correlations, and the GOE. Precambrian Res. 310, 348-364.

Wegwerth, A., Eckert, S., Dellwig, O., Schnetger, B., Severmann, S., Weyer, S., Bruske, A., Kaiser, J., Koster, J., Arz, H.W. and Brumsack, H.J. (2018) Redox evolution during Eemian and Holocene sapropel formation in the Black Sea. Palaeogeography Palaeoclimatology Palaeoecology 489, 249-260.

Wheat, C.G., Mottl, M.J. and Rudnicki, M. (2002) Trace element and REE composition of a low-temperature ridge-flank hydrothermal spring. Geochim. Cosmochim. Acta 66, 3693-3705.

Willbold, M. and Elliott, T. (2017) Molybdenum isotope variations in magmatic rocks. Chem. Geol. 449, 253-268.

Willbold, M., Hibbert, K., Lai, Y.J., Freymuth, H., Hin, R.C., Coath, C., Vils, F. and Elliott, T. (2016) High-Precision Mass-Dependent Molybdenum Isotope Variations in Magmatic Rocks Determined by Double-Spike MC-ICP-MS. Geostand. Geoanal. Res. 40, 389-403.

Wille, M., Babechuk, M.G., Kleinhanns, I.C., Stegmaier, J., Suhr, N., Widdowson, M., Kamber, B.S. and Schoenberg, R. (2018) Silicon and chromium stable isotopic systematics during basalt weathering and lateritisation: A comparison of variably weathered basalt profiles in the Deccan Traps, India. Geoderma 314, 190-204.

Wille, M., Kramers, J.D., Nägler, T.F., Beukes, N.J., Schröder, S., Meisel, T., Lacassie, J.P. and Voegelin, A.R. (2007) Evidence for a gradual rise of oxygen between 2.6 and 2.5Ga from Mo isotopes and Re-PGE signatures in shales. Geochim. Cosmochim. Acta 71, 2417-2435.

Wille, M., Nebel, O., Van Kranendonk, M.J., Schoenberg, R., Kleinhanns, I.C. and Ellwood, M.J. (2013) Mo–Cr isotope evidence for a reducing Archean atmosphere in 3.46–2.76Ga black shales from the Pilbara, Western Australia. Chem. Geol. 340, 68-76.

Wronkiewicz, D.J. and Condie, K.C. (1987) Geochemistry of Archean shales from the Witwatersrand Supergroup, South Africa: source-area weathering and provenance. Geochim. Cosmochim. Acta 51, 2401-2416.

Yang, W., Gao, Y. and Casey, J. (2018) Determination of Trace Elements in Crude Oils and Fuel Oils: AComprehensive Review and New Data, pp. 159-205.

Yang, W., Holland, H.D. and Rye, R. (2002) Evidence for low or no oxygen in the late Archean atmosphere from the ∼2.76 Ga Mt. Roe #2 paleosol, Western Australia: Part 3. Geochim. Cosmochim. Acta 66, 3707-3718.

Yano, M., Yasukawa, K., Nakamura, K., Ikehara, M. and Kato, Y. (2020) Geochemical Features of Redox-Sensitive Trace Metals in Sediments under Oxygen-Depleted Marine Environments. Minerals 10, 1021.

Yin, Q., Jacobsen, S., Yamashita, K., Blichert-Toft, J., Télouk, P. and Albarede, F. (2002) A short timescale for terrestrial planet formation from Hf–W chronometry of meteorites. Nature 418, 949-952.

Zhang, F., Lenton, T.M., del Rey, Á., Romaniello, S.J., Chen, X., Planavsky, N.J., Clarkson, M.O., Dahl, T.W., Lau, K.V., Wang, W., Li, Z., Zhao, M., Isson, T., Algeo, T.J. and Anbar, A.D. (2020) Uranium isotopes in marine carbonates as a global ocean paleoredox proxy: A critical review. Geochim. Cosmochim. Acta.

Zheng, Y., Anderson, R.F., van Geen, A. and Kuwabara, J. (2000) Authigenic molybdenum formation in marine sediments: a link to pore water sulfide in the Santa Barbara Basin. Geochim. Cosmochim. Acta 64, 4165-4178.